BICEP Array Detectors and Instrumentation at 30/40 GHz: Design, Performance, and Deployment to the South Pole for Constraining Primordial Gravitational Waves

Thesis by
Ahmed Mohamed Soliman (أحمد محمد سليمان)

In Partial Fulfillment of the Requirements for the
Degree of
Doctor of Philosophy

CALIFORNIA INSTITUTE OF TECHNOLOGY
Pasadena, California

2023
Defended February 6, 2023

Ahmed Mohamed Soliman (أحمد محمد سليمان)
ORCID: 0009-0007-9335-1326

ACKNOWLEDGEMENTS

I first would like to thank my advisor Jamie Bock for his support, mentorship, and invaluable guidance through my graduate school to be a better scientist. I came from an engineering background and I couldn't have achieved my passion in science without his help and patience. Jamie is a great scientist and wonderful person who has influenced me a lot on my PhD journey. I also would like to thank my co-advisor Jakob Van Zyl (RIP) for supporting me from day one of my PhD program. I will never forget Jakob for all his unconditional support. I would briefly send a message to his family; "Jakob was a great friend. I really miss him so much."

I would like to express my deepest acknowledgement to the members of my doctoral committee, including Professors Barry Barish and Sunil Golwala, for their continuous encouragement and support throughout my PhD. I also would like to thank my direct mentor Roger O'Brient for our productive discussions and exchanging ideas about the detector design, resulting in our innovative detector work in this thesis. He taught me lots of research skills that positively impacted my PhD. I also owe a deep thanks to Bryan Steinbach for supervising me on detector tests and analysis until I become an independent researcher. I was lucky to work with a wonderful team in the CMB group members at Caltech, who had an enormous impact on this work as well. I was blessed to work with my colleagues in the lab Lorenzo Moncelsi, Alessandro Schillaci, Sinan Kefeli, Ritoban Basu Thakur, Jon Hunacek, Howard Hui, Cheng Zhang, Silvia Zhang, Hien Nguyen, Albert Wandui, and Lorenzo Minutolo. I was also really blessed to work with brilliant students, postdoctoral researchers, scientists, and professors as part of the BICEP/Keck Collaboration. We shared amazing team work and friendships, during our collaboration meetings and our BICEP Array project deployment at the South Pole. I have gained a wide range of skills from working with these amazing people. I also had a great time working with Marion Dierickx, James Cornelison, Jamie Cheshire, and Kenny Lau at the South Pole.

I would like to thank the National Science Foundation (NSF) for funding our BICEP Array Telescope and providing the operation and support during BICEP Array deployment to the South Pole. It was my honor to be a contributor and member of the two awarded projects, "Collaborative Research: Imaging the Beginning of Time from the South Pole: The next Stage of the BICEP Program", and " MRI: Development of a 150 GHz Receiver for the BICEP Array CMB Polarimeter". A special thanks to NASA for funding our detectors, which were fabricated at the

Microdevices lab (MDL), Jet Propulsion Laboratory (JPL).

I am grateful to our role model in Egypt, Professor Ahmed Zewail (RIP) for his unconditional guidance with various challenges during my earlier time at Caltech. I feel so fortunate to meet Zewail at Caltech who has influenced me on science together with my engineering background. I have been also privileged to learn a lot from Professor Kip Thorne who initially guided me for my PhD. In 2016, I came to Kip's office to ask for some advice about my PhD research plan. Kip inspired me about astrophysics and who I want to express my gratitude to on my way to science. I also would like thank Professor Rudolph Marcus for his guidance and productive conversations during my earlier time at Caltech in 2015. I am grateful to my wonderful friends in the graduate office and the International Student Office; Douglas Rees, Natalie Gilmore, Laura Flower, Daniel Yoder, and Jennifer Blankenship for the invaluable guidance and support during my PhD journey. They make me feel like I have another family at Caltech along with my family in Egypt. I also thank my friends in Los Angeles, including Dr. Mohamed Aly (formal Caltech PhD graduate) for his great friendship.

I am also grateful to my wonderful parent, Mohamed Soliman (محمد سليمان) and Fatma Abu El-Azm (فاطمة عبد المهيمن أبو العزم) for keeping me in their prayers every day in Egypt. You have always been there and I am blessed to have you in my life as well as my beautiful siblings Hajar (هاجر) and Omar (عمر). I also would like to thank the love of my life, my beautiful wife Eman Badr (إيمان بدر) for her love and unconditional support since I have met her in 2011, Cairo, Egypt. Eman; I love you for everything that you have done for me. Thanks for taking care of our beautiful kids, Noah (نُوْح) and Aaron (هَارُونِ) when I was at the South Pole. Thanks for being on my side when I worked during the holidays or stayed in the lab till 3 a.m. for taking a high quality data. Special thanks to my father-in-law Badr Eldin Abdel-ghafar (بدر الدين عبد الغفار) and my mother-in-law Afaf Hassan (عفاف حسن) for coming to the US to help my wife while I was at the South Pole for two seasons. I love you all and I wish a long life of happiness.

ABSTRACT

The discovery of the Cosmic Microwave Background (CMB) in the 1960s has provided strong observational evidence for the Big Bang cosmological model to describe the origin and evolution of the universe. The theory of cosmic inflation was developed in the 1980s to account for the initial density perturbations by a period of exponential expansion in the early Universe to solve the horizon, flatness and monopole problems. Many inflation models predict potentially detectable primordial gravitational-waves (PGWs) background that imprint a B-mode polarization pattern in the CMB. The amplitude of the inflationary B-mode polarization depends on the energy scale of inflation and is parameterized by the tensor-to-scalar ratio r. The detection of a B-mode pattern would open a new window to probe the energy scale at the beginning of time when the universe was a mere fraction of a second old after the Big Bang.

The BICEP/Keck collaboration is building a series of experiments located at the Amundsen-Scott South Pole Station to map the polarization of the CMB at degree angular scales using small-aperture telescopes. Our latest BICEP/Keck publications use data collected through 2018 and report the strongest constraints $r_{0.05} < 0.036$ at 95% confidence. The current sensitivity on r is limited by the variance from the gravitational lensing. BICEP/Keck is starting a collaboration with the South Pole Telescope (SPT) team to develop delensing techniques to improve future constraints on r. Characterizing Galactic foregrounds, especially synchrotron emission, remains a priority in order to improve constraints as statistical sensitivity continues to improve. The motivation for this thesis is to develop a highly sensitive receiver at 30 and 40 GHz, at frequencies where the synchrotron foreground dominates. BICEP Array represents the latest phase in the BICEP/Keck experiments, and will map the polarization of the CMB at 30/40, 95, 150, and 220/270 GHz. BICEP Array will search for PGWs with unprecedented sensitivity levels on r by characterizing and removing Galactic synchrotron and dust emission from our maps of the CMB.

My PhD thesis focuses on the technology development for high sensitivity detectors and instrumentation to successfully deploy the first BICEP Array receiver at 30 GHz and 40 GHz to the South Pole in order to constrain the Galactic synchrotron foreground. My dissertation presents the receiver design and performance. I will first explain the engineering design principles, the fabrication and a laboratory demonstration of single-color antenna-coupled Transition Edge Sensor (TES) bolometers.

Secondly, I will discuss the design and demonstration of dual-color detectors at 30 and 40 GHz that gain receiver sensitivity by increasing the optical throughput and bandwidth of each pixel. I also developed microstrip diplexer circuits that divide the detector bandwidth into two CMB observing channels. I optimized this approach to design the dual-color bowtie-coupled detector at 90/150 GHz. Thirdly, I will introduce a new wide-band corrugated focal plane module design to minimize the beam mismatch systematic at 30 and 40 GHz bands simultaneously. Our receivers map polarization of the CMB by taking the difference between co-located and orthogonally polarized pair of detectors. Polarized beam difference measurements show a differential beam response due to a shift between the polarization beam centers within a pixel due to an electromagnetic interaction with the focal plane frame. The residual beams leak a temperature to polarization (T-P) in the CMB polarization maps and can produce a false B-mode signal that introduces non-negligible systematic errors for BICEP Array measurements to come with improved sensitivity. The wide-band design reduces this effect and associated systematic errors for 30 and 40 GHz receiver. I also developed a new single-band corrugated focal plane module design for 150 GHz receiver. I performed laboratory measurements of these designs at 30, 40, and 150 GHz to verify the modelled response. The corrugation design will also be extended to the 220/270 GHz receiver. Fourthly, I will show my contributions to the receiver deployment, integration and calibration during the first 2020 observing season. The measurements will include the full optical characterization of the detector camera, in-lab and on-sky sensitivity at the South Pole. I will also describe the tests done to diagnose the challenges during the first season and new upgrades during the second 2022 season to improve the overall sensitivity of the receiver. Improved detector modules have been installed during the 2023 season to further boost the mapping speed for measuring the synchrotron foreground.

The technologies developed for BICEP Array feed into capabilities for the upcoming CMB-S4 program. For example, I used similar methods to design a diplexer for a CMB-S4 dual-color feedhorn-coupled detector design at 90/150 GHz. I will also detail my work on the cryogenic implementation and test of an Adiabatic Demagnetization Refrigerator suitable for demonstrating 100 mK CMB-S4 detector arrays in a prototype 95/150 GHz telescope planned to observe on the BICEP Array.

PUBLISHED CONTENT AND CONTRIBUTIONS

We aim to probe the direct evidence for cosmic inflation as one of the most important goals in fundamental physics today. The BICEP/Keck series of CMB experiments continues to lead the world in this extremely exciting and competitive field through our recent released BK18 results. Ahmed Soliman is co-leading the technology development for high-sensitive single-color, dual-color detectors and instrumentation for BICEP/Keck collaboration. He also worked on the design and implementation of the focal plane frame engineering for minimizing the beams systematic. He also led the optical testing and analyzing of the laboratory data using Python and Matlab languages at Caltech and South Pole. He also contributed to the receiver cryogenic systems assembly, testing, calibration, and deployment to the South Pole (two seasons). He also worked on modelling the engineering challenges by using the simulated scientific tools, ran diagnostic tests, and proposed the potential solutions to improve the sensitivity. He worked on analyzing the cosmological data of the current BICEP telescopes from the South Pole to ensure higher quality CMB observations. Additionally, he worked on the implementation and testing of the cryogenic Adiabatic Demagnetization Refrigerator for the next generation low noise detectors (CMB-S4) in BICEP Array telescope. A portion of my research work in this thesis has not been published yet, and I have added this work to benefit our experiments toward our science goals. This remarkable achievement on the instrumentation work for BICEP Array telescope will improve our constrains on the inflationary gravitational waves, as we will see in our upcoming science papers.

[1] Soliman, Ahmed, et al. (BICEP/Keck Collaboration), “2022 upgrade and improved low Frequency camera sensitivity for CMB observation at the South Pole,” In: *Millimeter, Submillimeter, and Far-Infrared Detectors and Instrumentation for Astronomy XI*, International Society for Optics and Photonics, vol.12190, 2022. DOI: 10.1117/12.2628058.

[2] Ade, P.A.R., Z. Ahmed, et al. (BICEP/Keck Collaboration, including Ahmed Soliman) “Improved Constraints on Primordial Gravitational Waves using Planck, WMAP, and BICEP/Keck Observations through the 2018 Observing Season,” In: *Phys. Rev. Lett.* 127, 151301, 2021. DOI: 10.1103/physrevlett.127.151301.

[3] BICEP/Keck (including Ahmed Soliman) and SPTpol Collaborations “A demonstration of improved constraints on primordial gravitational waves with delensing,” In: *Phys. Rev. D* 103, 022004, 2021. DOI: 10.1103/PhysRevD.103.022004.

[4] BICEP/Keck Array Collaboration (including Ahmed Soliman) "Constraints on axion-like polarization oscillations in the cosmic microwave background," In: *Phys. Rev. D* 105, 022006, 2020. DOI:10.1103/PhysRevD.105.022006.

[5] BICEP/Keck Array Collaboration (including Ahmed Soliman), "Constraints on primordial gravitational waves using Planck, WMAP, and new BICEP2/Keck observations through the 2015 season," In: *Phys. Rev. Lett.* 121, 221301, 2018. DOI:10.1103/PhysRevLett.121.221301

[6] Soliman, Ahmed, et al. (BICEP/Keck Collaboration), "Optical design and characterization of 40-GHz detector and module for the BICEP Array," In: *Journal of Low Temperature Physics*, vol.199, 1118–1126, 2020. DOI: 10.1007/s10909-019-02299-z.

[7] Soliman, Ahmed, et al. (BICEP/Keck Collaboration), "Design and performance of single/wide band corrugated walls for the BICEP array detector modules at 30/40 GHz," In: *Millimeter, Submillimeter, and Far-Infrared Detectors and Instrumentation for Astronomy XI*, 107082G, International Society for Optics and Photonics, 2018. DOI: 10.1117/12.2312942.

[8] BICEP/Keck Array Collaboration (including Ahmed Soliman) "BICEP2/Keck Array XI: beam Characterization and temperature-to-polarization leakage in the BK15 data set," In: *The Astrophysical Journal*, vol.884, 2019. DOI: 10.3847/1538-4357/ab391d.

[9] Moncelsi, Lorenzo, et al. (BICEP/Keck Collaboration including Ahmed Soliman), "Receiver development for BICEP Array, a next-generation CMB polarimeter at the South Pole," In: *Millimeter, Submillimeter, and Far-Infrared Detectors and Instrumentation for Astronomy XI*, vol.11453, International Society for Optics and Photonics, 2020. DOI: 10.1117/12.2561995.

[10] Hui, Howard, et al. (BICEP/Keck Collaboration including Ahmed Soliman), "BICEP Array: A multi-frequency degree-scale CMB polarimeter," In: *Millimeter, Submillimeter, and Far-Infrared Detectors and Instrumentation for* Astronomy XI, vol.1070807, International Society for Optics and Photonics, 2018. DOI: 10.1117/12.2311725.

[11] Schillaci, Alessandro, et al. (BICEP/Keck Collaboration including Ahmed Soliman), "Design and performance of the first BICEP Array receiver," In: *Journal of Low Temperature Physics*, vol.199, 2020. DOI: 10.1007/s10909-020-02394-6.

[12] BICEP/Keck Array Collaboration (including Ahmed Soliman),"BICEP / Keck XV: The BICEP3 CMB polarimeter and the first three year data set," In: *The Astrophysical Journal*, vol.927, 2022. DOI: 10.3847/1538-4357/ac4886.

TABLE OF CONTENTS

LIST OF ILLUSTRATIONS

LIST OF TABLES

Chapter 1

SCIENCE BACKGROUND

1.1 Background and Motivation

We are basically designing highly sensitive telescopes to precisely address the most fundamental question, “How did the universe begin and evolve over time?” The observational evidences in the past decades supported that the universe is uniformly expanding and cooling down with time, suggesting that we should have started at time = 0, so called “Big Bang” where the universe was in an extremely hot and dense state. The Cosmic Microwave Background (CMB) radiation was formed 380,000 years after the Big Bang. The universe allows for this radiation to travel through billions of years after which we can see it today through our telescopes.

The observation of the CMB radiation and its anisotropies along with other observational evidences led to the successful hot Big Bang and the Λ cold dark matter (ΛCDM) standard cosmological model to describe the universe expansion and evolution with six-parameters. The early hot Big Bang model in the 1980s did not explain the initial conditions of the universe that would generate the observational measurements of remarkable isotropy and spatial flatness of Universe. The Cosmic Inflation theory was developed to describe the earliest moments of time and complete these unanswered questions with the Big Bang model by a period of “inflationary” rapid expansion when the universe was a mere fraction of a second old. Originally, inflation explained the almost perfect isotropy of the CMB. Since 2000, CMB temperature measurements have confirmed further predictions of inflation, specifically a very flat spatial geometry on large scales and initial density perturbations.

The B-mode polarization pattern (e.g. Kamionkowski, et al., 1997 and Kamionkowski and Kovetz, 2016), predicted by the Inflation and sourced by the gravitational waves, has been an interesting topic in the modern cosmology. The first recommendation of the 2003 National Research Council (NRC) report, Connecting Quarks with the Cosmos, was to “Measure the polarization of the CMB with the goal of detecting the unique geometric signature of Inflation.” The 2010 Decadal Survey described the search for B-modes from inflation as “the most exciting quest of all.” Most recently, the 2021 Decadal Survey (National Research Council, 2021) strongly endorsed the scientific importance of the quest to detect inflationary B-modes and stated, ”the panel suggests that third-generation CMB experiments aligned with CMB-S4 including the SPO be high priorities for federal support.” SPO is the combination of the BICEP Array and SPT-3G projects. High sensitivity instruments are required to investigate the inflationary epoch of the universe and provide an evidence for the inflation theory. Generations of scientists and engineers have inspired to build various experiments such as Polarbear, SPT, SPIDER, BICEP/Keck collaborations, etc. These experiments aim to reach the required sensitivity to measure this faint B-mode signal, the sign of inflation after the Big Bang that would have imprinted on the CMB. The TES bolometer technology has been developed with hundreds to thousand of detectors to provide much higher sensitivity CMB experiments compared to the old generations.

BICEP/Keck program has been leading the world on constraining the primordial gravitational waves using BK18 data set by mapping the polarization of the CMB from the South Pole. The program started with BICEP1, BICEP2, BICEP3, Keck Array, leading to BICEP Array telescope. Improving the upper limit on r would also have major implications, as classes of previously popular single-field slow roll inflation models are ruled out. One of the more significant findings from BICEP/Keck results has been that the once compelling inflation model $m^2\phi^2$ is now strongly disfavored. The recent successes in CMB and inflationary physics history show that the progress sensitivity of the CMB experiments came from the advancement of the focal plane, detectors, and cryogenic instrumentation technology, which are the motivation of this thesis for the latest developed telescope, BICEP Array, and the coming CMB-S4 to probe inflationary cosmology with unprecedented precision. In this chapter, we discuss the standard cosmological model, CMB polarization, the motivation for the cosmic inflation, the current observation sensitivity of primordial gravitational waves and its ultimate detection challenges that motivate the research work of this dissertation.

1.2 ΛCDM Standard Cosmological Model

Various observational evidences have concluded the standard (ΛCDM) cosmological model to describe the history and evolution of the universe. The most basic understanding of the modern cosmology was highlighted by Albert Einstein’s general theory of relativity paper (Einstein, 1915), which relate the evolution and geometry of the universe to its contents.

$$G_{\mu\nu} - \Lambda g_{\mu\nu} = \frac{8\pi G}{c^4} T_{\mu\nu} \tag{1.1}$$

Λ is the cosmological constant, $G_{\mu\nu}$ is the Einstein tensor = $R_{\mu\nu} - \frac{1}{2}Rg_{\mu\nu}$, $R_{\mu\nu}$ is the Ricci curvature tensor. These parameters are related to the energy content of the universe described by the stress-energy tensor $T_{\mu\nu}$, and attributed to matter and radiation by Einstein field equation. This equation could be applied to the very large scale in cosmology since the universe is observed to be isotropic and homogeneous everywhere we look at the sky. Edwin Hubble was the first scientist to detect the expansion of the universe in 1929 (Hubble, 1929). Under these observations, the universe could be modeled by the Friedmann-Walker-Robertson (FRW) metric in the spherical spatial coordinates (r,θ, ϕ)

$$ds^2 = -c^2dt^2 + a(t)^2[\frac{dr^2}{1-kr^2} + r^2(d\theta^2 + \sin^2\theta d\phi^2)] \tag{1.2}$$

where ds^2 is the space-time metric, K is universe geometry curvature that takes value of 0 for flat universe according to the experimental observations, t is the temporal coordinate, $a(t)$ is the time-dependent scale factor that indicates the expansion rate of the universe.

The first Friedmann equation (Friedman, 1922) could be derived by solving Einstein Field Equation 1.1 with FRW metric Equation 1.2.

$$H^2 \equiv \frac{\dot{a}^2}{a^2} = \frac{8\pi G\rho}{3} - \frac{K}{a^2} + \frac{\Lambda}{3} \tag{1.3}$$

where $\dot{a}(t)$ represents the time derivative of the scale factor, ρ is the energy density, $H(t) = \frac{a(\dot{t})}{a(t)}$ is the universe Hubble expansion rate parameter. The first Friedmann equation relates the total energy density of the universe to spatial curvature of the universe. The recent observations of the CMB anisotropies such as Planck satellite suggests that the universe is nearly geometrically flat.

Similarly, the second Friedmann equation could be derived from the Einstein field equations to relate the scale factor a, energy density ρ, and the total pressure p to form the acceleration equation.

$$\frac{\ddot{a}}{a} = \frac{\Lambda}{3} + \frac{4\pi G}{3}(\rho + 3p) \tag{1.4}$$

These equations provide us with information about the history of universe expansion, composition, and their densities changes through billions of years. The energy density $\rho(t)$ comes from contributions from cold matter, radiation, and dark energy, which are the main components of ΛCDM model. Each component of the universe evolve and dominate differently over time. The equation of state relates the energy density and pressure by the cosmological constant $\omega = \frac{p}{\rho}$. Given the energy conservation equation, this leads to the energy density and scale factor proportional relationship $\rho \propto a^{-3(\omega+1)}$. ω takes values between 0 for matter component-dominated, $\frac{1}{3}$ for radiation component-dominated, and -1 for dark energy component-dominated (cosmological constant). In the early universe, the universe expansion was dominated by the energy density of radiation since the scale factor was small $\rho_r \propto a^{-4}$. The universe transitioned into matter domination as the universe expanded over time ($a \uparrow$) until we reached the dark energy density $\rho_\omega \propto a^0$ to be the current dominant content in the universe evolution stages.

We also define the critical energy density parameter which separates the universe between expanding forever ($\rho < \rho_c$ and $K = 1$) and collapsing ($\rho > \rho_c$ and $K = -1$). The critical energy density (ρ_c) could be derived by solving Friedmann equations for a flat universe (K = 0).

$$\rho_c = \frac{3H^2}{8\pi G} \tag{1.5}$$

The total energy density of the universe is defined as the ratio between the energy density to the critical density.

$$\Omega_{total} = \frac{\rho}{\rho_c} = \Omega_\gamma + \Omega_m + \Omega_\Lambda + \Omega_K \tag{1.6}$$

Ω_{total} provides the summation of contributions from the universe contents. We could rewrite the Friedmann equation 1.3 as a function of universe composition.

$$H^2 = H_0^2(\Omega_{0,\Lambda} + \Omega_{0,k}a^{-2} + \Omega_{0,m}a^{-3} + \Omega_{0,r}a^{-4}) \tag{1.7}$$

H_0 is the Hubble constant today. The cosmological observation provided by Wilkinson Microwave Anisotropy Probe (WMAP) concluded the spatial curvature to be flat ($\Omega_{0,\Lambda} = 0, K = 0$, and $\rho = \rho_c$) at the present time. The scale factor is related to the red shift by a(t) = 1/(1+z) for $a(t_0) = 1$ at the present time. We could re define the Friedmann Equation for a flat geometry as a function of the expanding universe.

$$H(z) = H_0\sqrt{(\Omega_{0,\Lambda} + \Omega_{0,k}(1+z)^{-2} + \Omega_{0,m}(1+z)^{-3} + \Omega_{0,r}(1+z)^{-4})} \tag{1.8}$$

This equation showed the contents of an inflationary ΛCDM model. The density parameters of different components of the universe evolve with different powers of the scale factor a. The universe is going through epochs of different dominant components as it expands, radiation ($\Omega_{0,r}$), ($\Omega_{0,m}$) is the sum of baryonic matter ($\Omega_{0,b}$) and dark matter ($\Omega_{0,c}$). The dark energy is represented by a cosmological constant ($\Omega_{0,\Lambda}$). The universe was dominated by radiation in the beginning. At the present time, the most recent Planck measurements (Aghanim, et al. (Planck Collaboration), 2021) showed that the energy density consists of matter (31%) which combined the cold dark matter (26%) and baryonic matter (5%), and insignificant radiation content (0.005%). The remaining universe energy density is dominated by the dark energy (69%).

Hubble's observations confirmed the expansion of the universe by recording the relationship between the distance of extragalactic objects and their recessional velocity (Hubble, 1929). This led to the conclusion that there was a beginning at some point if we turn the clock backwards. This was not enough evidence to the cosmologists who supported the competing steady state theory back in the mid-20th century. The acceptance of the hot Big Bang would require a clear evidence for an early extreme hot and dense state than today. The detection of the Cosmic Microwave Background (CMB) provided a strong evidence for the hot Big Bang theory. In the 1990s, the measured CMB spectrum by the Far Infrared Absolute Spectrometer (FIRAS) instrument of the Cosmic Background Explorer (COBE) mission cemented the Big Bang model. In 1998, the detection of accelerated universe from the supernovae has also added a new parameter (Λ) to the (ΛCDM) model. The standard (ΛCDM) model fully describes the origin and evolution of the universe, including the cosmic inflation, which is foundation of modern cosmology.

1.3 The Cosmic Microwave Background

The measured cosmological parameters in the standard (ΛCDM) model have estimated that the universe has a finite age of about 13.8 billion years old. The early universe was initially in an extreme hot and dense state during the first few moments after the Big Bang. The early Universe was a highly coupled photon-baryon fluid through the Thompson scattering interaction between photons, electrons, and baryons. The universe expanded and cooled down with time. About 380,000 years after the Big Bang, the universe temperature had dropped enough to $\sim$ 3000 K (redshift of z =$\sim$ 1100), so that the protons and electrons combined to form neutral hydrogen in a process called recombination, forming the surface of last scattering. The universe became transparent to these photons to freely travel to us through billions of years. The redshift pushes the temperature of these photons down and their wavelengths have been stretched due to the expansion of the Universe. This ancient optical image of the universe is called the Cosmic Microwave Background (CMB) radiation. The CMB was first measured in 1965 by Penzias and Wilson at Bell Labs (Penzias and Wilson, 1965) to provide a strong observational evidence to the Big Bang cosmological model over the competing steady state theory at that time. Various generations of scientists and engineers around the world have developed many experiments to further unveil secrets about our observable universe through CMB observations. These observations indicate that the temperature is nearly the same in all directions on the sky. The universe expansion caused the temperature (T_{CMB}) to decrease with the scale factor (a^{-1}). The measured CMB temperature by FIRAS instrument of the COBE satellite is T_{CMB}= 2.728 ± 0.004 K (95% CL) (Fixsen, et al., 1996), as an extremely well-described blackbody spectrum (Figure 1.1). The COBE experiment and Differential Microwave Radiometer (DMR) experiment (Smoot, et al., 1992) also detected small temperature anisotropy of the CMB. These observations provided significant milestones to the Big Bang model.

Further precise measurement of the CMB temperature came out to 2.7548 ± 0.00057K (Fixsen, 2009) as the current temperature of the universe. Over the past 20 years, these measurements have been further refined to breathtaking precision by two satellites—the Wilkinson Microwave Anisotropy Probe (WMAP) and Planck. The measured high resolution temperature anisotropy of the CMB measured by Planck satellite (Aghanim, Akrami, et al. (Planck Collaboration), 2018) is shown in Figure 1.2. The tiny temperature fluctuations of cold and hot spots correspond to regions of slightly different densities of CMB anisotropy. These temperature fluctuations are due to the acoustic oscillations during Recombination at the early universe. This interaction process between radiation pressure and gravity repeats in a harmonic series, producing a pattern of spots shown in Figure 1.2. The CMB temperature anisotropy $\Delta T_{CMB}(\theta, \phi)$ can be decomposed in terms of spherical harmonics $Y_{l,m}(\theta, \phi)$:

$$\Delta T_{CMB}(\theta, \phi) = \sum_{l=1}^{\infty} \sum_{m=-l}^{l} a^{T}_{l,m} Y_{l,m}(\theta, \phi). \tag{1.9}$$

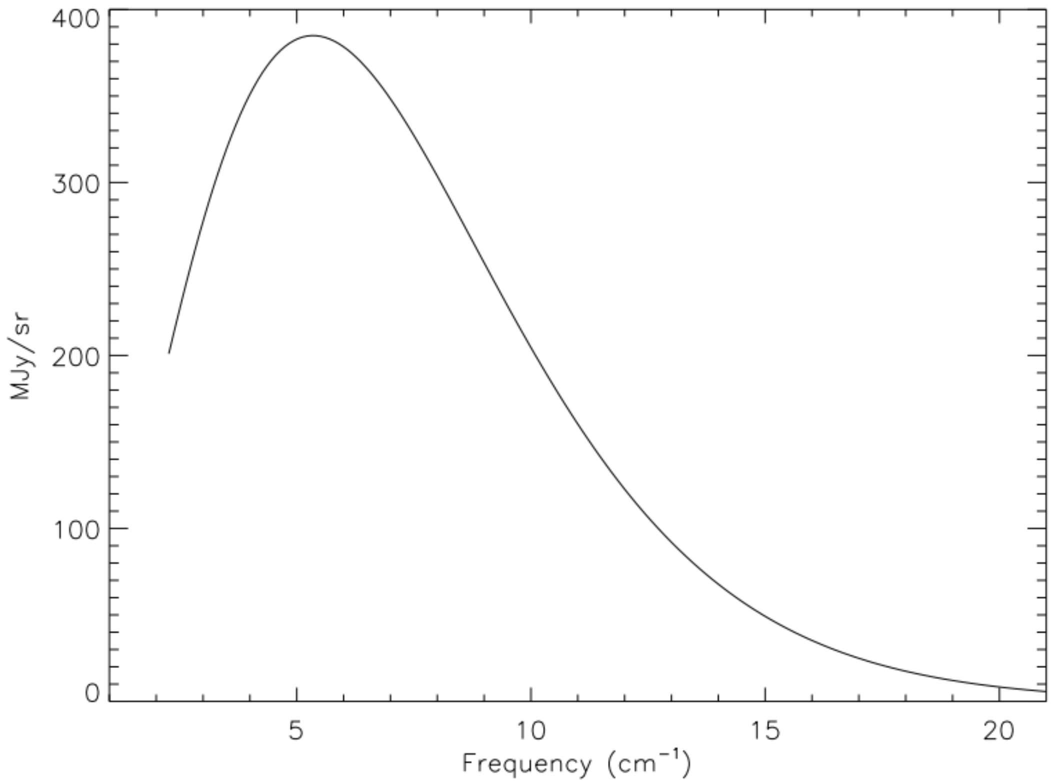

Figure 1.1: The measured Frequency Spectrum of the CMB by the FIRAS Instrument. Reprinted from (Fixsen, et al., 1996).

The multiple (ℓ) shows the angular size for m modes. We expressed the CMB temperature fluctuations in the form of a Gaussian random field described by the statistical distributions $a_{l,m}$. Given the isotropy and orthogonality of the spherical harmonics, we implicitly define the angular power spectral of the CMB:

$$C_l = \frac{1}{2l+1} \sum_{m=-l}^{l} a_{l,m} a^*_{l,m}. \tag{1.10}$$

where the star denotes the complex conjugate. We average over all possible orientations of each mode. The CMB anisotropies contain wealth of additional information about evolutionary history of the early universe. The CMB TT spectrum measured by Planck is shown in Figure 1.3. The power spectrum peaks of the CMB temperature fluctuations of the observable universe can be fitted with the 6-parameters ΛCDM model to constraint on the cosmological information. These peaks correspond to acoustic oscillations in the photon-baryon fluid before recombination process. The locations and amplitudes of these harmonic peaks support the initial

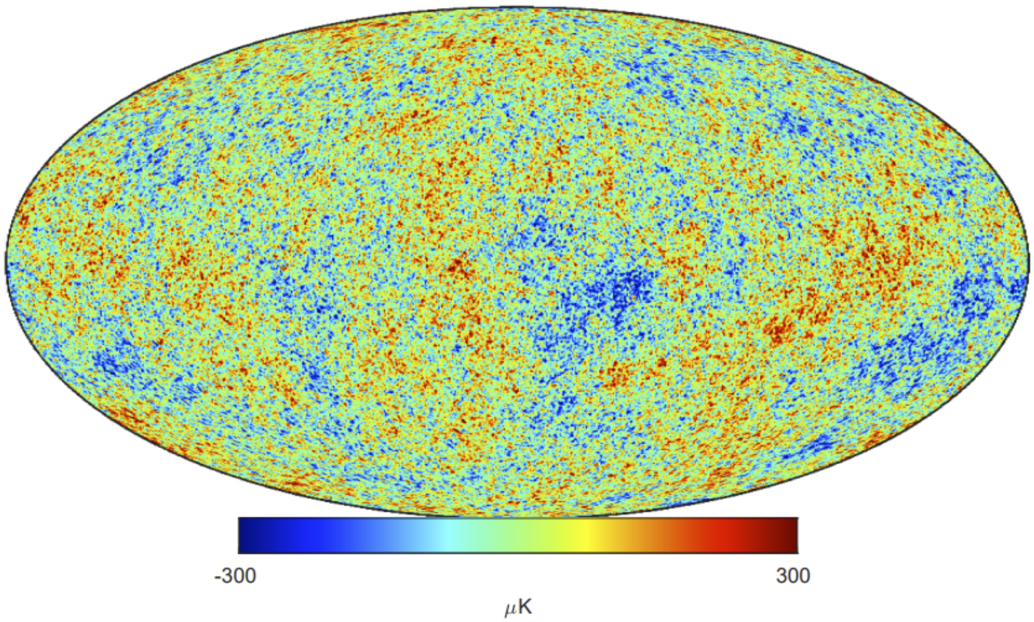

Figure 1.2: The measured CMB sky temperature anisotropy by Planck satellite. Reprinted from Aghanim, Akrami, et al. (Planck Collaboration), 2018.

adiabatic perturbations of the universe as expected by the cosmic inflation theory (next section). The first peak location constrain the universe curvature parameter Ω_k to spatially flat. The ratio of the first peak to the second peak constraints the baryonic and dark matter contents of the universe. For more information, see (Hu and Dodelson, 2002).

The observed CMB anisotropies show the surface of last scattering which is still limited by statistical information available at low multiple moment modes on the sky (ℓ), known as cosmic variance limit.

$$\frac{\Delta C_l}{C_l} = \sqrt{\frac{2}{f_{sky}(2l+1)}}. \tag{1.11}$$

The cosmic variance shows the uncertainty of the power spectrum at low (ℓ) which limits our sensitivity to constrain the inflation parameters.

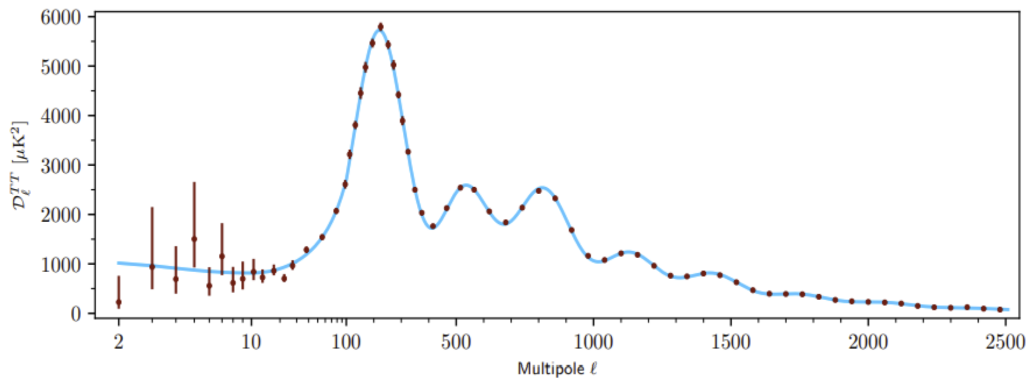

Figure 1.3: The CMB temperature (TT) angular power spectrum as function of the scale-independent quantity $D_l = \frac{l(l+1)}{2\pi} C_l$. The blue lines show the best-fitting model. The uncertainties of the spectrum at low (ℓ) are dominated by cosmic variance variance. Reprinted from Aghanim, Akrami, et al. (Planck Collaboration), 2018.

1.4 Cosmic Inflation

In 1980s, the cosmologists were deeply troubled to understand the observational measurements of remarkable isotropy and spatial flatness of universe. The early hot Big Bang model failed to explain three remarkable problems,

- *The Horizon Problem*: Why the measured CMB temperature is highly uniform everywhere we look at the sky (Aghanim, Akrami, et al. (Planck Collaboration), 2018 and other experiments). Also, why the measured statistical CMB anisotropies distribution is very small (Mather, et al., 1994). The earlier hot Big Bang model does not explain the homogeneity and isotropy of the universe. The Big Bang model proposed that the universe is expanding through billions of years since the Big Bang, i.e., the last scattering photons on the early universe should have never be in a casual contact with each other. Meaning that the today's CMB temperature of two separated regions of more than $1-2^{\circ}$ angular scale on the sky should not have the same temperature. However, the CMB observations suggested that the entire observable universe was in a thermal equilibrium state at some point in the evolution of the universe. The inflation was required in the 1980s to explain the CMB isotropy. The first successful tests of Inflation came from the CMB anistropy measurements with COBE/DMR experiments.

- *The Flatness Problem*: Why the measured universe curvature density is close to spatially flat. The joint measurements of Planck with BAO on spatial curvature is consistent with a flat universe, Ω_K = 0.0007± 0.0019 (Aghanim, et al. (Planck Collaboration), 2021) suggesting that the value in the early universe was "fine-tuning" as predicted by the inflationary paradigm. However, the standard Big Bang model proposed that the expansion of the Universe should deviate the energy density $\Omega_K = (\Omega - 1)$ to be away from zero, either $\Omega_K > 0$ or $\Omega_K < 0$. The physics of the Big Bang model could not give an explanation to that. The inflation was required to explain the flatness when the experiments were claiming just ≈10% of the critical density, which was a huge problem in the 1980s. The theorists who supported the inflation said that the critical density of the universe had be exactly 100 %, which has been confirmed 30 years later to sub-percent accuracy by Planck and other experiments.

- *Magnetic-Monopole Problem*: The theorists expected the creation of stable particles from the extremely hot state of the early universe. They predicted the magnetic monopoles to be still around today. The inflation investigated the lack of magnetic monopoles in the universe. During the universe inflation, the density of magnetic monopoles has been highly decayed to undetectable levels by the current experimental efforts today.

The cosmic inflation theory was invented in the 1980s (Guth, 1981, Linde, 1982, Starobinsky, 1980, and Albrecht and Steinhardt, 1982) as an extension to the ΛCDM model to provide the initial conditions of the universe. The inflation theory proposed a rapid period of exponential expansion at the very beginning of the Big Bang. The CMB observations are consistent with the remarkable idea that the entire observable Universe began in a violently accelerated inflation of a microscopic volume. The accelerated expansion supposed to bring more casually connected volume (as we observe them today on the CMB) together at thermal equilibrium into the horizon during the inflation period ($\sim 10^{-35}$ s after the Big Bang), before the Recombination process (~ 380,000 years after the Big Bang). The inflation theory also estimated a ~ 60 e-folds inflation expansion before the standard Big Bang expansion to solve the horizon problem of the universe. Similarity, the inflationary accelerated expansion reduces the curvature density toward zero.

The Friedmann equation could relate the energy density to expansion rate and universe's curvature to further illustrate that. During the radiation or matter dominant epoch, the comoving Hubble length 1/(aH) reduces, $\Omega_K = - \frac{kc^2}{(aH)^2}$ is highly brought down to zero, which matches the today's observation of flat universe, solving the flatness problem. Finally, the inflation theory explains the physics of the perturbations as I will introduce in the next sections.

Single field slow-roll inflation model

There are various inflation models to describe the first few moments of the universe. I will present the most generic scenario to outline the inflation paradigm, "single field slow-roll" inflation model (for more information, see, e.g., (Kolb and Tunner, 1994) and drive the most important parameters for our experimental goals. Figure 1.4 demonstrates the dynamics of "slow-roll" inflation. The slow-roll inflation model uses a single scalar field $\phi(t)$ called inflation with a potential V(ϕ). We could eventually drive the density ρ and pressure p equations as function of $\phi(t)$ and V(ϕ).

$$\rho_\phi = \frac{1}{2}\dot{\phi}^2 + V(\phi) \tag{1.12}$$

$$P_\phi = \frac{1}{2}\dot{\phi}^2 - V(\phi) \tag{1.13}$$

Given the energy conservation equation,

$$\dot{\rho} = -3\frac{a}{\dot{a}}(\rho + p), \tag{1.14}$$

we derive the equation of motion for the field:

$$\ddot{\phi} + 3H\dot{\phi} + V'(\phi) = 0. \tag{1.15}$$

The field ϕ varies slowly with respect to the potential energy under the slow-roll condition. The inflation occurs when the potential energy of the field highly dominates over its kinetic energy, i.e., $\dot{\phi}^2 \ll V(\phi)$, yields to $P = -\rho$ for the acceleration expansion to happen. Given Eq.1.12, we arrange the Friedmann equation to:

$$H^2 = \frac{1}{3M_{pl}^2}\rho = \frac{1}{3M_{pl}^2}(\frac{1}{2}\dot{\phi}^2 + V(\phi)). \tag{1.16}$$

$M_{Pl} = \sqrt{\frac{1}{8\pi G}}$ is the reduced Planck mass. G is the gravitational constant. We set the speed of light c = 1. In the slow-roll scenario, we need the potential field to satisfy

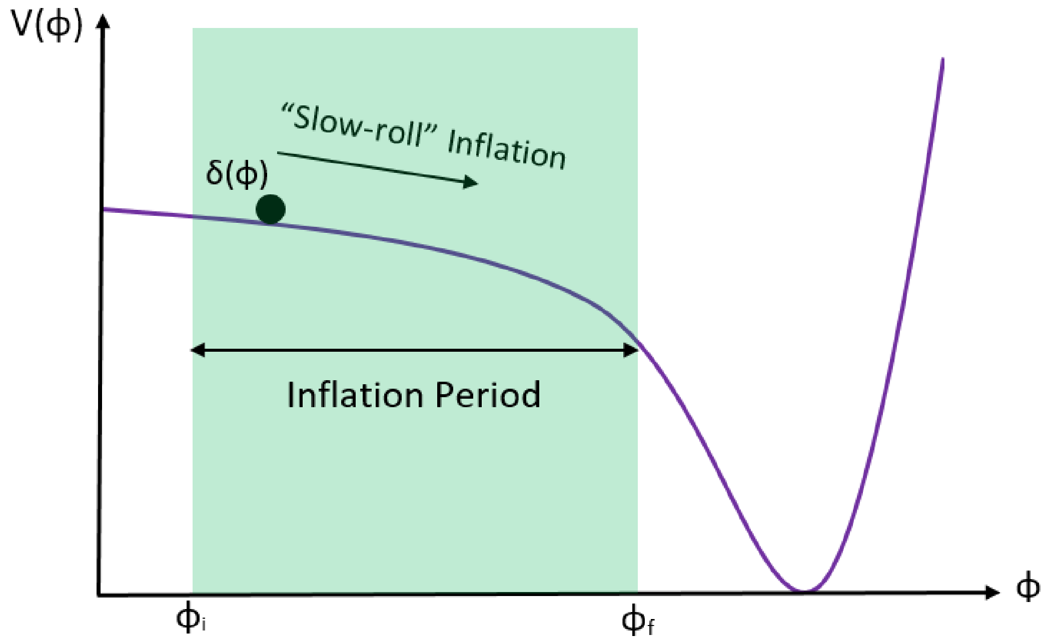

Figure 1.4: This cartoon shows an example of the "slow-roll" inflation potential. I made this plot to show the dynamics of the inflation(Kolb and Tunner, 1994). The inflation period must last the sufficient time to explain the homogeneous CMB observations of our universe. The inflation ends at ϕ_f when the two slow-roll conditions are no longer satisfied.

the slow roll conditions which described by two parameters. The first slow-roll parameter could be derived as:

$$\epsilon = \frac{-\dot{H}}{H^2} = \frac{M_{Pl}^2}{2}(\frac{V'(\phi)}{V(\phi)})^2. \tag{1.17}$$

The second slow-roll parameter is used to keep track of the rate at which ϵ changes for a sufficient inflation period, and could be obtained as:

$$\eta = -2\frac{\dot{H}}{H^2} - \frac{\dot{\epsilon}}{2H\epsilon} = M_{Pl}^2\frac{V''(\phi)}{V(\phi)} \tag{1.18}$$

$V'(\phi)$ and $V''(\phi)$ are the first and second derivative with respect to the field ϕ, respectively. The two slot-roll conditions are $\epsilon \ll 1$ and $\eta \ll 1$, which must be satisfied for a dominated potential field. The inflation ends when these two conditions are broken. We define the necessary expansion period during inflation N_e , which estimated to be $\approx 50 - 60$ e-folds to solve the horizon problem. The e-folding N_e is calculated as:

$$N_e = \int_{a_i}^{a_f} d\ln a = \int_{\phi_i}^{\phi_f} \frac{d\phi}{M_{Pl}^2}\frac{V(\phi)}{V'(\phi)} \tag{1.19}$$

The metric fluctuations

The accelerating expansion during inflation amplified the quantum fluctuations and stretched it out to cosmic size, which provided the initial conditions for the structure formation in the Universe, i.e., inflation generates perturbations. The metric perturbation could be decomposed into three independent components:

- *Scalar Perturbations*: The inflation produces density fluctuations which is sourced by scalar perturbations. Scalar perturbations are due to energy density fluctuations in the plasma at the last scattering surface and represent the temperature anisotropies in the CMB map. They left an even parity E-mode polarization on the CMB. In 2002, DASI experiment has detected the E-mode polarization of the CMB as expected (Kovac, et al., 2002). E-mode polarization anisotropy measurements confirm that the polarization anti-correlates with temperature on large scales, consistent with coherent structures generated by inflation on scales larger than the classical causal horizon.

- *Tensor Perturbations*: The inflation also generates a tensor perturbations which are the primordial gravitational waves, creating over and under densities by compressing and expanding space and expect to leave a B-mode polarization pattern on the CMB polarization (section 1.5). The tensor perturbation produces both parity even E-mode and parity odd B-mode polarization. While the scalar perturbation dominates the E-mode power, the tensor perturbations are a unique source of primordial B-mode polarization signal and its detection would be a direct evidence for the inflation theory. However, the amplitude of the tensor perturbations produced by inflation varies significantly depending on the model.

- *Vector Perturbation*: The vector perturbations are called vorticity modes and we did not expect the inflation to generate vector modes due to the absence of velocity fields. They decay rapidly during inflationary stage with the universe's expansion.

As per Dodelson's book of modern cosmology, the scalar perturbations are a mixture of metric and inflation quantum field. The linear evolution of cosmological perturbations could be described mathematically by the first-order the FRW metric:

$$\phi(\vec{x}, t) = \overline{\phi}(t) + \delta\phi(\vec{x}, t) \tag{1.20}$$

$$g_{\mu\nu}(\vec{x}, t) = \overline{g}_{\mu\nu}(t) + h_{\mu\nu}(\vec{x}, t). \tag{1.21}$$

The metric perturbations came from the fluctuations in the field ϕ. $h_{\mu\nu}(\vec{x}, t) = \delta g_{\mu\nu}(\vec{x}, t)$ is the perturbation of the metric. We could break down the perturbed metric according to their spin with respect to a local rotation of the spatial coordinates into two main perturbations:

$$g_{\mu\nu} = \begin{cases} g_{ij} = a^2\delta_{ij}e^{2R(\vec{x},t)} & Scalar \\ g_{ij} = a^2(\delta_{ij} + 2h_{ij}) & Tensor. \end{cases} \tag{1.22}$$

$R(\vec{x}, t)$ is the curvature perturbation. The quantum fluctuations of the gravitational waves are represented by the transverse metric h_{ij} in the tensor perturbations, and has two polarization h_+ and $h_\times$ for co $+$ and cross $\times$ modes.

The inflation brings the super-horizon modes to re-enter the horizon. The power spectrum of scalar and tensor perturbations could be evaluated at the horizon crossing (wave number $k = Ha$) for the single field slow-roll inflation model.

$$\Delta_s^2 = \frac{H^2}{8\pi^2 M_{Pl}^2 \epsilon} \tag{1.23}$$

$$\Delta_t^2 = \frac{2H^2}{\pi^2 M_{Pl}^2} \tag{1.24}$$

We first define the spectral index for the scalar perturbations from Equation 1.23 as follow:

$$n_s = \frac{d \ln \Delta_s^2(k)}{d \ln k} + 1. \tag{1.25}$$

The ideal scale-invariant scalar perturbation spectrum has $n_s = 1$. The inflation models expect $n_s = 1$ to be slightly less than 1. The spectral index could be related to the slow-roll parameters of Equations 1.17 and 1.16, $n_s = 1 - 4\epsilon + 2\eta$. The current measurement from Planck and BAO constrain $n_s = 0.9665 \pm 0.0038$ (Aghanim, et al. (Planck Collaboration), 2021).

The spectral index for the tensor perturbations has obtained from Equation 1.24 as follow:

$$n_t = \frac{d \ln \Delta_t^2(k)}{d \ln k}. \tag{1.26}$$

The scale-invariant tensor perturbation has not been measured yet and expect to have value of $n_t = 0$. The spectral tilt could be related to the slow-roll parameters, $n_t = -2\epsilon$.

The tensor-to-scalar ratio r could be obtained from equations 1.23 and 1.24 to parameterize the primordial perturbations:

$$r = \frac{\Delta_t^2(k)}{\Delta_s^2(k)}. \tag{1.27}$$

We define r at pivot scale 0.05 Mpc^{-1} and spectral tilt $n_t = 0$. Among inflation models, single-field slow-roll models produce gravitational waves with r in the range 0.001 to 0.1. Searching for primordial gravitational waves, or ruling them out at these levels, is among the most important goals of fundamental physics and cosmology today.

r has not been detected yet and is estimated to be 16ϵ for the slow-roll inflation model. Various inflation models anticipate r at much lower levels ($r < 0.01$), where its detection requires a very sensitive instrument with tight control and characterization of instrumental systematics, and a reliable means of detecting and controlling for Polarized Galactic foregrounds through a multi-component template. The successful measurement of r would probe the physics of the first few moments on the universe and would be the "smoking gun" for the energy scale of inflationary gravitational waves. Our experimental goal is search for r or put constraints on it to limit the popular inflation models. The tensors perturbations could be constrained from the CMB temperature measurement. However, the sensitivity on r is limited by the comic variance at low l and can not be improved below the reported value by Planck, $r < 0.11$ at 95% confidence. We thus require a different means of constraining r.

1.5 Search for r on the CMB Polarization

The CMB photon is polarized by Thomas scattering off electrons during recombination, resulting a linearly polarized scattered photon perpendicular to the line of sight if the incident electron is illuminated by a quadrupole anisotropy. The polarization of CMB expects to carry wealth information about the tensor perturbations and mapping this CMB polarization has became a primary topic in the cosmological field that rapidly help us understanding the early Universe.

The CMB polarization could be represented by Stokes's parameters. Consider an electric field E travel in $\hat{z}$ direction with two components $E_x = E(x,t)$ and $E_y = E(y,t)$. The resulting four Stokes's parameters could be obtained:

$$I = |E_x|^2 + |E_y|^2 \tag{1.28}$$

$$V = -2Im(E_x E_y^*) \tag{1.29}$$

$$Q = |E_x|^2 - |E_y|^2 \tag{1.30}$$

$$U = 2Re(E_x E_y^*) \tag{1.31}$$

I is the total radiation intensity. V is the circular polarization component, which is not expected to be generated from the standard cosmological model ($V = 0$). Q and U are the two orthogonal polarization states (+ and $\times$) to represent the linear polarization of the CMB. For more information, see (Emory, et al., 2003).

The CMB polarization represented by Q and U, could be derived interns of the spin-2 harmonic coefficient ${}_{\pm 2}Y_{lm}$:

$$(Q \pm iU)(\hat{n}) = \sum_{l=1}^{\infty} \sum_{m=-l}^{l} a_{\pm 2,lm \pm 2} Y_{l,m}(\hat{n}). \tag{1.32}$$

Q and U are symmetric under the rotation of 180° and coordinate dependent parameters. The linear polarization Q and U can also be decomposed to two invariant spin-0 fields, E-mode and B-mode in Fourier space for flat-sky patch approximation (Zaldarriaga and Seljak, 1997).

$$\tilde{E}(\overrightarrow{l}) = \tilde{U}(\overrightarrow{l}) \sin(2\phi_l) + \tilde{Q}(\overrightarrow{l}) \cos(2\phi_l) \tag{1.33}$$

$$\tilde{B}(\overrightarrow{l}) = \tilde{U}(\overrightarrow{l}) \cos(2\phi_l) - \tilde{Q}(\overrightarrow{l}) \sin(2\phi_l) \tag{1.34}$$

We define the basis functions Y^E_{lm} and Y^B_{lm} for E-mode and B-mode, respectively. Equation 1.32 could be written interns of the scalar field components, E and B-modes coefficients:

$$a^E_{lm} = -\frac{1}{2}(a_{2,lm} + a_{-2,lm}) \tag{1.35}$$

$$a^B_{lm} = \frac{i}{2}(a_{2,lm} - a_{-2,lm}). \tag{1.36}$$

We calculate the cosmological parameters in our pipeline analysis by fitting our cosmological model to the observed power spectra data. The power spectra formulas for E-mode, B-mode, and temperature T anisotropy fields are derived as function of spherical harmonic quantities:

$$C^{EE}_l = \frac{1}{2l+1}\sum_{m=-l}^{l} a^{E*}_{lm} a^E_{lm} \tag{1.37}$$

$$C^{BB}_l = \frac{1}{2l+1}\sum_{m=-l}^{l} a^{B*}_{lm} a^B_{lm} \tag{1.38}$$

$$C^{TT}_l = \frac{1}{2l+1}\sum_{m=-l}^{l} a^{T*}_{lm} a^T_{lm} \tag{1.39}$$

$$C^{TE}_l = \frac{1}{2l+1}\sum_{m=-l}^{l} a^{T*}_{lm} a^E_{lm}. \tag{1.40}$$

The E-modes polarization is sourced by the density fluctuations in the plasma that generate the temperature anisotropies and could travel either parallel or perpendicular to the direction of the propagation (0°, 90°), as shown in Figure 1.5. The E-modes generate distinct “curl-free” pattern in the CMB polarization and does not change with parity inversion. However, the primordial gravitational waves are uniquely predicted by some classes of inflation model and expected to imprint a divergence-free B-mode polarization pattern on the CMB. Other inflation models, such as mutli-field inflation, predict undetectable small levels. The B-mode pattern is odd and flips the sign under parity inversion. The resulting B-mode photon scattering off an electron should be polarized at an angle of ±45° with respect to the travelling field.

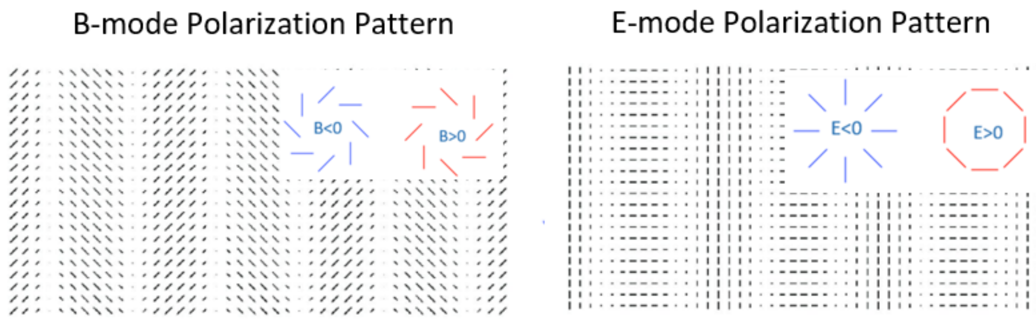

Figure 1.5: Examples of B-mode and E-mode patterns generated by the gravitational waves and density waves, respectively. The top figures show E-mode and B-mode polarization patterns with associated signs.

The ΛCDM model angular power spectra that describe the CMB (TT, TE, EE, and BB) are plotted in Figure 1.6 using the cosmological parameters, which encodes the information about the universe composition, the magnitude of tensor and density fluctuations, lensing and the reionization period. The scalar perturbations can only generate temperature and E-mode ansitropy due to the flow of baryon-photon fluid but it can not generate B-mode pattern. The tensor perturbations could generate temperature, E-mode and B-mode, making it a unique source of B-mode signature in the CMB polarization.

1.6 Primordial B-mode: Challenges, Current Status and Path Forward

The detection of the B-mode pattern has been identified to be an exceptional evidence for the inflation paradigm and can be used to probe the inflationary gravitational waves (Kamionkowski, et al., 1997). However, there are some challenges associated with the ultimate detection of the B-mode pattern from the CMB polarization. The extremely small amplitude r is limited by contamination from much brighter sources, such as lensing and Polarized Galactic Foreground.

- *Primordial faint B-mode*: Figure 1.6 shows that the amplitude of the primordial B-mode is orders of magnitude fainter than other fields (Ex: 5 order of

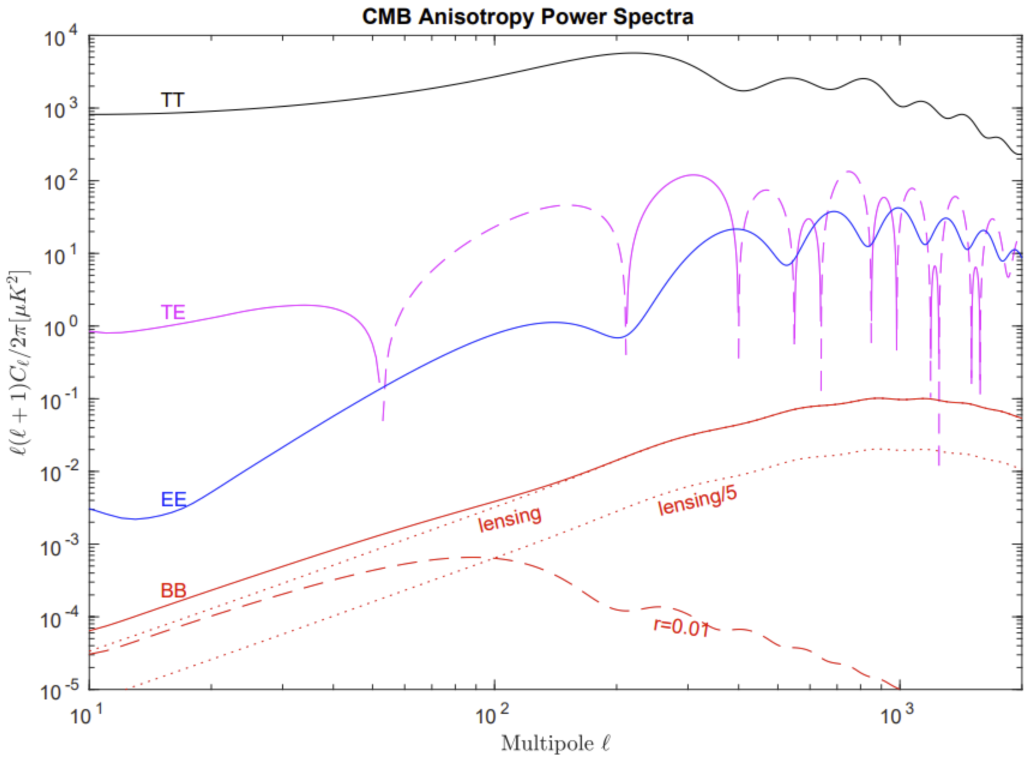

Figure 1.6: The angular power spectrum of CMB anisotropies (temperature and polarization). The cosmological parameters from Planck (Aghanim, Akrami, et al. (Planck Collaboration), 2018) have been fed to the Code for Anisotropies in the Microwave Background (CAMB) (Lewis, et al., 2002) to generate these anisotropies. The temperature anisotropy (TT) are orders of magnitude brighter than EE and BB. The primordial unlensed primordial BB spectrum is our target and expects to peak multiple of $l = 100$. The lensing B-mode is brighter than the primordial B-mode, showing the critical important of delensing to highly improve the sensitivity on r.

magnitude smaller than EE). We need a telescope with unprecedented sensitivity to be able to detect this faint signal at the nK level. One solution is to increase the number of the detectors within the focal plane to collect more CMB photos (Chapter 7). The high sensitive instruments also require a tight control of the systematics challenges, such as beam mismatch leakage (Chapter 4 at the instrument level and (Karkare, 2017) at the science level), unmodeled point sources (Crumrine, 2022), etc.). One primary challenge comes from our ability to rotate the entire instrument around the line of sight to separate sky from instrumental polarization. More instrumental systematics and our efforts to minimize these errors are described in (Ade, P.A.R., et al. (BICEP2 Collaboration), 2015).

- *Gravitational Lensing*: r is contaminated by the variance from the gravitational lensing due to the distortion of E-mode caused by large scale structures during its travel to us from the early universe, resulting into the creation of B-mode pattern by lensing, known as “Gravitational lensing.“ The amplitude of primordial B-mode is also smaller than the amplitude of lensing B-mode. Our small-aperture telescopes have delivered high sensitivity at the l=80 angular scales where the B-mode signal is predicted to peak. However, the lensing reconstruction requires high sensitivity in the range $300 < l < 5000$ where the lensing B-mode is peaking (Figure 1.6). The angular resolution of the 10-meter diameter South Pole Telescope is more than sufficient. We have therefore launched a partnership between the BICEP/Keck and SPT-3G groups to jointly analyze the data from both experiments to develop “delensing“ techniques to improve future constraints on r, calling this new collaboration ”South Pole Observatory” (SPO). Our preliminary joint analysis (The BICEP/Keck and SPTpol Collaborations, 2020) shows that the simulated uncertainty on $\sigma(r)$ reduced by $\approx$ 10%, from 0.024 to 0.022. Based on BK14 data, the constraint on r is improved from $r_{0.05} < 0.090$ to $r_{0.05} < 0.082$ (95 % C.L.), as shown in Figure 1.7. The improvement seems to be small as expected due to the limited sensitivity in both experiments at that time but this is just a demonstration of B-mode lensing signal removal via “delensing“. We expect to have better constraints with the current and future BICEP Array data.

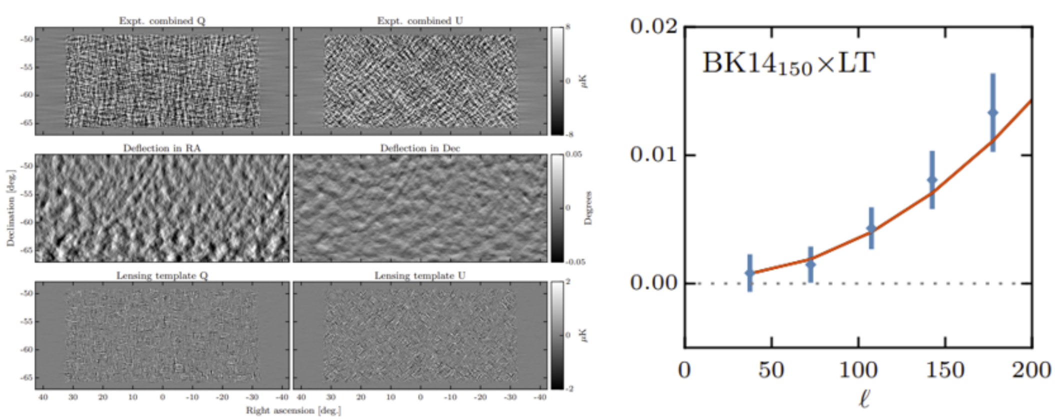

Figure 1.7: The first demonstration of “delensing” on SPTpol+BK14 data (The BICEP/Keck and SPTpol Collaborations, 2020). Further deep search for r with high sensitive BICEP Array data is coming soon.

- *Polarized Galactic foregrounds*: Our Galaxy has other sources that could generate B-mode polarization, such as Dust, synchrotron, AME in our galaxy, other point sources, etc. r is also contaminated with contributions from the two primarily polarized Galactic foregrounds, thermal dust that comes from the interstellar space and synchrotron emission due to the cosmic rays interaction with the galactic magnetic field. The foregrounds and CMB signal can be separated since each has a different spectral energy distribution. Each has much higher brightness which varies with observing frequency, compared to the potentially detectable primordial gravitational waves. The thermal dust is peaking at high frequencies, and synchrotron is dominating at low frequencies, as shown in Figure 1.8. These foregrounds must be removed by making CMB observations at multiple frequencies, which will constrain the foreground parameters to be removed from our CMB science maps. Our current analysis technique relies on comparing the auto- and cross-spectra of the multi-band maps to a parametric model of CMB plus galactic synchrotron and dust foregrounds.

The observation of the CMB for mapping the faint B-mode polarization pattern is very sensitive to the Galactic foregrounds which could produce a false B-mode signal. Figure 1.8 shows that the thermal dust and synchrotron emission are much brighter than the expected band-power for the primordial BB ($r = 0.001$). Multi-frequency observations are essential toward constraining the preliminary foreground parameters. We are currently define basic seven parameters to describe the foregrounds, amplitudes A_{sync} and A_{dust} at multiple $l = 80$ and pivot frequency of 23 GHz and 353 GHz, respectively, frequency spectral indices β_{sync} and β_{dust}, spatial spectral indices α_{sync} and α_{dust}, and dust and synchrotron spatial correlation ϵ. We also define the dust and synchrotron decorrelation between two bands, $\Delta^{'}_{sync}$ and $\Delta^{'}_{dust}$. We expect to have more complicated foregrounds models as we go deeper in sensitivity. We have been looking at the thermal dust on the past years using previous high frequency BICEP/Keck generations and we constrained its parameters but the synchrotron emission, remains a priority in order to improve the sensitivity on r, especially below BICEP3 at 95 GHz. This shows the motivation for this thesis to develop the first BICEP Array receiver at much lower frequencies, 30/40 GHz for pushing down our limits to further constrain synchrotron signal where it highly dominates. We model the polarized synchrotron spectral energy distribution in our baseline analysis as a simple power law, $I_s \propto \nu^{\beta_{sync}} l^{\alpha_{sync}}$. We use multicomponents likelihood analysis to constrain these foreground parameters in our parametric model (lensed−ΛCDM and the primordial B-mode component with different values of r). In BK18, we use a Gaussian prior of β_{sync} = -3.1 ± 0.3 (Fuskeland, et al., 2014), and do not detect synchrotron. Results of our baseline analysis $A_{sync,23GHz}$ < 1.4 μK^2 at 95% confidence (Ade, et al. (BICEP/Keck Collaboration), 2021). Extrapolation of the S-PASS data indicates that A_{sync} in our field is about one third of the BK18 95% upper limit, and hence as the first BICEP Array receiver at 30/40 GHz improves, we expect to both detect synchrotron, and to be able to remove the prior on β_{sync}.

These B-mode detection challenges require high sensitive instruments with a minimized systematic errors, multi-frequency coverage and extremely low statistical noise to map the polarization of the CMB and image the B-mode polarization pattern. Many CMB experiments have been working these challenges for B-mode measurements such as SPT, POLARBEAR, BICEP, Planck, ACT collaborations, and published their constraining results on r, as shown in Figure 1.9. The BICEP/Keck Array collaboration has been published world-leading constraints on r. Our latest published upper limit from BK18 (Ade, et al. (BICEP/Keck Collaboration), 2021) shows $r_{0.05} < 0.036$ and $\sigma(r) = 0.009$ at 95% C.L. These are the strongest constraints to date on primordial gravitational waves, which ruled out many inflation models including the single field slow-roll inflation model, as shown in Figure 1.9. Starting 2020, BICEP Array telescope has replaced Keck Array receiver, along with BICEP3 at 95GHz, expect to probe the primordial B-mode with unprecedented sensitivity of $\sigma(r)$ < 0.003 after the full BICEP Array receivers deployment to the South Pole. The detection of primordial B-modes at the levels to which BICEP Array will be sensitive would provide evidence that the theory of quantum gravity must accommodate a super-Planckian field range for the inflation. This means that a detection would open up an observational window into quantum gravity and provide very strong motivation to better understand how large-field inflation can be naturally incorporated in quantum gravity. The detection would also rule out alternative models to inflation that predict no detectable level of tensor modes. On the other hand, the non-detection would improve our upper limit on r which helps us to better understanding how (or if) this rapid expansion occurred by narrowing down the possible inflation models. We still do not have a lower bound on r, or absolute confidence of its existence. However, our attempts to measure the inflation's signature will provide widespread answers, ranging from understanding the physics of the newborn universe to properties of our observed universe today.

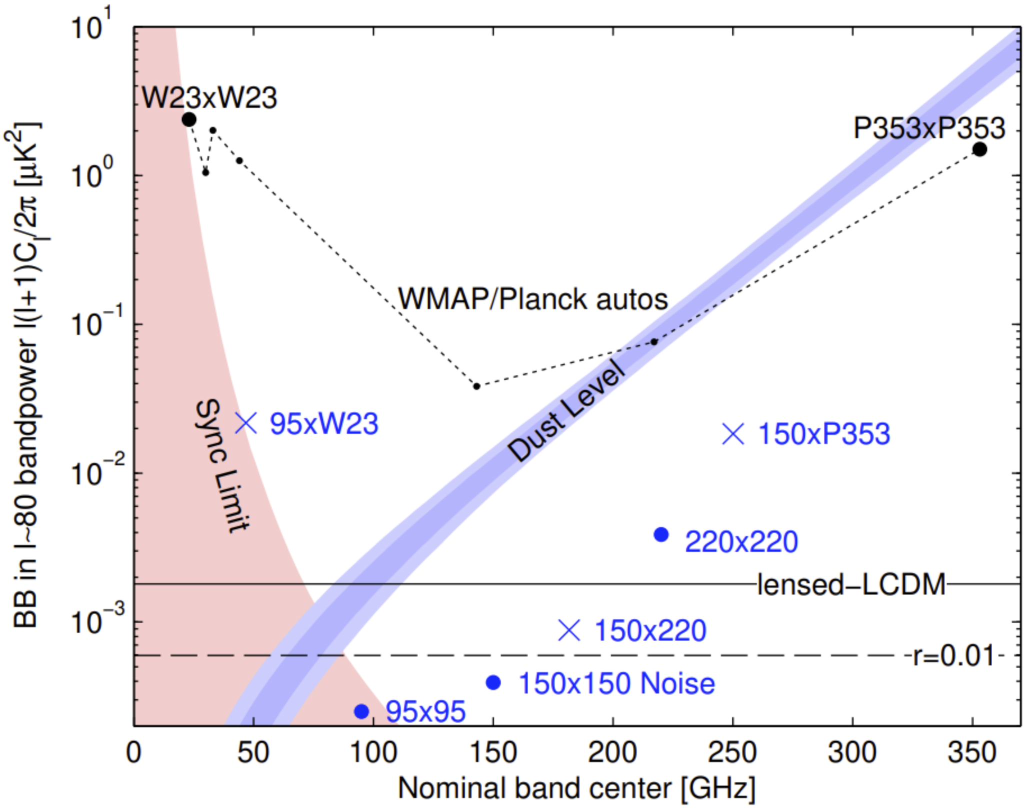

Figure 1.8: Expectation values and noise uncertainties of the l = 80 BB bandpower spectrum in the BICEP/Keck field, reprinted from (Ade, et al. (BICEP/Keck Collaboration), 2021). The blue band region shows the thermal dust upper limit which peaks at high frequency. The red band region shows the 95% synchrotron upper limit including parameters uncertainties, which dominates at low frequency. The blue dots and crosses show the noise uncertainties of the BICEP/Keck auto-spectrum and cross-spectrum. The upper dashed line shows the sensitivity of WMAP and Planck data. We can not distinguish between the foreground and CMB with one observation band, even with deeper measurements at that single frequency. The detection of synchrotron at 95 GHz in the near future (as BICEP3 goes ever deeper) would limit its use in CMB measurements, unless there is another band that also detects synchrotron. Our previous BICEP/Keck experiments does not have any science data below 95 GHz for constraining the synchrotron, which shows the important of the first low frequency BICEP Array receiver at 30/40 GHz to drive progress on constraining r due to the need to measure the synchrotron. Similarity, our previous additional CMB measurement at 220 GHz would jointly help constraining the dust emission along with the CMB measurement at 150 GHz.

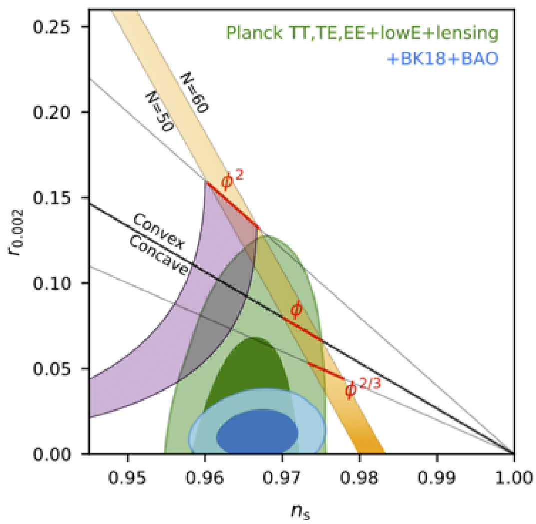

	arXiv	$\sigma(r)$ BB
DASI	0409357	7.5
BICEP1 2yr	0906.1181	0.28
WMAP 7yr	1001.4538	1.1
QUIET-Q	1012.3191	0.97
QUIET-W	1207.5034	0.85
BICEP1 3yr	1310.1422	0.25
BICEP2	1403.3985	0.10
BK13/*Planck*	1502.00612	0.034
BK14/WP	1510.09217	0.024
ABS	1801.01218	0.7
Planck	1807.06209	~ 0.2
BK15	1810.05216	0.020
POLARBEAR	1910.02608	0.3
SPTPOL	1910.05748	0.22
Planck/Tristram	2010.01139	0.07
Spider	2103.13334	0.13
BK18	2110.00483	0.009

Figure 1.9: The status of inflationary gravitational wave parameter r. Left: Constraints in the r versus n_s for the Planck 2018 baseline analysis, in conjunction with BICEP/Keck data through the end of the 2018 season plus BAO data (Ade, et al. (BICEP/Keck Collaboration), 2021). The constraint on r tightens from $r_{0.05} < 0.11$ to $r_{0.05} < 0.035$. The yellow band region shows the inflation period (50-60) e-folds. Right: The published constraints history on $\sigma(r)$ by different experiments so far, leading by the BK18 results. The *blue* colored texts show our efforts in the past two decades. It also shows the improvement on $\sigma(r)$ from BK15 (Ade, et al. (BICEP/Keck Collaboration), 2018) to BK18 by using three years of 95 GHz data from BICEP3 and more 220 GHz data from Keck Array.

1.7 Thesis Outline

I have organized the contents of this dissertation in a chronological order since I started in 2017 and contributed to the engineering design and testing of BICEP Array telescope toward the deployment and the science observation at the South Pole.

Chapter 1 gives an overview about the scientific motivation behind my PhD journey including the Big Bang model, CMB, the important of inflation, the current status, challenges and path forward for constraining the inflationary gravitational waves.

Chapter 2 provides a brief history of BICEP experiments, describing the design considerations, telescope's observation site, and the motivation leading to the newly deployed BICEP Array telescope that will map the CMB polarization with unprecedented sensitivity. This chapter also provides details on the cryogenic instrumentation, optical design, focal plane and detector tiles of the first BICEP Array receiver at 30/40 GHz.

Chapter 3 focuses on the engineering design principles of the antenna-coupled transition edge sensor bolometers detector, for covering the nominal single CMB observing band (30 GHz or 40 GHz) as well as the two CMB observing bands (30/40 GHz) at the same time for the first time. The dual-color detector is a new technology for further improving the sensitivity of the receiver. I will also introduce other detector studies for the sensitivity improvement.

Chapter 4 details the focal plane engineering of the 30/40 GHz BICEP Array receiver. I will start with the important of this problem that limited our sensitivity on r on BK15 data due to beam systematics and the needed for improvement for BICEP Array. I will discuss the wide-band design 30/40 GHz and laboratory demonstration of broad-band focal plane frame to minimize the systematic errors. This technology has been extended to be used for higher frequency BICEP Array receiver at 150 GHz and 220/270 GHz.

Chapter 5 shows the laboratory demonstration of 30/40 GHz BICEP Array detectors at Caltech. The full optical characterization will be discussed and compared with our simulations. This includes the effect of shielding the cryostat against the external RF sources for reducing the noise on our CMB data.

Chapter 6 reports the deployment of 30/40 GH BICEP Array receiver to the South Pole and its performance during three deployment seasons. This chapter addresses the engineering challenges and upgrades to improve the mapping speed for constraining the synchrotron foreground, toward improving our constraints on inflationary gravitational waves amplitude r.

Chapter 7 explains the demonstration of the dual-color detectors at 30/40 GHz and on-sky performance at the South Pole. I will also introduce the extended dual-color detectors to cover the higher two CMB observing bands at 90/150 GHz as well as 150/220 GHz .

Chapter 8 illustrates the implementation and tests of the Adiabatic Demagnetization Refrigerator (ADR) for the next generation 100 mK CMB-S4 detector arrays in a prototype Small-Aperture 95/150 GHz telescope (PSAT) planned to observe on the BICEP Array.

Chapter 9 summarizes my PhD research work and future path forward.

Chapter 2

BICEP ARRAY CMB EXPERIMENT

The measurement of Cosmic Microwave Background in the 1960s opened a new window of physics to study the early universe. The CMB detection inspired generations of scientists around the world to build advanced experiments to further explore the universe's age, formation, geometry and evolution over billions of years. The current science goal in the cosmological field is to build very sensitive instruments to measure the degree scale B-mode polarization pattern of the CMB that arises from the inflationary gravitational waves.

The BICEP/Keck Array collaboration has deployed a series of telescopes to the Amundsen Scott South Pole Station, Antarctica to search for the cosmic inflation's signature, while steadily increasing map depth. I will give an overview about BICEP/Keck projects history leading to the current advanced stage in this program, the degree-scale BICEP Array telescope with unprecedented sensitivity levels on the inflationary gravitational waves amplitude r.

2.1 BICEP/Keck Experiments Overview

Figure 2.1 shows the progression of BICEP/Keck Array CMB experiments. The program started with BICEP1, which operated feedhorn-coupled NTD polarization sensitive bolometers at 95 GHz and 150 GHz simultaneously. BICEP2 fielded the first antenna-coupled bolometer arrays at 150 GHz. They extended the deep polarization maps by covering wide range of frequencies at 150 GHz and 220/270 GHz with Keck Array along with 150 GHz band for foregrounds constraining and separation. During stage 2 of BICEP/Keck program, Keck Array telescope was designed to be about 5 times BICEP2. Then, we moved to stage 3 with BICEP3 at 95 GHz which accomplished about ≈ 10 times higher detector count compared to a single Keck Array receiver at a given frequency band. BICEP3 also has faster optical throughput compared to Keck Array. Each of BICEP/Keck telescopes are designed to detect the faint and degree-scale B-mode peak. All generations shared a similar core design of a compact, cold optics and on-axis refracting telescope to observe a small patch of the sky with maximized sensitivity, low instrument loading, and excellent polarization systematic control. In order to improve the sensitivity of the instrument, we increase the number of detectors for collecting more CMB photons,

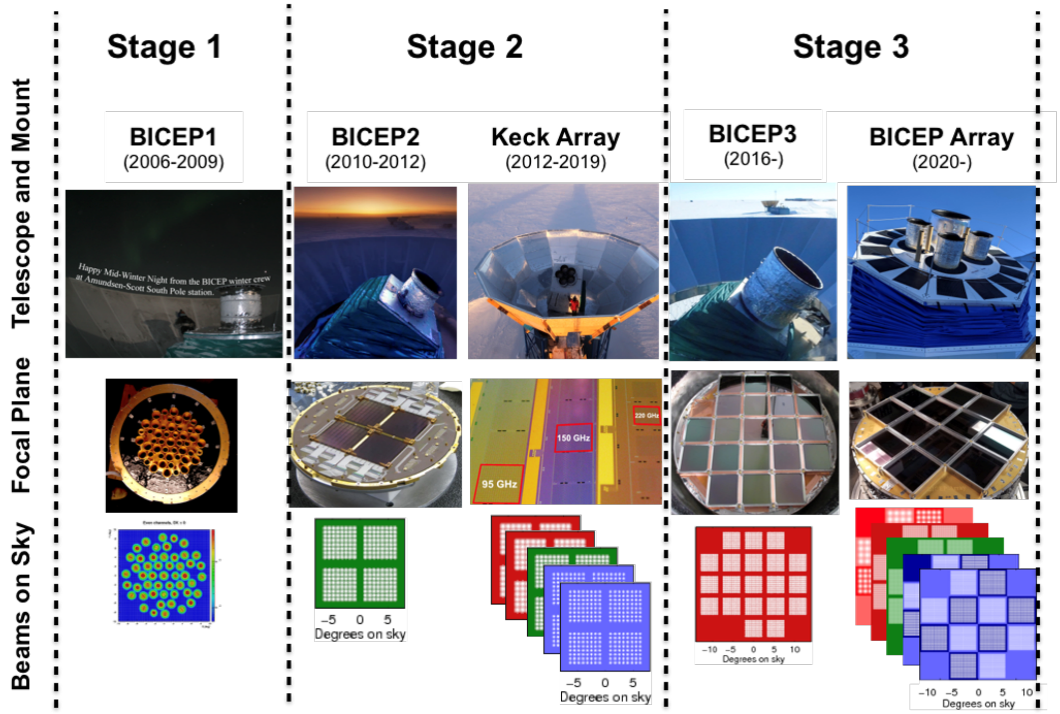

Figure 2.1: The progression of the BICEP/Keck Array program leading to the BICEP Array with an exceptional sensitivity, which will map the sky from 30 GHz to 270 GHz with over 10,000 detectors. The top row shows the telescopes as installed at the South Pole. The middle row shows the focal plane. The bottom row presents the detector beams as projected on the sky. Each color represents the frequency coverage. The plot is made by BICEP/Keck Collaboration.

and over wide frequency coverage for constraining the polarized foregrounds.

The growth of technology improvement on these generations for maximizing the sensitivity led BICEP/Keck (BK) program to have the world-leading constraints on r (Ade, et al. (BICEP/Keck Collaboration), 2021) by using up to three years of BICEP3 data at 95 GHz and Keck Array data at 220 GHz, as shown in Figure 1.9. The current sensitivity is limited by the modeling of both gravitational lensing and polarized Galactic foreground, especially synchrotron emission, leading to the important of the advanced telescope, BICEP Array (Hui, Ade, et al. (BICEP/Keck Collaboration), 2018). For more information about the latest BICEP experiments, see (Kang, 2020; Hui, 2018; Palladino, 2021; Crumrine, 2022; Karkare, 2017; Willmert, 2019; Yang, 2021). BICEP/Keck experiments are currently making CMB observations with BICEP3 and BICEP Array.

Telescope site and mount

The BICEP/Keck CMB experiments are running from two sites, the Dark Sector Laboratory (DSL) and The Martin A. Pomerantz (MAPO) building which are located by $\approx$ 1 Km from the Amundsen-Scott South Pole station building. The National Science Foundation (NSF) provides the operation and support for our all station needs including our team members in the last three decades. MAPO building hosted DASI experiment from 2000-2003, QUaD experiment from 2005-2007, Keck Array (2011-2019), and currently BICEP Array (2019-present). DSL building hosted BICEP1 (2006-2009), BICEP2 (2010-2012), and currently BICEP3 (2015-present). BICEP3 and BICEP Array telescopes are currently observing CMB from the South Pole. The station opens up for the science team during the austral summer to easily perform upgrades, maintenance, and instruments calibrations and prepare the telescope for excellent science observation during the winter season. The South Pole station is an ideal site for CMB millimeter-wave observations for various reasons. The geographic South Pole is an extremely dry desert since it is located an elevation of 9,300 feet and thus the water vapor amount in the atmosphere is extremely low. The winter season at the South Pole has an extreme cold and stable weather (up to -90° C) due to the 6- months of continuous darkness. The South Pole does not have the daily sunrise/sunset that might stir up the atmosphere. The South Pole has a stable atmosphere with a minimized sky noise leaking into our measurements due to the absent of diurnal turbulence. These factors provide an excellent transparency at mm-wave band for CMB observation. Additionally, the location of the South Pole station with respect to the Earth allows the sky to rotate around the zenith with fixed elevation angle. Thus our telescopes are constantly observing the same small sky patch ($\approx$ 1% of the full sky) all the time, leading to larger integration times and consequently improving the map depth for the potential faint B-mode signal. We also design our receiver for a single band coverage over 25% band width, where the atmospheric spectrum at the South Pole provides a microwave transparent window, as shown in Figure 2.2.

Observation strategy

There are two popular CMB observation strategies, either observe a large area of the sky with lower pixel resolution or small patch of the sky with maximum pixel resolution. Since we have not detect the B-mode polarization, BICEP/Keck has observing a small patch of the sky (1%), where the foregrounds could be safely ignored due to it's lower intensity. This would conduct deep CMB polarization

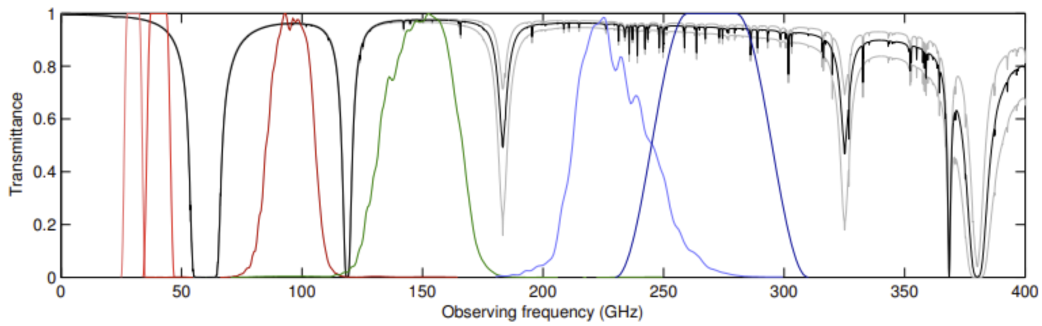

Figure 2.2: The median atmospheric transmission at the South Pole during the winter season (black) overlaid with the BICEP/Keck bandpasses and observation band centers of 30/40 GHz, 90 GHz, 150 GHz, 220/270 GHz. We have designed our detectors to cover 25 % bandwidth to avoid the out of band atmospheric features.

maps with building up sensitivity on a fewer modes that are needed for the initial B-mode detection. We are observing the sky over $20 < l < 200$ (0.05 to 1 Hz) since the B-mode signal is expected to peak at $l = 100$. We start mapping the sky area of 400 square degrees for the earlier BICEP/Keck experiments then we increase the field of view to 600 square degrees for BICEP3 and BICEP Array. BICEP Array scans the sky with -70° < δ < 40° and -60° < RA < 60°, where R.A. is the right ascension of the telescope. BICEP3 and BICEP Array have been observing a lowest foreground possible region on the sky, away from the galactic plane, known as " Southern Hole", and centered at a declination center of the patch $\delta = -55°$. Our telescopes can move in three axes: Azimuth (AZ), Elevation (EL), and Deck angle (DK). We scan back and forth through the entire field with a speed of ≈ 2.8° per second in Az and at constant EL over 50 minutes. A collection of roughly 50 back-and-forth halfscans which are known as "scansets". About 7-10 Scansets are grouped into phases which cover different ranges of AZ and EL. The receiver also rotates around boresight in DK for the beam systematic minimization between the detector pair and for the CMB polarization measurements. BICEP Array observed the CMB over eight DK angles of 23°, 68°, 113°, 158°, 203°, 248°, 293°, and 338°.

BICEP Array telescope could observe the sky for three days at least during the fridge hold time at the base temperature but we expect to change with the upcoming BICEP Array receivers at higher frequencies. Various schedules have been running with different DK angle and EL offsets for obtaining a uniform sky coverage and a better control of the systematics.

2.2 BICEP Array Telescope

BICEP Array is the stage 3 telescope in the BICEP/Keck program that replaced Keck Array with four-BICEP3 class receivers with wide frequency coverage to look for inflationary signals with the ultimate sensitivity of $\sigma(r) \leq 0.003$ (Hui, Ade, et al. (BICEP/Keck Collaboration), 2018) at the l=80 angular scales where the PGW signal is predicted to peak. A huge number of photon-noise limited polarization-sensitive detectors count will map the polarization of CMB over 30/40, 95, 150, and 220/270 GHz channels to fully characterize the Galactic synchrotron and thermal dust emissions. The expected sensitivity of the 4 receivers are calculated in table 2.1 based on the achieved on-sky performance of the existing receivers. We also moved to further enhance the sensitivity of each pixel by increasing its bandwidth to cover two CMB observation bands at the same time, as I will show in details in Chapters 3 and 7. The sensitivity on r is getting better. These progressive strategies would produce high-sensitive and low noise observed CMB maps with an improved mapping speed.

The first low frequency BICEP Array receiver (BA1) at 30/40 GHz (Schillaci, Ade, et al. (BICEP/Keck Collaboration), 2020) has been deployed to the South Pole during the austral 2019-2020 season for constraining synchrotron foreground. The second BICEP Array receiver (BA2) at 150 GHz has been deployed this past season. The fourth BICEP Array receiver (BA4) will deploy next year for constraining the thermal dust. The technology developed for BICEP Array will feed into demonstrating 100 mK CMB-S4 detector arrays in a prototype 95/150 GHz telescope planned to observe on the BICEP Array, as I will discuss in Chapter 8. Thermal Kinetic Inductance Detectors (TKIDs) (O'Brient, R., et al., 2018) are currently being developed and tested to be used for higher frequencies BICEP Array receivers. The rest of this chapter gives an overview of fundamental design aspects of BICEP Array receiver design at 30/40 GHz.

Cryostat

The cryostat is designed to be as compact with sufficient angular resolution to observe the degree-scale B-mode. The compact design enables the entire telescope to be rotated around its boresight. Constraining the faint B-mode signal requires detectors operating in ultra-cold temperatures with a minimum instrument internal loading. This could be achieved with an optimal cryogenic cryostat. BICEP Array cryostat has designed based on the successful former BICEP/Keck receivers. The first low frequency BICEP Array cryostat at 30/40 GHz contains 3 stages of shells,

Receiver observing band (GHz)	Number of detectors	Single detector NET ($\mu K_{CMB}\sqrt{s}$)	Beam FWHM (arcmin)	Survey weight per year ($\mu K_{CMB}{}^{-2}yr^{-1}$)
Keck Array				
95	288	288	43	24,000
150	512	313	30	30,000
220	512	837	21	2000
270	512	1310	17	800
BICEP3				
95	2,560	288	24	213,000
BICEP Array				
30	192	260	76	19,500
40	300	318	57	20,500
95	4,056	288	24	337,400
150	7,776	313	15	453,000
220	8,112	837	11	32,000
270	13,068	1,310	9	21,000

Table 2.1: The BICEP/Keck receivers parameters for Keck Array, BICEP3 and BICEP Array. You could notice the big jump in sensitivity between Keck Array and BICEP Array for a given frequency band. The blue colored numbers are the achieved performance at the South Pole. The survey weight values of BICEP Array are scaled from achieved survey weights.

cooling down from the ambient temperature of 300K at the out-most shell to 50K and 4K by using a pulse-tube Cryomech PT415 cryocooler, as shown in Figure 2.3. The Pulse-tube is mounted outside the three shells as the primary refrigerator for providing continuous cooling. The top side of the receiver contains a vacuum window that is made of HDPE High-density polyethylene (HDPE) and a stack of 12 layers of HD30 foam filter behind it for blocking undesired IR radiation. The 50K shell has about 30 layers of Multi-layer insulation (MLI) and 4K shell has about 5 MLI layers to minimize the radiation absorption between the vacuum jacket and the cryogenic stages. The 50K shell contains a high μ sheet for magnetic shielding. The 50K stage has An IR-absorptive alumina filter at the top with anti-reflection coated for filtering out of band radiation. We also installed about 10 layers of mylar "Skirt" around the 50 K shell to minimize the loading. A 6 low-conductivity G10 fiberglass supports the 50K radiation weight. The bottom side of the cryostat has the Multi-Channel Electronics (MCE) and "House-Keeping" backpack. The house-keeping controls all thermometers and heaters that are connected inside the cryostat. The Lake-shore Cernox RTDs read out the sub-k temperature stages while the silicon diodes Lake-shore DT-670 track the general thermometers down to the 4K.

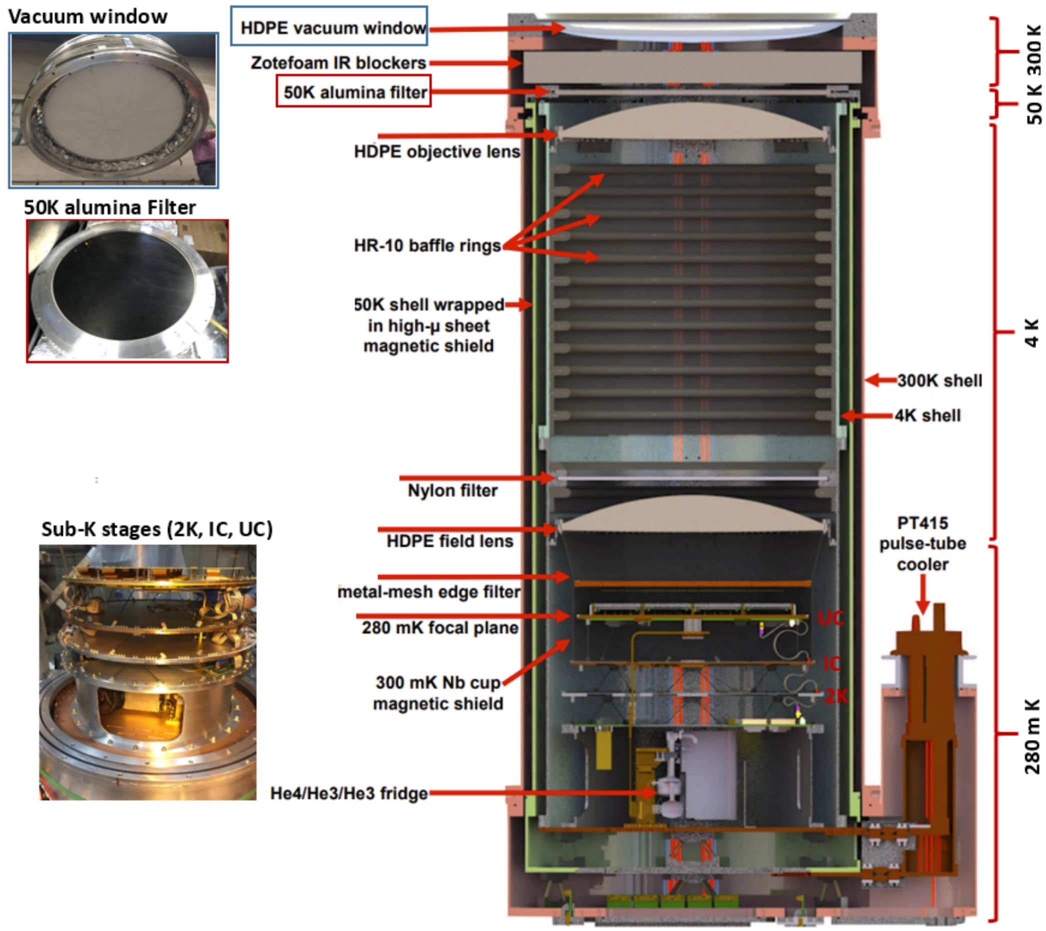

Figure 2.3: A cross section view of BICEP Array cryostat at 30/40 GHz indicating the cryogenic stages (300K, 50K, 4K, 250 mK).

Sub-Kelvin stage

A combination of filters are mounted at the cryogenic stages to reduce the photon loading on the focal plane and sub-K stage. The sub-K stage, known as 2K, intermediate-cold (IC), and ultra-cold (UC) are mechanically supported by low conductivity carbon fiber trusses because of its high ratio of stiffness to thermal conductivity at 280 mK. the IC stage hosts a superconducting Nb Spittoon for dampening the radial magnetic fields and superconducting NB plate for reducing the axial magnetic fields before reaching to the focal plane. The three-stage ^{4}He/^{3}He/^{3}He sorption fridge cools the focal plane to the base temperature of 280 mK, as shown in Figures 2.3 and 2.4. BICEP Array focal plane hosts 12 detector tiles. The ^{4}He stage condenses ^{3}He in the IC and UC stages for cooling the focal plane to that base temperature. For more information about the fundamental process of the fridge design principles, see (Duband, et al., 2018). The fridge needs to be periodically re-cycled before it runs out by heating the helium pumps to a given temperature (roughly 40 K), leading to desorption of the helium gas from the activated charcoal pumps. The hold time of the fridge determines the CMB observing schedule.

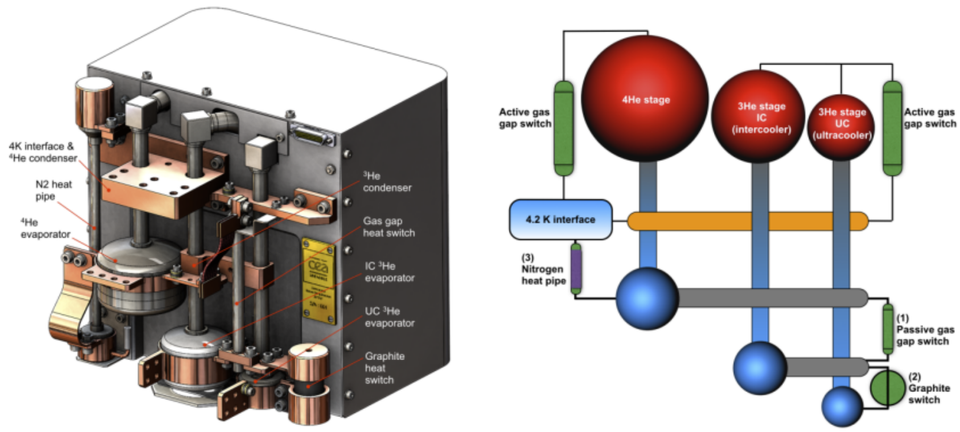

Figure 2.4: The 3D model diagram of the sorption fridge installed on BICEP Array receiver, reprinted from (Duband, et al., 2018).

Optical design

BICEP Array is an aperture telecentric refracting and on-axis telescope. Our telescope is optically designed with a given aperture size for the optimal sensitivity around the angular scale where the B-mode is expected to peak, like the former BICEP Keck receivers. BICEP Array receiver employs two HDPE optical elements, the objective and field lenses, which are housed at 4K stage for low thermal loading on the detectors. A Nylon IR filter is installed between the two optical elements to minimize the loading on the focal plane. BICEP Array features faster optics and wider field of view than Keck Array and are similar to BICEP3, resulting in a dramatically increased throughput and mapping speed, as shown in Table 2.2. The Zemax simulation ray tracing diagram for different detector locations within the focal plane are shown in Figure 2.5. The speed (f/ #) for the detector centered at the focal plane is 1.57 but slightly larger at the edge of the focal plane. A 550 mm stycast loaded HR-74 Eccosorb aperture stop is located around the objective lens to minimize the side-lobe pickup and unwanted reflections. Additionally, a Biaxially-Oriented Polypropylene (BOPP) membrane is pressurized by a dry gas nitrogen to prevent condensation on the window, and mounted above the cryostat at the South Pole to protect the vacuum window against any accumulated snow or ice.

	BICEP2/Keck Array	BICEP3	BICEP Array
Aperture size	264 mm	520 mm	550 mm
Field of View	15°	27.4°	29.6°
Beam Width	12’	8.9’	-
Speed (f/ #)	2.2	1.7	1.57

Table 2.2: Optical design parameters for BICEP2, Keck Array, BICEP3, and BICEP Array.

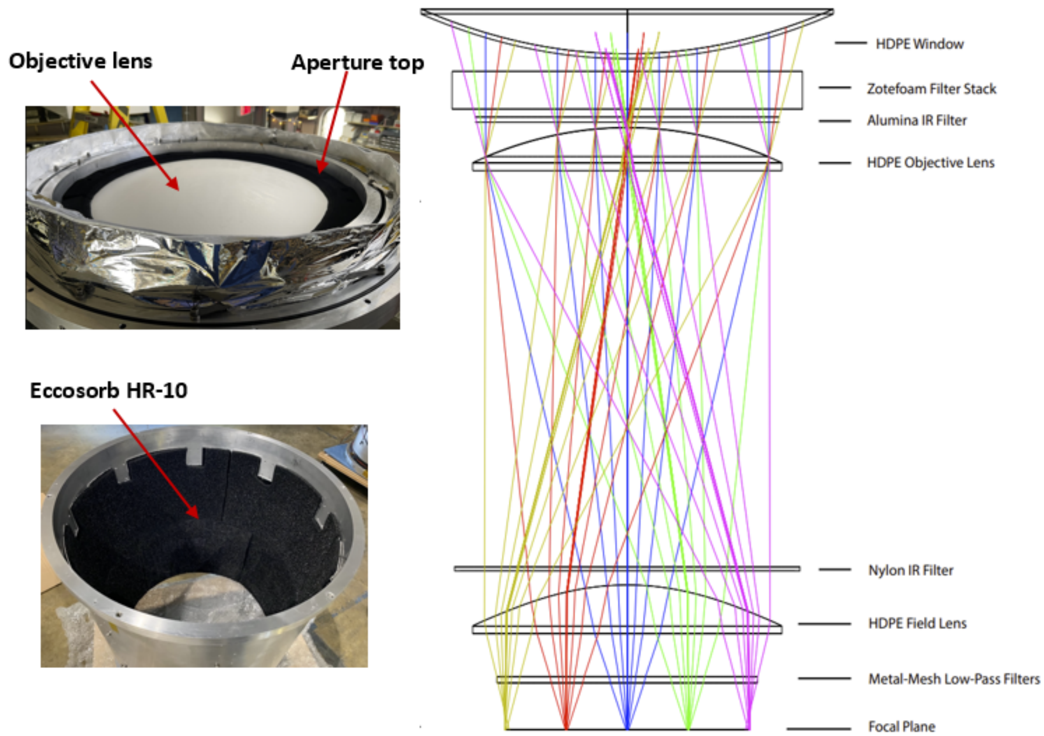

Figure 2.5: The optical design of BICEP Array receiver at 30/40 GHz. Right: ray-tracing diagram of optical chain in ZEMAX software. Left: pictures of the actual objective lens and the aperture stop at the 4K stage. The aperture stop terminates the side-lobe of the detector with an optimized spillover efficiency. The inner 4K stage between both lenses are covered with Eccosorb HR-10 for the internal reflection rays minimization.

Shielding: Magnetic and RF

Shielding the cryostat is very essential for the very sensitive magnetometer, Superconducting Interference Devices (SQUIDs) amplifiers from the external magnetic resources such as Earth’s magnetic field while our telescope is scanning CMB observation at the South Pole. We provide several stages of shielding against the magnetic field. A superconducting niobium box and very thin sheet of A4K high permeability Amuneal material are attached to the detector module. The SQUIDs are also wrapped with about 10 layers of high-μ Metglas 2714A for further protection. Additionally, a 2 mm thick niobium flared cone is installed around the focal plane. The cryostat is also shielded at the 50K shell with 1 mm thick cylinder A4K material. The RF pick by the MCE read-out electronics and house-keeping system could be coupled to the detector time stream and produce 1/f noise within our science band. We had several layers of shielding against RF as I will show in details with tests in Chapter 5.

Additionally, BICEP/Keck telescopes have two layers of shielding. The absorptive cylinder “forebaffle” with HR-25 microwave absorbing material is located around the cryostat. The ground shield is surrounding the mount. These shielding layers are used to minimize the unwanted beam reflections and radiation outside our field of view such as RFI from the base communication, as well as protecting the cryostat against the wind and snow.

Focal plane and detector tile

The CMB photos have been collected by the focal plane. The focal plane of BICEP Array receiver at 30/40 GHz is populated with twelve 6-inch detector modules, a mixture of single band slot detector modules and dual color Bowtie detector modules for higher detector counts, as shown in Figure 2.6. I will discuss the design principles of these modules in details in Chapter 3. Each detector module connects to a distribution board in the focal plane by three flex cables, which allow to easily swap or remove the modules. All modules are mounted to a gold plated, oxygen-free high thermal conductivity copper (OFHC) plate, providing a thermal sinking to the coolers. The sub-k stages (2k, IC, UC) are cooled by the sorption fridge. The focal plane is temperature controlled with resistive heaters to about 280 mK. The temperature control modules (TCMs) control the thermal fluctuations on the detector tiles.

The detector module design is based on the successful BICEP3 design, except the detectors are now fabricated on 6“ silicon wafers instead of the 4“ wafers. The detector tile are arranged in a detector pair of antenna-coupled polarization-sensitive Transition-Edge Sensors (TES), containing 32 to 50 detectors per tile depending on the observing frequency, either 30 GHz or 40 GHz. We also have additional dark detectors which are used to study noise and loading characterization of the detectors without any input optical power. These dark detectors consist of the full complete

TES island but are not connected to the slot-array antenna. The detectors have been fabricated in the Microdevices laboratory (MDL) at Jet Propulsion Laboratory.

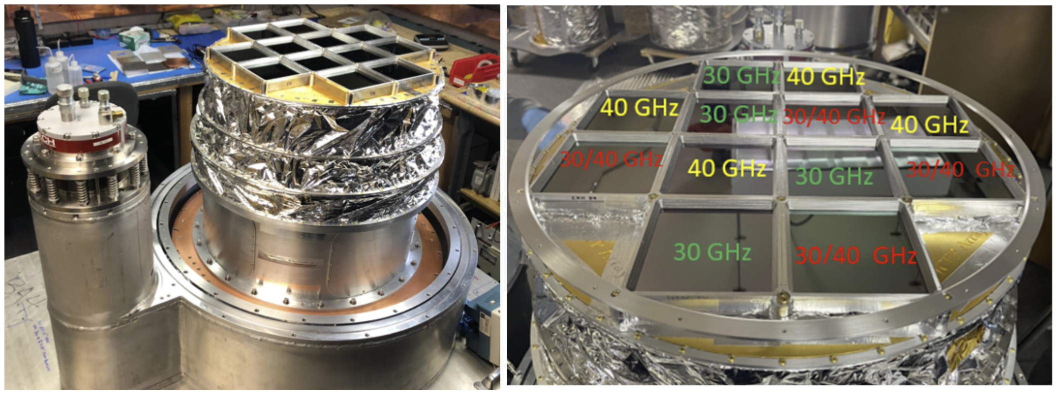

Figure 2.6: The focal plane configuration for BICEP Array receiver at 30/40 GHz during the deployment season at the South Pole.

The module packages the detector tile and its readout electronics in a compact and magnetically-shielded volume. The detector tile packaging are designed to provide the mechanical alignment and thermal stability for operating and reading out the pixels as well as an ease of upgrading any defected part if exists. Figure 2.7 shows the sky-side of the detector tile facing downward. The sky-side of the module begins with an aluminum frame to mechanically support the all the inner elements including substrates. A wide-band corrugated frame has been designed to minimized the interaction between the frame and the detectors located along the at the frame edge (Soliman, Ade, et al. (BICEP/Keck Collaboration), 2018) as I will describe in-details in Chapter 5. We received the CMB photons from the sky through quartz $\frac{\lambda}{4}$ anti-reflection (AR) tile and silicon substrates to minimize the reflections at the air substrate interface and undesired modes with the silicon substrate. We terminated the back response on the vacuum side with a $\frac{\lambda}{4}$ back-short. An additional A4K layer combined with the superconducting niobium case and back-short to provide an excellent magnetic shielding for the SQUID chips. A very thin Alumina circuit board holds the multiplexing (MUX) and Nyquist (NYQ) read-out chips, and capped by high permeability material. An H shape read-out PCB circuit board is located inside the module for routing the wiring connections to the slot-array through few flex cables. The bottom of the detector contains a Cu heat-sinking plate for making a thermal contact at the center of the niobium for superconducting phase transition. The backside of the detector module has 60-pins flex-circuit ribbon cables connected to Zero-Insertion Force (ZIF) connectors which we use as the interface connection to the focal plane.

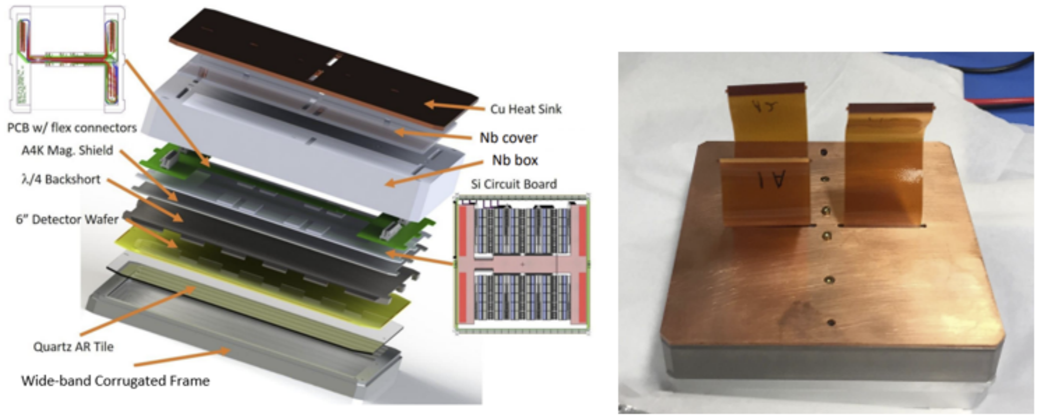

Figure 2.7: The detector tile components. Left: BA detector module exploded overview. Right: the backside of the detector module with flex-circuit ribbon cable and ZIF connectors for the focal plane connection interface.

Amplification, multiplexing, and read-out

BICEP Array TES detector is inductively coupled and read out by two-stages SQUID (SQ1 and SSA) which amplify and multiplex the signal by using the time-domain multiplexing (TDM) scheme developed by NIST (Korte, et al., 2002). The TDM scheme reduces the total number of wires going to the focal plane. Each TES detector is coupled to the first stage SQ1 by changing the coil flux, which is connected to its own row select (RS) switch. When we apply current to RS lines to be on, the TES current passes through SQ1 to be amplified by the second stage of SQUID Series Array (SSA) board which packaged in a niobium box at the 4K stage. The RS and SQ1 are located inside the detector tile. We tune the SSA by picking up an appropriate bias value and flux through sweeping the SSA flux feedback line, and reading the output V-ϕ response, as shown in Figure 2.8. We are similarly tuning the SQ1 for the optimal response. The Multi-Channel Electronics (MCE) developed by the UBC, and mounted outside at the bottom of the cryostat control the bias and read out the amplified and multiplexed TES channels. BICEP Array receiver at 30/40 GHz has one MCE crate with 24 read-out columns. Each column has 33 rows. Each row could read out one TES detector signal. The high frequency receivers such as 90 GHz and 150 GHz, require more than one MCE crate for reading huge numbers of detectors. The Nyquist sampling frequency for the 30/40 GHz is set to about 6 KHz to avoid aliasing. The MCE has an internal low-pass filter with cut off frequency of 60 Hz to block the leaking noise from our science band.

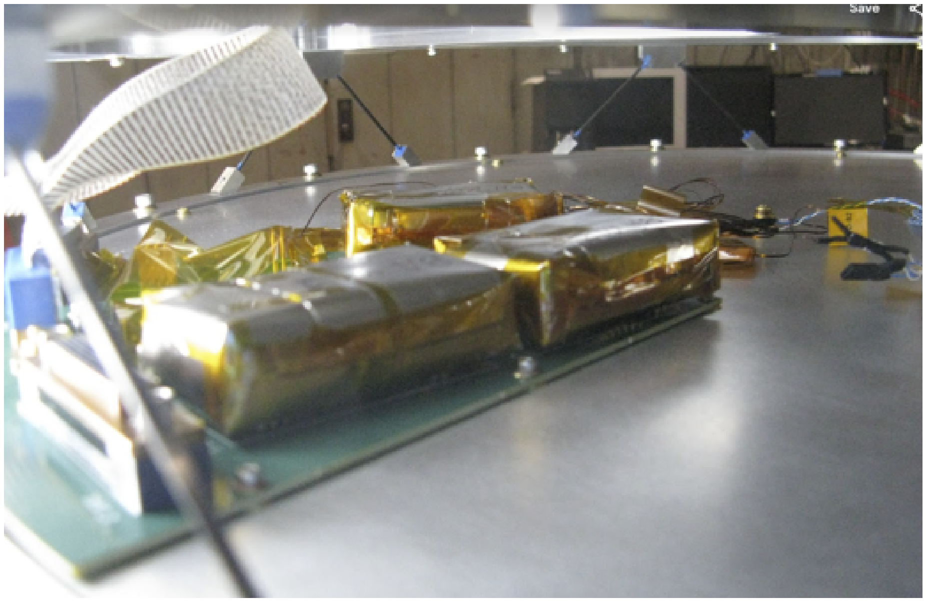

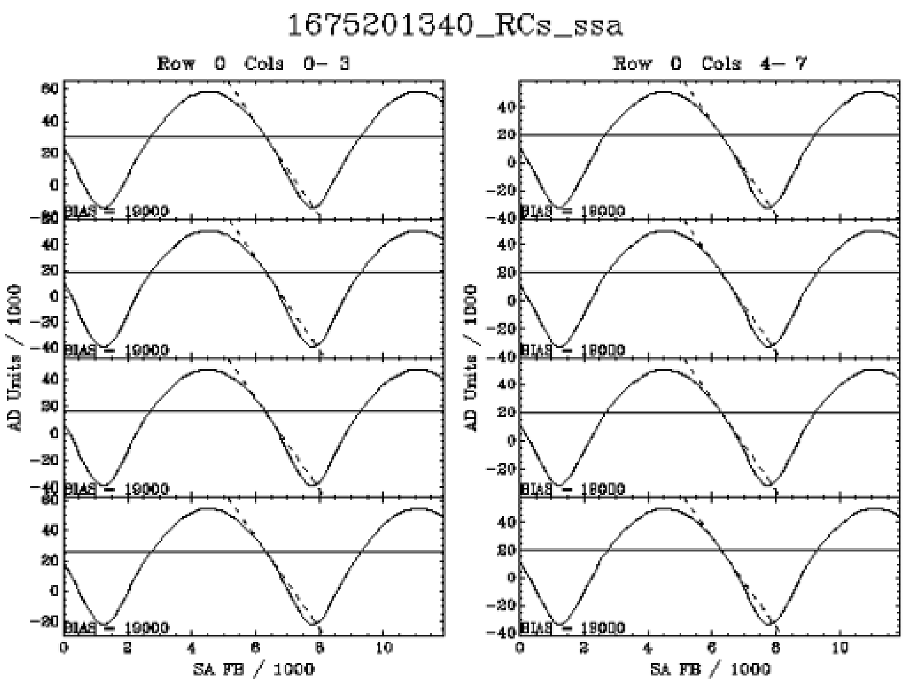

Figure 2.8: The SSA modules and the corresponding response. Top: the wrapped SSA modules inside 30/40 GHz receiver. Bottom: an example of V-ϕ sine-wave response for SQUIDs-SSA stage of BICEP Array detectors. The horizontal line shows the flux lock value. The voltage bias determines the optimal peak-to-peak value.

Chapter 3

BICEP ARRAY DETECTORS DESIGN

The previous chapters highlight the necessary detector camera design considerations for constraining the degree-scale B-mode polarization from the sky at the South Pole. Antenna-coupled Transition-Edge Sensor (TES) detector camera needs

- to be a dual- and linearly-polarized for the independent measurement of each CMB polarization.
- to have well matched polarized beams between both co-located detector pair, both at the center of the tiles and near the edges adjacent to the detector tile's frame, resulting in a tight control of beam systematic errors.
- to cover a single CMB observation band (nominal design) with 25% spectral bandwidth to fit the observation window of the atmosphere at the South Pole and avoid the atmospheric lines for a minimized noise performance (NET). We should also consider this requirement while designing the Band-pass filter.
- to observe over two or more CMB observation windows simultaneously by exploring the dual- and multi- color detectors and consequently improving the telescope's sensitivity. A novel diplexer circuit is also needed to partition the antenna's broad bandwidth into narrow CMB channels with a 25% spectral bandwidth.
- to have a stable impedance over a wide band for maximizing the power transfer with reduced mismatch losses.
- to have an optimal TES bolometer design with a stable performance to avoid saturation from the sky loading conditions at the South Pole and with photon-noise dominated characteristics.

These requirements drive our CMB detector design. Antenna-coupled TES detectors have been used in numerous successful CMB experiments, including BICEP Array (Ade, et al. (BICEP2, Keck Array, and SPIDER Collaborations), 2015 and Soliman, Ade, et al. (BICEP/Keck Collaboration), 2020). Our pixel design contains two co-located and orthogonally polarized planar antenna-arrays, each polarization is consisting of slot or Bowtie sub-antenna coherently combined through a microstrip summing network. The summing power from each polarization passed through an on-chip band defining filter designed to select the frequency of interest and reject out-of-band signals, specifically those on atmospheric lines. The collected in-band power is finally dissipated into a superconducting TES bolometer island. Figure 3.1 shows the deployed BICEP Array detectors at 30/40 GHz, single-color and dual-color. I will talk about the design of each of these elements in this Chapter before performing the measurements to validate our simulations in the Chapter 5.

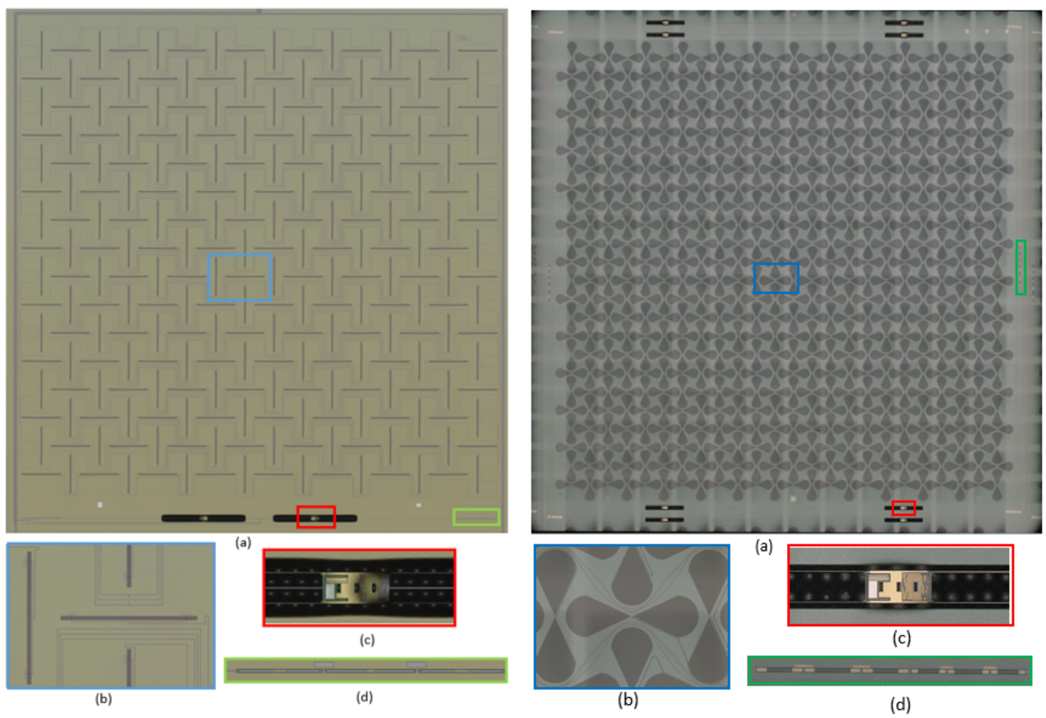

Figure 3.1: Photograph of the fabricated BICEP Array detectors at 30/40 GHz by the MDL/JPL. Left: single-color slot array (a): The full lithographic pixel showing 8x8 grid of antenna pair, (b) Vertical and horizontal polarization, (c) Transition Edge Sensor Bolometer (TES) and (d) Band-pass defining filter. Right: Dual-color Bowtie array (a): The full lithographic pixel showing 12x12 grid of antenna pair, (b) Vertical and horizontal polarization, (c) TES Bolometer and (d) Band-pass diplexer filter. Slot-array and Bowtie Array are patterned on a niobium (Nb) ground plane.

3.1 Phased Array Design Principles

We use arrays of rectangular slot antennas for single color detector and arrays of broadband bowties for dual color detector design. The individual phased array antenna in each detector should be spaced to Nyquist sample the focal plane surface to avoid the rapid change of antenna impedance with frequency, known as the grating lobes (Ade, et al. (BICEP2, Keck Array, and SPIDER Collaborations), 2015):

$$S \leq \frac{\lambda_{0,min}}{\sqrt{\epsilon_r}}(1 - \frac{1}{N}) \tag{3.1}$$

where S is the required slot spacing to avoid these unwanted lobes, $\lambda_{0,min}$ is the minimum wavelength of operation, ϵ_r is the relative permittivity of the surrounding medium, and N is the number of elements on each axis. Figure 3.2 shows the electromagnetic HFSS simulated infinite array for the single color slot array and dual color Bowtie array. We first scaled the slot size at 40 GHz from 95 GHz. Further optimization parameters have been studied in the simulation for an improved performance. The resulting electromagnetic frequency response is shown in Figure 3.12. Our detectors have side-lobes that have been terminated at the 4K aperture stop. The pixel size has been slightly reduced in f/λ spacing at 30 GHz to fit the detector 6" detector tile. The spacing between the slots at 30 GHz has been slightly decreased between the slots, keeping the slot dimension to be the same scaled version of 40 GHz detector. The slot Bowtie dimension have been optimized to operate at 30/40 GHz. The CMB photons have been received through A $\lambda_g/4$ thick quartz tile over the silicon (ε_r = 11.8) that serves as an anti-reflection coating (ε_r = 3.9-4) for the incoming radiation. The silicon wafer thickness is 0.625mm. Each detector tile has been arranged to an array to 5×5 pixels at 40 GHz, and 4×4 pixels at 30 GHz. Each pixel contains two orthogonally polarized detectors, each has a 8×8 slot-array that are sensitive to vertical "Pol A" and horizontal "Pol B" polarization. A $\lambda/4$ backshort cavity has been located underneath the tile to maximize the radiation coupling to the antennas and to terminate the back response, where $\lambda_g = \frac{\lambda}{n}$ is the guided wavelength in that medium, λ is the free-space wavelength and n is the material index. The Bowtie length has been optimized to be 1617 um for 35 GHz band center. The slot size are carefully optimized to be 1493 um × 43.5 um, and 1984 um × 57.8 um for band center of 40 GHz and 30 GHz, respectively. The pixel effective side length of 30 GHz and 40 GHz are 21.6 mm and 17.9 mm, respectively, to match our optics design shown in Figure 2.5 for a nearly uniform illumination and minimized spillover at the aperture stop and a given beam size and sinc pattern in the far-field of the telescope at the South Pole.

The array antenna illumination pattern of each polarization is calculated from the N elements as follows:

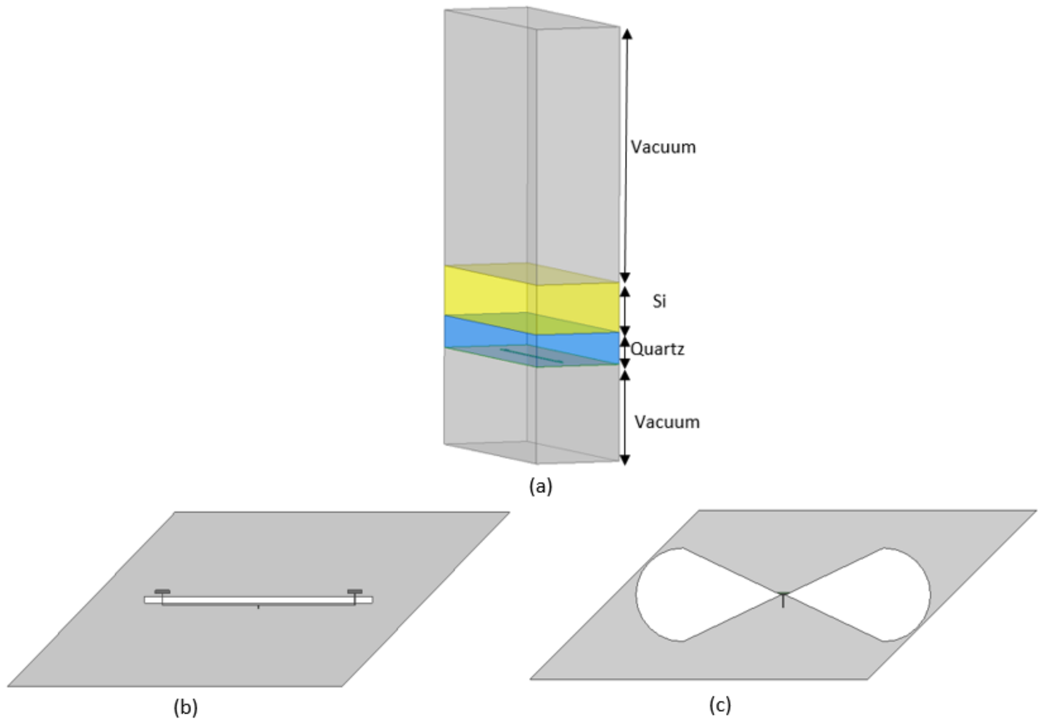

Figure 3.2: The 30/40 GHz detector modelling. (a) The HFSS EM simulated infinite array Bravais lattice unit cell, (b) Single-color at 40 GHz, and (c) Dual-color at 30/40 GHz.

$$A(\theta) = \sum_{m=-(N-1)/2}^{(N-1)/2} = e^{-j2\pi \frac{ms\sqrt{\varepsilon}}{\Lambda_o} sin\theta} = \frac{sin(N\pi s\sqrt{\varepsilon_r}\sin\theta/\lambda_{o,min})}{sin(\pi s\sqrt{\varepsilon_r}\sin\theta/\lambda_{o,min})}. \tag{3.2}$$

We sum the power pattern over the each antenna indexed by m, spaced by distance S. BICEP Array detector has been simulated with different sizes N, 2×2, 4×4, 6×6, 8×8,10×10, 12×12, as shown in Figure 3.3. The power pattern of the individual slot or individual Bowtie structure have fairly elliptical shape. As we increase the number of elements (N), the beam becomes close to have a circular shape, which minimizes the beam mismatch error due to the differential ellipticity between both polarization. The beam mismatch could potentially leak temperature into our polarization maps since we map the polarization of CMB by taking the difference between both polarization. At the same time, we need to minimize number of elements per pixel to get more detectors for packing density. Keck Array detector had 12×12 slot-array. BICEP Array detector size has been optimized for 8×8 slot-array to match the camera faster optical parameters shown in Table 2.2 as well as a minimized spillover loss at the camera's stop, reduced differential ellipticity beam systematics and an improved packing density within the focal plane. This would produce higher mapping speed to constrain Galactic foregrounds parameters. The beam pattern of each individual slot or Bowtie element sum up to form a high sensitive radiation beam with a minimized elliptical mismatch loss. This optimal sub-antennas would avoid excessive excitation of substrate modes that might degrade the detector's efficiency.

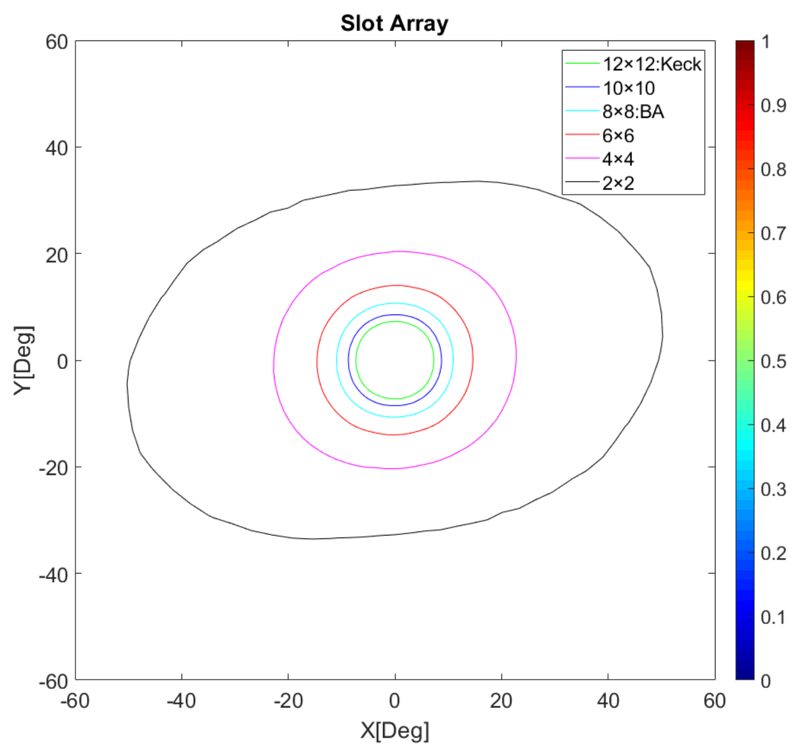

Figure 3.3: The radiation pattern of slot Array with different antenna pair. Keck Array telescope used 12×12 slot array configuration. BICEP Array telescope has been optimized for 8×8 slot array configuration. We gain faster optics, better FOV, packing density and consequently higher mapping speed.

Simulated beam pattern

The CST microwave studio is used to model the detector beam in time domain. Similar current is applied to each port on the slot. The optimized 8×8 slot phased array antenna has been simulated in Figure 3.4. The beam width of the detector is proportional to the slot array diameter $B.W. \propto \frac{\lambda}{D}$. The 30 GHz detector is slightly smaller by 9 % from the scaled version of the 40 GHz detector. The simulated beam size of 30 GHz detector is a little wider than the 40 GHz detector, as shown in Figure 3.4. The measurements will be discussed in Chapter 5.

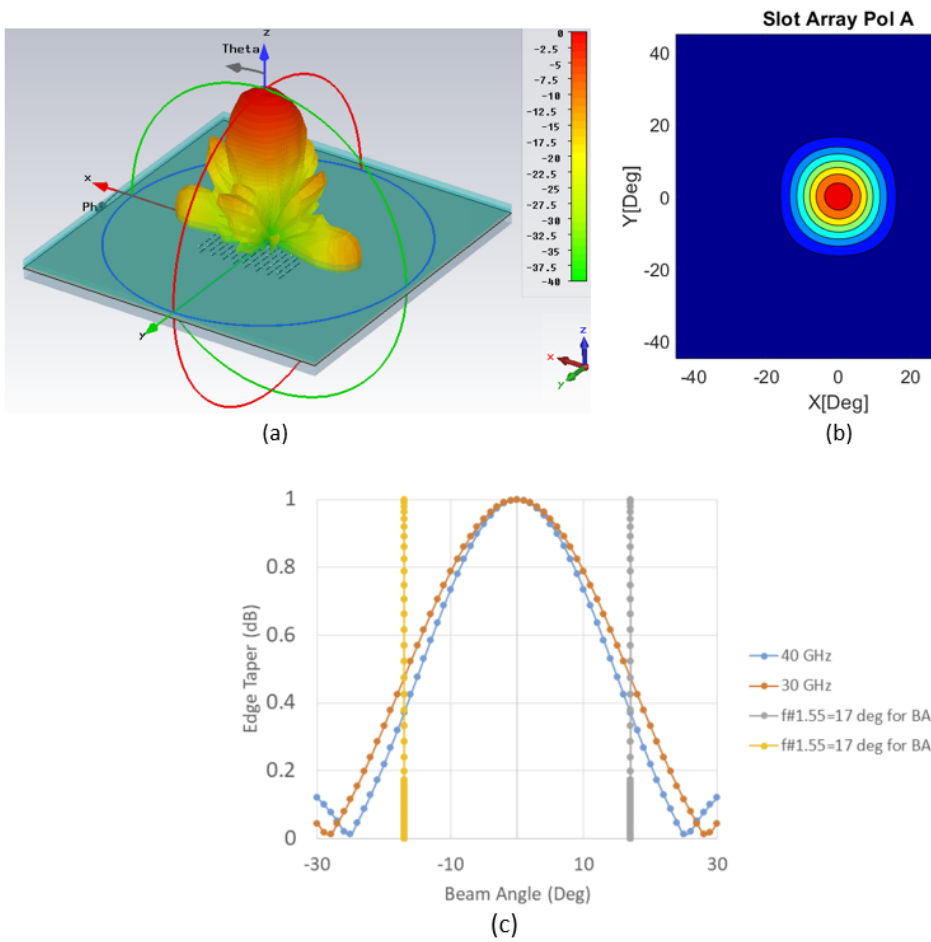

Figure 3.4: The 30/40 GHz detector optical modelling in time-domain. (a) The CST model of one slot array polarization “Pol A” at 40 GHz, showing the 3D beam pattern, (b) The computed pattern from an illumination where we assume uniformly illuminated slots with a cosine current distribution on each, (c) The simulated CST 1D-beam profiles of the 30 GHz and 40 GHz detectors. The aperture stop is roughly at 17° where the side-lobes are suppressed.

Feed location

The optical power collected of the slots or Bowties couples to the microstrip summing tree. To maximize the power transfer and minimize the return loss, we need to calculate the input impedance of the antenna array for designing an appropriate matching network. The feed location along each slot has been carefully optimized at certain location with respect to the edge where we could have a reasonable real and imaginary impedance to be able to match using our fabrication facilities. The HFSS software has been used to model the slot array in the frequency domain. The unit cell contains one single slot and surrounds by master/slave boundary conditions and a Floquet port for an infinite array modelling, as shown in Figure 3.2. We initially used two ports to feed the slot with a constant input impedance. The complex impedance of the slot antenna could be derived from the resulting scattering matrix S.

$$Z = Z_{in} \frac{1+S}{1-S} \tag{3.3}$$

The applied current to each port is identical. For the two ports system, the characteristic impedance of the slot antenna is obtained by

$$Z = \frac{Z_{11}I_1 + Z_{12}I_2}{I_1} = Z_{11} + Z_{12}. \tag{3.4}$$

where the positive sign in the equation arises from how the currents into ports 1 and 2 are perfectly in phase. This assumption is well motivated by an antenna that accepts plane waves incident on the focal plane with a Poynting vector normal the focal plane, modeled here as the fundamental mode of the Floquet Port. Z_{11} is the impedance at one edge of the slot. We used $Z_{in} = 50\ \Omega$. Figure 3.5 shows that the resulting impedance at the center-fed slot has a maximum of $\sim 500\ \Omega$ caused by the current node which is difficult to fabricate a transmission line that could match this huge impedance. We highly reduce the radiation resistance by asymmetrically feeding the slot with a pair of off-center microstrip lines. We choose the feed location at 114 um distance from the edge of slot at 40 GHz detector. The feed location at 30 GHz has been scaled from this value. The real and imaginary impedance of the Bowtie infinite array at the center showed a reasonable impedance to match using the co-planar wave-guide (CPW), as shown in Figure 3.6.

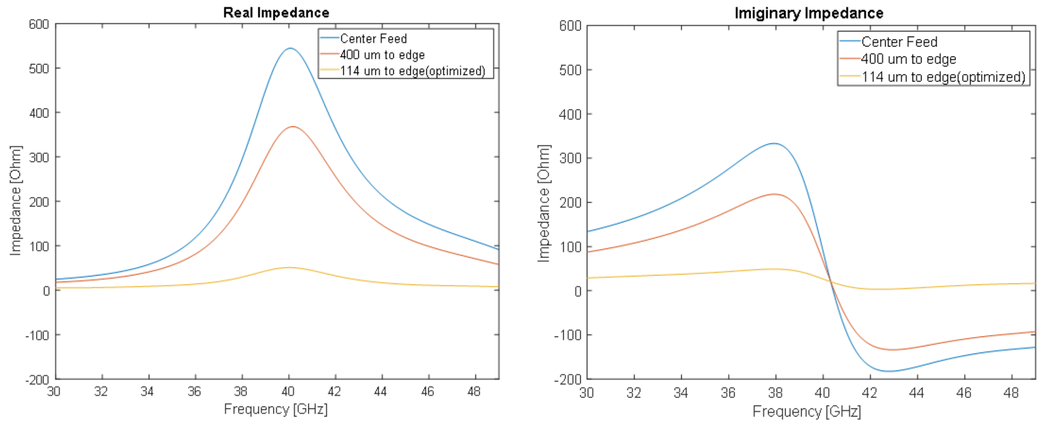

Figure 3.5: The computed input real and imaginary impedance versus feed location at the slot antenna. The maximum voltage is located at the center of the slot where the current is minimum. The impedance reduces as the feed location moves toward the slot's edge.

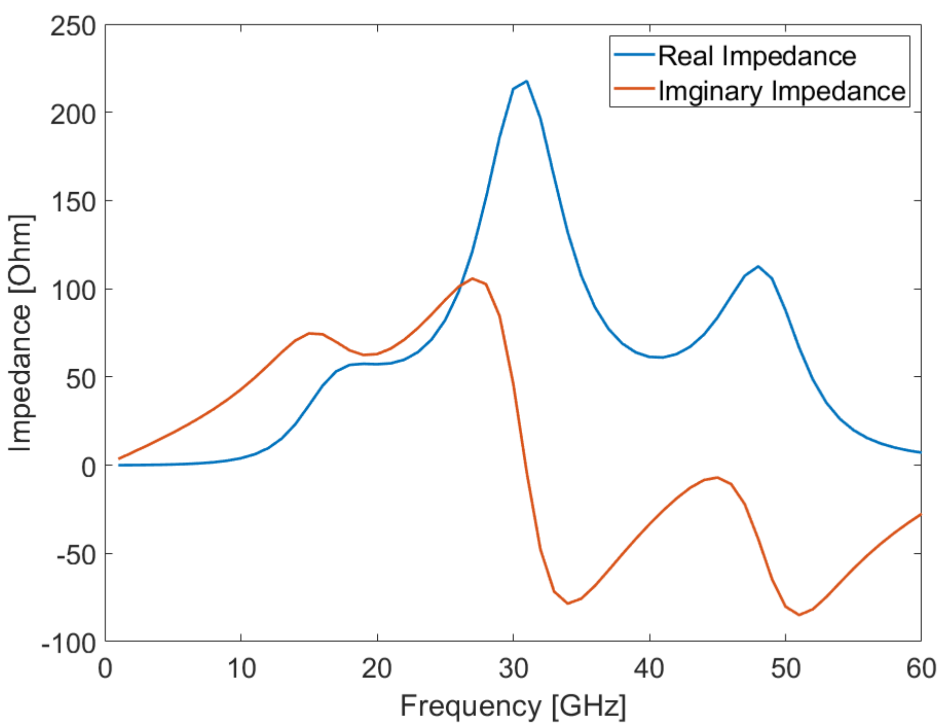

Figure 3.6: Real and imaginary impedance of the Bowtie infinite HFSS array unit cell. We extracted these plots from HFSS using Equations 3.3 and 3.4.

3.2 Matching network and summing tree

The optical efficiency of the detector is maximized by minimizing the mismatch losses and thus null out the reflection between the antenna and the TES. We export these impedance data shown in Figures 3.5 and 3.6 at the optimized feed location. We design the microwave circuit that match the antenna impedance , as shown in Figure 3.7. We minimized the return loss by matching real impedance part of the antenna with the microstrip impedance and cancel the antenna reactance part with a shunt capacitor.

The reflection coefficient between two complex impedance is defined as:

$$\Gamma = \frac{\mid Z_{TL} - Z_A^c \mid}{\mid Z_{TL} + Z_A \mid} = \frac{\mid R_{TL} - (R_A + JX_L - \frac{1}{2\pi f c}) \mid}{\mid R_{TL} + (R_A + JX_L - \frac{1}{2\pi f c}) \mid} \tag{3.5}$$

where R_A and X_L are the real and inductive part of the antenna, R_{TL} is the transmission line impedance, and X_c is the capacitive part that match the inductive part of the antenna for a maximum power transfer.

Each microstrip-feed T-junction has summed the power from both slot feed edges, as shown in Figure 3.8. We computed the micrstrip transmission line width to be ~ 0.94 um at each slot edge that combined into a 2.4 um width at the T-junction feed of the unit cell. These calculations considered the properties of superconducting materials including the kinetic inductance. The microstrip line layer is Nb material with 0.4 µm thick. The simulated and fabricated section for the slot-array is shown in Figure 3.8. The microstrip line thickness is 0.170 um of niobium ground plane. The summing network collects the waves from all feed junctions with uniform phase for each polarization independently to be delivered to the TES bolometer. The microstrip impedance ratio on the feeding ports are carefully chosen to determine the uniform illumination pattern. The accurate knowledge of properties of the dielectric materials such as loss tangent and the superconducting material penetration depths would help to synthesize the uniform top-hat sinc pattern in the far-field. The spacing between the adjacent microstrip lines has been optimized to minimize this coupling and the resulting phase errors across the array. The parasitic microstrip cross-talk has been reduced with the appropriate separation between the lines. Similarity for the dual-band Bowtie structure, Figure 3.9 shows the simulated and fabricated feed part for matching the antenna impedance shown in Figure 3.6. The Band-averaged simulated optical efficiency ranges between 84% – 90% over 25% bandwidth, as shown in Figures 3.15 and 3.16 for single-color and dual-color detectors. We also have design microstrip loss device to measure the transmission line loss due to the dielectric materials properties. The correct modeling of the ILD SiO_2 dielectric/Nb microstrip behavior will affect the performances of the detector including the TES summing feed network, slots and filters. In order to address these concerns, we have developed test devices (Ade, et al. (BICEP2, Keck Array, and SPIDER Collaborations), 2015) to measure microstrip wave speed, where each detector pair receives power through a single polarization broad band integrated antenna. The microstrip feed evenly divides power in a microstrip T-junction between a reference bolometer and device under test (DUT). The spectral response of the bolometers has been measured through the Fourier Transform Spectroscopy (FTS). Our measurements suggest a negligible and minimized effect on the detector optical efficiency.

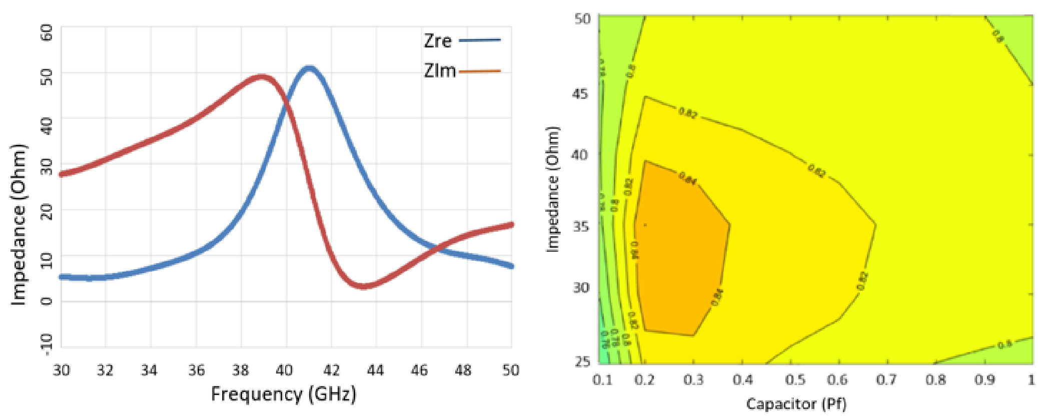

Figure 3.7: The simulated results. Left: The real and imaginary impedance at the optimized feed point on the slot vs. frequency for 40 GHz detector. Right: The contour matching of the input microstrip impedance/capacitor to the antenna impedance over 25% bandwidth.

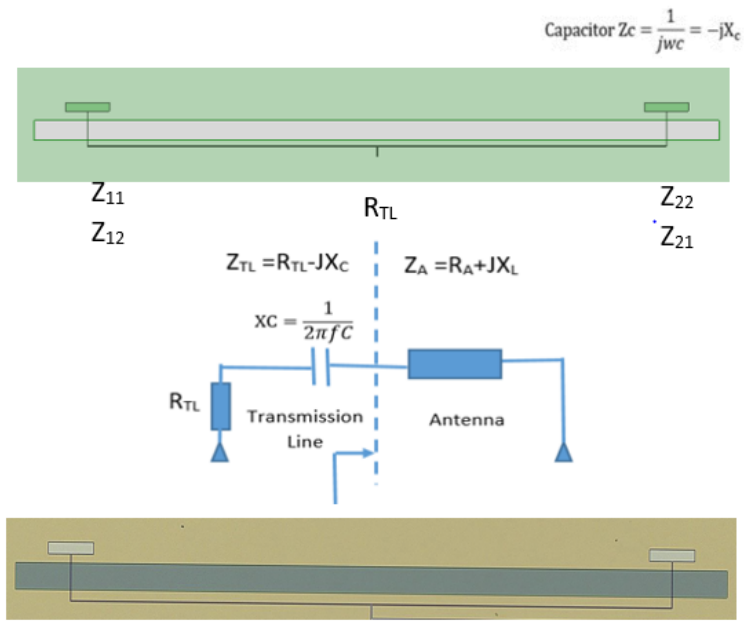

Figure 3.8: The slot antenna matching. Top: snapshot of HFSS slot microstrip T-junction feed, middle: the equivalent matching circuit, bottom: the fabricated feed section.

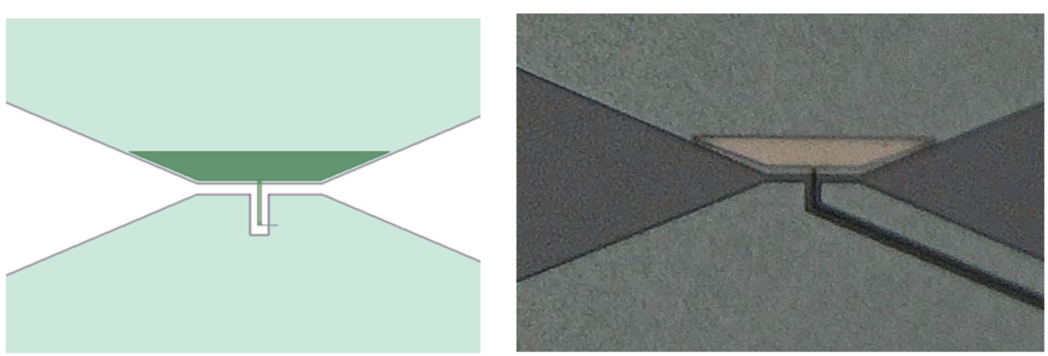

Figure 3.9: The Bowtie antenna matching. Left: snapshot of HFSS Bowtie microstrip feed with transmission line and trapezoidal capacitor (72 um × 34 um × 10um). Right: the fabricated feed section.

3.3 On-chip Band-pass Filter Design and Fabrication

The electromagnetic waves from from the beam-forming antenna array pass through a on-chip three pole Chebyshev band pass filter to avoid atmospheric lines and to reject out-of-band radiation before going to the TES bolometer. The filter also defines upper and lower frequency cutoff of the science band. We use a three-pole Chebyshev filter configuration for having a sharper transition between the passband and the stopband with a lower order polynomial. The design parameters are 0.1 dB ripple size for a minimized in-band reflections, 10 Ω input impedance and 26% fractional bandwidth to fit the CMB observation window at the South Pole.

Lumped elements design

The first step on designing the filter is to estimate the lumped components needed to satisfy the filter requirements. We use microwave book (Pozar, 2004) to calculate the initials lumped elements. We simulate these lumped elements in the AWR Microwave studio as shown in Figure 3.10. Each pole represents an LC resonator. The resulting reflection and transmission coefficients are shown in Figure 3.11. The S_{11} is below -10 dB over our band of interest with 40 GHz band center. The half power band edges are 35 GHz and 45 GHz. The filter has been tuned for a minimized loss and low reflection in our band of interest.

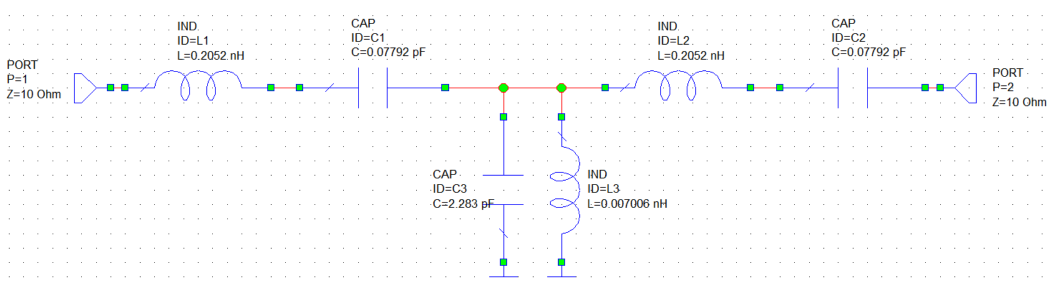

Figure 3.10: Three-pole Chebyshev Band pass filter equivalent lumped elements with band center of 40 GHz.

L_1 (nH)	L_2 (nH)	C_1 (pF)	C_2 (pF)
0.2052	0.007	0.0779	2.28

Table 3.1: The preliminary design parameters for Figure 3.12 (a) in the AWR microwave studio, f_0 = 40 GHz and Z_0 = 10 Ω. We converted these lumped inductance and capacitance to a lithographic version in Sonnet Software.

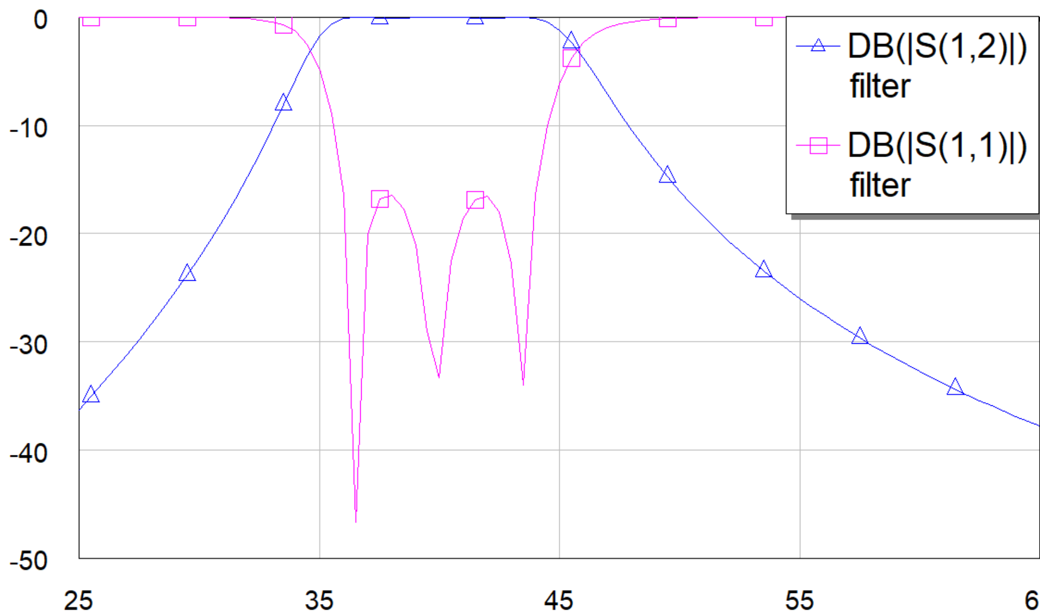

Figure 3.11: The S-parameters results in the AWR Microwave Studio of the circuit shown in Figure 3.10.

Lithographic design

The lumped elements shown in Figure 3.10 have been converted to the equivalent lithographic components using Sonnet Software. The lumped inductors are represented by high-impedance CPW with impedance $Z = \sqrt{\frac{L}{C}}$. The capacitors are described by a parallel plates between the lower and upper niobium films with SiO_2 dielectric material in-between. For the ease of fabrication and to avoid the shunt indicator (L_2), we transform the simple circuit topology to the equivalent T-circuit network topology (Pozar, 2004) shown in Figure 3.12 (b). Further optimization has been done for minimizing the parasitic elements. We will explore the Π-circuit network in Section 7.3 to have better tuning parameters and with a minimized in-band reflections. The 30 GHz band pass filter has been scaled from this design. Similar exercise has been done for the diplexer circuit design. The filters are part of a diplexer circuit that partitions the antenna's broad bandwidth into narrow photometric channels at 30 GHz and 40 GHz, as shown in 3.14. The simulated diplexer results show that we have an interaction between 30 GHz and 40 GHz bands. A new diplexer configuration that composed of series two band pass filters, has been designed to minimize that effect as shown in Figure 3.13. These dual-band technologies have been extended and optimized for dual-color detector at 90 GHz and 150 GHz in Chapter 7.

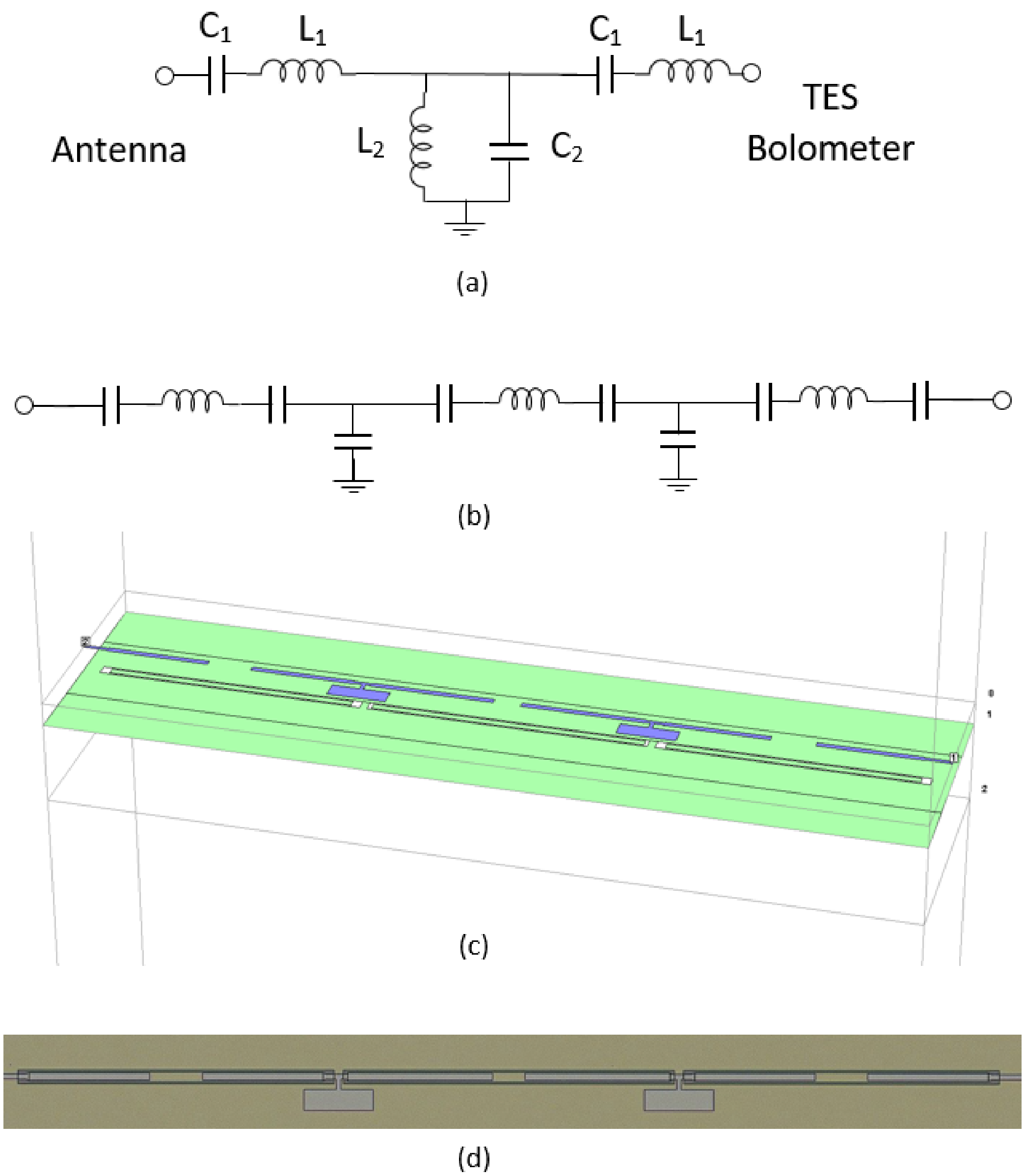

Figure 3.12: The filter design and fabrication. (a) The simple band-pass filter topology, (b) The equivalent circuit with T-capacitive network, (d) The 3D filter lithographic version in Sonnet software, and (c) The micro-graph fabricated filter.

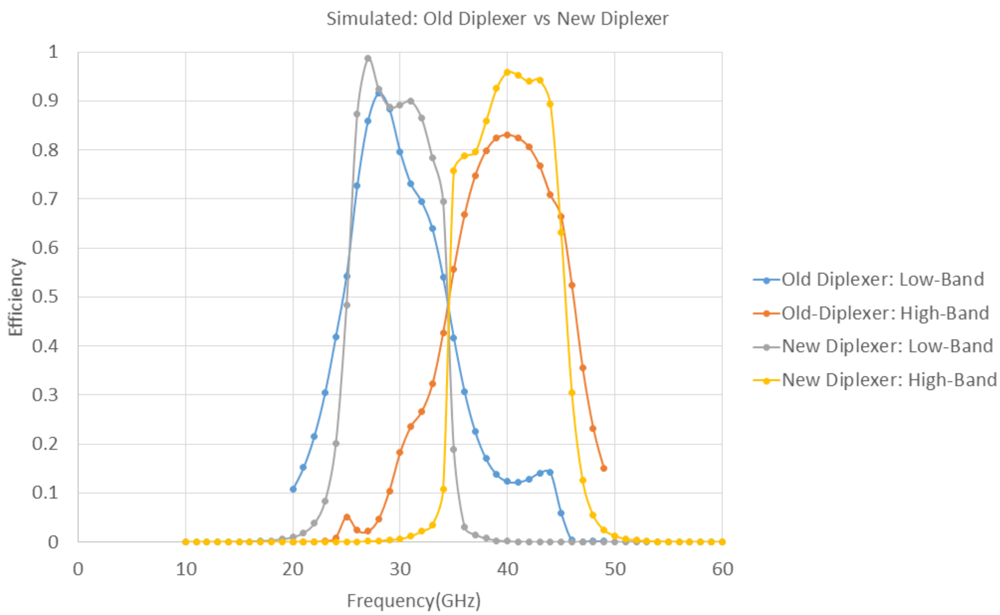

Figure 3.13: The simulated response of the first diplexer versus the second diplexer design. The second design minimized the interaction between both bands and with sharper edges (data by Corwin Shiu) in sonnet (S_{21}^2, S_{31}^2).

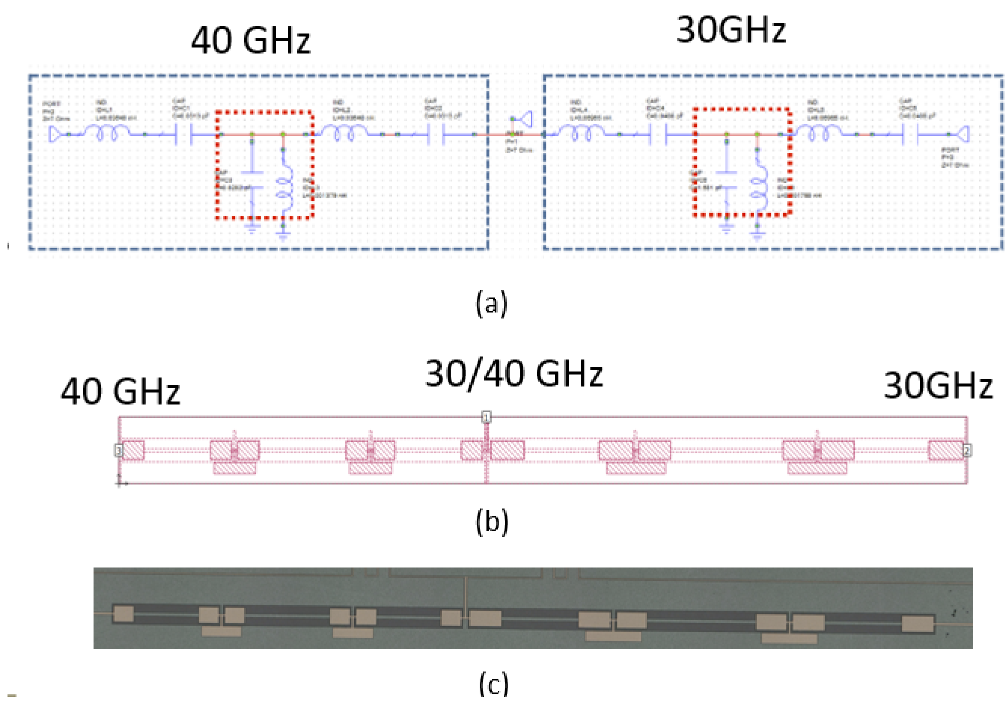

Figure 3.14: Dual-band diplexer composed two band-pass filters: (a) Circuit topology, (b) Lithographic version in Sonnet software, and (c) The micro-graph fabricated filter.

3.4 Simulated Optical Efficiency and Frequency Response

The simulated results verified the design requirements to fit the CMB observation window at the South Pole, and avoid any overlapping with the atmospheric line at 60 GHz, as shown in Figures 3.15 and 3.16. The HFSS simulation of the antenna array and sonnet simulation of the band-pass filter show that the detectors have been designed for frequency band centered at 30 GHz and 40 GHz with about 26% fractional bandwidth for the single-color and the dual-color BICEP Array detectors, respectively. The measurements will be provided in Chapter 7.

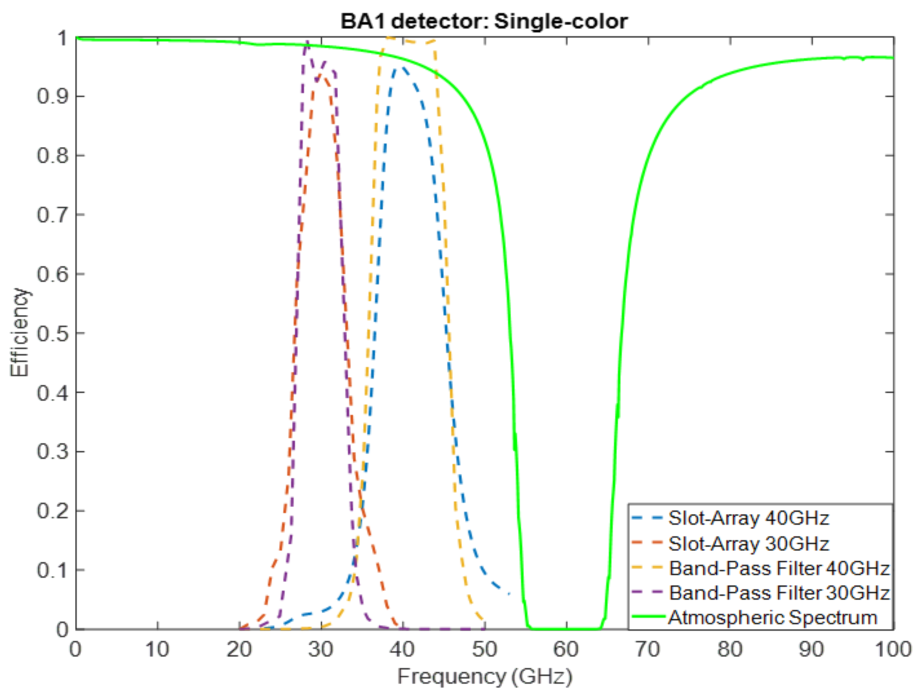

Figure 3.15: Single-color BICEP Array detector at 30/40 GHz: Bands of antennas and filters as individually simulated in HFSS and Sonnet. We co-plot these with the atmospheric transmission to show that these do not overlap with the H2O emissions. The measured end to end Optical Efficiency (OE) is approximately between 30% to 40%.

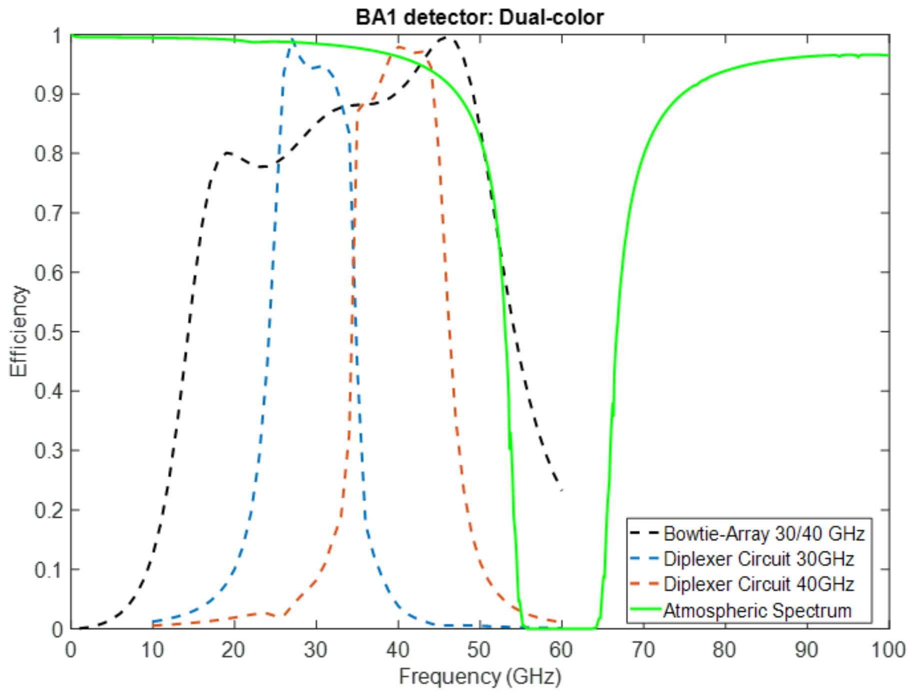

Figure 3.16: Dual-color BICEP Array detector at 30/40 GHz: Bands of antennas and filters as individually simulated in HFSS and Sonnet. We co-plot these with the atmospheric transmission to show that these do not overlap with the H2O emissions. The measured end-to-end Optical Efficiency (OE) is approximately between 30% to 45%.

3.5 Transition Edge Sensor Bolometer

The incoming microwave power from each beam-forming antenna array deposited into a thermalized island in a meandered lossy gold microstrip of the Transition-Edge Sensor (TES) bolometer which converted coupling radiation into heat. The TES bolometers have proven an excellent performance with large detector arrays for various CMB experiments such as SPT, SPIDER, ACT, and BICEP Array. This section presents an overview of the TES theory following the review in the articles such as (Irwin and Hilton, 2005) and (Zmuidzinas, 2003). The TESs are very sensitive to very small variation in the collected photons at the superconducting transition and read out temperature. During that transition between normal and superconducting states, the resistance rapidly depends on the a small temperature changes. The TES is working at its transition temperature T_c with two TESs, as shown in Figure 3.17. There is an aluminum TES with a high saturation power and T_c = 1.2 K for our in-lab calibration and far-field measurements. We also use a titanium TES with a T_c = 0.5 K for CMB science observations due to its better noise and stability performance on the sky at the South Pole. Figure 3.17 shows the fundamental TES bolometer circuit diagram. The TES is a voltage biased by an input current source I_{bias} going through a parallel shunt resistance R_{Shunt} (~ 3 m Ω), much smaller than the normal resistance of the TES $R_{TES} = R_n$. The TES current is readout by the SQUID that is coupled to an inductor placed in series with the TES resistance. The terminated power across the TES island using the voltage divider rule is obtained as:

$$P_{TES} = \frac{V_{TES}^2}{R_{TES}} = R_{TES} I_{TES}^2 \tag{3.6}$$

where,

$$V_{TES} = I_{bias} \frac{R_{TES} R_{shunt}}{R_{TES} + R_{shunt}} \tag{3.7}$$

and,

$$R_{TES} = R_{shunt} \left(\frac{I_{bias}}{I_{TES}} - 1 \right). \tag{3.8}$$

$V_{TES} \approx I_{bias} R_{shunt}$ for the very small shunt resistance compared to the TES resistance. When the TES is biased with a constant voltage, the deposited electrical joule power across the TES, $P_{TES} = P_e$ to keep the TES in transition phase. The negative feedback makes the TES detector operate in a stable performance and linear response without unwanted electrothermal oscillations. The electrothermal feedback tracks the joule heating power from the bias circuit to ensure a fixed total loading power P_e during the transition phase. We characterize the TES detector performance by taking the load curve and deriving P_e versus the TES resistance, as shown in Figure 3.18. The plot shows the TES is passing from the superconducting state, transition state to the normal state (R_n). The strong electro-thermal feedback allows for P_e to have a fixed and flat value during the TES transition, suggesting a sufficient electrothermal feedback loop gain $L \propto P_e$.

$$P_{sat} = P(T_c) = G_c T_c \frac{1 - (T_{bath}/T_c)^{(n+1)}}{n+1} \tag{3.9}$$

The thermally isolated TES island connect the absorber structure to the surrounding heat bath $T_{bath} \approx 280$ mK with a thermal conductive link that has a conductance

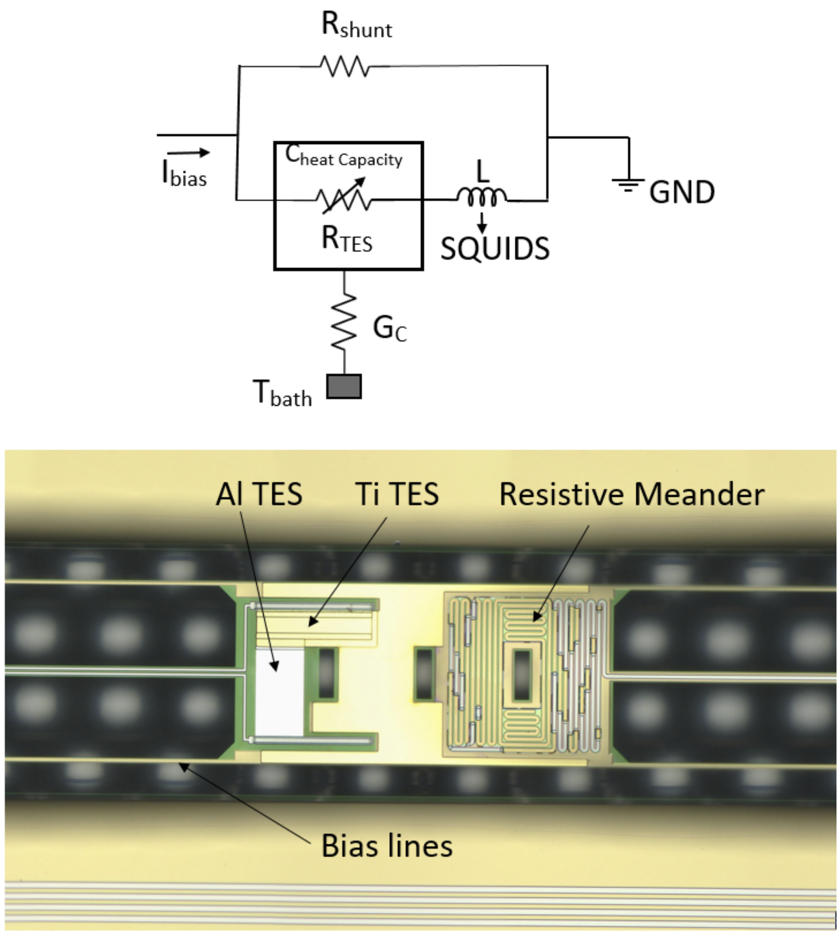

Figure 3.17: The microwave power collected by the antenna-array comes from the right to be terminated on the island. Top: The TES thermal and electrical circuit diagram. Bottom: The released/fabricated TES bolometer at 40 GHz module. The TES legs are made of an extremely thin film of Low Stress Silicon Nitride (LSN). Each TES bolometer has DC bias lines.

$G_C = \frac{dP}{dT}$ set by the few thermal isolation legs. The detector parameter G_C of the detector is designed to minimize Noise equivalent power (NEP) while keep G_C high enough to avoid saturation from the sky loading conditions at the South Pole. The saturation power needed to bring the TES temperature to T_C is:

$$P_{sat} = P(T_c) = G_c T_c \frac{1 - (T_{bath}/T_c)^{(n+1)}}{n+1} \tag{3.10}$$

where P_{sat} is the summation of the optical and electrical power. We need to keep the total power less than the saturation power for a linear TES response. n is the thermal carriers in the legs and takes typical values of 2.1 to 2.5. We also define

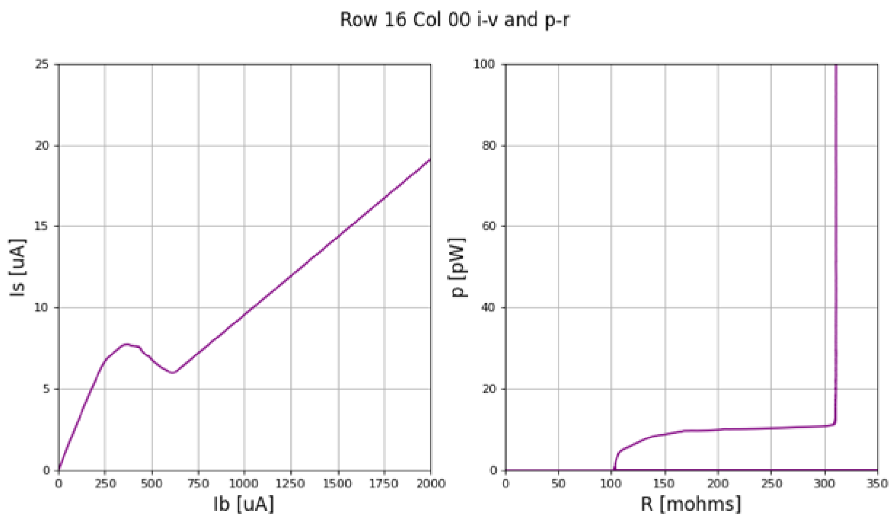

Figure 3.18: An example of the I-V aluminum TES load curve. The power held constant during transition. Left: The bias current versus the current drop on the TES. Right: The deposited electrical power versus the TES resistance.

the natural thermal time constant $\tau = \frac{C}{G}$. C is the heat capacity. The TES detector noise resources are the photon noise, phonon noise, read-out noise and Johnson noise resulting from the TES and the parallel shunt resistor. The detector noise are mainly dominated by the photon noise and phonon noise since we could improve the detector's responsivity to minimize the read-out noise and optimize the electro-thermal feedback loop gain to suppress TES Johnson noise. These noise sources along with excess noise and shunt resistor noise are negligible at low frequencies. The first biggest contribution is the thermal fluctuations noise across the thermally conducting Silicon Nitride (SiN) legs of the detectors (Phonon noise), which is defined as the internal noise of the bolometer:

$$NEP^2_{phonon} = 4K_B T_c^2 G_c F(T_c, T_{bath}) \tag{3.11}$$

where $F(T_c, T_{bath})$ is a function of bath and TES island temperature and accounts for the non-equilibrium effects rather than nonlinear effects (Mather, 1982). It takes values between 0.1 and 1. T_c is the bolometer temperature. NEP is proportional to the square root of the thermal conductance. We tune G_C by optimizing the geometry of the bolometer legs to achieve the design thermal conductance and keep the phonon noise subdominant to the photon noise.

The second biggest noise contribution is the photon noise, which is defined as the summation of Bose noise and shot noise:

$$NEP^2_{Photon} = \int q^2 dv + + \int 2hvqdv = 2\frac{Q^2_{load}}{\Delta v} + 2hv_0 Q_{load} \tag{3.12}$$

where, Q_{load} for one polarization is defined as:

$$Q_{load} == \frac{1}{2}\int dv A\Omega_{beam}\epsilon(v)B(v,T)\eta(v). \tag{3.13}$$

Q_{load} is the total detected power that includes the loading from the sky and internal receiver loading. ϵ is the emissivity. $B(v,T)$ is the black body spectrum as function of temperature and wavelength. θ is the elevation angle of the receiver. v_0 is the center frequency. $\Delta v = \frac{(\int S(v)dv)^2}{\int S^2(v)dv}$ is the fractional bandwidth. The sensitivity of BICEP Array instrument can be defined as the Noise Equivalent Temperature (NET) in uK$_{CMB}\sqrt{s}$ and the mapping speed (NET^{-2}).

$$NET = \frac{NEP}{\frac{dQ_{CMB}}{dT}}\sqrt{2} \tag{3.14}$$

where we define Q_{CMB} for one polarization of the CMB to be:

$$Q_{CMB} = \frac{1}{2}\int dv A\Omega_r(1 - \frac{1-T(v)}{\sin\theta})B(v,T_{CMB})\eta(v). \tag{3.15}$$

$\eta(v)$ is the receiver end-end optical efficiency including the elements receiver stack. T_{CMB} is the CMB temperature today, 2.73 K. $A\Omega_r = f(v)\lambda^2$ is the throughput. $f(v)$ is the dimensionless coupling efficiency. $T(v)$ is the atmospheric absorption spectrum at the South Pole. The total calculated expected optical loading (Q_{total}) of BICEP Array detectors is the summation of atmospheric Rayleigh-Jeans loading (Q_{atm}), CMB loading (Q_{CMB}) and receiver instrument loading ($Q_{Instrument}$). We expect to have the loading highly comes from the atmosphere due to the low-internal loading of BICEP Array receiver design. Given the detector parameters and calibration values, the expected Q_{total} are 0.416 pW and 0.95 pW for 30 GHz and 40 GHz, respectively, which are consistent with the time-stream calculations. With the assumptions of $P_{sat} > Q_{total}$ and $NEP^2_{photon} > NEP^2_{Read_{out}+phonon+Johnson_{TES}+R_{Shunt}}$, the average estimated $G_c \approx$ 14.8 pW/K and 7.2 pW/K for 40 GHz and 30 GHz detectors, respectively. The expected resulting NET is 280 $uK_{CMB}\sqrt{s}$ and 360 $uK_{CMB}\sqrt{s}$ for 40 GHz and 30 GHz detectors, respectively.

3.6 Further Detector Studies

Finite Array vs Infinite Array

This section shows the effect of finite array simulation to improve the detector optical efficiency. The impedance and efficiency plots shown in Figures 3.5 and 3.6 draw from simulations that model a single radiator surrounded by master/slave boundary conditions and constant input feed impedance matching. These boundary conditions effectively model an infinitely large array. In practice, the antenna is finite in size and impedance varies from the center to the edge, most closely matching the infinite case for the center slots. This results in an impedance mismatch losses. We simulated an 8×8 array in the CST software, as shown in Figure 3.19. There are significant variations in radiation impedance. The software computes an S-matrix between excitations at lumped ports over the slots and a free traveling plane wave above the antenna. We can also construct an S-matrix from a simple circuit model of the feed network that describes coupling between the slot feeds and the bolometer. Cascading the two matrices results in an aggregate efficiency between a free space plane wave and the bolometers. We compute that a feed network designed to match the infinite array impedance but connected to the finite array achieves a respectable 84 % efficiency. However, our infinite array results suggest an optical efficiency of $\approx$ 93 %. We estimated about 5-6 % OE improvement over 26 % fractional bandwidth for the non uniform T-junction feed due to the input impedance variation.

Effect of Detector's Back-short

The detector's back short should be located at $\frac{\lambda}{4}$ from the slot-array to terminate the back response. The non-optimal location of the back-short could create a notch resonance in the middle of the band, as shown in Figure 3.20 for BA2 at 150 GHz. The HFSS simulation suggests that the resonance dip in the spectrum varies with the back-short distance, as shown in Figure 3.21. The $\frac{\lambda}{4}$ distance is the optimized value for getting the electromagnetic reflected response out of our band of interest. The spectral measurements with the correct back-short distance removed that dip.

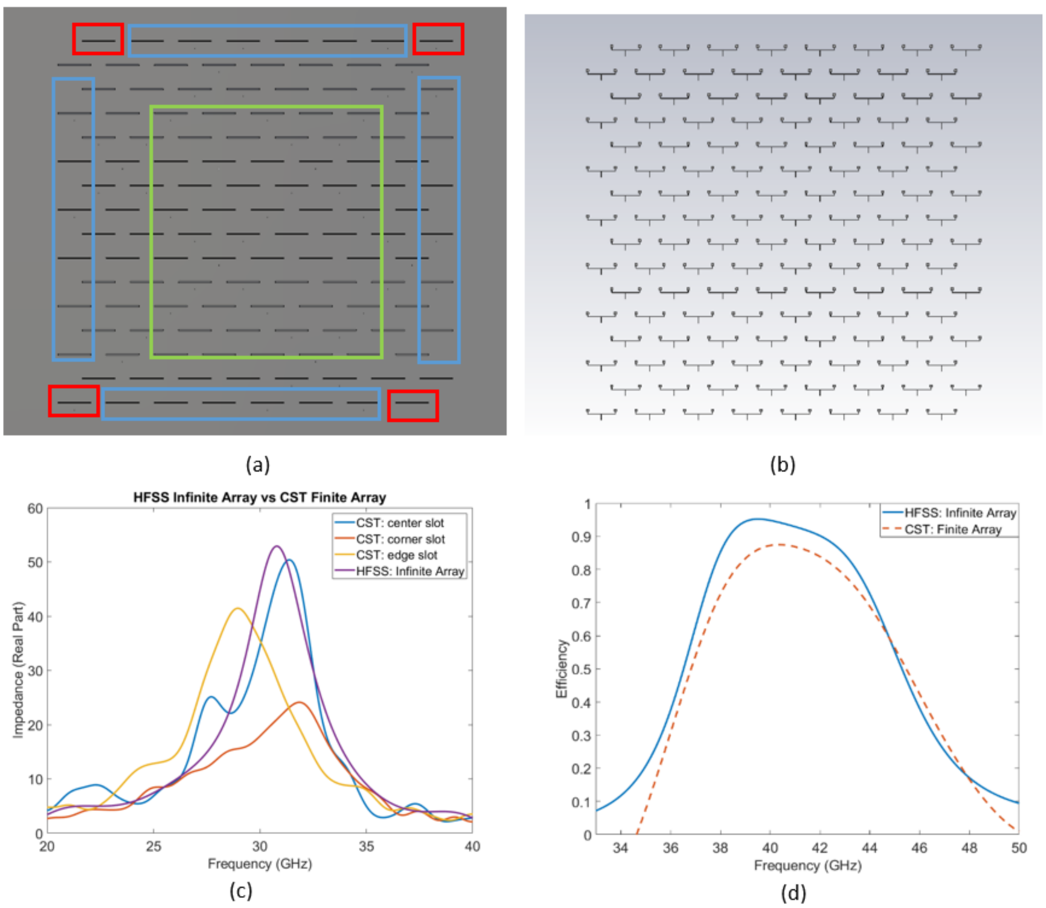

Figure 3.19: The infinite array vs finite array. (a) the CST model of 8×8 finite array showing the corner, edge and middle slots, (b) the uniform T-junction feed network in CST, (c) the expected real impedance for infinite array versus finite array (edge vs middle vs corner slots). The impedance is about factor of 2 lower for the corner slot compared to the middle slot in the array, and (d) the expected efficiency of infinite array vs finite array for the same input feed network.

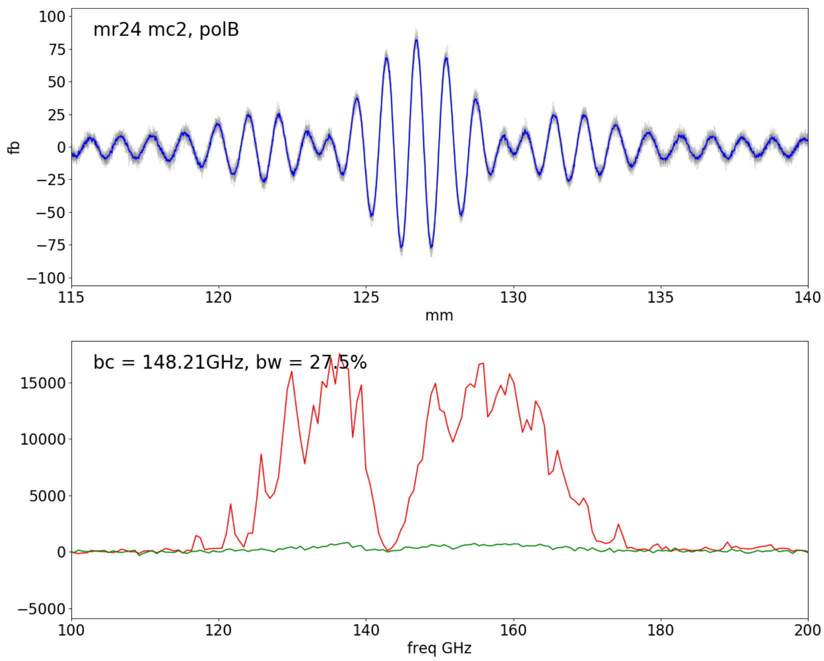

Figure 3.20: The measured spectra of 150 GHz module showing a dip in the middle of the spectrum due to the wrong back-short distance (≈1 mm). Plot by Silvia Zhang.

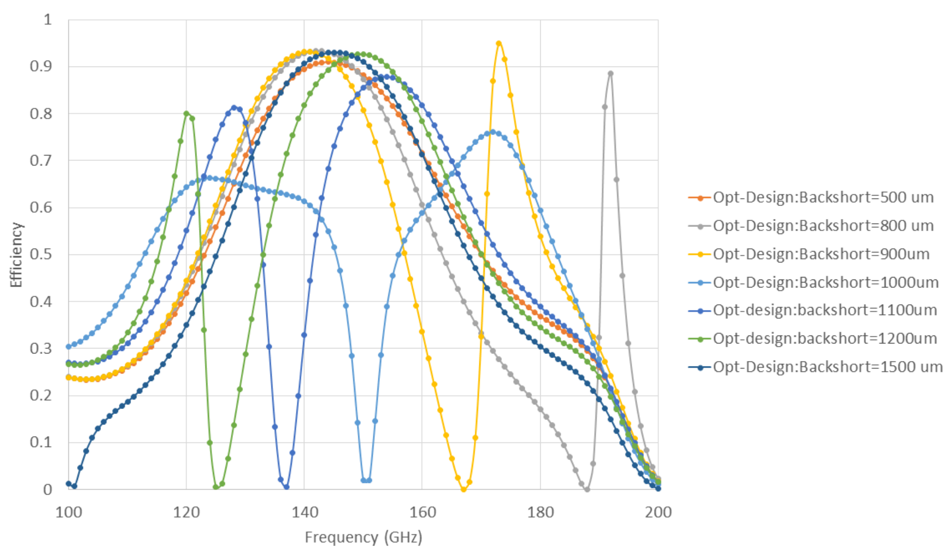

Figure 3.21: The HFSS simulation of the 150 GHz detector with various back-short distances.

Chapter 4

FOCAL PLANE CORRUGATED MODULE DEVELOPMENT

The polarization of CMB has been measured by differencing the co-located and orthogonally polarized detector pairs “Pol A” and “Pol B” in the same pixel. The beam mismatch response between both polarization pair could introduce a prominent systematic errors that causes a Temperature-to-Polarization (T $\rightarrow$ P) leakage that can bias the cosmological parameter constraints in our CMB maps. These residual beam errors come from different resources such as ellipticity, beam-width, gain and pointing. The most remarkable causes are

- *The Differential Ellipticity*: The beam shape of the vertical and horizontal antenna-array are not perfectly circular, as I showed in Figure 3.3. The simulated difference beam shows about 4-8 % peak-to-peak differential offset, depending on number of array elements. We optimized our detector array size for a minimized differential ellipticity errors, as shown in Chapter 3.
- *The Differential Pointing*: The non-uniformity of the film wafer could steer the detector beam center off boresight, which could be different between both polarization pair, causing a differential pointing errors. The most dominant source of the differential pointing is the interaction between the antenna-array pixel and the surrounding frame that causes an offset errors between the polarization detectors. The differential pointing is generally the most significant contributor to the most amount of T$\rightarrow$ P in our science maps. the focal plane frame has greatly contributed to the mismatch errors that potentially limit our sensitivity on r (Ade, et al. (BICEP/Keck Collaboration), 2019).

We used the deprojection technique and coadding our maps over multiple boresight rotation angles (Germaine, 2021 and Karkare, 2017) to filter out most of these residuals, especially the information from the contaminated modes. These residual systematic and noise have been quantified through jackknife tests and simulations. We generate the jackknife maps by differencing the polarized maps made with data taken in the opposite azimuth scan directions. This technique heavily removes the low-order beam effects in the full map and keep the real CMB signal, but higher-order beam effects are still present due to large differential pointing errors that come from the focal plane frame. We want to minimize that effect at the optical design, which is the motivation for this chapter. We have developed broad-band and single-band corrugated frames (Soliman, Ade, et al. (BICEP/Keck Collaboration), 2018) for BICEP Array receivers, as shown in Figure 4.1 for 30/40 GHz BICEP Array receiver. In this chapter, we will describe our efforts on the design, implementation and testing the final designs to verify our modelled response.

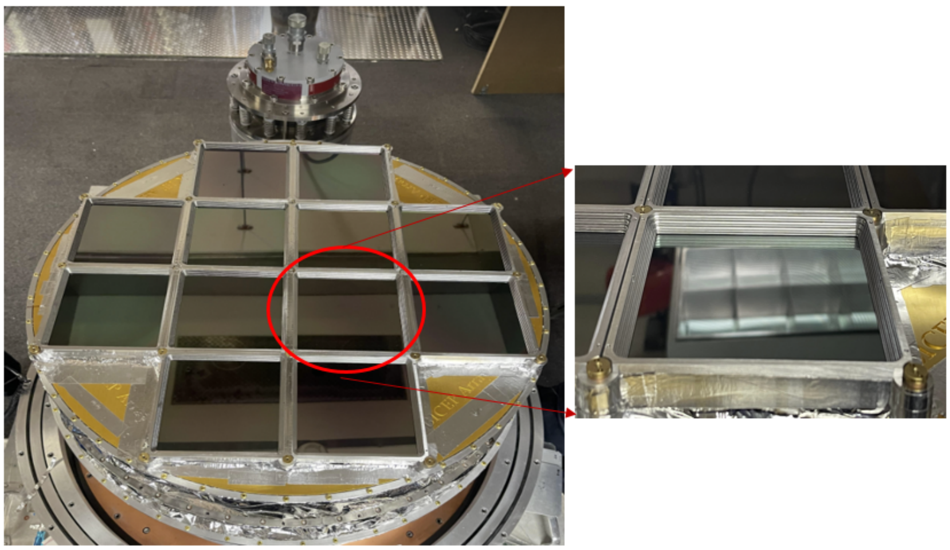

Figure 4.1: The new broad band corrugated focal plane frame of 30/40 GHz BICEP Array receiver inside MAPO building at the South Pole. The new design minimizes the beam systematic errors over a broad CMB observation band for the single color 30 GHz and 40 GHz detectors, and dual color 30/40 GHz simultaneously.

4.1 $T \to P$ Leakage on r for BK15 Data

The focal plane frame is made of aluminum and used to mechanically support the entire detector tile's components. However, the frame will interact electromagnetically with the detectors located at the edge. The interaction with the frame causes unwanted polarization-dependent beam distortions. In BK15 data, a large pair difference residuals remain after deprojection due to the interaction between the detector tile and the non-optimal corrugated frame at keck Array telescope at 95 GHz. The Q maps of residual T$\to$ P shows the undeprojected leakage into our BK15 map, as shown in Figure 4.2. The difference beam map shows a strong dipole/quadruple difference beam pattern which leaks temperature to polarization in the CMB polarization maps and produces a false B-mode signal (Ade, et al. (BICEP/Keck Collaboration), 2019). The measurements notably show a differential beam effect between two orthogonal polarization detectors, a shift between the "Pol A" and "Pol B" beam centers. At the data analysis level, we developed a deprojection technique to effectively remove low-order beam effects, but higher-order beam effects could still be present. The resulting leakage consistent with cross spectra yields a high uncertainty of $\Delta r = 0.0027 \pm 0.0019$, mostly due to the differential pointing from the pixels located close to the frame. This error distorts the observed B-mode signal and might be acceptable with respect to the BK15 constraints $\sigma(r)$ = 0.020, but this will be non-negligible for BICEP Array target sensitivity ($\sigma(r) \sim$ 0.003). These effects were visible in the beam maps taken in the near-field of the detector for edge pixels in Keck Array, as shown in Figure 4.3, as a huge differential pointing residuals (>40%) for BK15 data. This systematic error has been minimized and corrected with a new detector's focal plane design of BICEP3 telescope (Ade, et al. (BICEP/Keck Collaboration), 2022). In this Chapter, we developed a new focal plane frame to minimize this systematic error over a broad CMB observation band and enable the levels of systematics control needed for BICEP Array telescope's sensitivity, especially at 30/40 GHz. We have about 16 edge pixels out of 25 total pixels at 40 GHz detector and 12 edge pixels out of 16 total pixels at 30 GHz detector, showing the motivation for addressing this problem.

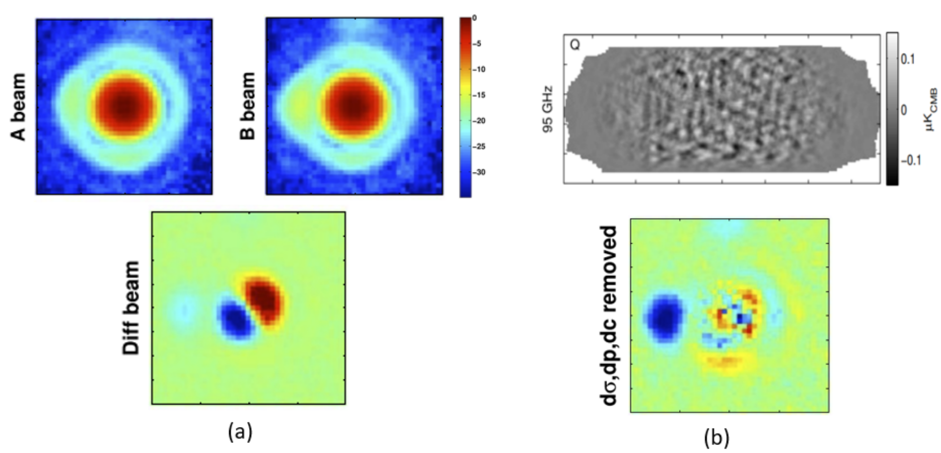

Figure 4.2: The measured far-field beam maps at 95 GHz (Ade, et al. (BICEP/Keck Collaboration), 2019). (a) The measured maps for both polarization and the resulting beam map difference before "deprojection." (b) The high-order residual after "deprojection" showing > 20 % due to the differential pointing. The large residual also features in the 95 GHz Q map that contributes to the T→ P leakage in our BK15 CMB map.

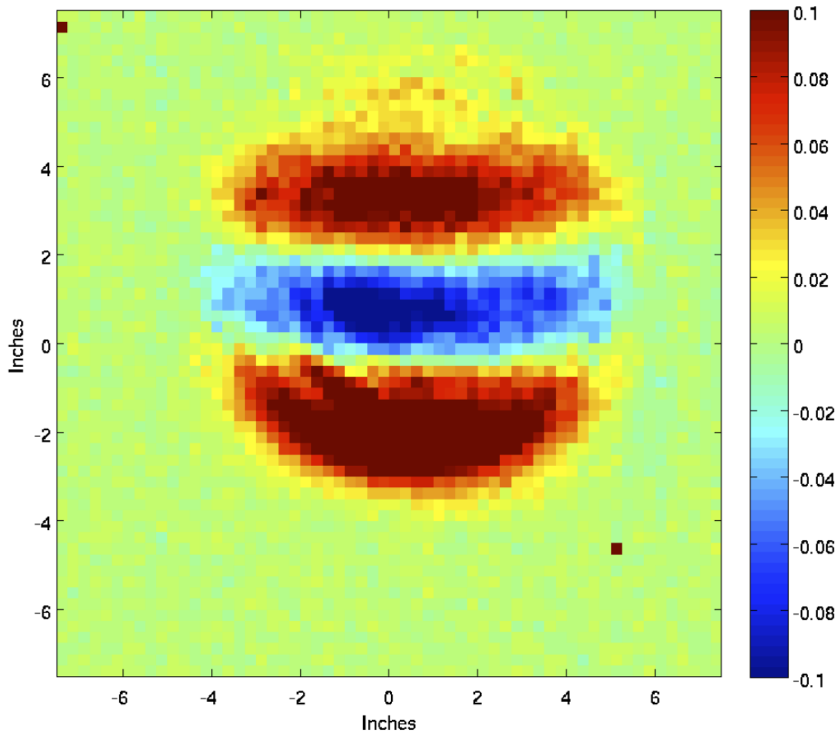

Figure 4.3: The differential pointing effects between "Pol A" and "Pol B" in the near-field of Keck Array telescope, which causes the far-field residuals shown in Figure 4.2. This is the worst measured differential offset on BK15 data that we need to highly reduce for the target sensitivity of BICEP Array telescope.

4.2 Focal Plane Engineering for Sensitivity Improvement on r

Figure 4.2 shows the important of designing a new corrugated focal plane frame that minimizes this high leaking residual, reduces our T→P leakage and consequently reduces our systematic error on r. We have developed different corrugated frames to work for different BICEP Array receivers. A broad-band corrugated focal plane has been designed for single-band slot-array and dual-band Bowtie-array simultaneously in BICEP Array receiver at 30/40 GHz (Soliman, Ade, et al. (BICEP/Keck Collaboration), 2018) to cover 25-45 GHz, which derive our motivation for having a wide-band design. A new single-band corrugated frame has been also developed to work for BICEP Array receiver at band center of 150 GHz.

Broad-band design 30/40 GHz

We carried out the numerical analyses using the transient solver in the CST Microwave Studio, which is based on a finite difference time domain (FDTD) method and very convenient for large radiation elements. Figure 4.4 shows the simulated antenna-coupled detector for one polarization at 40 GHz, used in initial beam simulations. The slot-array has been rotated by 90° for the other polarization. Figure 4.5 shows the normalized beam with respect to the peak. The resulting band-averaged beam map difference shows a quadruple pattern of about 5-7 % peak-to-peak differential offset due to the ellipticity of the beams. This is our baseline beam map difference for our the corrugations design.

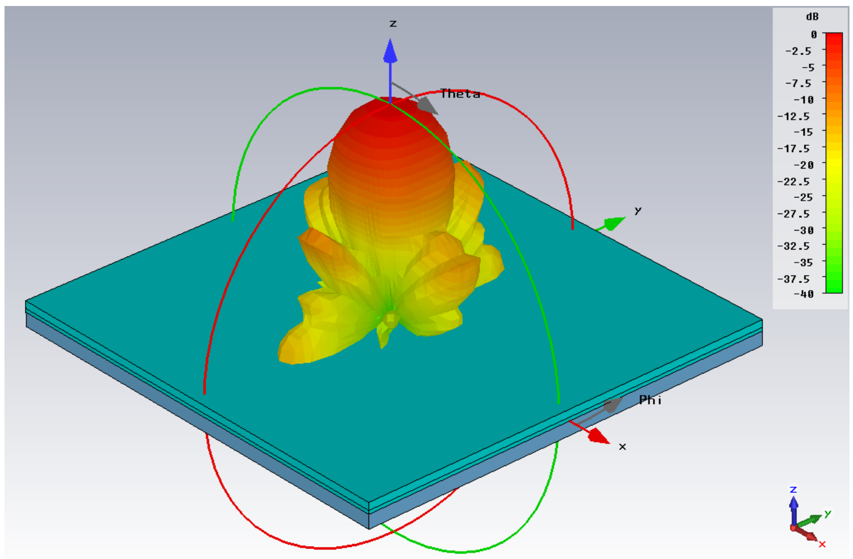

Figure 4.4: The CST Model of 8×8 BICEP Array slot-array at 40 GHz.

The next step is placing a metal frame without corrugations at certain location ($\frac{3\lambda}{8}$ distance to the slot-array. The resulting band-averaged Beam map difference shows a strong dipole effect of about about > 40 % peak-to-peak differential offset due to the differential pointing of the beam centers. When the slot-array is in the proximity of a conductive metal frame, interactions between the radiation pattern of the antenna and the conductive frame result in unwanted coupling, which alters the beam pattern of the antenna. These interactions result in highly polarized edge effects, which cause polarized beam mismatch, as shown in Figure 4.6.

In order to reduce these unwanted interactions, the corrugated surface is built on the conducting frame with a carefully optimized depth. The grooves change the properties of the conducting wall to minimize the reflections and beam mismatches. They are usually analyzed by treating the corrugations as quarter-wavelength transmission lines. Each corrugation in the frame acts as a short-circuited waveguide with one quarter wavelength depth to a surface wave traveling across it, so that the reflected wave from it is in opposite phase to the incident wave and will tend to cancel it out

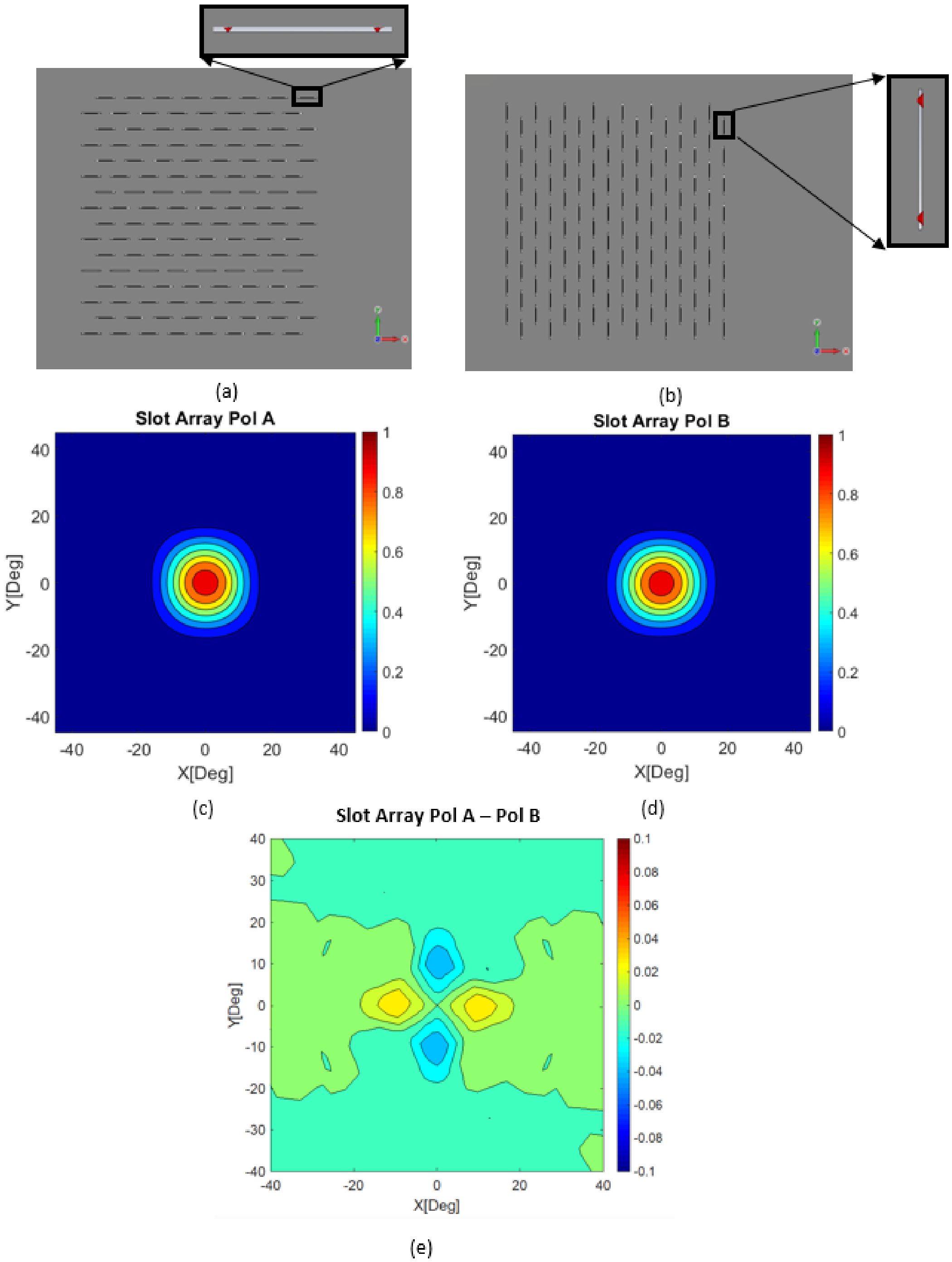

Figure 4.5: The 40 GHz detector model in CST Software. (a) The 8×8 slot array of "Pol A." (b) The 8×8 slot array of "Pol B" after rotating by 90°. (c) The normalized beam map of "Pol A," (d) The normalized beam map of "Pol B," and (e) The band-averaged (25 % bandwidth) peak-to-peak beam map difference for detector without any frame next to it, called middle pixel, showing a quadruple pattern. This is our baseline beam map difference for the our corrugations design next.

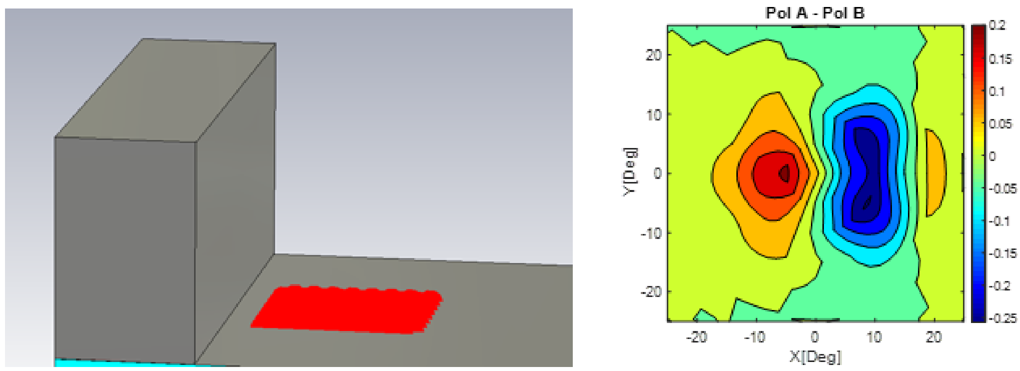

Figure 4.6: The slot-array with metal frame without corrugations and the resulting beam map difference showing a huge diffrential pointing error (dipole pattern).

so that the corrugated frame looks like an open space rather than a short circuit. We built our corrugations in CST Microwave studio and we started to optimize the parameters for a minimized differential offset. The corrugated frame is designed and optimized with specifically chosen grooves depth, phase, the corrugated step and distance between the antenna and the frame. The optimization parameters are listed in Figure 4.7. The corrugations are parameterized by the corrugation depth (L), corrugation step (P), corrugated frame angle (θ) and distance between the antenna and the frame (D). The field patterns are exported from CST into Matlab to plot the contour beams of the vertical polarization and horizontal polarization pixels, as well as the beam difference. We vary each design parameter individually while keeping the other parameters fixed. We estimated the optimized values for all the parameters (market green dot) with a minimum peak-to-peak beam map difference.

We simulated the slot-array with the optimized corrugated parameters over our 25-50 GHz, as shown in Figure 4.8. The peak-to-peak polarization subtraction for the broad-band corrugated frame shows a minimized differential offset (< 10 %), which is close to our baseline shown in Figure 4.5 (e), suggesting that the corrugated frame has a slightly effect on the beam shape mismatch. These results show the improvement compared to the large measured differential offset shown in Figure 4.3 (> 40 %).

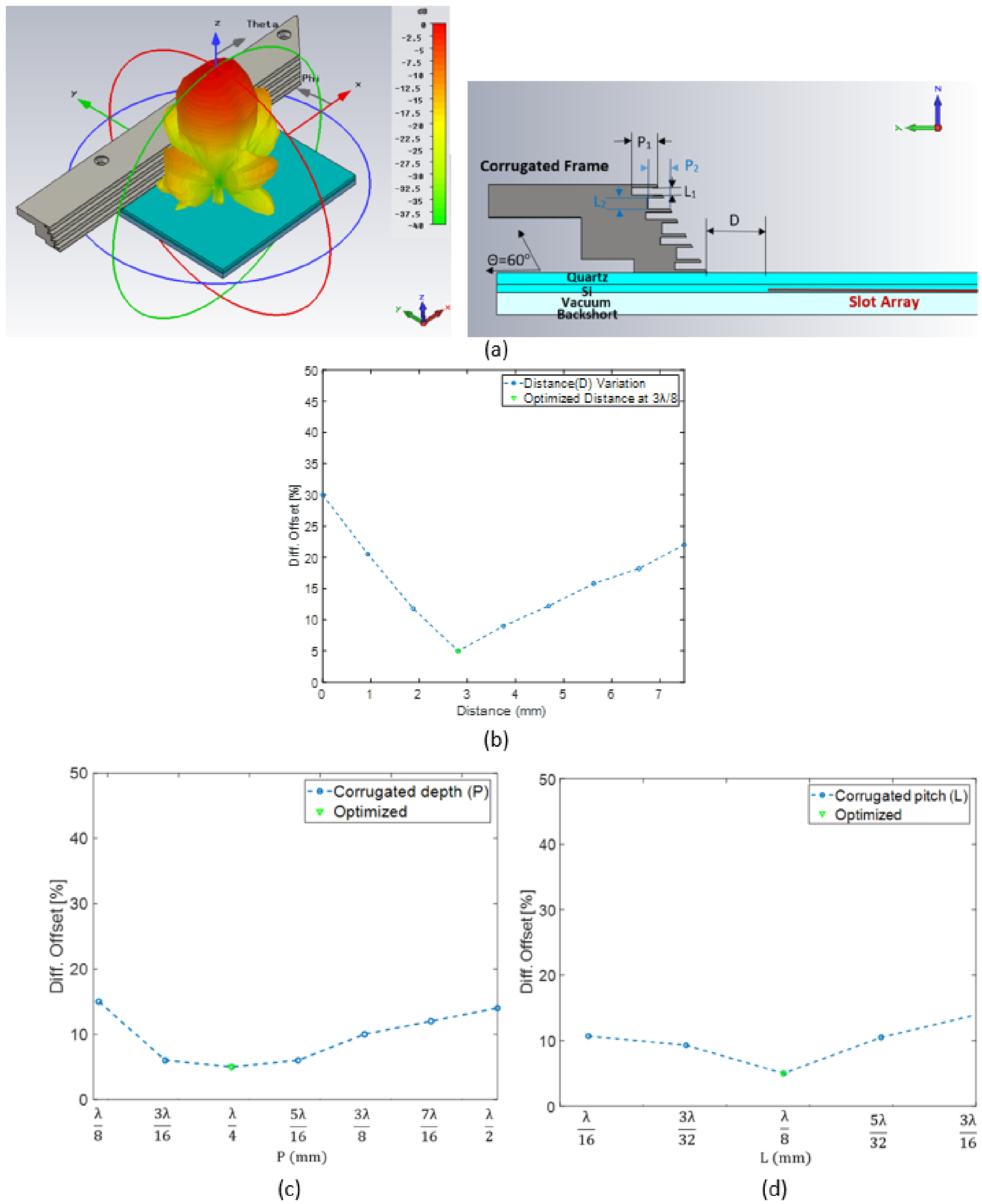

Figure 4.7: The corrugated frame study. (a) The CST model of slot-array antenna with the corrugation parameters. The parametric analysis of the corrugation parameters as function differential offset, (b) distance of the slot-array to the wall "D," (c) corrugated depth "P," and (d) corrugated pitch "L."

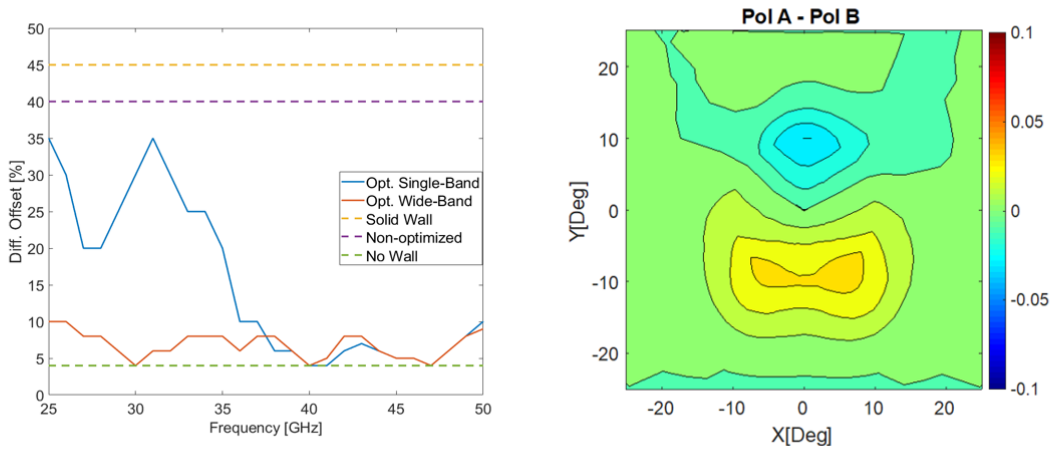

Figure 4.8: The simulated response of the optimized design. Left: The peak-to-peak differential beam amplitude over our frequency of interest. Solid curves are the simulated values at each frequency ("Pol A" – "Pol B"), and dash lines are the average value over the 25% fractional bandwidth. Right: The simulated band-averaged beam map difference of the optimized wide-band design to cover the 30 GHz and 40 GHz detectors. Right: The band-averaged beam map difference.

Fabrication and results

The wide-band focal plane corrugated frame has been fabricated and tested at Caltech at 30/40 GHz detectors and it has been deployed to the South Pole. Figure 4.1 shows the fabricated broad-band frame inside MAPO building at the South Pole before we closed up and raised it to the mount for CMB observation. We first tested that design at Caltech before deployment to the South Pole. The beam pattern of the detectors has been measured for the middle pixels and edge pixels located near the edge. We fit a two dimensional elliptical Gaussian profile to the main beam of each detector:

$$B(x) = \frac{1}{\Omega} e^{\frac{-1}{2}(x-\mu)^T \Sigma^{-1}(x-\mu)} \tag{4.1}$$

where Ω is the normalization, and x is the beam map coordinate, and $\mu = (x_0, y_0)$ is the beam center. Σ is the covariance matrix:

$$\Sigma = \begin{pmatrix} \sigma^2(1+p) & c\sigma^2 \\ c\sigma^2 & \sigma^2(1-p) \end{pmatrix} \tag{4.2}$$

σ is the bandwidth. and p and c are the ellipticities in the plus and cross directions. Figure 4.9 shows the Gaussian fits (second and fourth rows) to measured beams of each polarization (first and third rows), as well as their in-pixel differences in the right most column. The top rows of the chart shows a pixel in the tile's interior (middle pixel), while the bottoms shows an edge pixel. They have comparable dipolar mismatch, suggesting that the corrugated frame has limited effect on beam synthesis. The remaining beam residuals are due to the differential ellipticity of the beams. Similarity, Figure 4.10 shows that the broad-band design also worked with the Bowtie-array for covering 25-45 GHz. These measurements verified our modelled response.

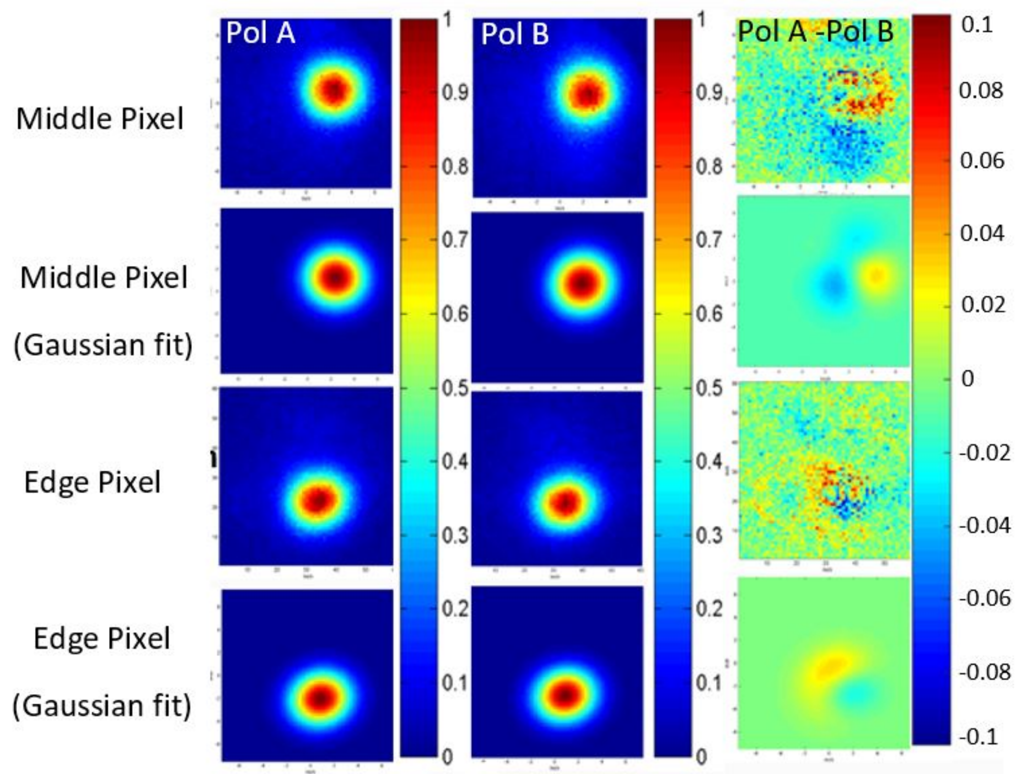

Figure 4.9: Single-color detector measurements: The measured contour plot of "Pol A", "Pol B" and beam map difference for two working middle and edge pixels over 25 % bandwidth, and the corresponding Gaussian fit. These measurements have been taken without BA1's optical elements.

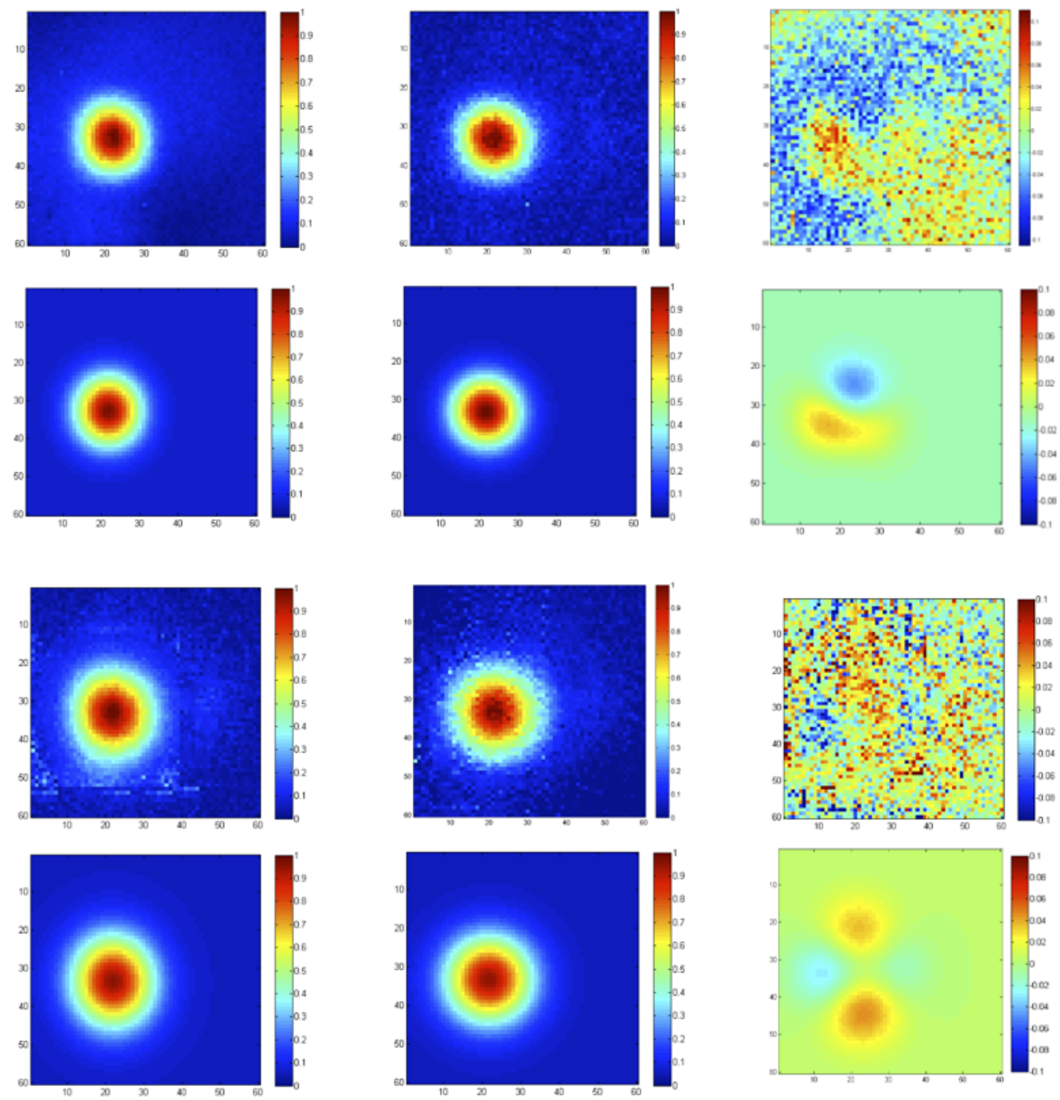

Figure 4.10: Dual-color detector measurements: The measured contour plot of “Pol A”, “Pol B” and beam map difference for two working middle and edge antenna array pairs over 25 % bandwidth, and the corresponding Gaussian fit. These measurements has been taken without BA1’s optical elements. Top two panels: 40 GHz band, and Bottom two panels: 30 GHz band.

Single-band design for BA2 at 150GHz

Similar procedures have been performed for single-band corrugated frame for the BICEP Array detector at 150 GHz. The focal plane frame has been designed to cover 25 % fractional bandwidth with 150 GHz band center, as shown in Figure 4.11. The single-band corrugated focal plane also has been fabricated and tested with BICEP Array receiver at 150 GHz. The measured differential beam offset verified our modelled response.

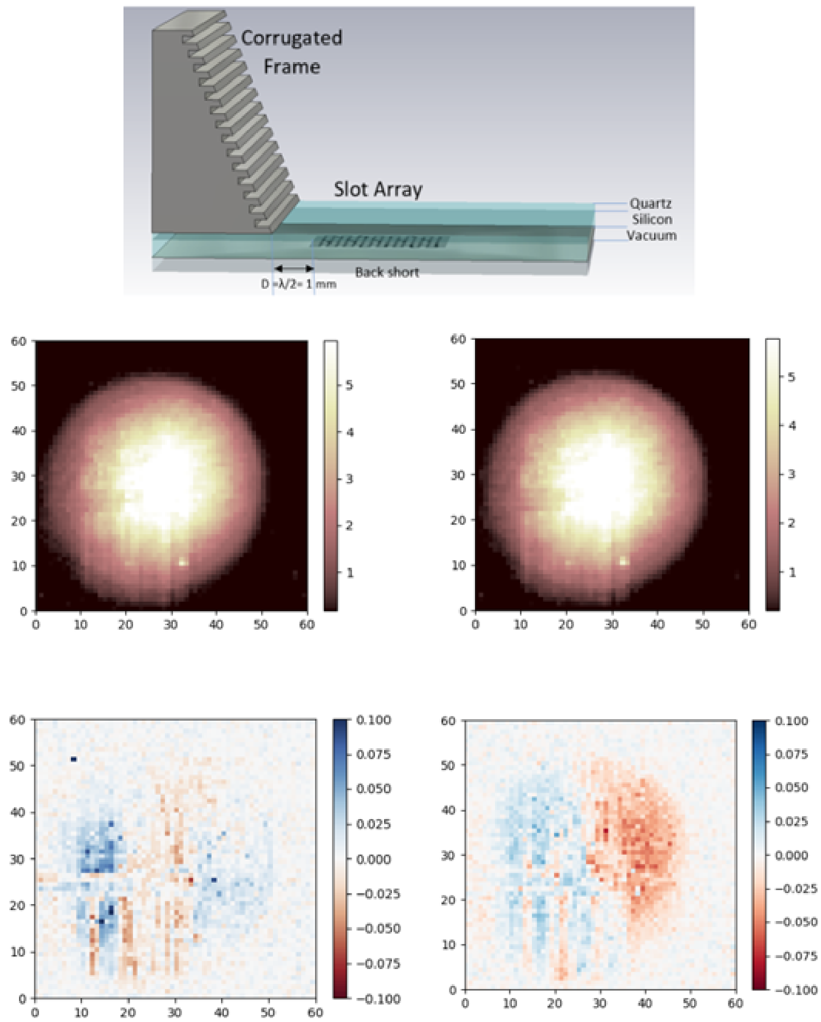

Figure 4.11: The 150 GHz detector model in CST with the optimized corrugations. Top: snapshot the finite-array model. Middle: The measured beam map of both polarization. Bottom: The measured beam map difference for edge pixels showing a minimized differential offset as designed which validated our simulation model.

Wide-band design for BA4 at 220/270 GHz

We scaled the 30/40 GHz corrugation focal plane frame to work for 220/270 GHz BICEP Array receiver. The scaled height exceeded the minimum fabrication limit. Additionally, the scaled corrugations dimensions reached to 50 um which require a special cutting technique in the fabrication room. WE have tried to avoid the corrugations but the simulation suggest that we need to locate the wall at distance of 15 λ from the antenna to avoid the effect of the frame, which is not practical. We decided to fabricate the final optimized design with corrugations shown in Figure 4.12. The fabricated prototype has been successfully evaluated underneath the microscope and looked promising with the optimized dimensions. The design will be fabricated and tested soon for the coming BICEP Array 4 receiver.

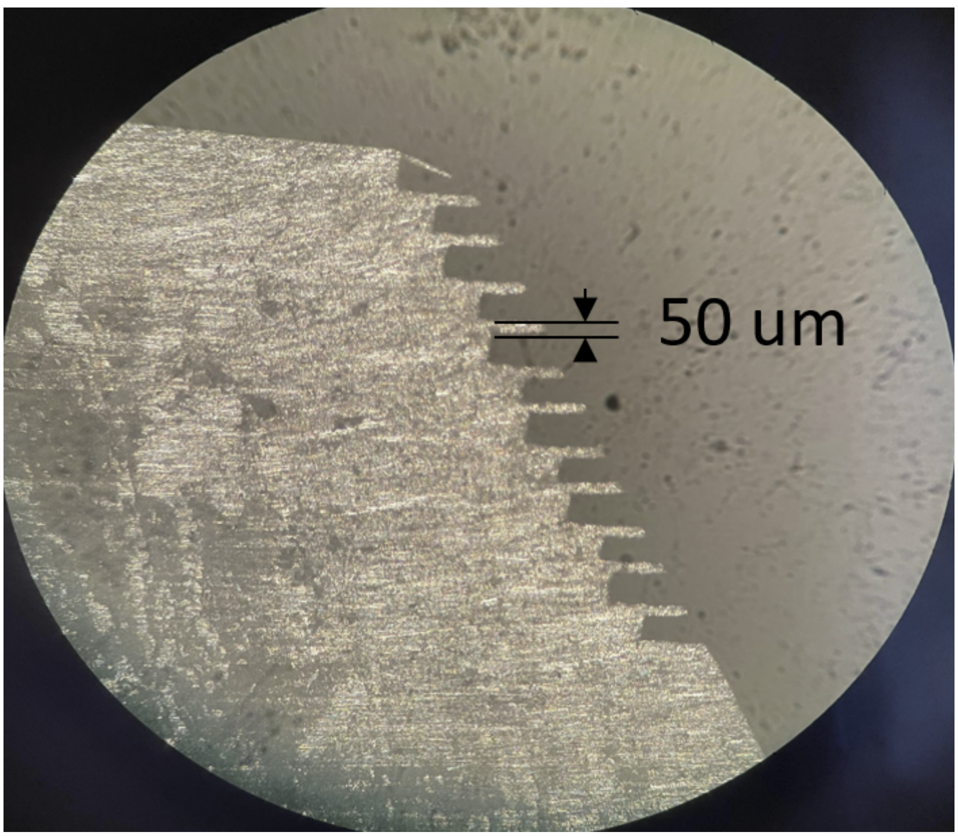

Figure 4.12: The fabricated 220/270 corrugated underneath the microscope, showing the minimum resolution of 50 um. The measured dimensions agreed with the designed values. The top lip is bended during transportation since it has a very thin thickness of 20 um. It will be fixed in the final design.

Chapter 5

30/40 GHZ DETECTORS MEASUREMENTS

Antenna-coupled TES detectors and focal plane module at 30/40 GHz have been well designed as I discussed in Chapters 3 and 4. This chapter reports the calibration measurements of the detectors at our CMB laboratory at Caltech to verify our modelled response before deployment the full BICEP Array receiver to the South Pole. We will also describe the full optical characterization process, from the near-field of the detectors (without optics), to the near-field of the telescope inside BICEP Array receiver (with optics) to the far-field of the telescope.

5.1 Optical efficiency

BICEP Array detectors have been tested inside our cold test-bed without optical elements. The test-bed is cooled down to ∼250 mK. A black-body is placed above the vacuum window of the cryostat. The end-to-end optical efficiency of the detectors has been measured by filling the aperture window under two loading conditions, room temperature at 300 K and liquid nitrogen at 77 K. The load curves (I-V) have been taken in both cases to characterize the TES response, as shown in Figure 5.1 as an example. Since the two sources are black bodies in the Rayleigh-Jeans limit, the deposited optical on the TES for a single-mode polarization is

$$P_{opt} = \int K_B T S(\nu) d\nu. \tag{5.1}$$

K_B is the Boltzmann constant. Given two optical loading conditions shown blue and red curves in Figure 5.1, we define $\frac{\Delta P}{\Delta T}$ as the ratio between the optical loading difference (ΔP) absorbed by the TES and the temperature difference ($\Delta T \approx 300K - 77K$) as follow:

$$\frac{dP}{dT} = K_B \eta_\nu \Delta\nu. \tag{5.2}$$

The end-to-end optical efficiency yields

$$\eta_\nu = \frac{\frac{dP}{dT}}{K_B \Delta\nu}. \tag{5.3}$$

η_v accounts for the losses in the detectors and the dewar. 100 % efficiency is 0.15 pW/K for 40 GHz and 27 % bandwidth. The middle plot of Figure 5.1 shows an OE of 0.075 pW/K, which is the best efficiency with respect to other CMB experiments. This non-ideal OE from our simulated value shown in Figure 3.15 is probably due to the loading layers inside the cryostat, including stack of filters and materials as well as possible losses inside our devices. The actual measured optical power needs to account for the small dark power absorbed by the TES island in the dark detectors, which varies from a detector to another. I will explain this in details in Chapter 6. The measured dark detector Optical efficiency (OE) is 0.004 pW/K dark for that module, i.e., the resulting real optical response for the light detectors $dP/dT_{lightdetector} = dp/dT_{measured} - (dp/dT)_{darkdetector} \approx 0.0071$ pW/K. An additional losses will be added when tested the detectors inside BICEP Array receiver. The OE measurements inside BICEP Array receiver is ~ 0.8 of the measured value in Caltech' test-bed due to the full optical elements and spillover loss. The measured median OE of that specific module is 0.066 pW/K inside BICEP Array receiver during 2023 season at the South Pole.

5.2 Near-Field Beam Map

The near-field beam maps (NFBM) of the detectors have been measured at the aperture plane using a thermal source. We preformed the NFBM measurement after we cooled down the detectors to 250 mK. The NFBM measurements have been used to check whether all detectors have sensible-looking beams. These beams are also useful for comparison with our simulated models and for diagnose any optical issues for a feed back into our fabrication's team at MDEL/JPL. Figure 5.2 shows the measurement setup of the NFBM at Caltech test-bed. We simultaneously map the near-field of all detectors by scanning a chopped thermal source above the aperture window. The source contains a ceramic thermal source chopped (10−25 Hz) behind a Thorlabs MC2000 optical chopper. The source is enclosed in a box to minimize reflections. The chopper rotating blade is blackened with an eccosorb HR-10 coated plate so that the heat source chops between the heater and an ambient temperature.

The NFBM has been taken with detector biased at aluminum transition due to the higher loading of the heating source that might saturate the detectors. We used the x-y stage to move the chopper to the center of the aperture and verifying that a chopped signal is visible in the recorded timestreams at the given chopper frequency. After that, we optimally record the detector's time stream for longer time, in a 60×60 grid pattern by using a Velmex Bi-slide x-y translation to cover the whole field of view.

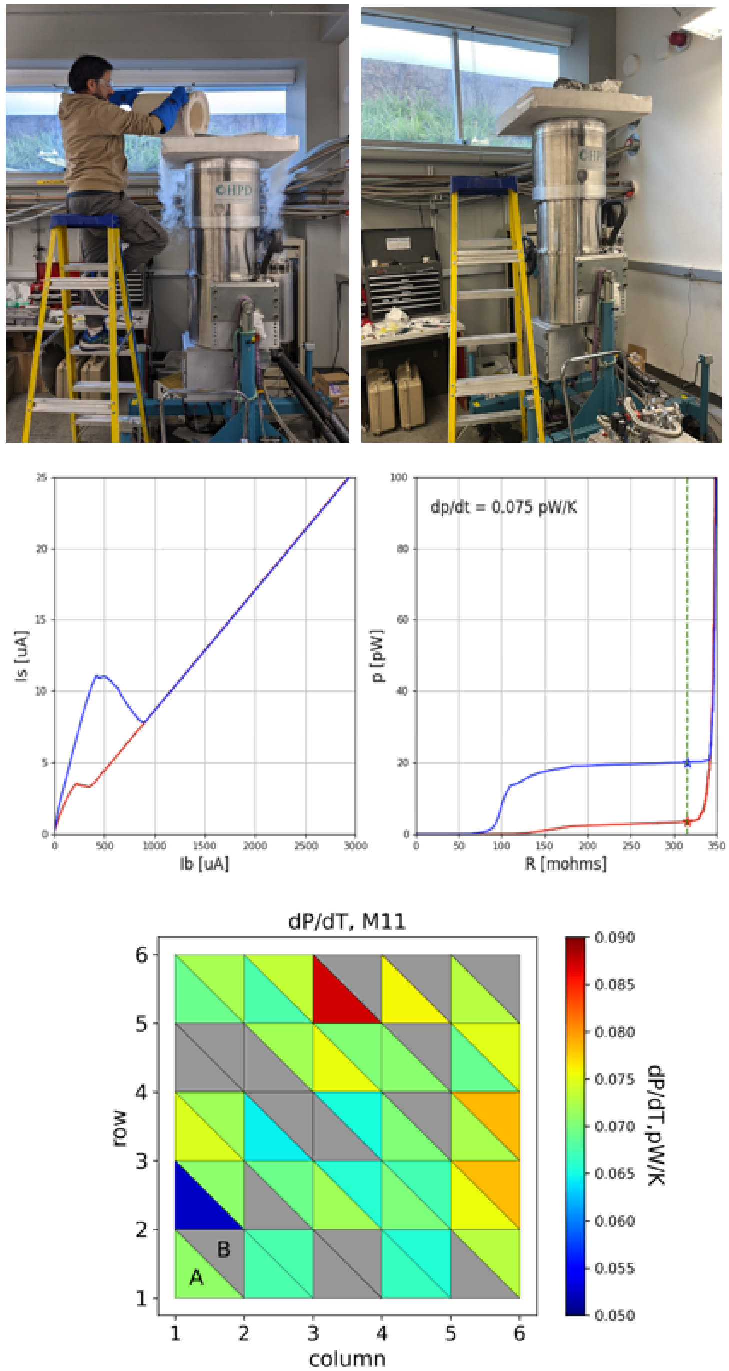

Figure 5.1: The Optical Efficiency (OE) measurements setup of the detectors. Top: with 300K (right) and 77K liquid nitrogen (left). Middle: An example of load curve taken with 300K room temperature (red) and 77K liquid Nitrogen (blue). Bottom: The resulting OE rectangular plot of the 2023 deployed module M10. The median OE is about 0.077 PW/K. The grey detectors are not shown due to few broken rows in our test bed. We expect to have a detector yield of ~ 90%. The top photos were taken by Bryan Steinbach.

An integration time of 10-15 seconds at each position is sufficient for a high Signal-to-Noise Ratio (SNR), which took > 15 hours to cover the full aperture. We record this data during night time for having high quality and high SNR beams as well as avoiding any RF or WIFI sources. Then, we construct the beam map in the analysis by demodulating with the chopper reference and remove any bias noise, resulting in the in-phase quadrature beam maps, as shown in Figure 5.3. The expected and measured 1D beam profiles of edge antenna array at 40 GHz. The simulated 1D pattern is calculated over 25 % bandwidth. The measured and simulated half width at full maximum are 10.9° and 10.25°, respectively. The F# 1.55 for BICEP Array (17°) shows that the measured azimuth beams averaged (red and blue dashed lines) for two detectors agree well with the simulated beam profile (solid black), and that they match the optical design.

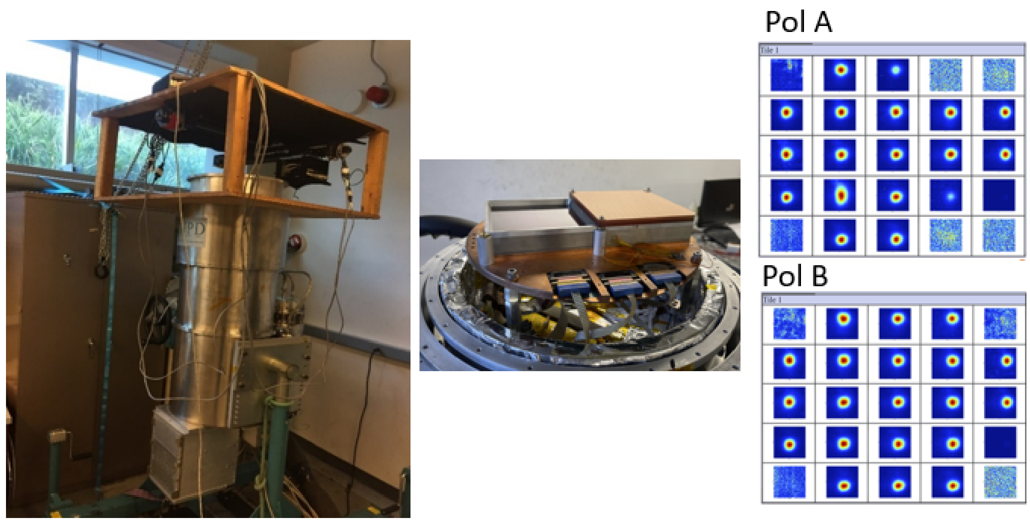

Figure 5.2: The Near-Field Beam Map (NFBM) measurements setup of the detectors (without optical elements). Left: The NFBM at the top of the cryostat, which is cooled down to ~ 250 mK. The entire NFBM assembly is mounted in a wooden crate attached to the top of the telescope. The source is located few inches above the aperture. Middle: the detector modules inside the test-bed. Right: The measured NFBM in the detector physical coordinates for both polarization.

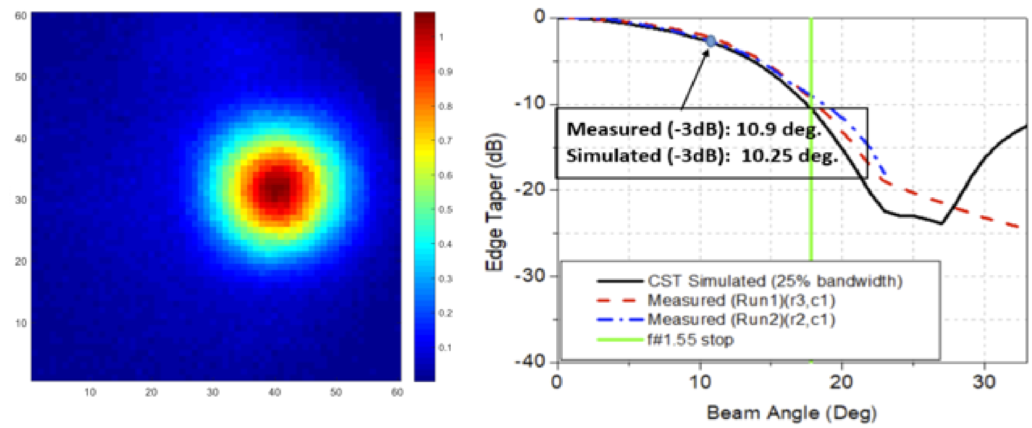

Figure 5.3: The measured and simulated NFBM. Left: the measured beam for one detector polarization at 40 GHz as function of grid's steps, peak-normalized. Right: The measured and simulated beams at 40 GHz (from Chapter 3) after the conversion to the angle scale.

5.3 Near-field Beam Map of Telescope

The near-field beam maps of the detectors have been measured after passing through BICEP Array optical elements shown in Figure 2.5. The resulting NFBM of BICEP Array telescope is used to diagnose any defect in our optical systems if exists, such as "beam steer" or "beam defocusing" which might be truncated at the aperture stop at the 4K stage. The NFBM of the telescope has been taken by using similar steps described in Section 5.2, but with a bigger beam mapper to cover the 550 mm BICEP Array aperture, as shown in Figure 5.4. We also used a PID temperature controller to better control the source for a stable temperature and chopper reference over the hours of data taken. Figure 5.5 shows the measured NFBM at 30 GHz and 40 GHz as function of the BICEP Array aperture size. The side-lobes have been truncated at the aperture stop. We also measured some beam anomalies and diagnoses and I will talk about that in Section 6.2.

GRASP Optics Simulation

We have demonstrated the good agreement between the measured and simulated beams on the near-field of the detectors without the optical elements. Additionally, we simulated our antenna's beam with CST MICROWAVE STUDIO software and then used the GRASP physical optics modeling software to propagate that beam through the BICEP Array optical elements. The resulting simulated beam agrees well with the measured beams, as shown in Figure 5.6. The vertical lines indicate

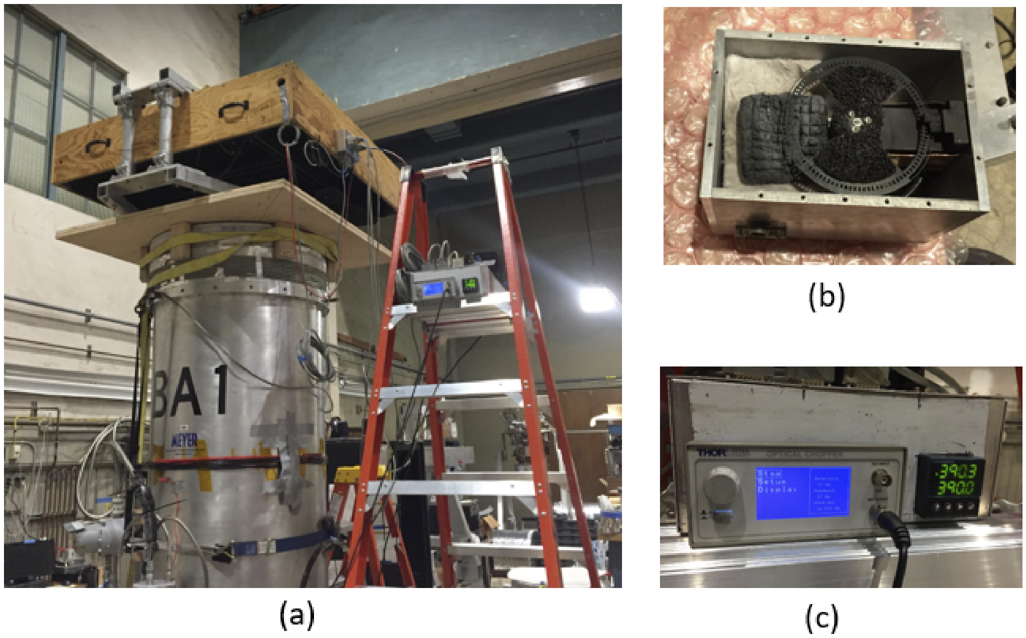

Figure 5.4: The NFBM setup with BICEP Array receiver at Caltech's high-bay to study the effect of the optical system. (a) NFBM setup installed at the top of the 30/40 GHz BICEP Array receiver (BA1) aperture window. (b) The thermal source with front cover removed, showing the optical chopper and heated ceramic element. (c) Thorlab optical chopper controller, showing the temperature and chopper reference.

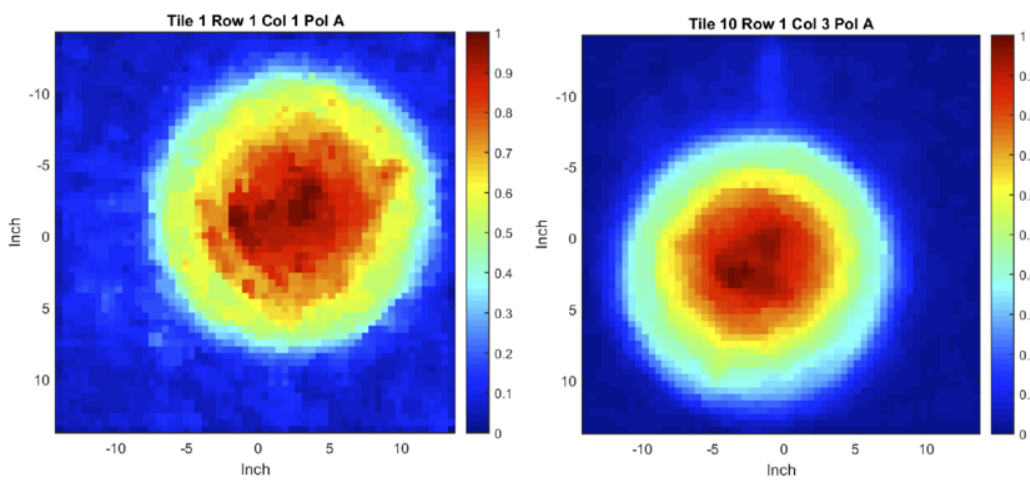

Figure 5.5: The measured NFBM of the detectors with BA1 receiver (with the optical elements). Left: The NFBM of 30 GHz detector. Right: The NFBM of 40 GHz detector. The x-axis is BICEP Array aperture window size at 30/40 GHz. The beam plots are peak-normalized

location of the aperture stop. We noticed that the measured beam does not drop beyond the aperture stop and we thought that the reflection around the aperture stop may have caused that issue.

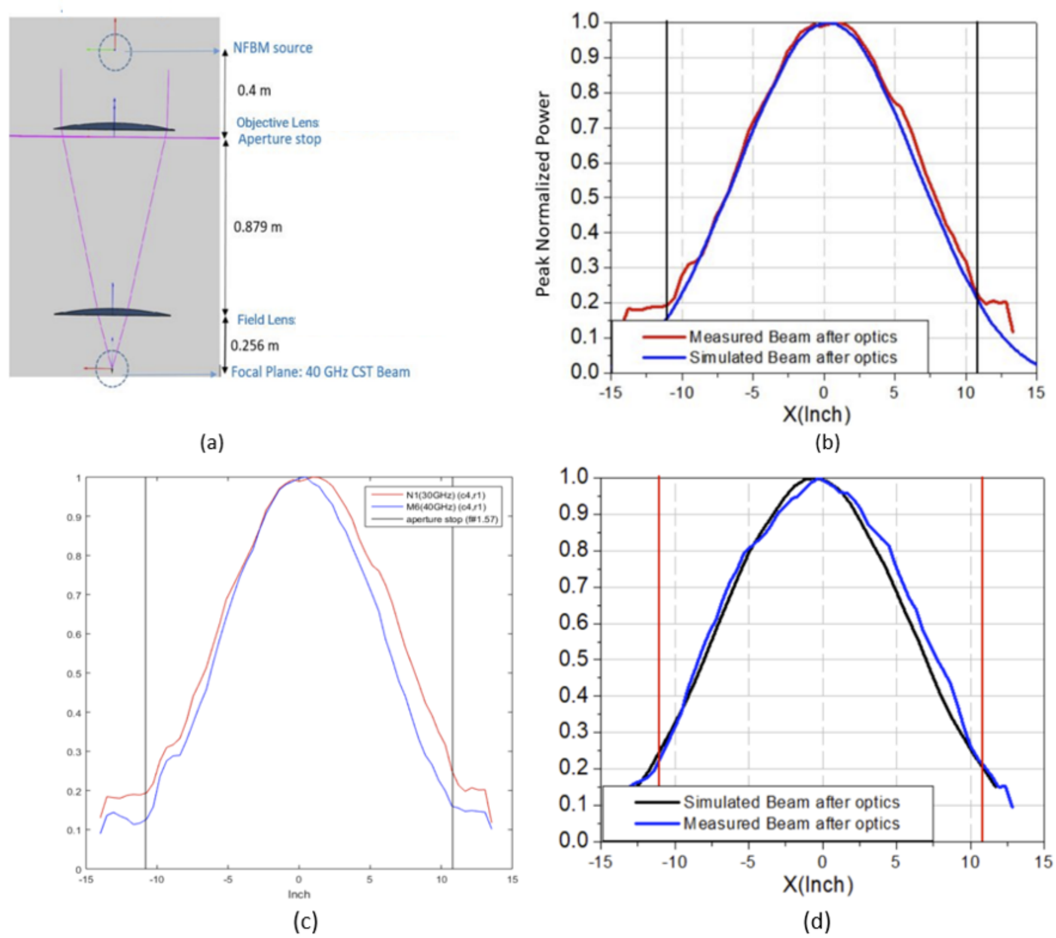

Figure 5.6: The detector beam modelling inside BA1 receiver. (a) The simple optics model of BA1 in Grasp Software for a detector input beam located at the middle of the focal plane, (b) the resulting output x-y beam plane cut of Grasp simulation shows a good agreement with the measured beam cut of 40 GHz detector, (c) the measured NFBM of 30 GHz and 40 GHz after BA1 optics and (d) the output beam cut at 30 GHz, over-plotting with the aperture stop (F#1.55).

5.4 Far-field Beam Map of Telescope

The far-field beam response of the telescope is important to verify the optical angular resolution of the telescope on the sky, quantify the beam systematic and consequently for our CMB polarization measurements. The source is considered to be in the "far field" of the detector at a distance R_{FF} of

$$R_{FF} = \frac{2D^2}{\lambda} \tag{5.4}$$

where D is the detector diameter, λ is the wavelength. We always measure the far-field at the sky of the South Pole but we were interested to verify our designed optical system before shipping BA1 to the South Pole. The far-field beam maps have been measured for the 40 GHz detector inside BICEP Array receiver at Caltech high-bay for the first time. This was a group team work to design, built, take data and analyze the resulting outcomes. The far field distance for 30/40 GHz BICEP Array telescope is $\sim$ 60-80 m. We located the heating source at end of Caltech high-bay, which is at 45 m distance to the BICEP Array receiver, so we are more in a "middle field" situation, as shown in Figure 5.7. We scan with $\pm$ 6-7° in order to scan the 30° telescope's field of view. The resulting FFBM of 40 GHz detector is shown in Figure 5.8. We fit the measured beams to the Gaussian function shown in equation 4.1. The measured Gaussian beam-width of 40 GHz detector is 0.38°, as shown in Figure 5.9, which is consistent with the scaled BICEP3 beam-width at 95 GHz (Ade, et al. (BICEP/Keck Collaboration), 2022). Later on, when BICEP Array receiver has been deployed during 2020 season, the on-sky measurement confirmed these measurements as well as measuring the beam-width of 0.47° for 30 GHz detector (Germaine, 2021), which is also consistent with the scaled BICEP3 beamwidth at 95 GHz. The far-field beam map has been measured at the South Pole using a chopped source at a frequency rate of 13-25 Hz , and located about 200 m away from MAPO where BICEP Array installed. The heating source chopped between the cold sky and ambient temperature. A flat aluminum mirror is mounted on top of BICEP Array during the beam mapping campaign. For more information, see (Karkare, 2017). Additionally, a high-powered broad-spectrum noise source is also used at the South Pole for measurements of the polarization angle and cross-polarization response as well as FFBM and the far-sidelobe response (Cornelison, et al. (BICEP/Keck Collaboration), 2020).

The FFBM simulations and measurements validate the detector and optical design of BA1 camera. The full optical performance of the detectors have been validated and agreed well with the simulations. Additionally, the resulting beam map difference of the edge pixel (Figure 5.10) validated our design response (Chapter 4).

Bands	FF beamwidth (designed)	FF beamwidth (measured)
40 GHz	0.37°	0.38°
30 GHz	0.47°	0.478°

Table 5.1: The designed and measured far-field beam-widths of 30 GHz and 40 GHz detectors. The FFBM of 40 GHz detector has been measured at Caltech and South Pole. The 30 GHz detector has been only measured at the South Pole.

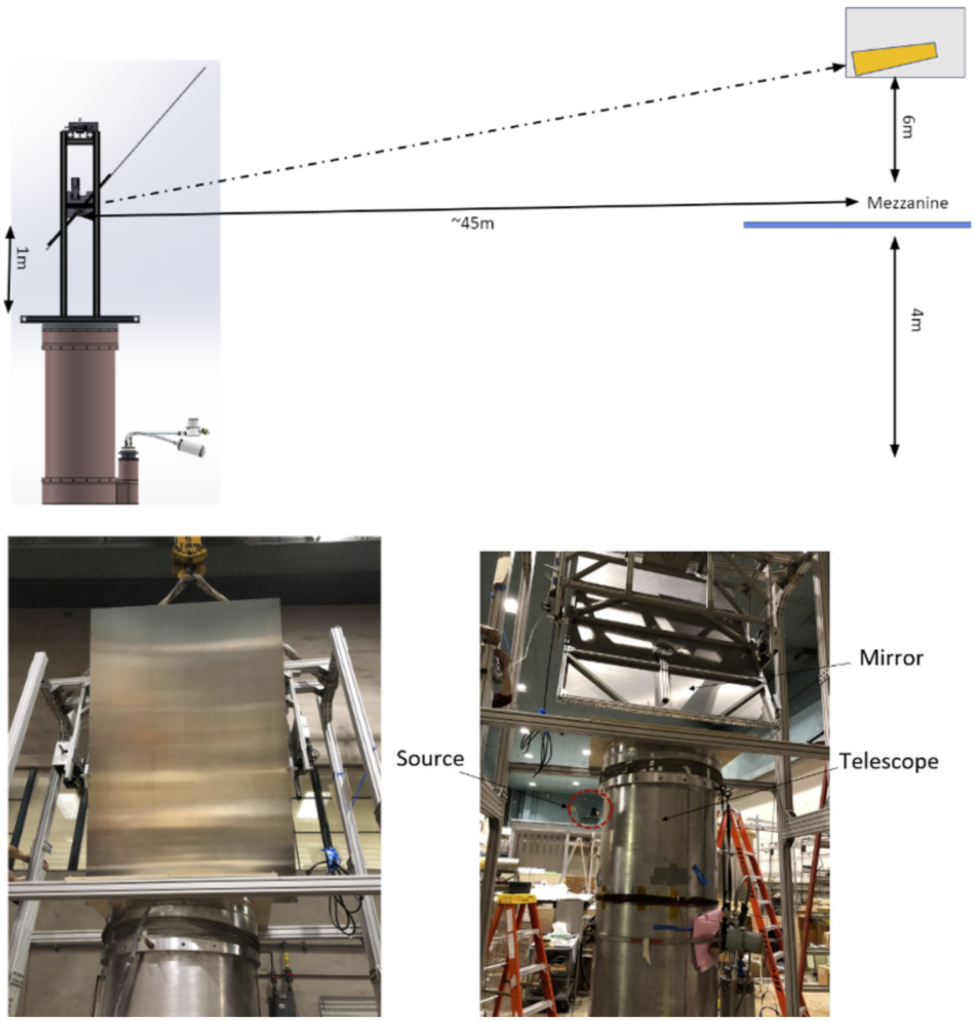

Figure 5.7: The far-field beam map setup in Caltech's high-bay. Top: The block diagram. Bottom: The side view of 30/40 GHz BICEP Array receiver with the mirror and source.

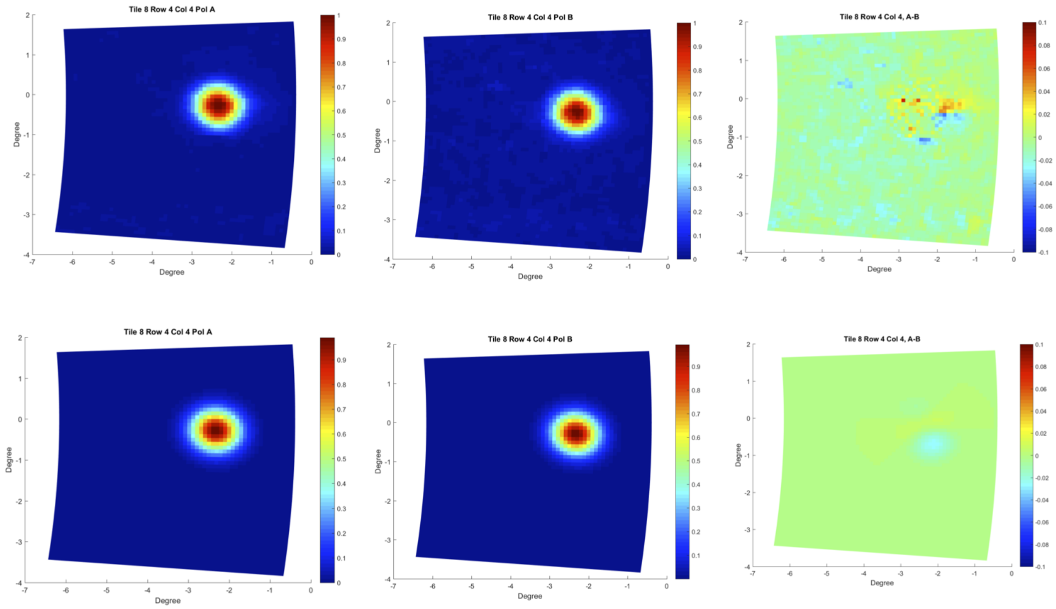

Figure 5.8: The measured far-field beam map for middle pixel of 40 GHz detector module, “Pol A” and “Pol B” and “Pol A” – “Pol B”. Top: The peak-normalized beam. Bottom: The corresponding Gaussian fit.

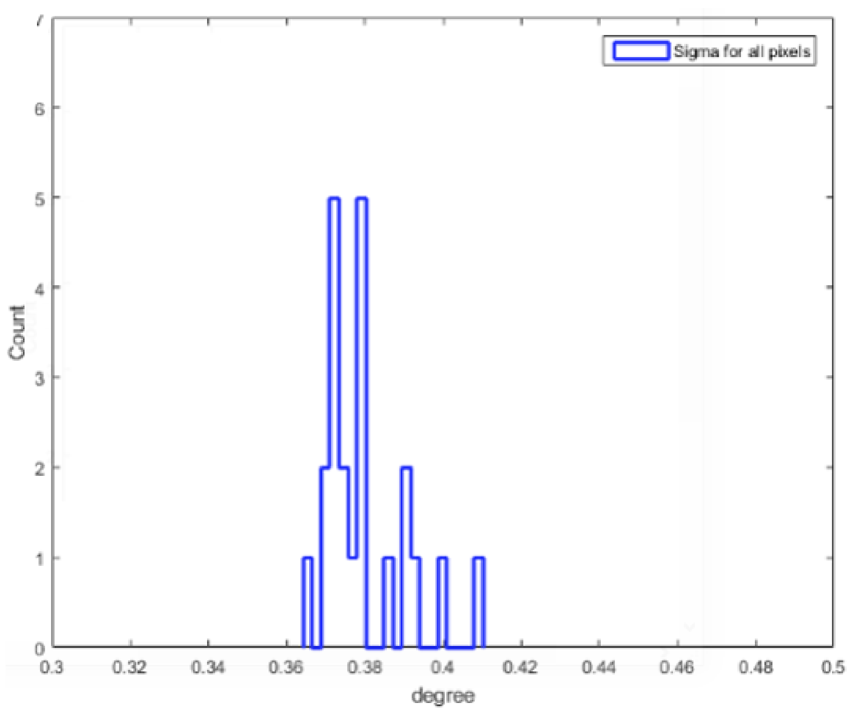

Figure 5.9: Differential Gaussian beam-width histogram of 40 GHz detector.

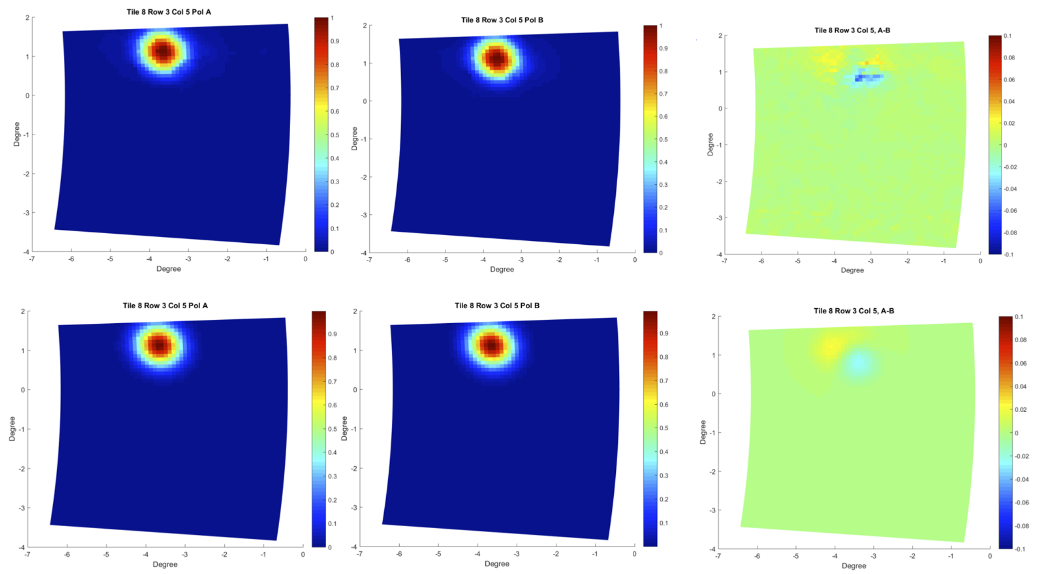

Figure 5.10: The measured far-field beam map for an edge pixel at 40 GHz detector. Top: The peak-normalized beam. Bottom: The corresponding Gaussian fit. The difference plots shows < 10 % peak-to-peak after fitting to the Gaussian function, and comparable to the beam difference of the middle pixel shown in Figure 5.8. These results validated our corrugated focal plane frame that was described in Chapter 4.

5.5 Radio Frequency Interference (RFI) Susceptibility Tests

Shielding our telescope against the RFI pick-up is necessary toward making a high quality observation and to minimize the noise pick-up into the detector's timestream while we are trying to measure the B-mode signal at nK level. The most important sources of the noise pick-up are the MCE and housekeeping system. This section shows the RFI tests on BA1 receiver. We aim to study the effect of different RF shielding configurations by installing a RF Cage with a given hole diameter to reject longer wavelengths. The RF cage made of wire mesh of size 1/8 inches, known as the "Chicken wire." We recorded the detector time streams while placing this RF cage on different positions around BICEP Array receiver, mainly around the bottom of the cryostat to shield the MCE and HK against any RFI pick-up. We also took the detector's time-steam while installing a LID at the top of cryostat to shield the window. We took the time streams while the disc-cone antenna point in the different directions, as shown in Figure 5.11. The power used for the broadcast signal was P=9 dBm. We swept with a disc-cone antenna, with frequencies from 100 MHz to 2 GHz and covered the entire bottom of the cryostat with the RF cage, then covered the HK box and top of the cryostat. We studied the RF pick-up effect for the following three cases: (1) there is no RF cage on the bottom nor the top of cryostat (blue line), (2) there is RF cage on the bottom of cryostat only (orange line), and (3) there are RF cage on the bottom and the top of cryostat (green line). We also took the time steams for 30 seconds by chopping at 11 Hz with a power of 19 dBm. We kept the disc-cone Antenna facing north. It is clear that the RF cage helps eliminating the RF pickup and reduces the white noise level. Figure 5.13 shows the time streams and the resulting Noise-Equivalent-Current (NEI) in PA/$\sqrt{(Hz)}$. The RF cage pushes the White noise to a minimized level in the Power Spectral Density (PSD). The average value of the NEI between our science band (0.01-0.5) Hz is minimized with installing the RF cage on and the lid. These figures show the important of the RF cage to reduce the RF pick up by our detectors. The pair-diff between both polarization will further push this limit to photon-dominated limit. The RF environment at the South Pole would have much lower RFI, as I will discuss in Chapter 6 about the deployment of BA1 receiver and its calibration to the South Pole.

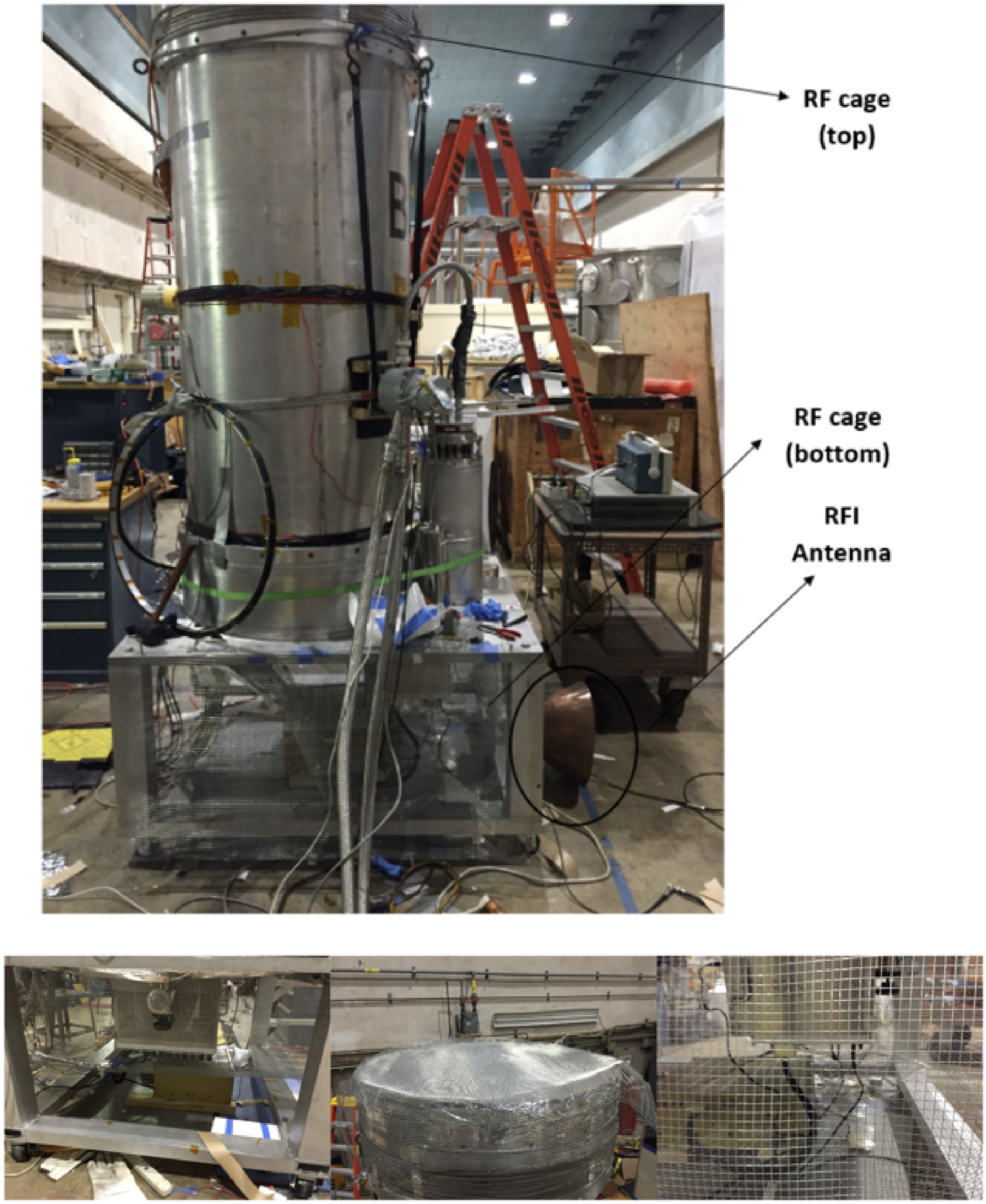

Figure 5.11: The measurement setup of RFI. Top: the overview of the BA1 with modifications to minimize the RFI. We placed the chicken wire around the read-out electronics at the bottom of cryostat. The disc cone antenna is also placed at the bottom of the cryostat close to the MCE to test the RF pick-up. Bottom: RF cage is covering the bottom/top of the cryostat.

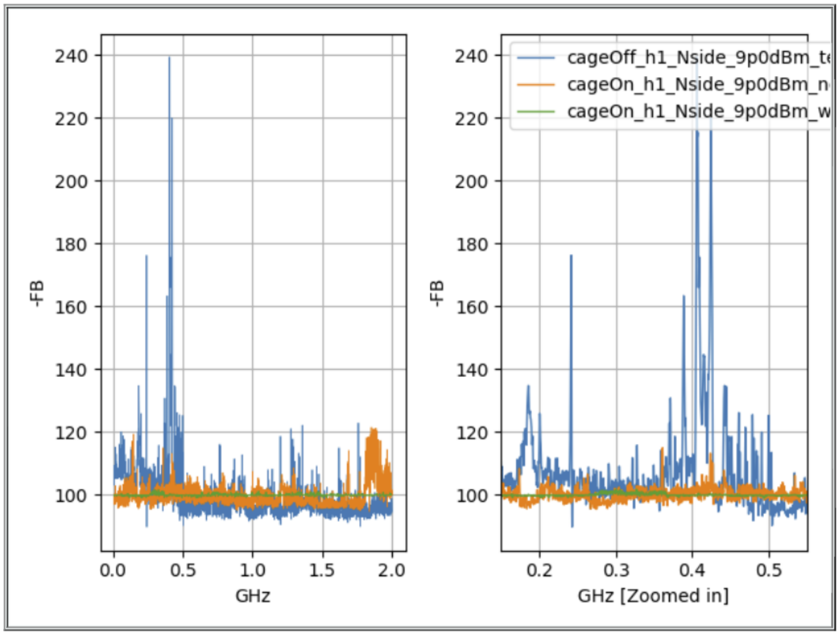

Figure 5.12: The chirps data have been acquired while covering the MCEs without/with RF cage on the bottom vs covering the top of the cryostat for the 40 GHz detector module. The RF cage highly minimized the RF pick-up.

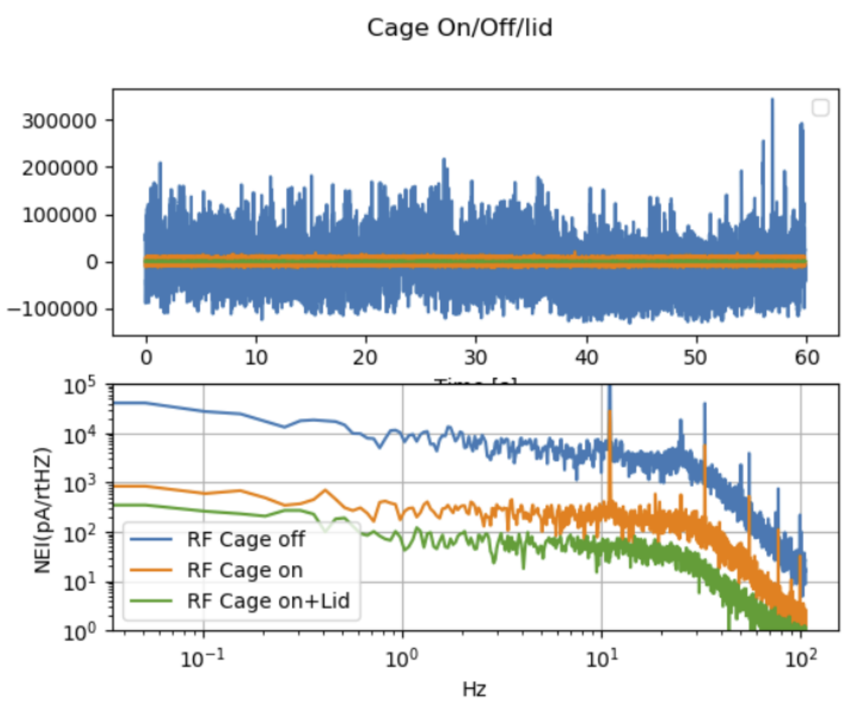

Figure 5.13: We studied the effect of the RF cage on minimizing the RF pick-up. Top: The detector time streams. Bottom: the resulting Power Spectral Density (PSD).

Chapter 6

BA1 DEPLOYMENT TO THE SOUTH POLE (2020 VS 2022 VS 2023 SEASONS)

The previous chapter showed that the measurements of the 30 GHz and 40 GHz detectors at Caltech validated our design. After that, we disassembled BA1 to be packed and shipped to the South Pole for science observation. We have successfully deployed the first low frequency BICEP Array receiver to the South Pole during 2019/2020 austral season for CMB polarization measurement (Moncelsi, Ade, et al. (BICEP/Keck Collaboration), 2020). The receiver calibration has been preformed in-lab and on-sky at the South Pole. Various challenges have been raised during the first deployment season. We ran lots of tests to address these challenges in our laboratory at the South Pole and at Caltech. Based on these test results, we went back to the South Pole during the 2021/2022 season to upgrade the receiver with better detector tiles and a new filter configuration to boost the overall sensitivity of the receiver. This chapter summarizes these diagnostic tests and upgrades. I will finally report BA1 upgrade with better performance detectors during this 2023 deployment season.

6.1 Three Years of BA1 Deployment Seasons

During the first deployment season, we deployed the full focal plane, 12 detector tiles, with a mix of four 30 GHz modules, seven 40 GHz modules and the first prototype of dual-band 30/40 GHz design, as shown in Figure 6.1. Chapter 7 will describe in details the demonstration of 30/40 GHz and its extended optimization prototype to cover two higher CMB observation bands at 90/150 GHz. The 40 GHz bands and 30 GHz detectors contains 25 and 16 detector pair, respectively. The total number of deployed detector counts was 542 in 2020 season. In 2022 season, we swapped few detector tiles with more 30/40 GHz tiles to increase the number of total deployed detectors to 584, as shown in Table 6.1. During 2022 season, the tests showed poorly performing dual-band detector modules which our team swapped during the 2023 season. We unfortunately were not be able to test these poorly performing tiles at Caltech before deployment because of COVID-19's delays. During 2023 season, we replaced Mx6 and Mx7 with new two high-yield 40 GHz detector modules and also replaced Mx8 with the refurbished detector tile

M8. We kept the best-performing dual-band module Mx2 this season as I will talk about its performance in the next chapter.

Deployment season	Frequency (GHZ)	Detector tiles (#)	Detector counts
2019/2020	30	4	128
	40	7	350
	30/40	1	64
2021/2022	30	4	128
	40	4	200
	30/40	4	256
2022/2023	30	4	128
	40	7	350
	30/40	1	64

Table 6.1: Summary of detectors deployed to the South Pole during the three years of BA1 seasons.

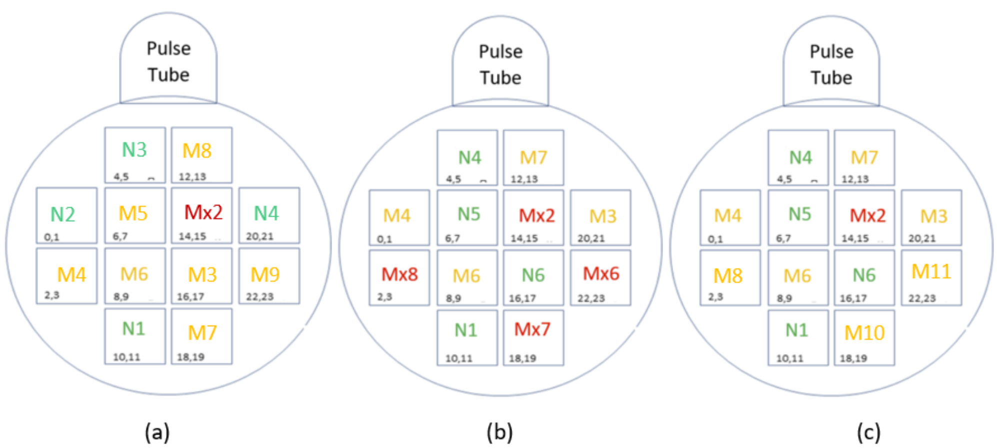

Figure 6.1: The focal plane arrangements of 30/40 GHz BICEP Array receiver at the South Pole. (a) 2020 vs (b) 2022 vs (c) 2023. "N," "M," and "Mx" refer to 30 GHz, 40 GHz, and 30/40 GHz, respectively. Figure 2.6 shows the actual focal plane and the 12 detector modules inside MAPO building at the South Pole.

6.2 BA1 Calibration

BA1 receiver has been closed up, pumped down and cooled down to the base temperature of about ~ 280mk inside MAPO building at the South Pole. The BA1 calibration has been performed in-lab and on the sky. The optical in-lab measurements will be similar to what we have done at Caltech to make sure that all are working properly and no broken detectors during transportation. Additionally, the dark sector of the South Pole is free- RF and no Wifi resources for getting high quality measurements. These calibration measurements have been taken during the three deployment seasons at the South Pole. The next few sections summarize some of the calibration work.

Load-curves

The load curves (I-V) have been taken for BA1 detectors to identify the working detectors and biasing values on aluminum TES transition for beam maps measurement. The load curves have been also measured on the titanium TES transition for science observation and on-sky noise sensitivity. Figure 6.2 shows an example of the load curve for all the detectors in the 40 GHz module. We basically took the beam map data two times with two different biasing values (red and blue vertical lines). We carefully choose these biasing values to maximize the yield.

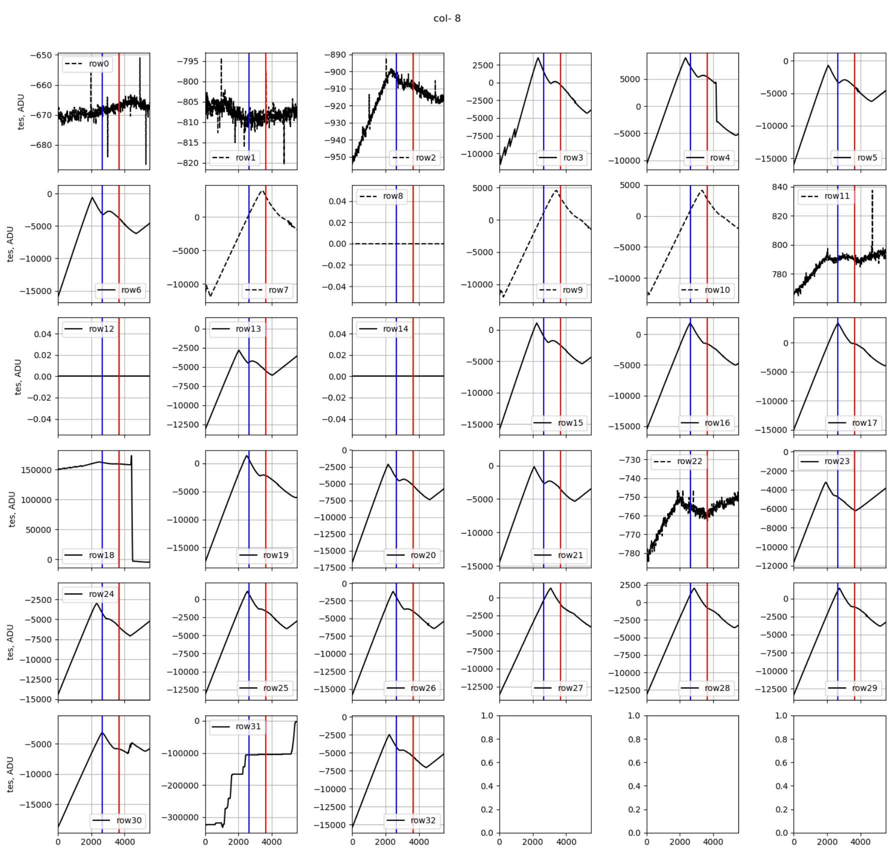

Figure 6.2: An example of Load curves (I-V) for all TES detectors within one detector tile. The two vertical lines show the biasing values for taking near-field or far-field beams measurements.

Composite beam maps

The near-field beam maps of BA1 has been taken by using similar steps as I showed in the previous chapter. The composite beams for each tile has been generating by stacking all beam maps that passed cuts. We co-add all beam maps from a given detector together. These composite beams are very useful to quantify T→P leakage via beam sims. The measured per-detector tile composite beam map taken on 30/40 GHz BICEP Array are shown in Figure 6.3. Figure 6.4 confirmed the near-field beam map difference to be less than 10% per design for the edge pixels located close to the focal plane frame.

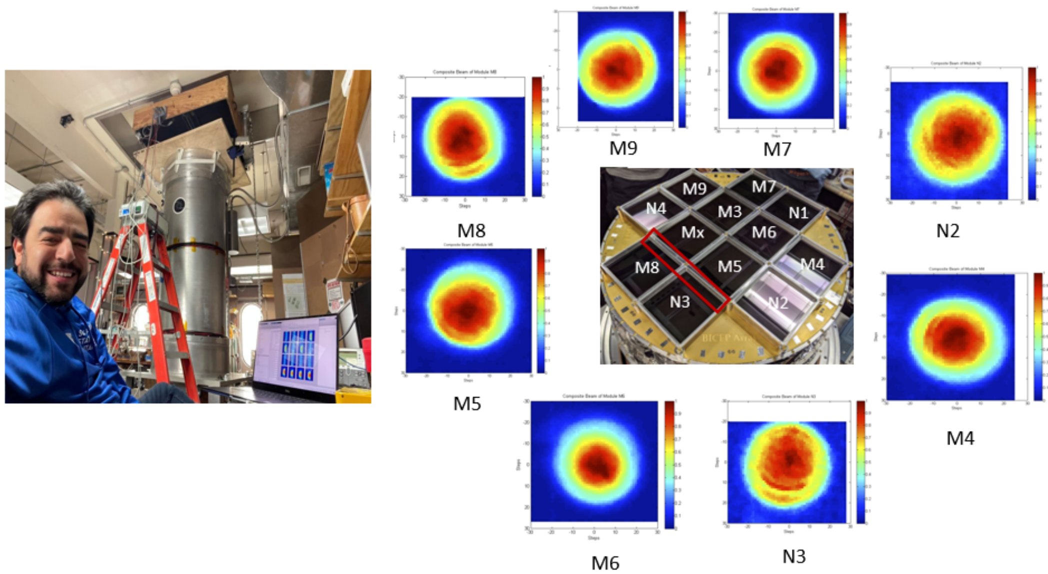

Figure 6.3: The NFBM measurement at the South Pole. Left: I was taking a live NFBM data inside MAPO building. Right: The resulting per-detector tile composite NFBM by co-adding the individual beam maps (Azimuth averaged).

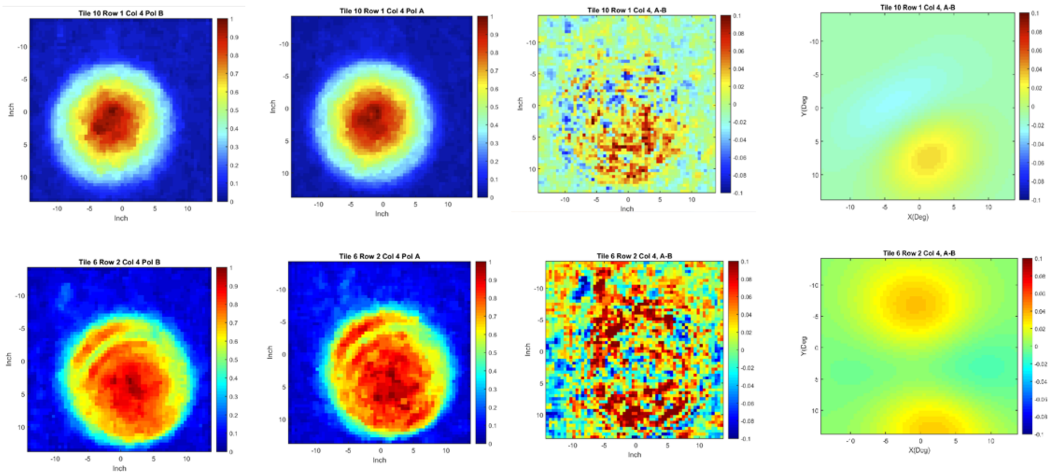

Figure 6.4: The “Pol A” and “Pol B” and “Pol A” – “Pol B” (normal and Gaussian) for two edge pixels. Top: 40 GHz detector. Bottom: 30 GHz detector. These results validated our wide-band corrugated focal plane as we discussed in Chapter 4.

Anomalies beams

Despite of measuring good-looking beam maps, we observed some anomalies beams. One example is the “beam steer”, as shown in Figure 6.5. The steered beam usually happens due to the excessive edge taper as well as due to the non-optimal biasing values within the aluminum transition, as shown in these plots. The blue vertical line shows the biasing near the end of aluminum transition, resulting in a no-ideal beam response. The red vertical line shows the biasing within the Al transition phase, resulting in a good-looking beam response. We bias one MCE column at a time, so, some of the biasing values will miss the transition phase, resulting in non-good looking beams. These plots taught us that we have to take the NFBM at different biasing to recover these detectors and maximize the yield. We previously observed these beams in BICEP2 era. These recovered beams with an appropriate biasing value contribute weight to the CMB maps and resulting science data.

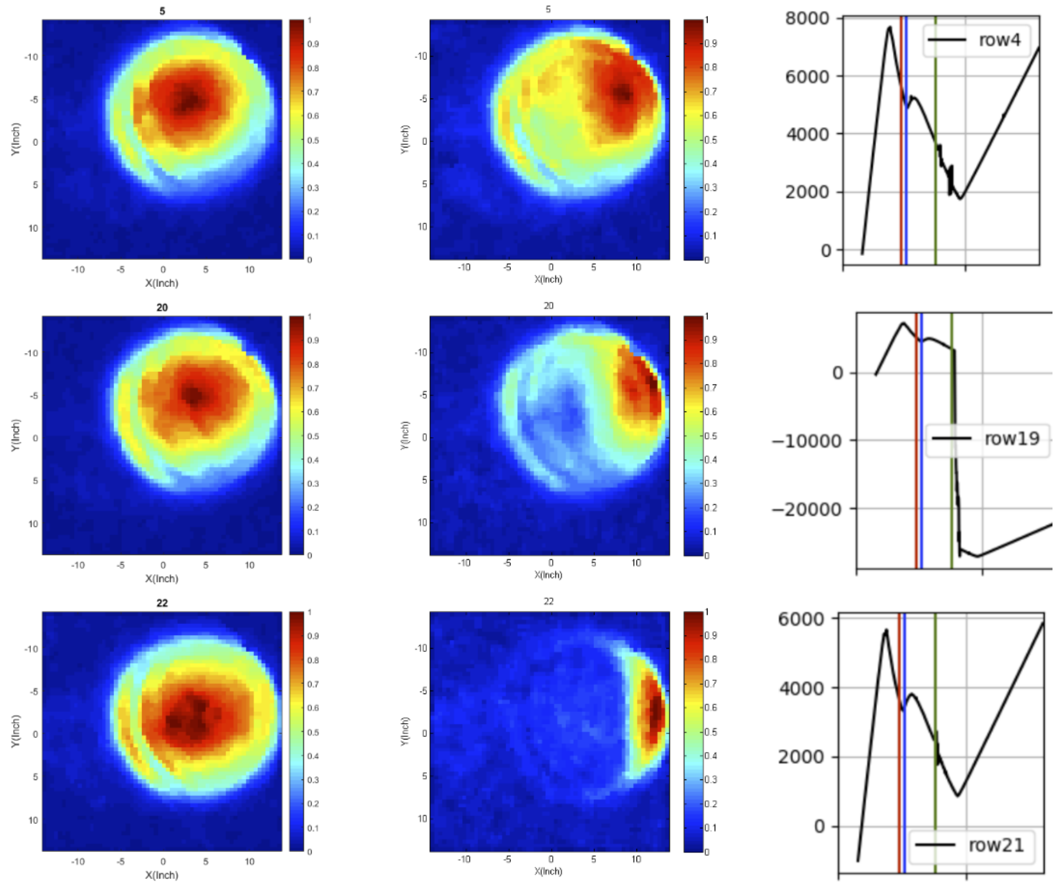

Figure 6.5: The NFBM measurements with different biasing values in the aluminium superconducting transition. Left and middle: The peak-normalized beam map of the same detector but with two biasing values (red and blue). Right: The load curve of that detector with a blue vertical bias value at the end of the transition (the truncated beams) versus the red vertical bias value within the transition phase (the good-looking beams).

Radio Frequency Interference Measurement

The RFI measurements have been taken at the South Pole and compared with the previous RFI measurements at Caltech for different RF shielding configurations. To minimize the RF pick-up, we taped all the holes around the MCE and HK, and we used chicken wire. We also added RF tape (aluminum and Mylar) in-between the modules to perform as an RF shielding, as shown in Figure 6.6. We used the low frequency discone antenna that has been designed and fabricated at the South Pole to operate from 100 MHz to 1.5 GHz, as shown in Figure 6.7. The resulting PSDs show that we have a low white noise level at the South Pole (Figure 6.8), compared to our previous measurements at Caltech (Figure 5.13).

Figure 6.6: RF cage cut off frequency = 270 GHz. An aluminum tape covered the holes around the MCE and HK as well as in between the modules before we closed up BA1. The tests that we have performed at Caltech pointed us to make these modifications to avoid any RFI pick up by the electronics and read-out system.

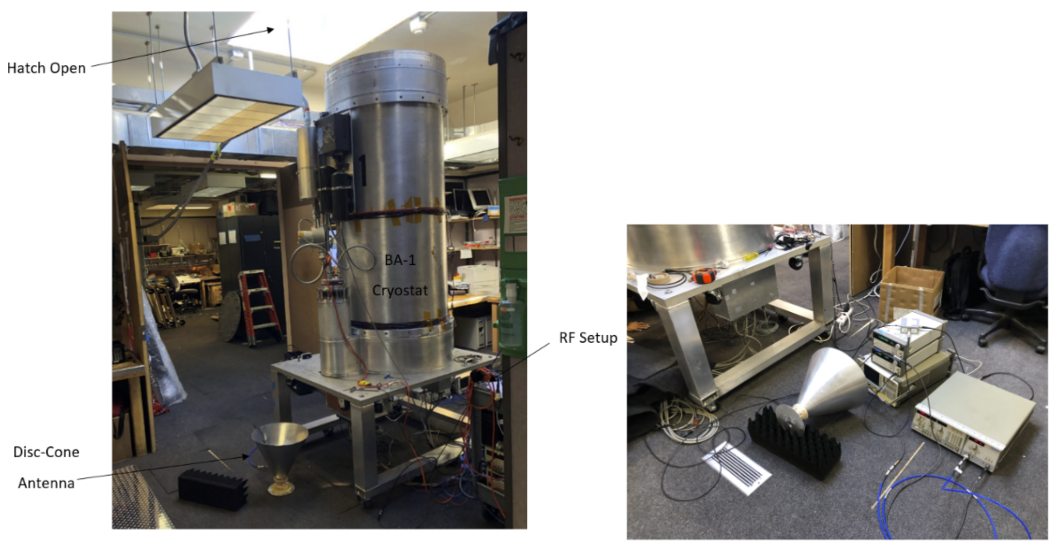

Figure 6.7: The measurement setup with BA1 cryostat inside MAPO building at the South Pole. The hatch was on and the BA1 was pointing toward the cold sky. We ran these test while the antenna is pointing to different directions around the cryostat to make sure that BA1 is fully shielded against any RFI pick-up.

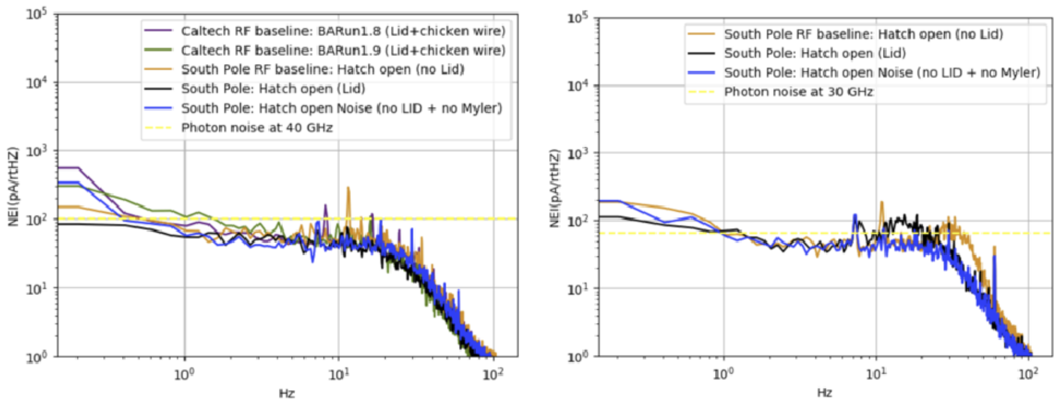

Figure 6.8: The PSDs comparison for BA1 run at Caltech (with LID at the top and RF cage around the bottom of the cryostat) and at the South Pole (Hatch open) for the 30 GHz and 40 GHz modules.

RF measurement: On-mount vs Off-mount

The effect of the noise pick and rays reflections around the telescope metal mount and motors has been addressed. Our telescope has been shielded against ant leaking RF signal. The disc-cone antenna has been pointing toward the receiver while at the mount, as shown in Figure 6.9. We also ran RFI tests on-mount and compare it with off-mount case and record the time streams in each case. This measurement helps us to check for any extra crazy noise pick up due to the mount metals, specifically the motor. The resulting time-steams concluded that we are not suffering from these issues. Our telescope is shielding against the electronics and read-out pick up. We noticed some narrow spikes in both measurements but they were located outside our science band, as shown in Figure 6.10. We just ran these tests since it was a problem in other CMB experiments.

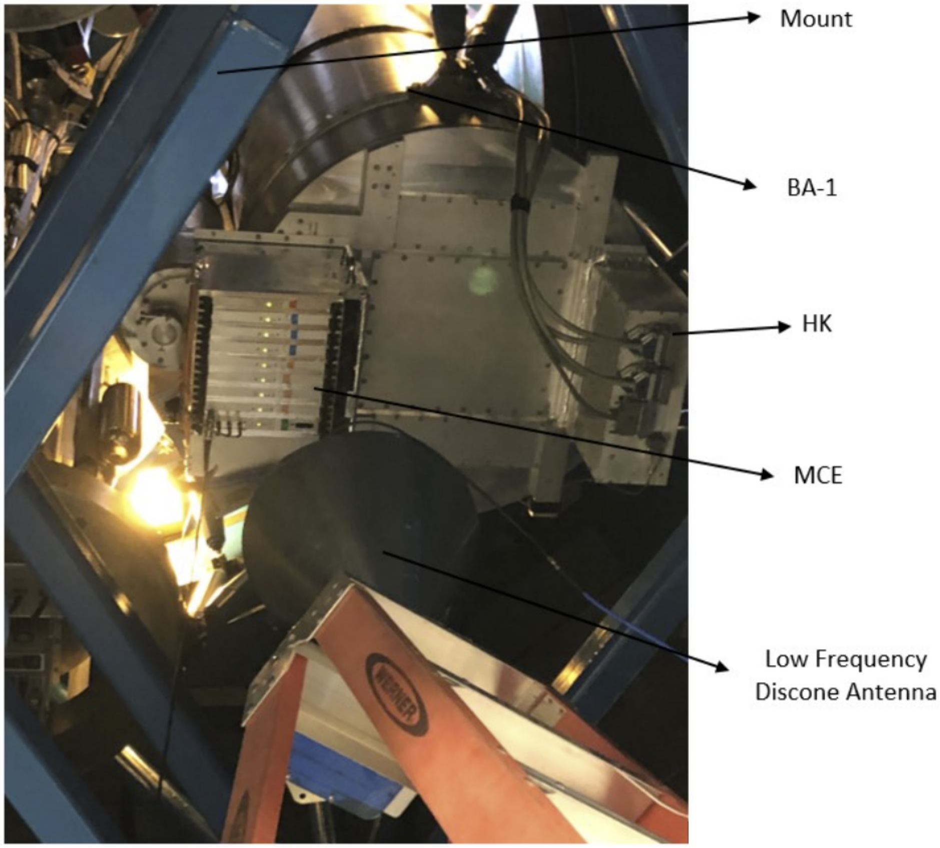

Figure 6.9: The measurement setup of the low frequency antenna with BA1 on the mount. We tested the effect of radio interference on the BICEP Electronics and readout systems inside the telescope at the South Pole. I used an antenna that transmit EM and record the data using python data acquisition.

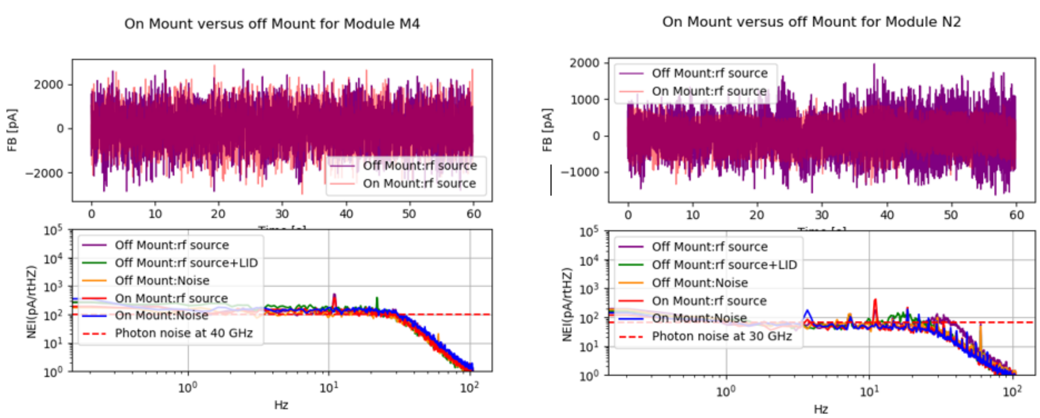

Figure 6.10: Time streams & PSDs comparison between on-mount versus off-mount with different cases at the South Pole for the 30 GHz and 40 GHz modules. This data was taken during 2020 deployment season

On-sky noise sensitivity at the South Pole

This section presents the noise measurement of BA1 telescope from the sky at the South Pole during 2022 season without any present RFI sources. The BA1 camera sensitivity can be measured using the detector timestreams noise data within the BICEP/Keck science band for sky observation (0.01 Hz to 0.5 Hz). The detectors were designed to be photon noise limited with loading from the South Pole sky. Figure 6.11 shows the 40 GHz and 30 GHz noise spectra before (purple) and after subtracting (grey) detector pairs to eliminate common mode noise. The suppression of 1/f noise down to below 0.1 Hz after pair-difference polarization pairs demonstrates that the instability was common mode to both optical detectors. Our experience with other BICEP and Keck cameras leads us to suspect that it likely originates from the atmospheric fluctuations but the 1/f noise could also arise from other effects. The resulting difference spectra (grey curves) agree well with the anticipated photon noise level according to the expected sky loading conditions and calibration parameters for both frequency bands at the South Pole (yellow lines). The resulting spectrum validates photon-noise dominated design. The measured NET from the 2022 season is lower than the measured NET from first deployment season after we upgraded BA1 receiver, as I will show in the next section.

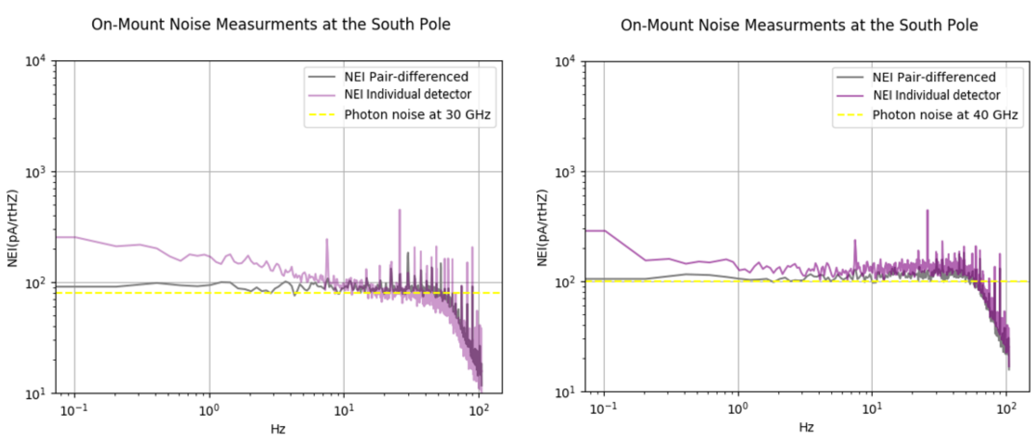

Figure 6.11: The on-sky noise sensitivity of the detectors at the South Pole. Left: 30 GHz detector. Right: 40 GHz detector. Purple curves show the measured noise equivalent current (NEI) at the South Pole while grey curves show the difference between pairs in the same pixel. Note that the grey curves agree well with the expected photon noise level shown in yellow, indicating that our detectors are background noise dominated. We biased the detectors in a Titanium superconducting transition. This data was taken during 2022 deployment season after we upgraded BA1.

CMB temperature map

The preliminary CMB temperature map has been plotted at 30 GHz and 40 GHz. These maps have been obtained from the observation of few thousand scansets, each has 50-minute. The comparison with Planck temperature map at 44 GHz shows a very good agreement with our observed temperature map, as shown in Figure 6.12. These are the initial co-added maps from the first two seasons to demonstrate our telescope. The polarization maps (Q and U) are still a little bit noisy. Further improved maps are currently produced by using the 2023 observing season.

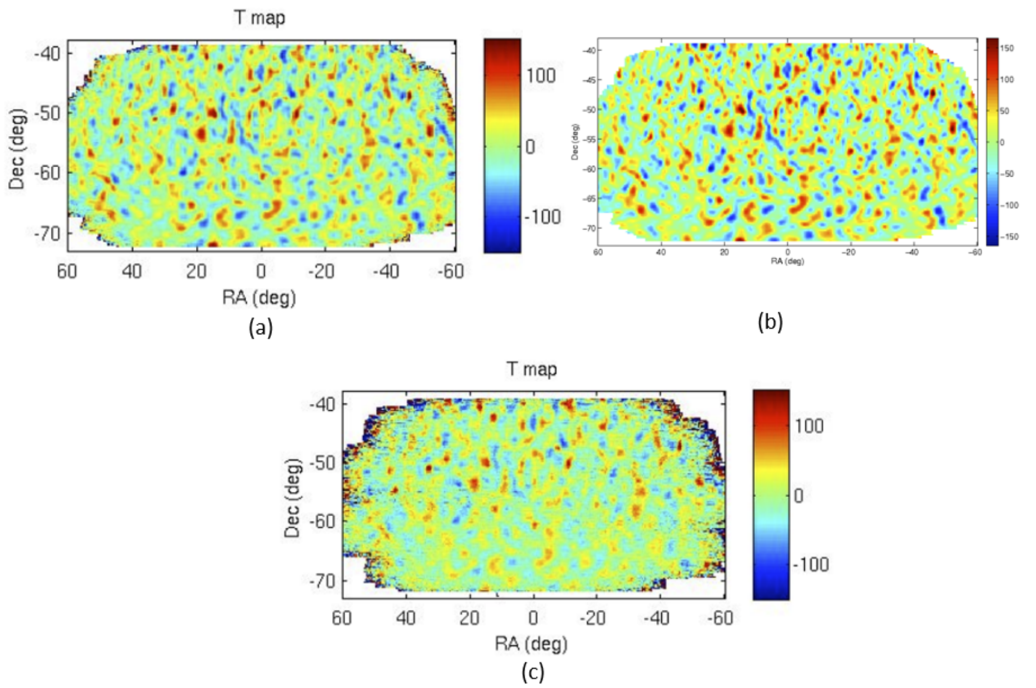

Figure 6.12: On-sky receiver performance. (a) Preliminary BICEP Array 40 GHz co-added temperature map covering 570 deg^2, obtained from 3,187 50-minute scansets from 2022 season, (b) the observed temperature map by Planck at 44 GHz for comparison (Adam, Ade, Aghanim, et al. (Planck Collaboration), 2016), and (c) The Preliminary BICEP Array 30 GHz co-added temperature map. These results validated our telescope design for CMB observation

6.3 BA1 Diagnoses between Three Seasons

The BA1 measurements validated our design at the South Pole as shown previously. However, some challenges arise from the first deployment season in 2020:

- *High TES detector loading Q_{total}*: known as Direct stimulation of the TES bolometers. The estimated NET from the CMB maps and detectors time-stream ranges from ~ 500-900 $uK_{CMB}\sqrt{s}$ (Crumrine, 2022), depending on the observing band in BA1, which is few times higher than the expected values shown in table 2.1. The resulting mapping speed was lower than estimated due to the significant noise level. A higher unexpected loading on the 30/40 detectors might be the reason and needs to be diagnosed and minimized.

- *Low-yield detector tiles.*: The Covid-19 period limited our accessibility to the fabrication facilities at MDL/JPL. Some of the detector tiles did not have the opportunity to be tested at Caltech test-bed before deployment to the South Pole. The measurements of some detectors inside our BA1 at the South Pole shows that they are suffered from low-yield. To solve this problem, we swapped these low-yield detector tiles with better performing high-yield tiles in the following seasons.

- *High normal resistance R_n (strong magnetic susceptibility)*: The measured normal resistance R_n is higher than expected with a non uniform distribution from the center to the edge of the tile (Zhang, 2023). The non-uniformity of the 6" tile might be the reason. To solve this problem, our fabrication team at JPL has developed a new "Inverted TES" process to improve the reliability of the 6-inch fabrication process. The fabricated detector with this new fabrication process shows promising result for 2023 deployment season.

- *Low OE at 30 GHz detector*: The 30 GHz detector modules were performed very poorly, especially compared to their 40 GHz counterparts. The 30 GHz detectors suffered from low optical efficiency underneath loading conditions at the South Pole. We suspect that there might be a reflections with the TES absorber. The diagnostic tests are in progress.

These challenges contributed to the measured high NET and the resulting low mapping speed during the first deployment season. We started with the first problem as I will describe next.

Out-band dark loading (Blue leak)

BICEP detector arrays include a small number of dark detectors (8 dark detectors for 40 GHz module) where the TES bolometers are not connected to the microstrip summing network. We use these dark detectors for noise and loading studies without any optical power. A low-pass mesh filter with 50 GHz cut-off frequency has been installed at the top of the focal plane during 2020 season to eliminate the high frequency power above 50 GHz, as shown in Figure 6.13. However, the dark detectors in our focal plane experienced excess loading that we understood to be **direct stimulation of the bolometers** or **Direct Island Coupling** (DIC) with high frequency out-of-band power (a Blue leak) as shown in Figure 6.14. The dark detectors allow us to measure detector properties without the influence of incoming optical power. The optical power supposed to reach the bolometers only through the slot-array antenna and microstrip feed network. However, a small portion of the optical power is absorbed by the TES island and contributed to the total loading of the detector (Q_{total}) during 2020 and 2021 seasons.

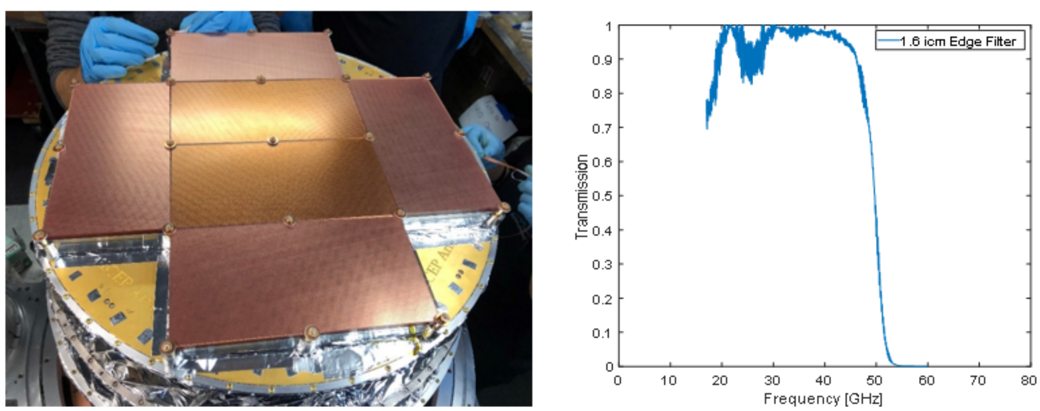

Figure 6.13: The filter configuration in 30/40 GHz BICEP Array receiver during 2020 deployment season. Left: The low-pass mesh filter installed at the top of the modules. Right: The measured spectrum of that filter by the team from Cardiff university (Ade, et al., 2006).

TES modelling in CST

We have tried to understand this problem by modelling the TES direct stimulation in CST software, as shown in Figure 6.15. We model the TES island as a PEC surface and use the CST field probes to get the current below and above the surface $n \times (H_2 - H_1) = Js$. n is the normal to the surface interface, H_2 is the magnetic field above, and H_1 is the magnetic field below the surface. The incoming plane

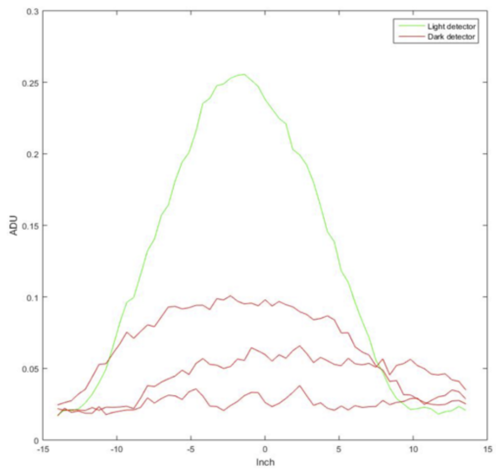

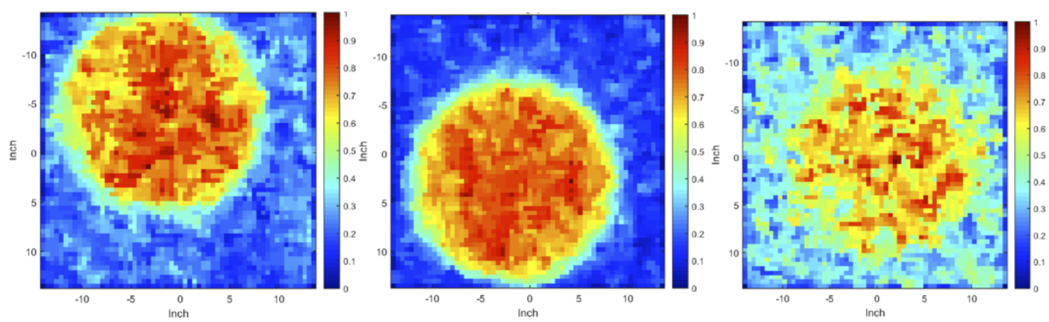

Figure 6.14: The NFBM measurements of dark detectors from the 2020 deployment season. Top: The 1D beam profile of light (green) overlaid with some dark detector beams (red). Bottom: various peak-normalized beam map of dark detectors. We did not expect to observe any signal on the dark detectors, which was a problem during the 2020 season.

wave from the top directly excites radiative coupling modes in the TES island. We experienced this direct stimulation problem in in an early prototypes for BICEP2 (Ade, et al. (BICEP2, Keck Array, and SPIDER Collaborations), 2015) and has been minimizing by reducing the cut-out between the TES and ground plane as well as connecting the TES legs to ground. We expect this DIC to have a high significant effect because the length of the legs are much longer than the previous designs since it is proportional to the wavelength. The TES meander microstrip has been treated as cavity model due to the limited physical dimensions of the TES island. We have the electric field (E_z), and transverse components of the magnetic field (H_x, and H_y). We could quantify this effect by installing magnetic field Probes (H_x, and H_y) in different places across the TES meander microstrip and ground plane, as shown in Figure 6.16, to monitor the current through the island by recording the H-field.

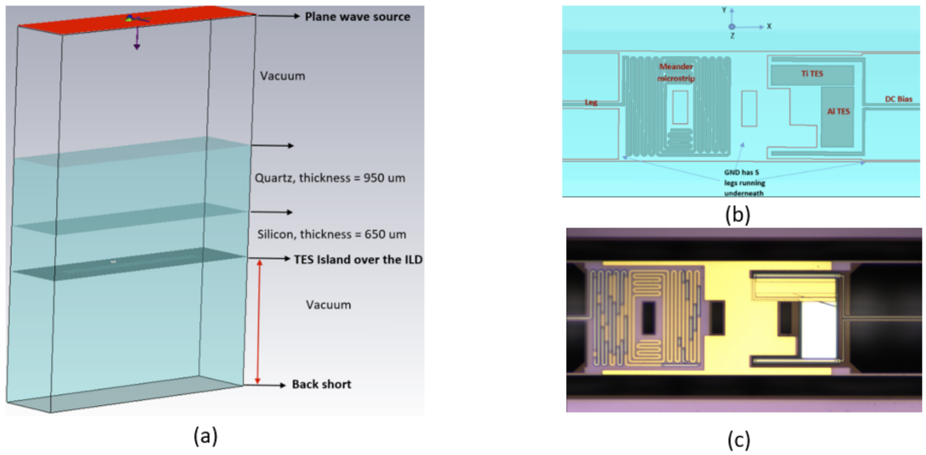

Figure 6.15: The TES model in CST Software. (a) The full TES structures, (b) The close-look at the TES island model in CST . (c) The corresponding fabricated TES.

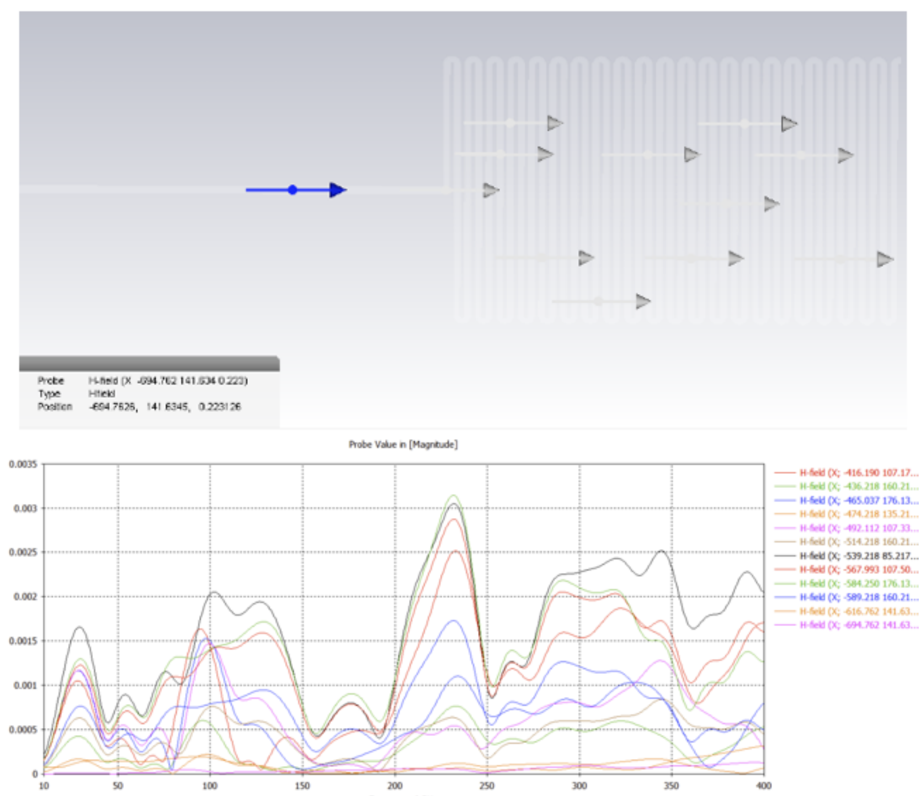

Figure 6.16: The TES simulated response. Top: the Meander island filled with Magnetic field probes in CST to model the direct island simulation. Bottom: The resulting CST output field probes amplitudes in x-axis (H_x) as a function of frequency (10-400) GHz.

The common and differential microstrip mode fields can be obtained from the field amplitude reading of each probe in meander microstrip and the ground plane.

$$p_c(f) = P_g(f) + P_m(f) \tag{6.1}$$

$$p_d(f) = P_g(f) - P_m(f). \tag{6.2}$$

The resulting common and differential mode power are proportional to the field probe magnitudes, $P_c(f) \propto p_c^2(f)$ and $P_d(f) \propto p_d^2(f)$. The figure of merit (power) represents the summation of theses filed probes magnitude.

$$P_c(f) = \sum p_c^2(f) \tag{6.3}$$

$$P_d(f) = \sum p_d^2(f). \tag{6.4}$$

Figure 6.17 shows the resulting P_d and P_c for two cases. The original case has large cutout in the ground plane and the niobium TES legs are not connected to the ground. The P_d and P_c have reduced by reducing the separation between the island and ground plane as well as connecting the TES legs to the ground plane. The field in the x and y directions, parallel to the wafer, produce a voltage between the TES island and the ground plane. This voltage results in a current to flow and deposit power on the TES island, resulting in a direct stimulation of the detector. The contact between the TES legs and ground plane reduces the RF impedance from island to ground and consequently minimizing P_d and P_c. The differential power modes of microstrip seems to be the reason for the large coupling factor. Figure 6.17 shows that the effect has been improved with these modifications, but we still have a good fraction of the deposited power in the island since we still have the current discontinuity between the island and ground plane.

Another way to model the TES island in the CST as gold film with a resistance of 0.074 Ω/square as fabricated, and get the surface current dissipated into that island. The surface current dissipated into the island in CST at each frequency has been extracted to plot the power shown in Figure 6.18. The grey curve also confirmed our theory of getting no dissipated power into the island when we fully covered the ground plane with a full current path between the island and ground plane. We also

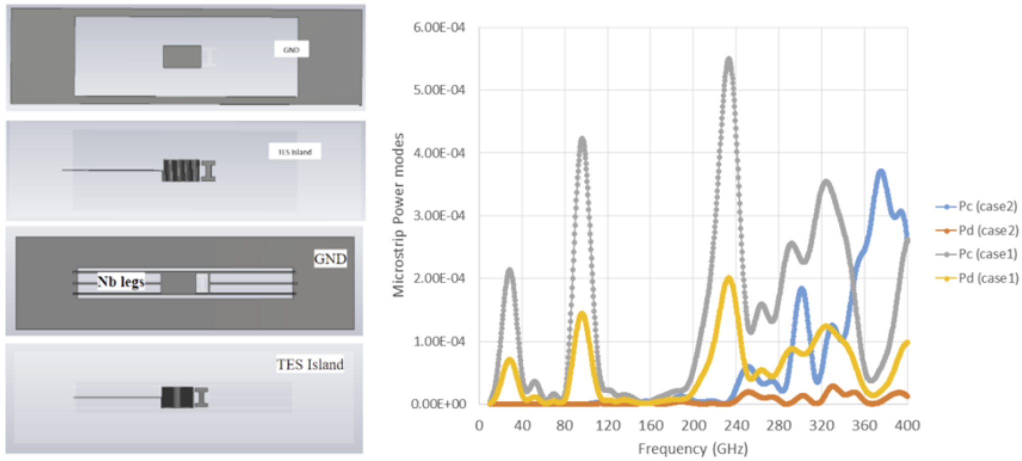

Figure 6.17: The P_d and P_C for two cases. Case (1): the Nb legs are not connected to ground and with a large ground cut-out separation. Case (2): the Nb legs are connected to ground and the separation between the ground and the TES island has been reduced. The differential and common modes power have been reduced with the new modifications.

thought about reducing the back-short to 200 um distance but it does not change the power dissipation. The reason is that the potential between the island and the backshort is very small. However, when we fully covered the TES ground plane, the surface current will go to a smaller level as expected since the potential between the island and TES ground will be very small with no ground-cuts. We tested this idea of a detector with the backshort separation distance = 200 um, known as “MESA Back-short.” We thought that the capacitive coupling between the backshort and TES ground at 200 um is high enough to minimize the DIC but the experimental results confirmed the simulation work shown in Figure 6.18. The measured results show that the mesa backshort with 200 um has a slight effect on direct island coupling, as shown in Figure 6.19. These simulations, where we model finite resistance and voltage gaps between the TES island and surrounding ground plane, are testable hypotheses that have inspired solutions about the importance of TES bolometer re-design. They have resulted in enough progress that there is likely some truth to them, but they may not be the full explanation of direct island coupling. Further tests with various design configurations are still needed to fully characterize that effect.

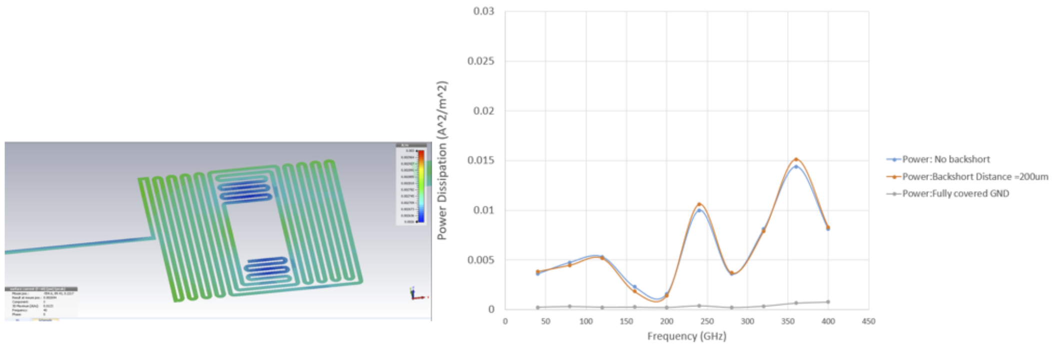

Figure 6.18: The meander TES island in CST software and the resulting response. Left: The resulting simulated surface current. Right: The power dissipated in the island ($P \propto I^2$) versus frequency.

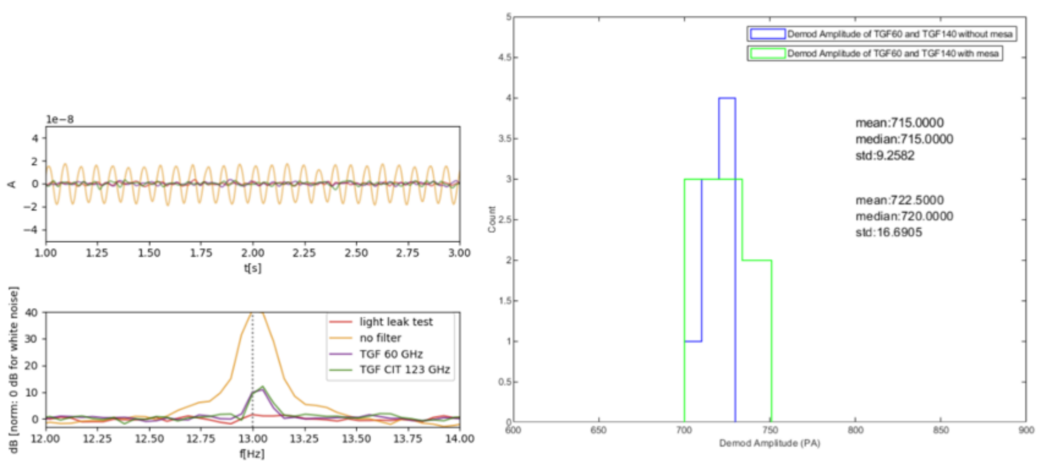

Figure 6.19: The measured detector response with and without MESA back-short. Left: The detector time-streams/PSDs with different cases in the presence of mesa back-short. Right: Histograms of demodulated amplitudes of many detectors with and without mesa back-short distance = 200 um, showing no effect as described by the simulation.

Blue leak diagnostic tests

We preformed a series of tests using combination of high-pass filter (Thick-grill filter (TGF)) and low-pass filter (LPF) with different cut off frequencies to diagnose the leaking bands within the 50 GHz LPE filter that we had at the South Pole. The FTS measurement could not spot the TES island coupling features. The NFBM succeeded to capture these effects. Figure 6.20 shows the measurements setup of our test-bed at Caltech with the NFBM at the top of the cryostat. Two detector tiles have been installed inside the cryostat. One of the detector has the similar LPE that we had during 2020 deployment at the South Pole. A combination of TGF and LPF has been inserted between the chopper source and the aperture of the test-bed. We simulated the TGF in CST with cut-off frequency = 60 GHz. The simulated results over plotted with the measured spectrum of the other LPF, as shown in 6.21. The purpose of these filters is to diagnose the leaking bands within the existing LPE filter that was installed at the module and caused the higher unexpected loading.

The NFBM data has been taken at a certain location where we have a maximum SNR for that module. The filters are located below the chopper cover plate. The chopper frequency was 17 Hz, and the integration time for the data taken was 6 minutes. The following cases were initially explored:

- *Light leak test*: We measured the light leak by putting metal plate in front of the aperture, and measured the TES power to see if we could have any leaking light. The measurements show that we have a very weak light signal.
- *No-filter case*: The data was taken while the chopper aperture was open and there was a free path of photons between the chopper source and the detectors.
- *TGF installed*: We added the TGF between the aperture window and the chopper source to check for any leaking power above 60 GHz.
- *TGF + 3.7icm LPE*
- *TGF + 4icm LPE*
- *TGF + 5icm LPE*
- *TGF + 12icm LPE*

The resulting PSDs show that most of the blue leak comes above 110 GHz. A good fraction of that power comes from between 120-150 GHz and fractionally

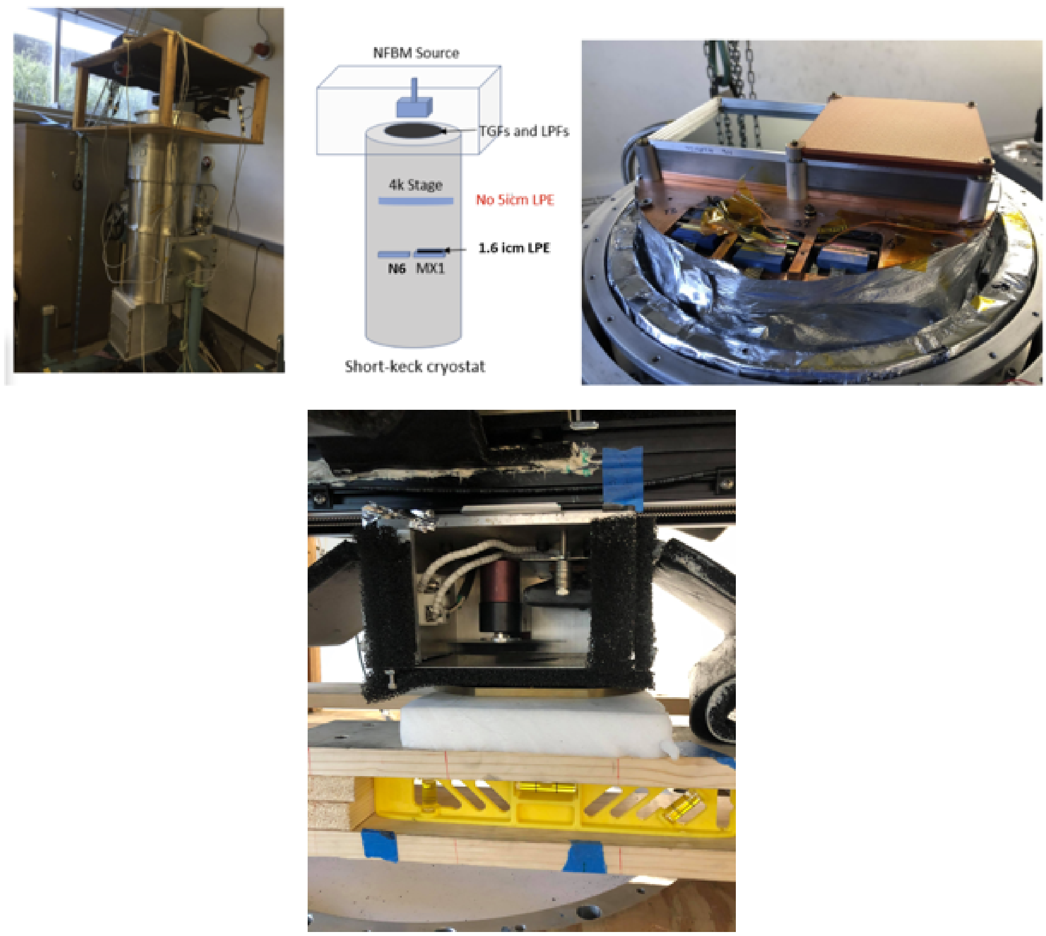

Figure 6.20: The TES island coupling measurement setup. Top/Left: Caltech testbed with NFBM at the top for DIC measurements. Top/Middle: The Cartoon shows the existing filters and the TGF and LPE combination for testing. Top/Right: the two detectors under test, one has the 50 GHz Cardiff Edge Filter on the top. Bottom: Zoom-in photo shows the setup of NFBM source with the filter at the aperture window.

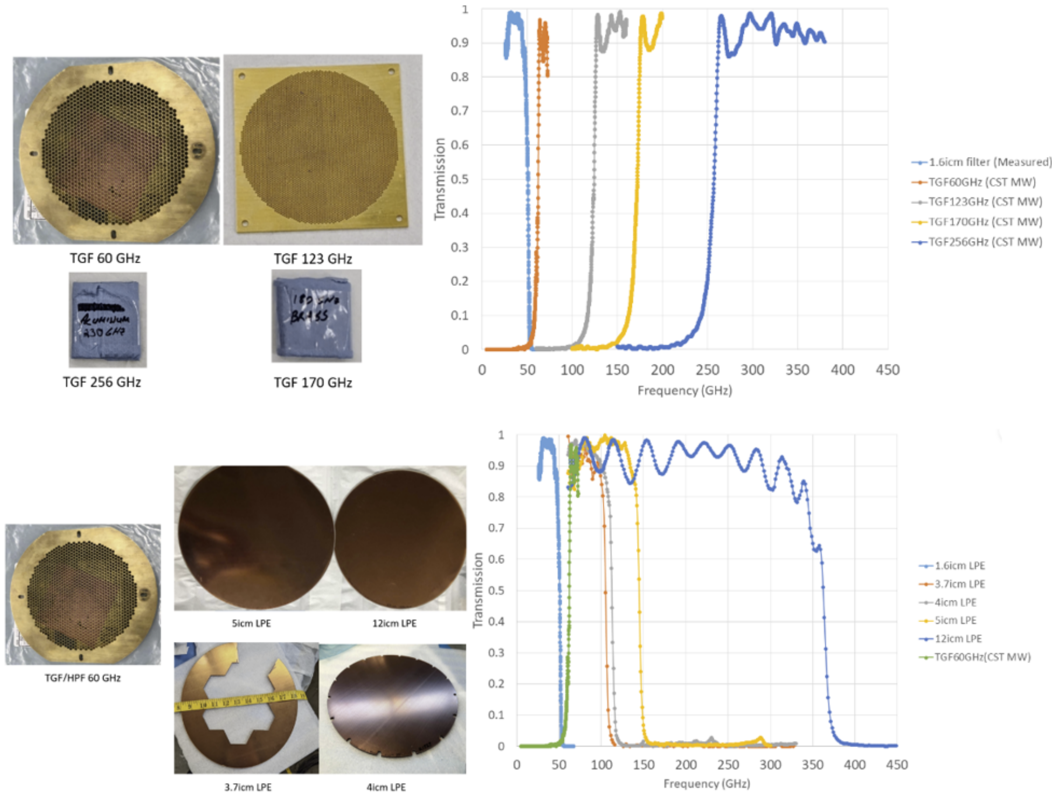

Figure 6.21: The low-pass (LPF) and high-pass (TGF) filters used for the TES island measurements. Left: the real TGF and LPFs. Right: The corresponding simulated and measured spectrum of these filters. We used combination of filters with different cut-off frequencies to determine the leaking bands (Blue leak).

most of the integrated blue leak is above 250 GHz, as shown in Figure 6.22. The TGFs measurements confirmed the same conclusion, as shown in Figure 6.23. Figure 6.24 shows a summary of these observation taking from the demodulated power. Similar tests have been done for 30 GHz detectors and confirmed the same conclusion. i.e. the current mounted 1.6icm (50 GHz) low-pass filter leaked substantially at 110-150 GHz band and above 250 GHz. We suspect that delamination of the filter layers during fabrication may have caused this defect. **The measurements show that the 3.7icm and 4icm LPE filters** clearly eliminate the leaking power, as shown in Figures 6.25, 6.26, 6.27, 6.28, 6.29 and 6.30 for 40 GHz, 30 GHz, and dark detectors, respectively. These measurements concluded the problem and solution. This was our first target to upgrade the BA1 receiver with a better filter configuration (4icm filter) during the 2022 deployment season.

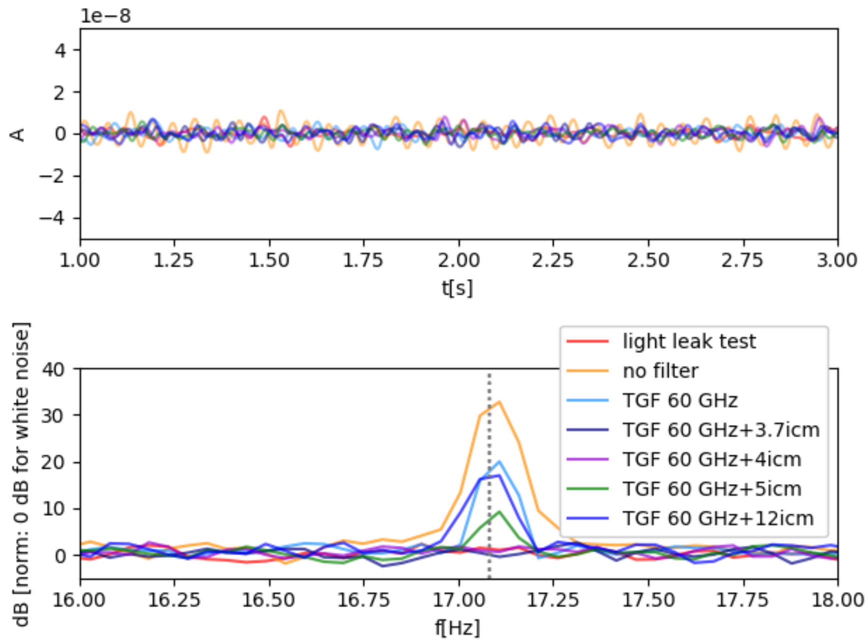

Figure 6.22: High-pass and low-pass filter measurements. This plot shows the time-streams and PSDs, black line is the chopped frequency as measured. Integration time is 6 min.

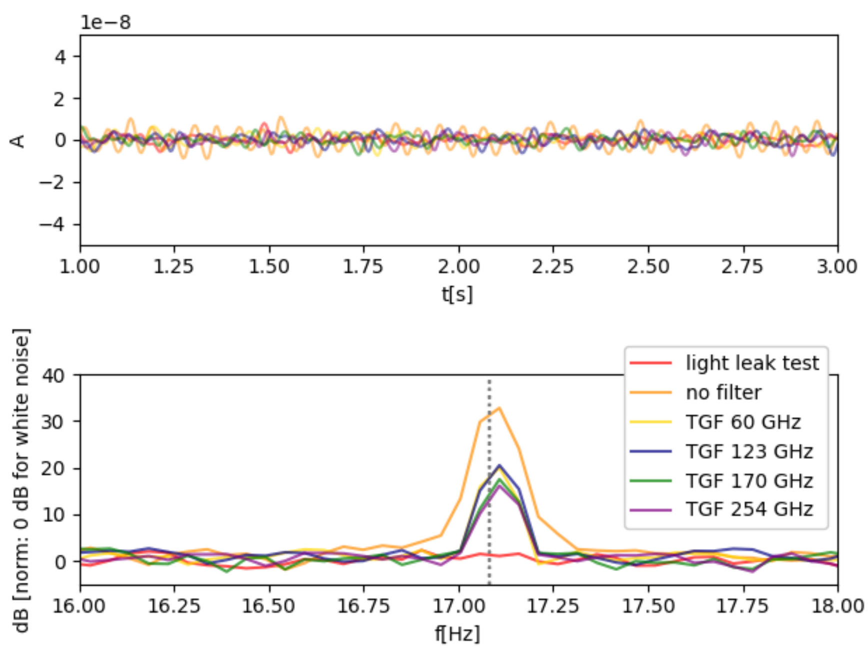

Figure 6.23: High-pass filter measurements. This plot shows the time-streams and PSDs, black line is the chopped frequency as measured. Integration time is 6 min.

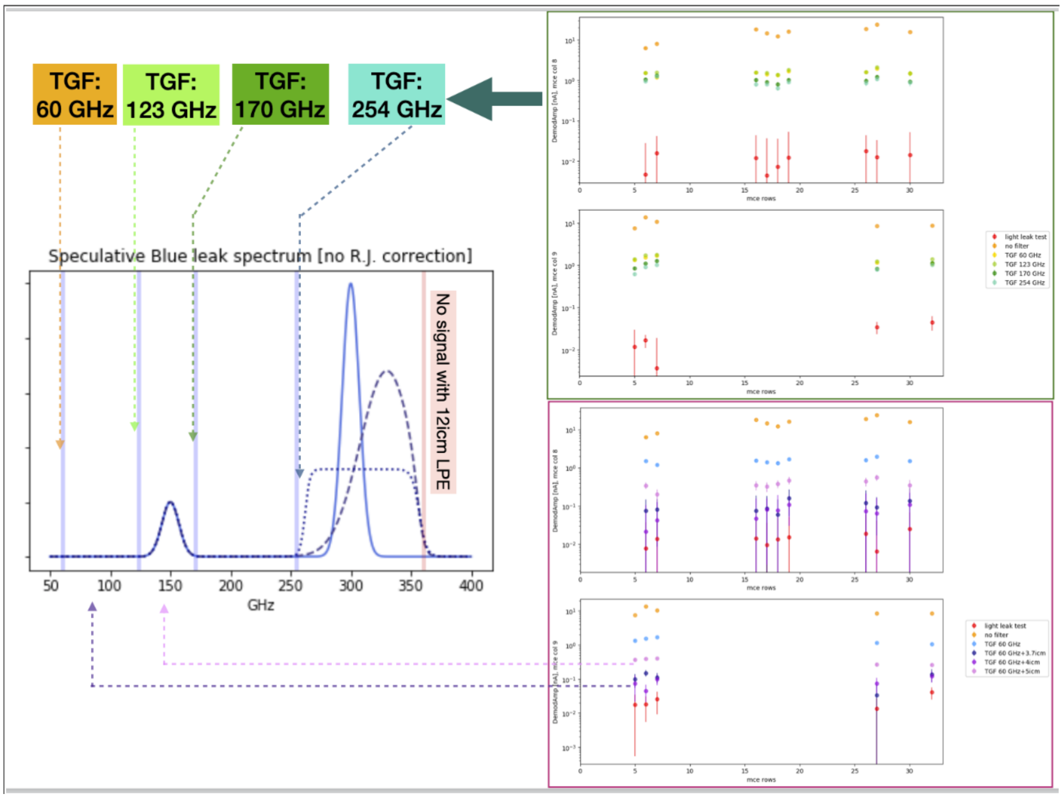

Figure 6.24: The spectral profile summary shows that the installed low-pass filter (Figure 6.13) during the 2020 season has two leaking bands into our measurement at 30/40 GHz, which was the reason for the receiver's sensitivity degradation during 2020 season.

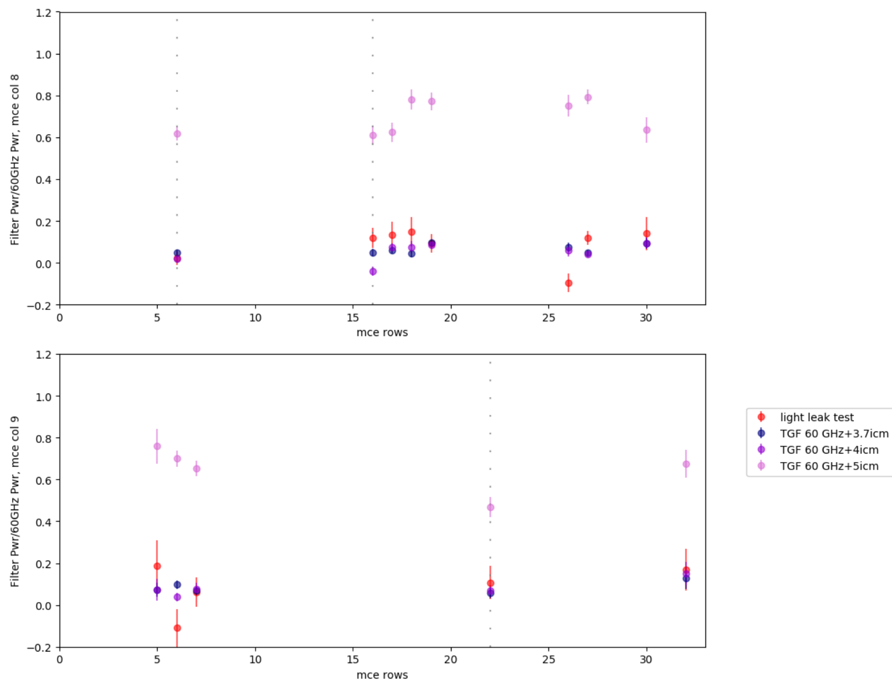

Figure 6.25: The demodulated power for 40 GHz detector DIC measurement at Caltech to determine the solution for the leaking power.

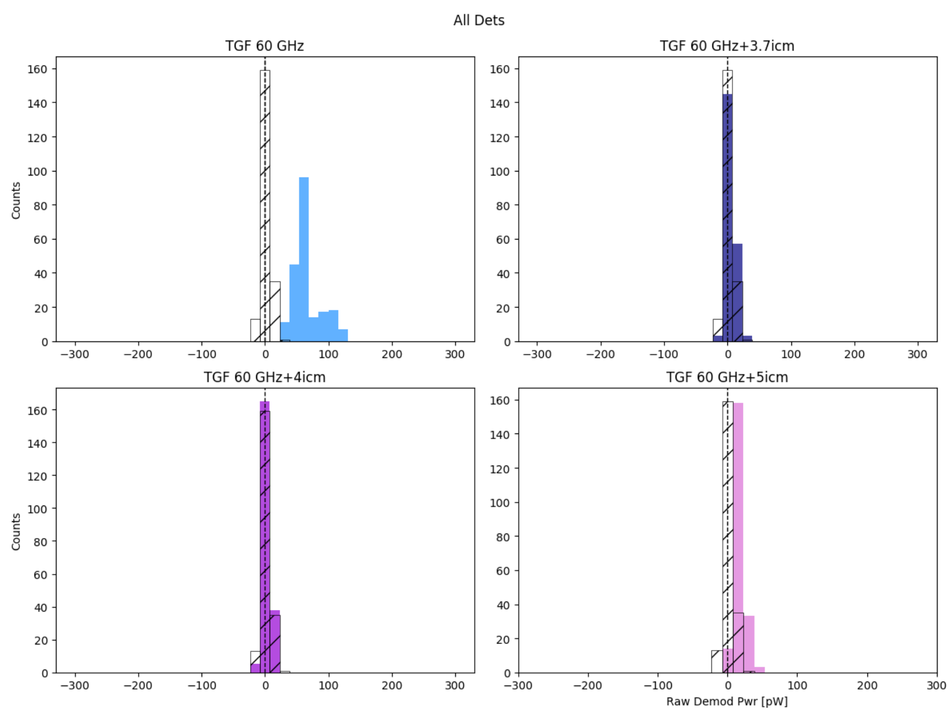

Figure 6.26: Histogram of the demodulated values for 40 GHz detector. We need to install a new 4icm filter to eliminate the leaking power.

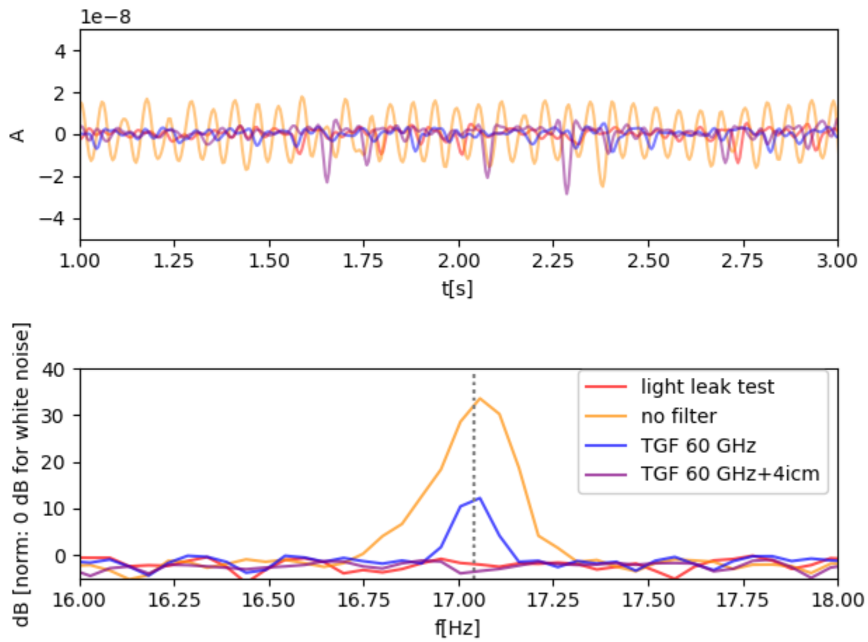

Figure 6.27: The timestreams/PSDs for 30 GHz detector DIC measurement at Caltech to determine the solution for the leaking power.

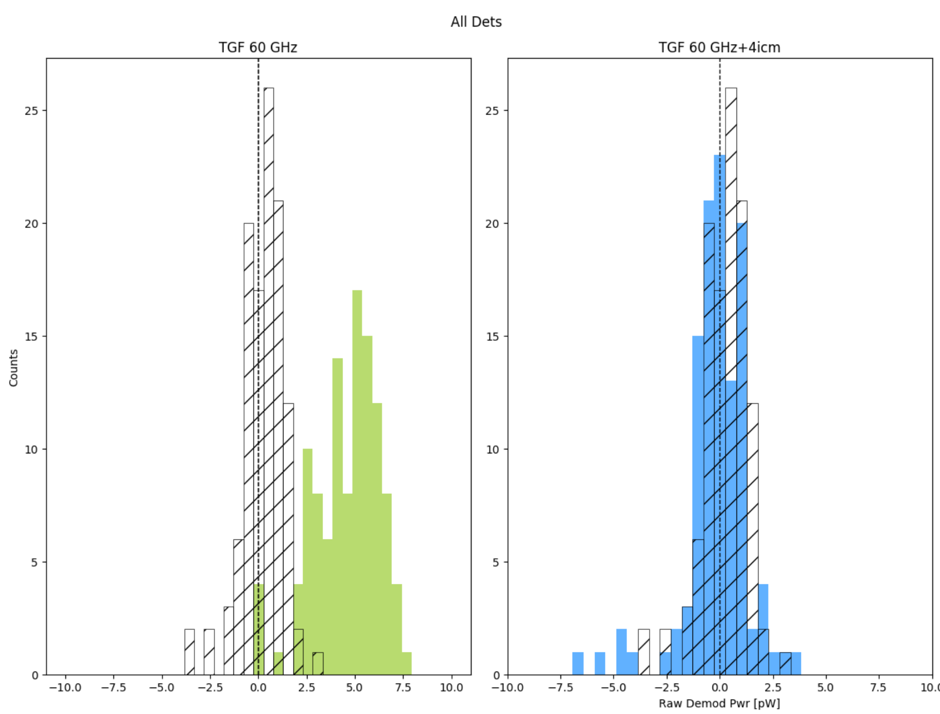

Figure 6.28: Histogram of the demodulated values for 30 GHz detector. The 4icm filter eliminates the leaking power.

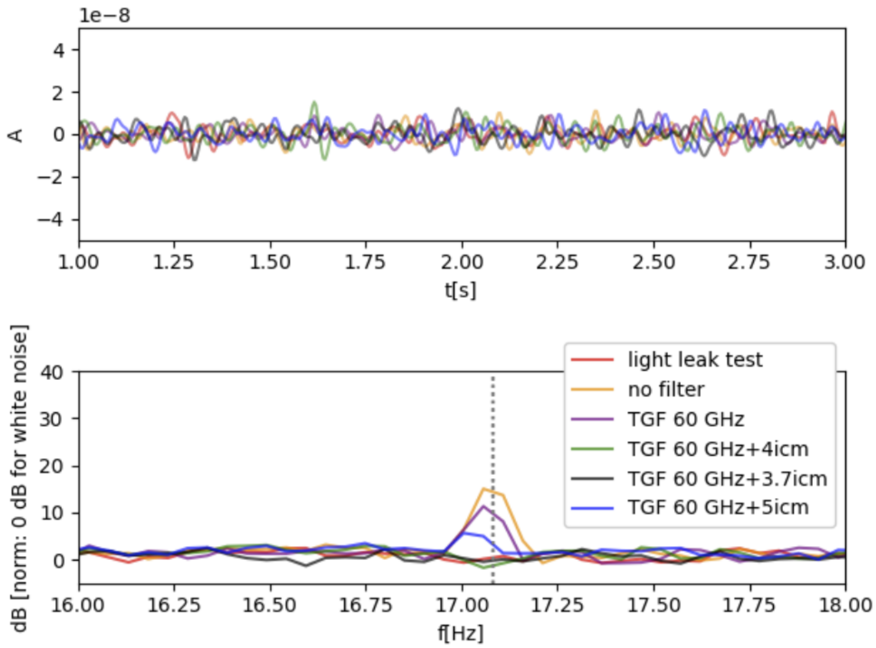

Figure 6.29: The timestreams/PSDs for dark detector DIC measurement at Caltech to determine the solution for the leaking power.

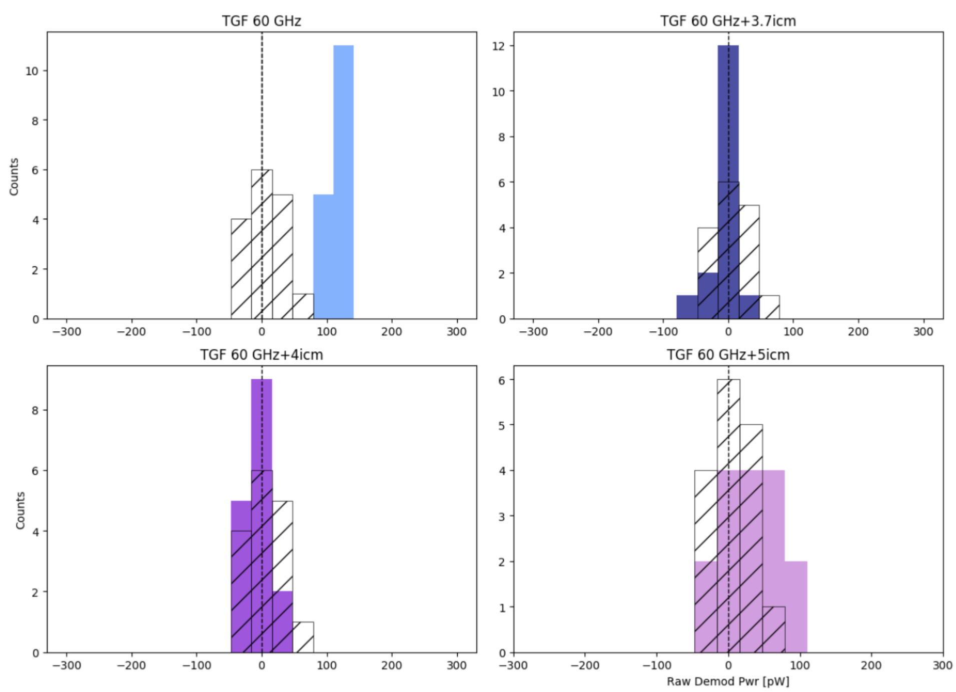

Figure 6.30: Histogram of the demodulated values for dark detector. The demodulated power shows that the out-band leakage has reduced to the noise level by using that filter.

6.4 2020 vs 2022 Seasons: Blue Leak reduction

The previous diagnostic tests and analytical studies concluded that BA1 needs an additional filter configuration to improve the BA1 loading by eliminating the out-band photons. In the 2022 season (Soliman, Ade, et al. (BICEP/Keck Collaboration), 2022), we installed a new additional 4icm (cut-off frequency = 120 GHz) along with the nominal low pass edge (cut-off frequency = 60 GHz) filter at the top of the focal plane camera to eliminate this Blue leak, as shown in Figure 6.31. We preformed the DIC measurement after we installed the new filter. The DIC measurements for 40 GHz module shows that the 4icm has eliminated the out-band power above 60 GHz, as shown in Figures 6.33 and 6.34. Additionally, The measured beam profile also shows a significant reduction in the dark pickup (Blue leak) after this upgrade for a dark detector which was common between both deployment seasons, as shown in Figure 6.35. The out- band dark loading is substantially reduced (by a factor of four) as shown in the histogram of Figure 6.36. Figure 6.37 shows that the beam profile of the 30 GHz detector slightly changes due to the presence of the new filter and the 40 GHz detector beam profile remains the same between both seasons. The first challenge of the 2022 season has been resolved by the new filter configuration that minimizes the total dark loading, resulting in a huge improvement in the total loading (Q_{total}) and NET compared to the 2020 season. The total loading Q_{total} of 30 GHz detector has been reduced by a factor of 3. The Q/U map noise has been significantly reduced from 153 uK arcmin to 56 uK arcmin for 30 GHz detector with the out-band power reduction. The total loading Q_{total} of 40 GHz detector has been also decreased to the designed value shown in Chapter 3. The filter upgrade enhances the mapping speed of BA1 detectors, especially for the 40 GHz detector. The resulting total sensitivity is improved from 73 nK to 28 nK for 30 GHz detectors and from 18 nK to 11 nK for 40 GHz detectors after the added modifications between 2020 and 2022 seasons.

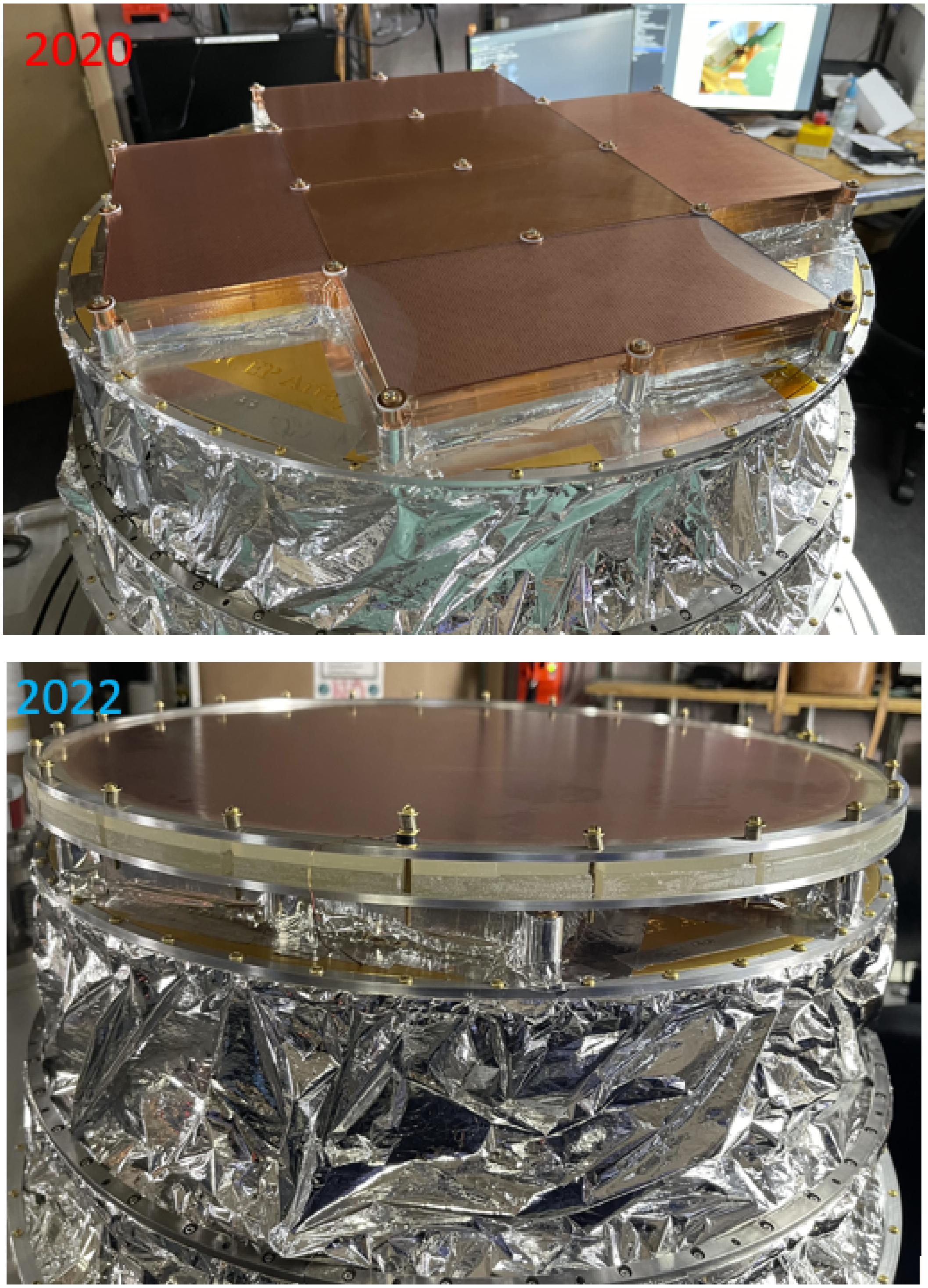

Figure 6.31: The low-pass filter configurations in 2020 versus 2022 deployment seasons. Top: An individual 1.6icm filter covers each module during 2020. This photo shows the sign of filter's delamination around the edges. Bottom: a stack of 1.6icm and 4icm together during the 2022 deployment season. The additional 4icm is for eliminating the out-band high-frequency leaking power that described earlier.

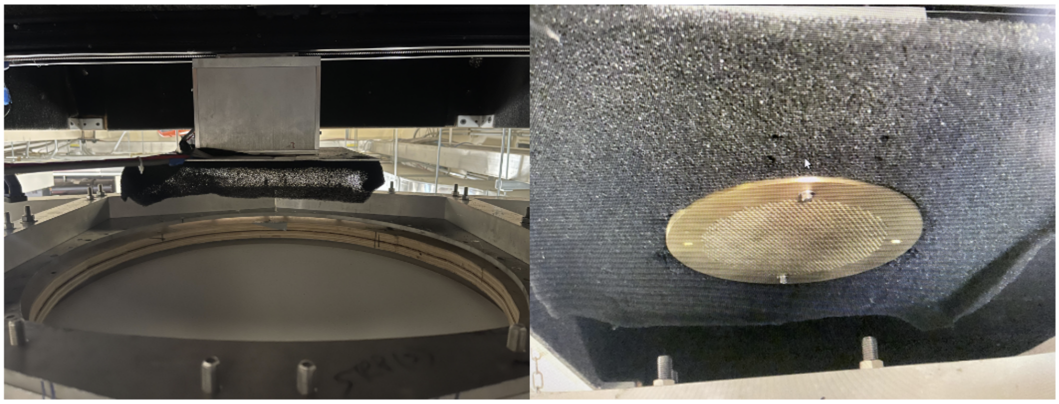

Figure 6.32: BA1 DIC measurement at the South Pole after we upgraded the receiver with the new 4icm filter during 2022 season, showing the TGF at 60 GHz attached to the NFBM source above the aperture.

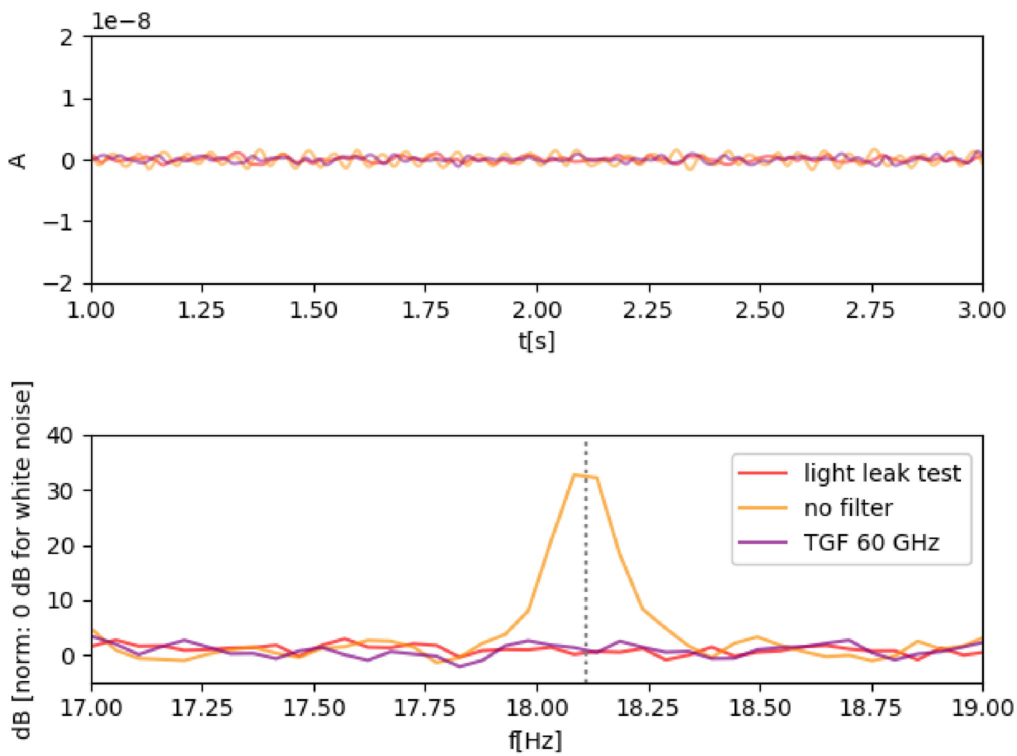

Figure 6.33: The timestreams and PSD for 40 GHz module, showing the successful elimination of the out-band photons with upgrades.

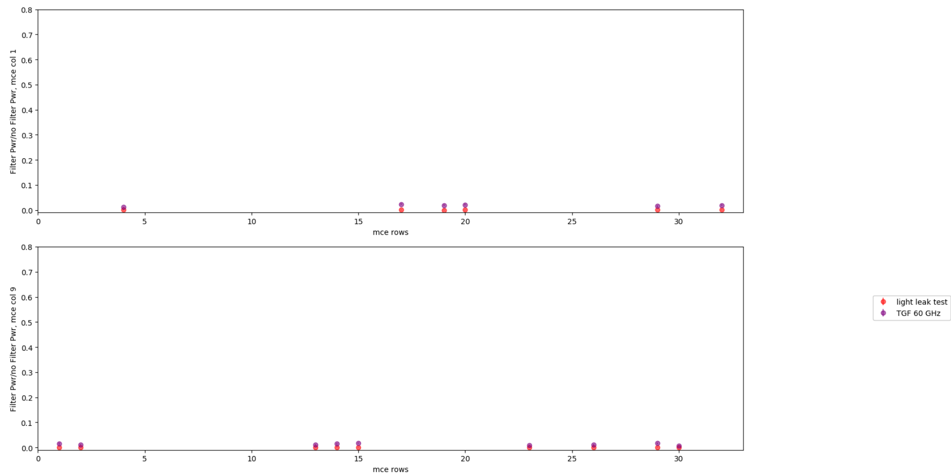

Figure 6.34: The demodulated power of the DIC measurement shows the residuals out-band photons are comparable to the noise level.

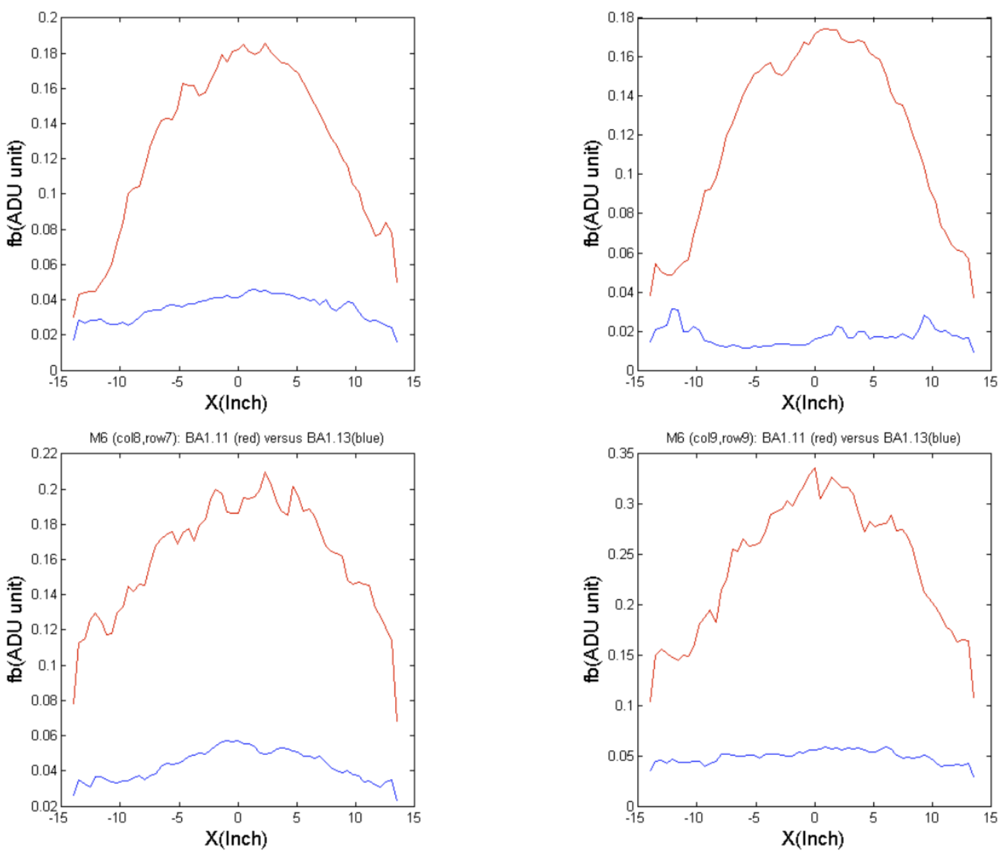

Figure 6.35: The dark detectors beam response (2020/red versus 2022/blue), vertical axis is in ADU unit, and horizontal axis is the full FPU aperture in inches. We observe a negligible in-band response that is comparable to the noise level.

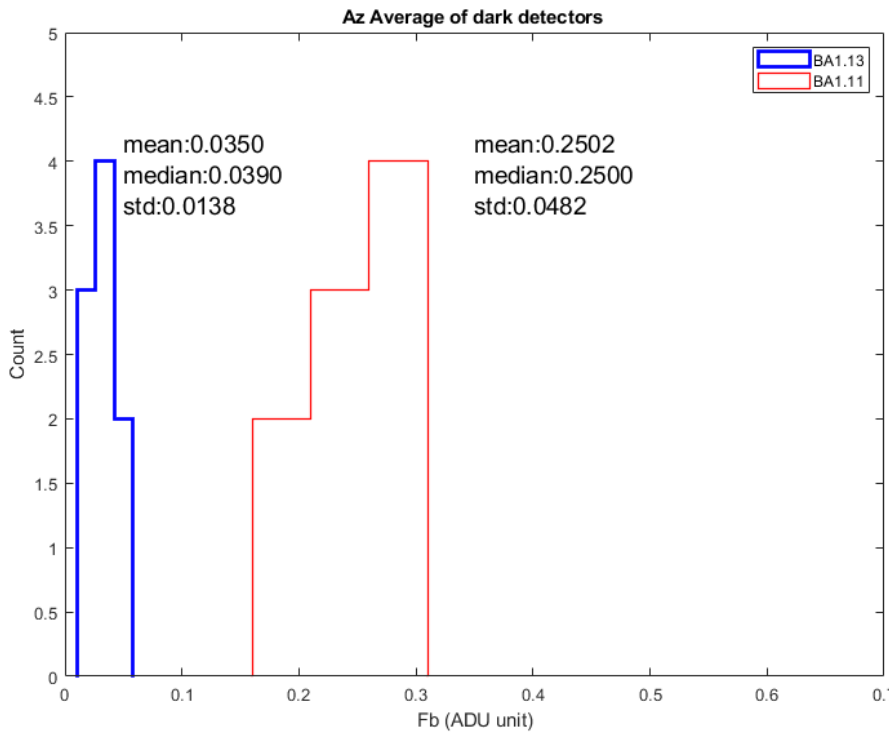

Figure 6.36: Histogram of dark detectors reduction for BA1.11 (2020 season) versus BA1.13 (2022 season). The additional filter largely eliminates the direct stimulation.

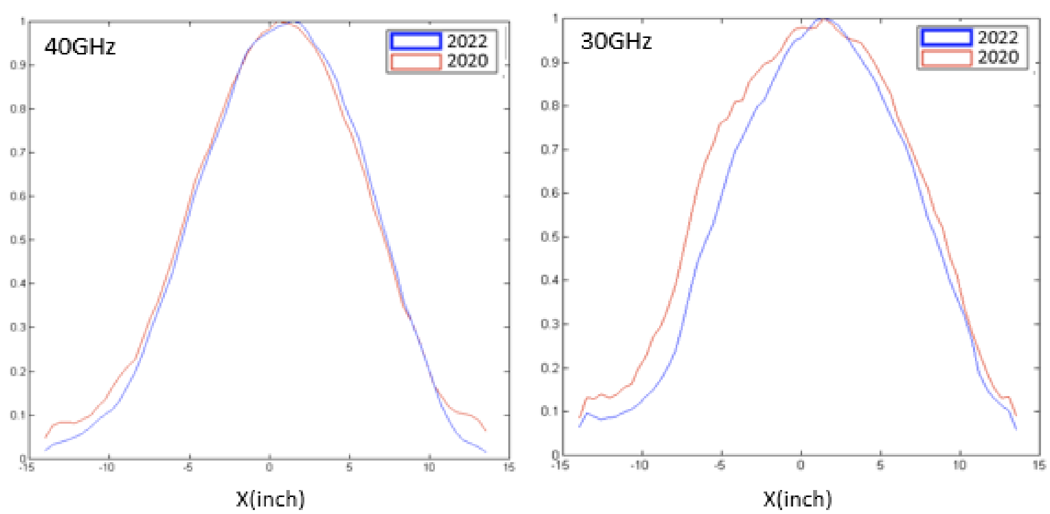

Figure 6.37: The beam profiles of 2020 season versus 2022 season after the 4icm LPE upgrade. Left: 40 GHz detector. Right: 30 GHz detector.

6.5 2023 Deployment Season

The second and third points on the 2020 challenges list have been addressed in the current season. The low-yield dual band tiles have been replaced with a better performing detector tiles. Our team at MDL/JPL has fabricated new two 40 GHz tiles (M10 and M11). These two tiles has been tested at Caltech's test-bed before deploying to the South Pole. The measured dP/dT has ≈ 50% for the light detectors at Caltech, and ≈ 42% inside BICEP Array receiver at the South Pole. The new modules show increased optical efficiency compared to the nominal detector tiles by using the inverted TES fabrication process, as shown in Figures 6.38 and 6.39. Given the optical parameters and assuming some dark parameters for these detector tiles, the basic calculations show that we expect to highly improve the NET with these 2023 upgrades. The data is currently analyzed.

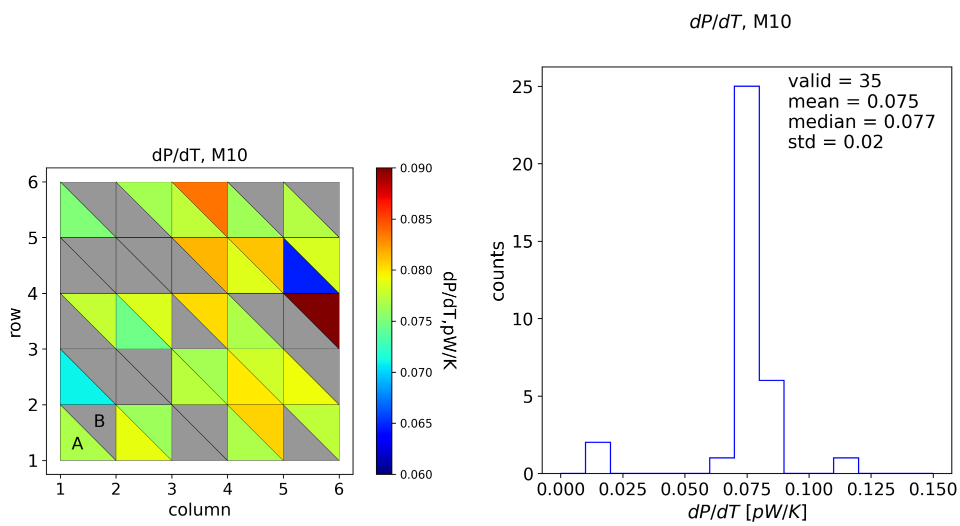

(a) (b)

Figure 6.38: The new 40 GHz tile (M10). Left: the measured OE in a rectangular detector tile physical coordinates. Right: The histogram of OE.

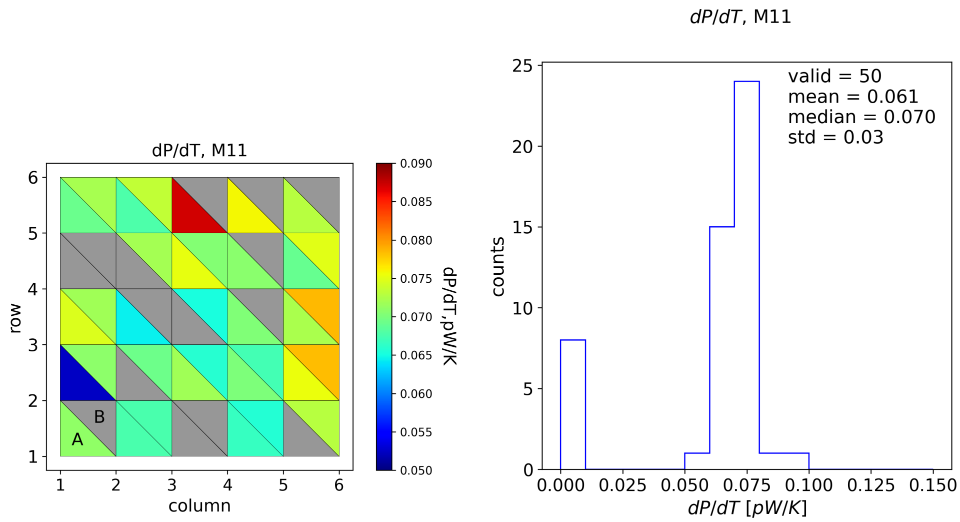

(a) (b)

Figure 6.39: The new 40 GHz tile (M11). Left: the measured OE in a rectangular detector tile physical coordinates. Right: The histogram of OE.

Inverted TES process

The measured TES normal resistance R_n of the BA1 detectors is higher than expected and has a radial distribution pattern across the tile (Zhang, 2023). The 6" fabrication process that mostly traced the old 4" process has resulted higher values of R_n in a way that is not yet fully understood. The previous BICEP/Keck experiments measured the normal resistance to be around 70-100 mΩ. A new "Inverted TES" fabrication process has been developed to improve the wafer reliability and consequently improving the uniformity of R_n across the tile. Figure 6.40 shows layers putting arrangements from the top to the bottom, as the arrow pointed down. The Ti-TES layer has been putting down first before the Al-TES layer. This process has been initially tested for the 150 GHz detector in BA2. The results show a better uniform R_n gradient from the center to the edge. Additionally, this process has been used for the fabrication of two new 40 GHz modules M10 and M11 that have been deployed this season to the South Pole. The resulting R_n for both modules have significantly reduced to the designed values (70-100 mΩ) and became more uniform across the tile than the other 40 GHz modules during the 2020 deployment season (previously $\approx$ 200 mΩ), as shown in Figures 6.41 and 6.42. Figure 6.43 shows that the measured load curve looks much uniform and stable. The new process has fortunately proved its higher performance with the 150 GHz and 40 GHz tiles to manage the normal resistance within the proposed values, resulting to a lower magnetic susceptibility compared to the previous tiles.

Layer	LO/EB
Ti-TES	EB
Al-TES	LO
Al-Plug	LO
GP (Nb)	LO
ILD (SiO2) / Via	EB
Resistor (Au)	LO
Res. Pro. (SiO)	LO
MS (Nb)	EB
FSN	EB
Heat Cap. (Pd+Au)	LO
Singulation	/
XeF2	EB

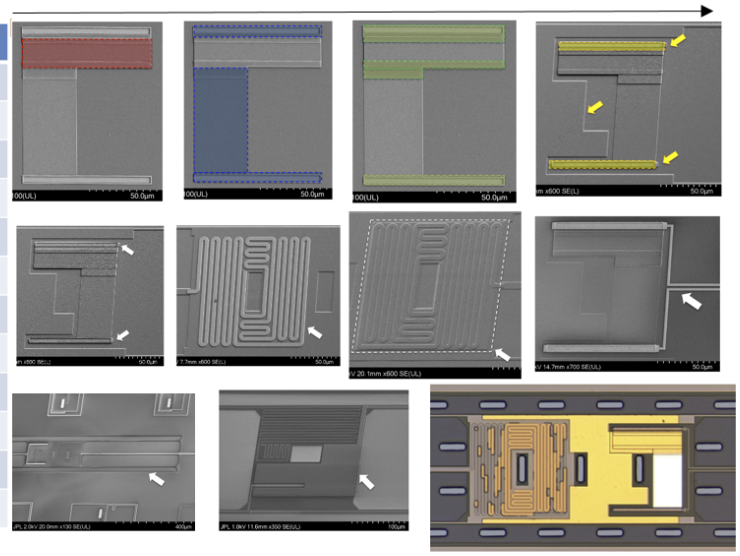

Figure 6.40: The fabrication process steps in the “Inverted TES” process as the arrow pointed down. The arrow direction points to the deposition layers flow for this TES process. Plots by our fabrication team at the MDL/JPL.

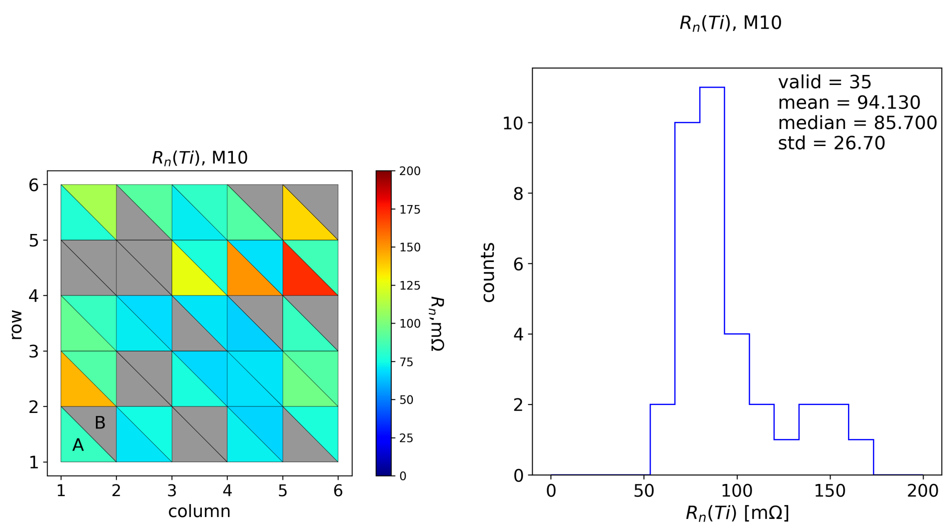

(a) (b)

Figure 6.41: The measured R_n for the 40 GHz module M10 using the “Inverted TES” process. Left: Rectangular plot in the tile physical coordinates. Right: Histogram. The median R_n has been reduced to the proposed values (70-100 mΩ) using this new process compared to the values in the 2020 season.

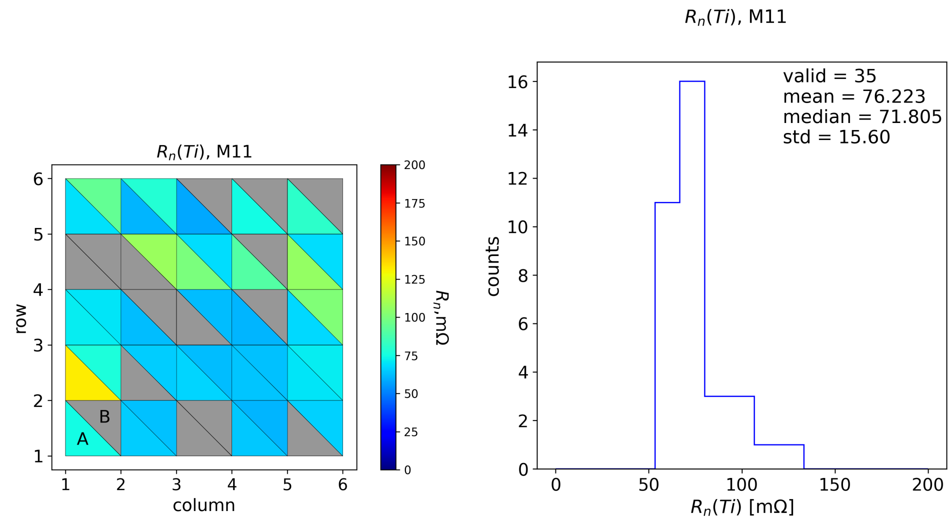

(a) (b)

Figure 6.42: The measured R_n for the 40 GHz module M11 using the "Inverted TES" process. Left: Rectangular plot in the tile physical coordinates. Right: Histogram. The median R_n has been reduced to the proposed values (70-100 mΩ) using this new process compared to the values in the 2020 season (previously 200 mΩ).

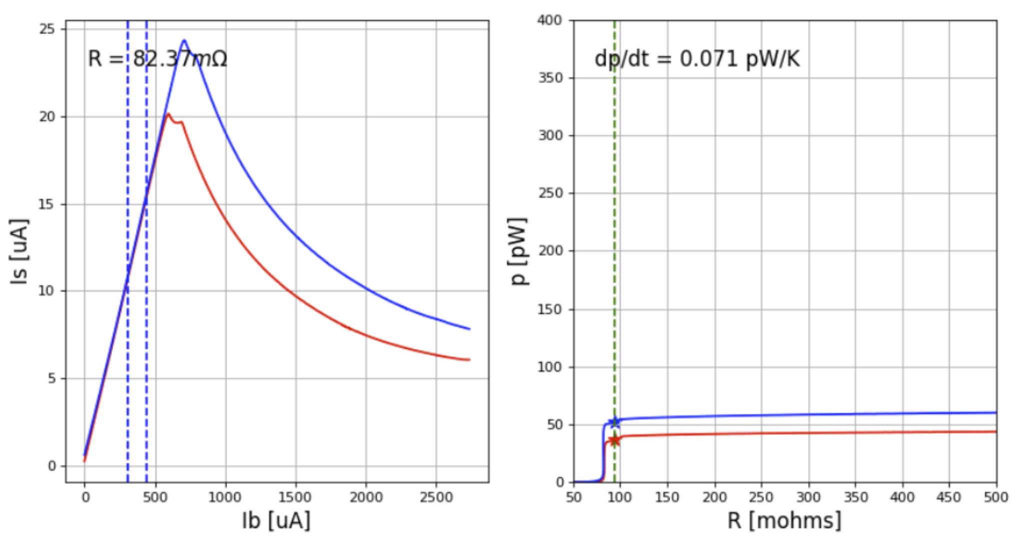

Figure 6.43: The measured I-V curve for one detector within the detector tile M10.

Chapter 7

MULTI-COLOR DETECTOR FOR CMB SENSITIVITY IMPROVEMENT

7.1 Motivation for Multi-color Detectors Technology

The sensitivity of the focal plane significantly drives the advancement of CMB polarization measurements. The sensitivity could be improved through different ways. One ways is to control the beam systematic errors as I described in Chapter 4. Another way is to minimize the internal noise of the TES bolometers by operating the detectors at lower base temperature (100 mK) as I will present in Chapter 8. The third way is to increase the number of detectors by expanding the focal plane as happened with BICEP3 (stage 3) compared to Keck Array (stage 2), resulting in at least 10× optical throughput improvement. The fourth way is to increase the optical throughput of each pixel by expanding their bandwidth to observe two CMB bands simultaneously (O'Brient, 2010). Chapter 3 introduced the design of dual-color Bowtie-array at 30/40 GHz BICEP Array receiver. Additionally, the diplexer circuits partitions that broad-band width of the Bowtie-array into two CMB observing channels before terminating each at the bolometers. The 30/40 GHz detector module contains more detector pair than the individual 30 GHz or 40 GHz detector module, resulting more detector counts per module, which are needed for constraining polarized galactic foregrounds. The simulated bands of the Bowtie-array and filters are shown in Figure 3.16. This chapter reports the demonstration of this promising technology for the current deployed 30/40 GHz module (Mx2) inside BICEP Array telescope for measuring synchrotron foreground at the South Pole. This chapter also addresses the engineering challenges to extend this dual-color technology as well as introduces a new diplexer technology for 90/150 GHz CMB observation bands.

7.2 Demonstration of 30/40 GHz Detector Module

The 30/40 GHz detector module has been fabricated and tested at Caltech and the South Pole. The measured optical response demonstrated this technology for synchrotron emission at 30/40 GHz, as shown below.

Spectral response

The end-to-end detector spectral response $S(v)$ has been measured using the Fourier Transform Spectrometer (FTS). The measured spectra of the dual-band detector has demonstrated this technology for covering two CMB observation bands, centered at 30 GHz and 40 GHz simultaneously, as shown in Figure 7.1. This measurements indeed avoid the atmospheric features at 60 GHz and validated the modelled response shown in Figure 3.16. The band center could be defined a function of the spectral response as

$$\langle v \rangle = \int vS(v)dv \tag{7.1}$$

and the bandwidth ΔV as

$$\Delta v = \frac{(\int S(v)dv)^2}{\int S^2(v)dv}. \tag{7.2}$$

Figure 7.1 shows that the band center of each band has been shifted up by 2-3 GHz. We thought the reason might be the wave speed inside the dielectric materials that possibly shift the band center of the current diplexer. Additionally, The measured spectra shows non-negligible interaction between the 30 GHz and 40 GHz bands, unlike the measured single-band spectra (Zhang, 2023). A new diplexer has been designed with sharper edges and minimized interaction between both bands, shown in Figure 3.13. This new diplxer was a series of two 25% fractional bandwidth that we used for single band 30 GHz and 40 GHz. But, the ripple size was 0.5 dB for much sharper band edges (BICEP uses ripple size of 0.1 dB). The resulting spectra of that diplexer was narrower (low OE) and with some in-band reflection than the first diplexer design. We swapped these low-OE dual-band tiles with better performing detector tiles during the 2023 deployment season. However, the dual-color with the first diplexer design is currently performing with high sensitivity toward synchrotron inside BICEP Array at the South Pole.

Near-field beam map

The NFBM has been characterized for the dual-color detector inside BICEP Array receiver using similar measurements shown in Section 5.3. The resulting beams matched our optical design shown in Table 2.2. The measured far-field beamwidth are 0.48° 0.437° for 30 GHz and 40 GHz bands, respectively.

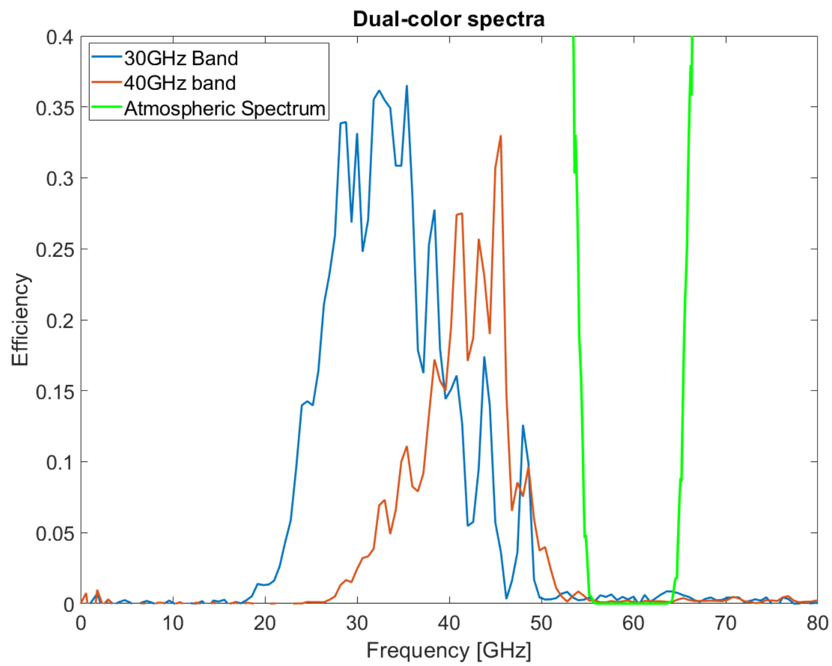

Figure 7.1: The measured end-to-end spectral response of 30/40 GHz detector module with the initial diplexer design. The results show the upper and lower bands. This detector module is currently taken CMB data at the South Pole.

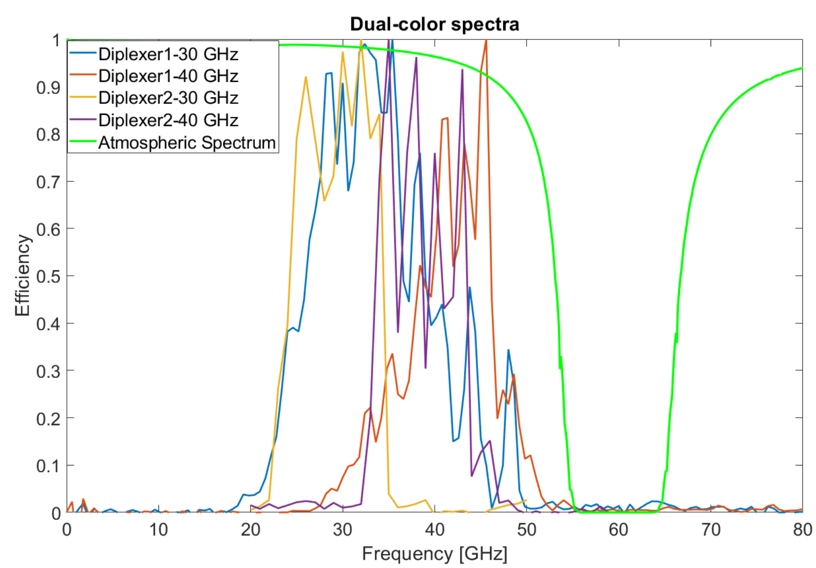

Figure 7.2: The measured normalized end-to-end spectral response of 30/40 GHz detector of two diplexer designs. The second diplexer indeed minimized the interaction between both bands but the bands became narrower (low OE).

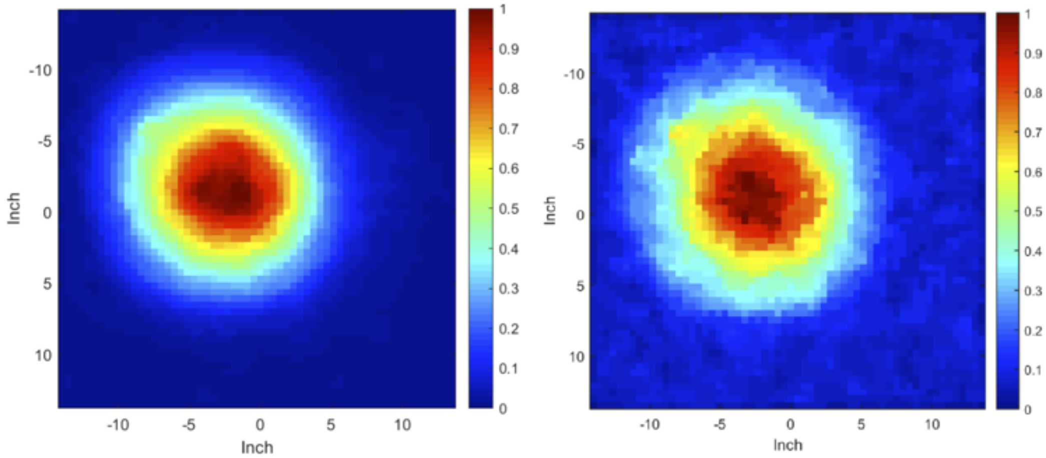

Figure 7.3: The measured near-field beam maps inside the 30/40 GHz BICEP Array receiver. Left: 40 GHz band, and Right: 30 GHz band.

CMB temperature map

The preliminary co-added CMB temperature map has been plotted for the dual-color detector, the upper and low bands at the South Pole. These maps have been obtained from the observation of few thousand scansets, each has about 50 minutes. These are the initial maps from the first two seasons to demonstrate the dual-band detectors technology. Further CMB maps are currently produced with better map depth from the 2023 season.

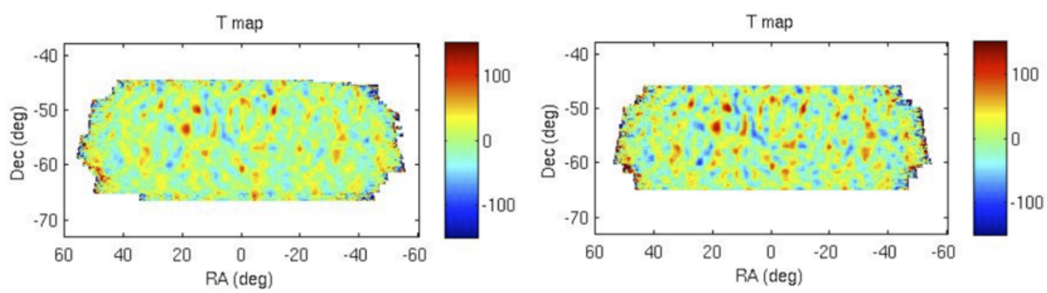

Figure 7.4: The on-sky performance at the South Pole. The preliminary CMB temperature maps for 30/40 GHz dual-color detector. Left: 30 GHz band, and Right: 40 GHz band.

7.3 Dual-color Detector for CMB Observation Bands 90/150 GHz

The dual-color technology has been optimized for mapping the CMB over higher frequency channels, 90/150 GHz for dust emission detection. The dual-color 30/40 GHz design can not be scaled directly to cover the 90 GHz and 150 GHz CMB observing bands. The scaled tight separation between the Bowtie antennas does not fit the routing feed lines, as shown in Figure 7.5. The bandwidth of Bowtie-array is significantly depending on that separation for covering broad spectrum. This section studied the design parameters to optimize the dual-color detector to map the sky over 90/150 GHz.

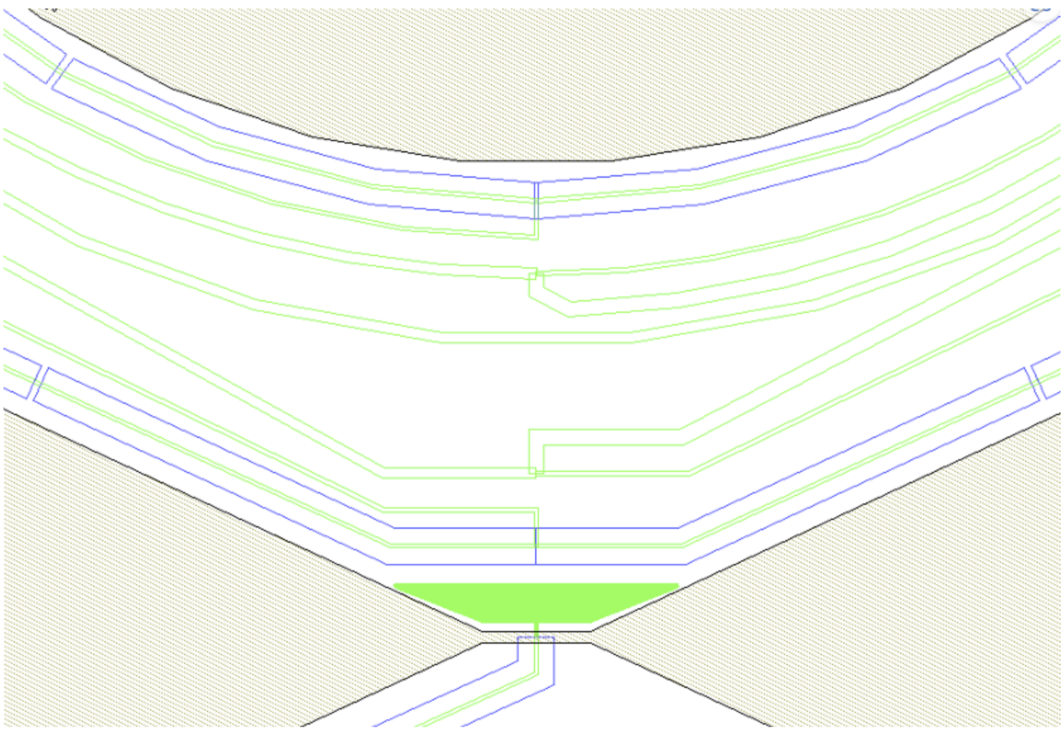

Figure 7.5: Snapshot from the 30/40 GHz layout mask showing the tight part of the summing tree between two adjacent Bowtie antennas. The scaled separation is not sufficient to contain the routing feed lines at 90/150 GHz and will introduce unwanted coupling and cross talk.

Phased-array design optimization

The design parameters of dual-color 90/150 GHz have been studies in the HFSS simulation including the dielectric substrates. The distance “D” between the Bowtie has been optimized for a minimized interaction between the adjacent feed network transmission lines to be 50 um. The final Bowtie-array configuration is shown in Figure 7.6. The feed network has been designed to match the real and imaginary impedance shown in Figure 7.7 using similar methods explained in Chapter 3. The silicon thickness has been optimized for $\frac{\lambda_g}{4}$ to avoid the undesired in-band reflections, as shown in Figure 7.8. The resulting efficiency is shown in the black curve of Figure 7.15.

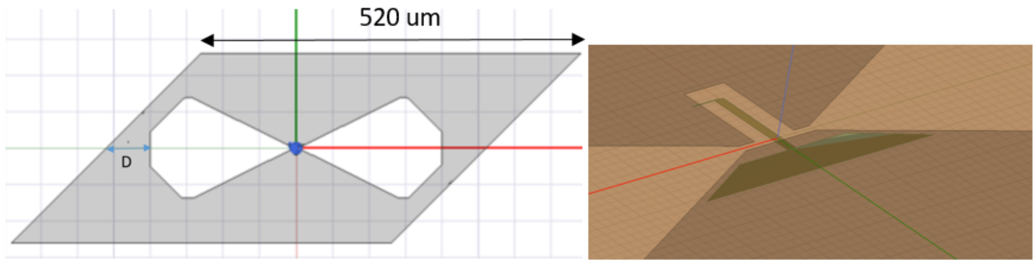

Figure 7.6: The HFSS unit cell for 90/150 GHz. Left: The modified optimized Bowtie-Array. Right: the feed network for a maximum power transfer. The capacitor has trapezoidal shape with dimensions of 26.2um × 12.2um × 3.6um.

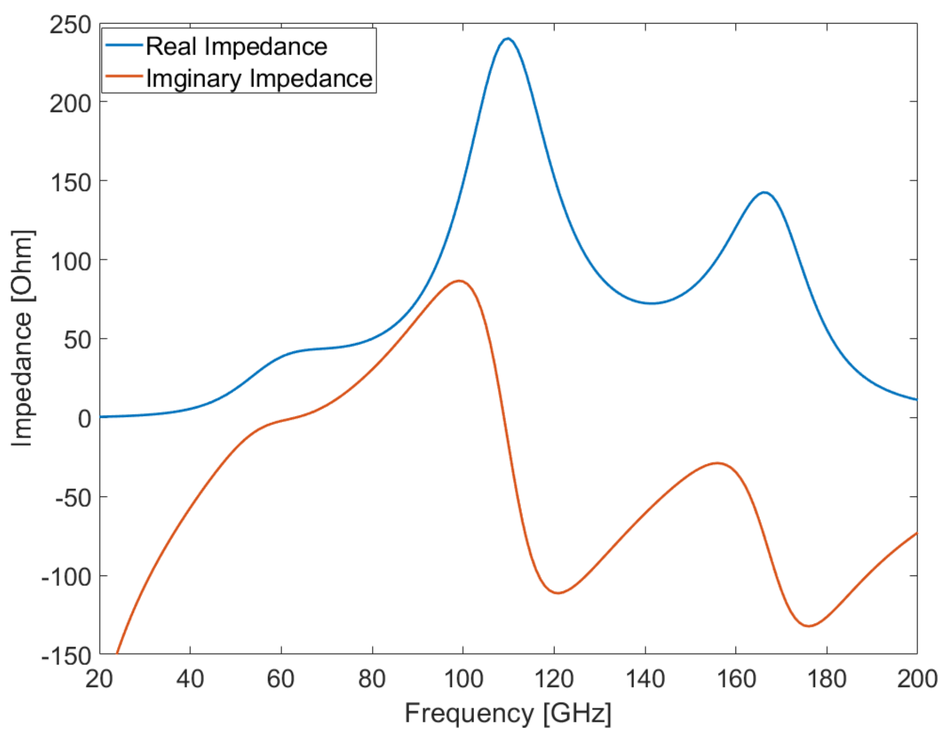

Figure 7.7: The resulting real and imaginary impedance of 90/150 GHz dual-color detector.

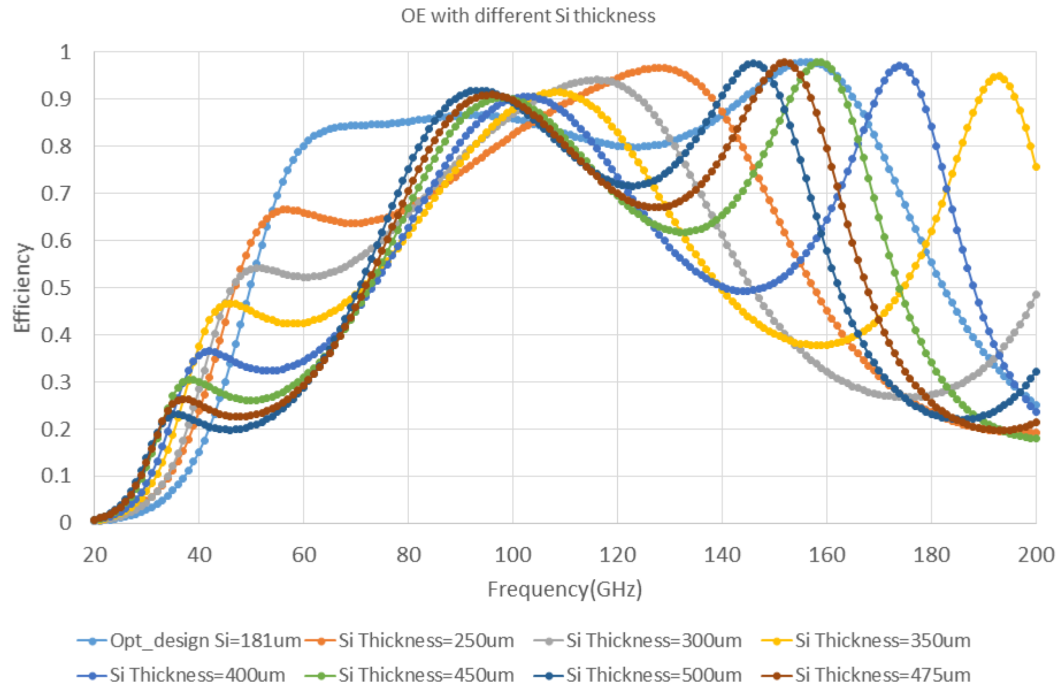

Figure 7.8: The simulated Optical Efficiency as a function of various silicon thickness. The original value is $\frac{\lambda_g}{4}$ = 181 um. The undesired substrate modes start to appear with increasing the silicon thickness and cause in-band reflections.

Diplexer circuit

The diplexer divide the broad-band bowtie spectrum into two CMB observing bands. the low-band in the diplexer design has a band center of 95 GHz with 22.8 GHz bandwidth, with lower band edge of 83.6 GHz and upper band edge of 106.4 GHz. The high-band in the diplexer design has a band center of 155 GHz with 44 GHz bandwidth, with lower band edge of 138 GHz and upper band edge of 172.1 GHz. The ripple size is 0.1 dB. The equivalent lumped elements are shown in figure 7.9. The resulting S_{11} in AWR microwave studio are below -10 dB within our band of interest. The diplexer has been designed using similar procedures shown in Section 3.3, but we used the Π circuit transformation network instead of T circuit transformation network to avoid the tuned resonant sections (O'Brient, 2010). We solve the following equations to extract the lumped element values for the circuit transformation.

$$C_A = \frac{C_{AB}C_{AC} + C_{AB}C_{BC} + C_{AC}C_{BC}}{C_{BC}} \tag{7.3}$$

$$C_B = \frac{C_{AB}C_{AC} + C_{AB}C_{BC} + C_{AC}C_{BC}}{C_{AC}}, \tag{7.4}$$

$$C_C = \frac{C_{AB}C_{AC} + C_{AB}C_{BC} + C_{AC}C_{BC}}{C_{AB}}. \tag{7.5}$$

Our studies show that Π circuit network is less sensitive to small changes on the diplexer parameters, as shown in Figures 7.12 and 7.13. The most obnoxious component to design is the series capacitor because it has parasitic series inductance from the holes in the ground plane. In practice, we compensate these parasitic by reducing the other inductors, thus providing the desired resonance. We optimized the diplexer section by section as shown in Figure 7.11 before we collect the full circuits shown in Figure 7.14. We slightly tuned the parameters for the optimized response. This improved technology will be used for the first time in BICEP telescope. The success of these technology strategies will be fed into the upcoming CMB-S4 90/150 GHz small-aperture telescopes (PSAT) in BICEP Array. Figure 7.15 shows the final simulated results of the Bowtie-array and the diplexer. We plan to fabricate this dual-color detector at MDL/JPL soon.

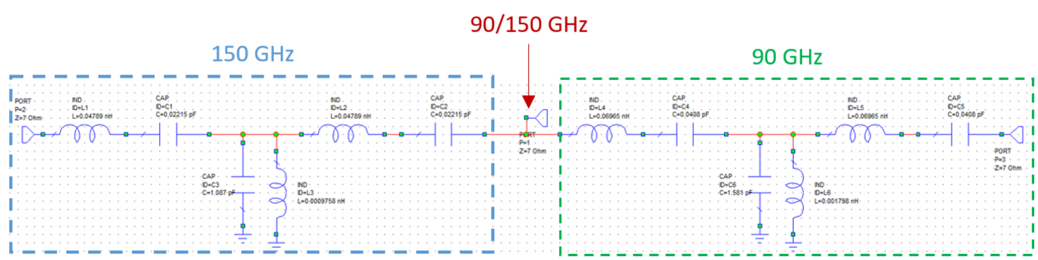

Figure 7.9: The preliminary lumped elements of the 90/150 GHz diplexer.

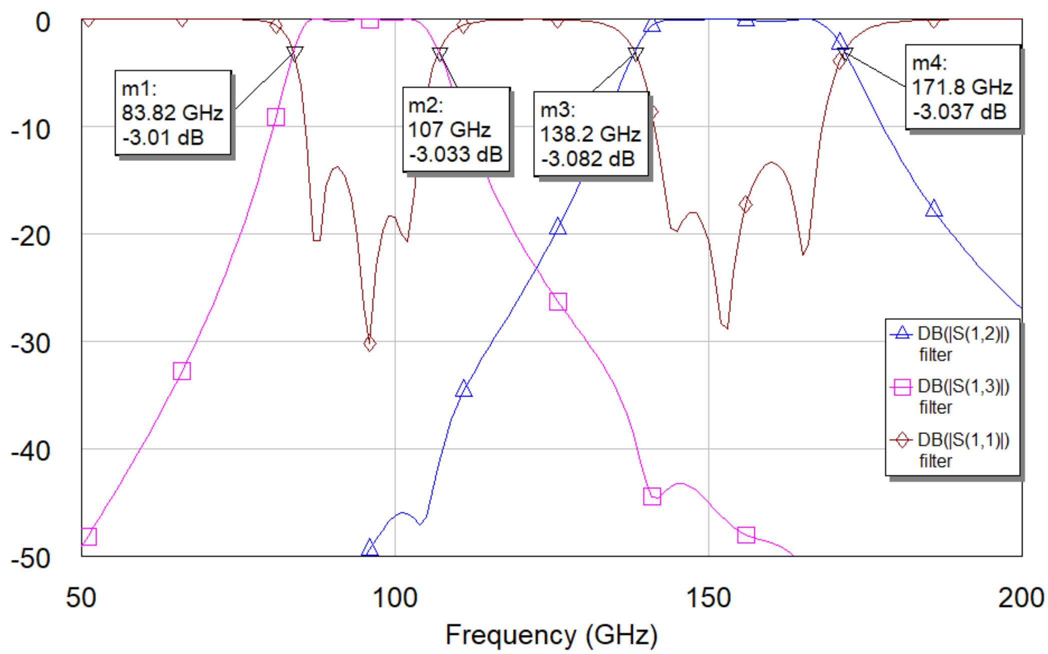

Figure 7.10: The simulated S-parameters of the dual-band diplexer.

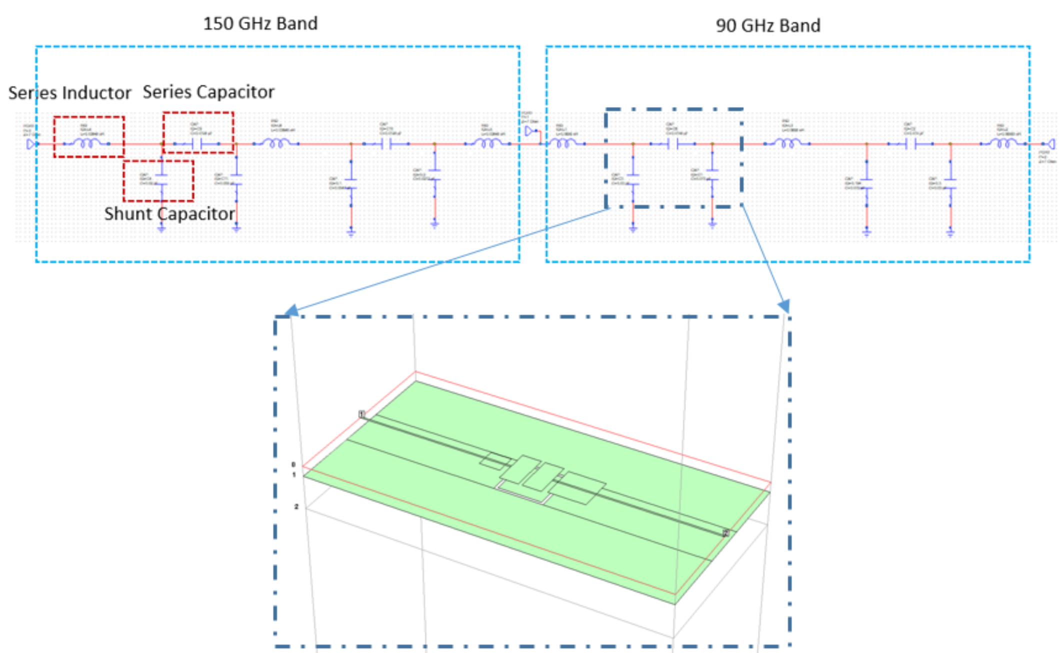

Figure 7.11: The lumped elements to the lithographic version representation of the diplexer. Top: The equivalent Π lumped network transformation. We represent the series inductor as a short CPW line, and series capacitor as a parallel plate. Bottom: The equivalent Sonnet simulation of the Π circuit section as an example of optimizing section by section before we gather the full circuit shown in Figure 7.14
.

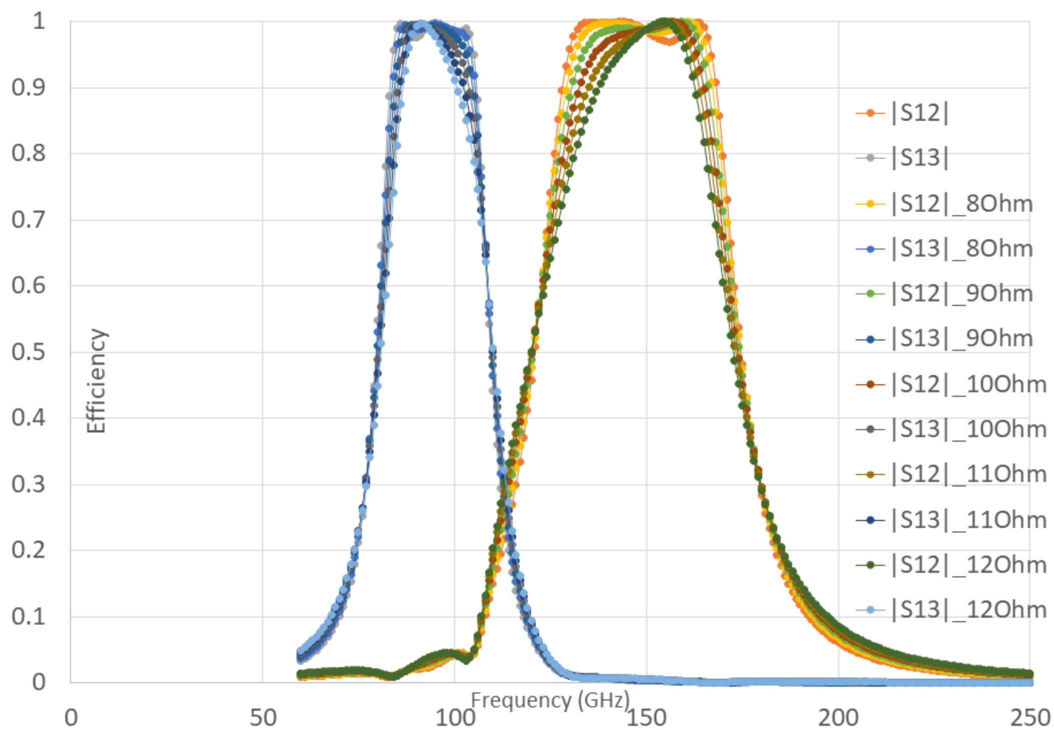

Figure 7.12: Diplexer study: The original input impedance is 7Ω. We vary the impedance and record the output spectrum. The results show a minimized in-band reflections.

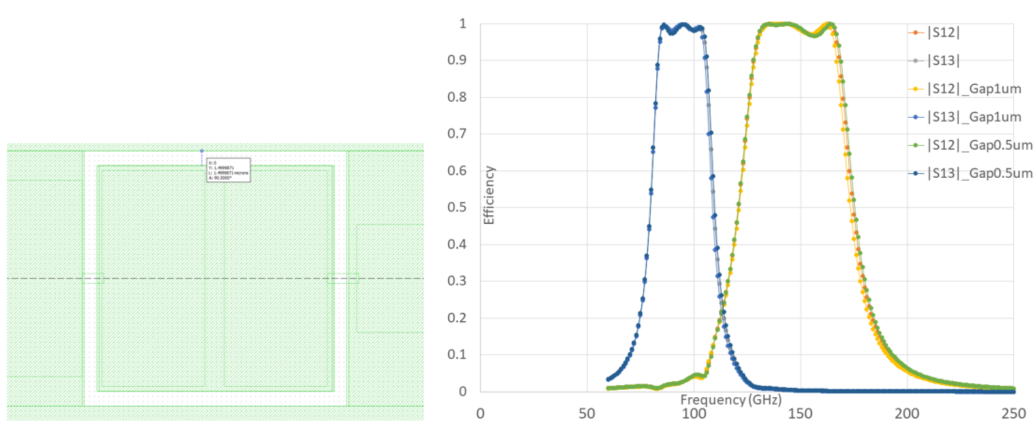

Figure 7.13: Diplexer study: The original capacitor plate distance with the ground plane is 1.5 um. The new circuit configuration seems to have a better stable performance against any fabrication tolerances.

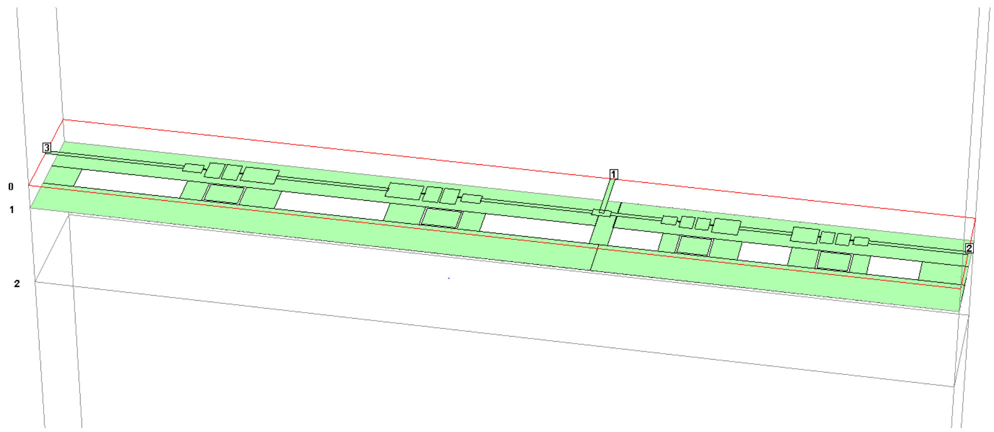

Figure 7.14: The equivalent lithographic version in Sonnet software from the lumped elements version.

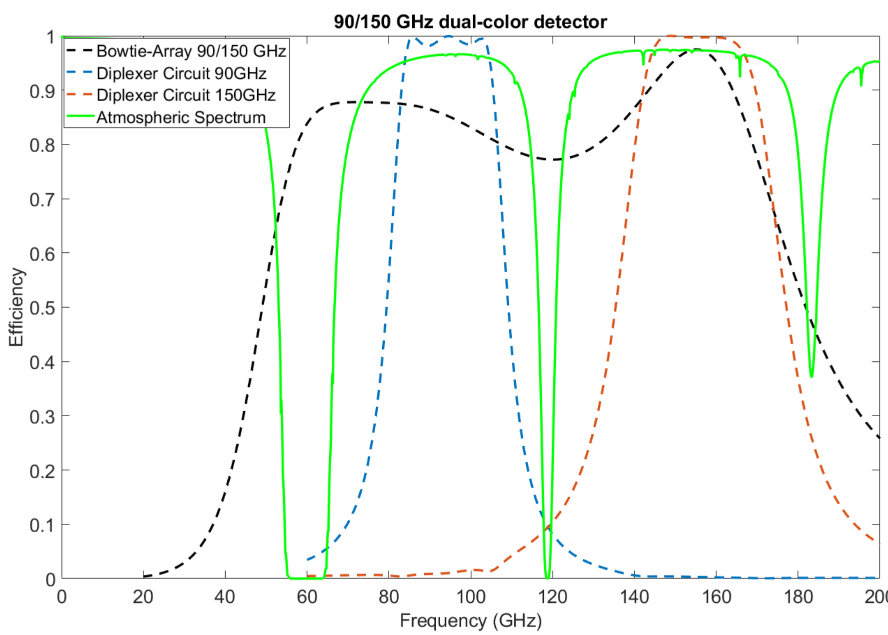

Figure 7.15: Dual-color 90/150 GHz detector: Bands of antennas and diplexer as individually simulated in HFSS and Sonnet. We co-plot these with the atmospheric spectrum at the South Pole to show that these do not overlap with atmospheric features at 118 GHz and 183 GHz. The final layout is ready for fabrication soon.

7.4 Dual-color Detector for CMB Observation Bands 150/220 GHz

We extended our dual color detector design to cover the two CMB observation bands at 150 GHz and 220 GHz simultaneously, as shown in 7.16. We explored another diplexer configuration similar to the old diplexer that we used for dual-color at 30/40 GHz. The simulated results suggest that the 6^{th} diplexer provides sharper edges between both bands. The estimated band-averaged NEP is 44 AW/$\sqrt{Hz}$ and 83 AW/$\sqrt{Hz}$ for 150 GHz and 220 GHz bands, respectively. We decided to postpone the fabrication of dual color detector at 150/220 GHz and focus on the fabrication of the dual color detector at 90/150 GHz (Section 7.3) for the coming CMB-S4 program.

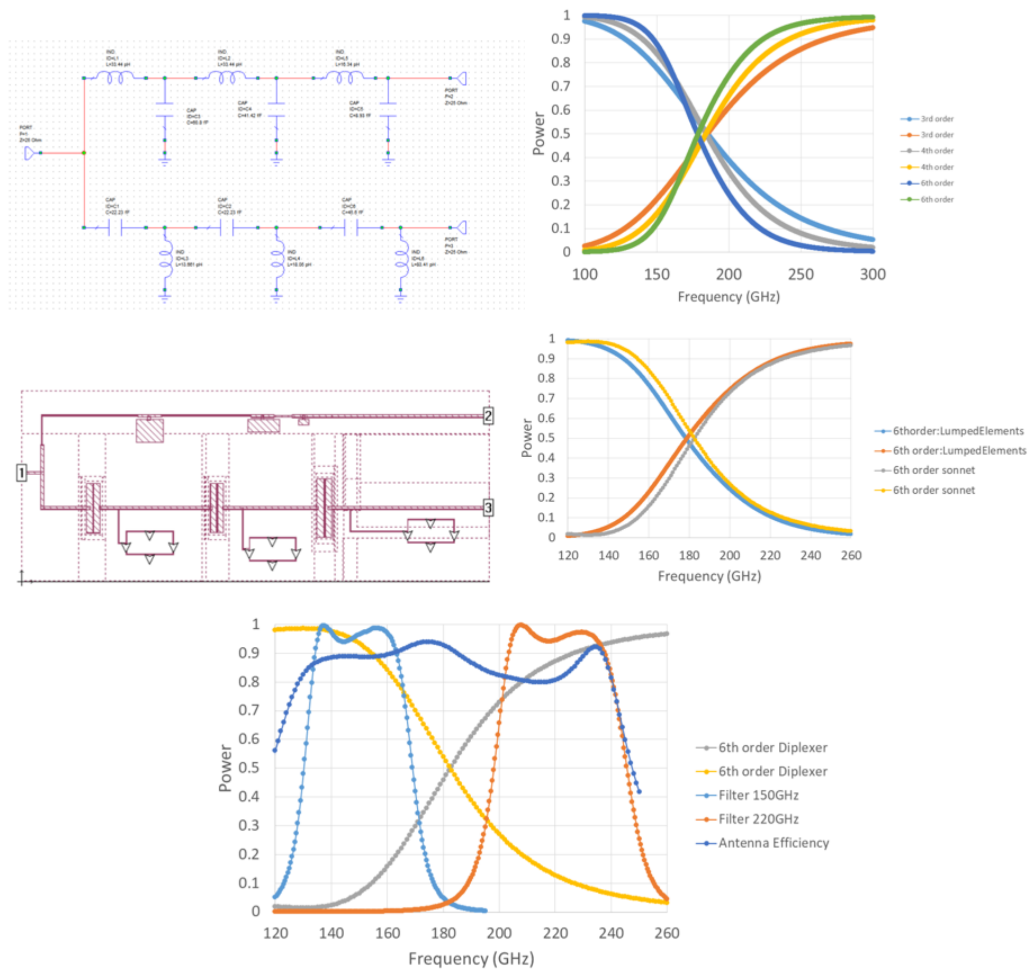

Figure 7.16: Dual-color 150/200 GHz detector. Top: diplexer design (3^{rd} , 4^{th} and 6^{th} order circuit models). Middle: The equivalent lithographic version in Sonnet. Bottom: The diplexer, bandpass filters and the phased Array response.

Chapter 8

NEXT GENERATION CRYOGENIC DETECTORS TESTING FOR CMB-S4

The success of our technology development for BICEP Array drives the world-leading constraints on inflationary gravitational waves. These technologies will provide crucial inputs into various design choices of the upcoming CMB-S4 Small-Aperture Telescopes (SAT) (CMB-S4 Collaboration, 2019). The CMB-S4 aims to design a cryostat with a focal plane base temperature of $\approx$ 100 mK by means of an Adiabatic Demagnetization Refrigerator (ADR) (Andre, et al., 1993). The ADR has been successfully worked with various cooling system. This chapter reports the cryogenic implementation and testing of ADR with BICEP cooler for 100 mK CMB-S4 detector arrays in a prototype 95/150 GHz dichroic telescope planned to observe on the existing BA3 receiver on BICEP Array telescope at the South Pole. This will enable the in-field performance for CMB-S4 technical developments.

8.1 Adiabatic Demagnetization Refrigerator (ADR) Implementation with BICEP Fridge

The Adiabatic Demagnetization Refrigerator (ADR) technology has been used for cooling infrared detectors for space application (Andre, et al., 1993 and Luchier, Duval, et al., 2012). The refrigerator provides an operating temperature down to few m-Kelvin with high cooling capacity that meets the detector noise requirements for far-IR space missions. The CMB-S4 (CMB-S4 Collaboration, 2019) aims to reduce the operating temperature (T_c) of the detectors, from the nominal 280 mk that we used for BICEP Array detectors to 100 mk using the ADR. The goal is to reduce the internal TES detector's noise equivalent power (NEP) by reducing (T_c), as shown in equation 3.9. However, we will be still limited by the photon noise.

A special test-bed has been used for our first ADR implementation with BICEP Fridge. The ADR system consists of a paramagnetic solid connected to the cooler to be cooled via a thermal switch. Figure 8.1 shows our first run of ADR implementation with BICEP cooler. The ADR has been installed on the new 4K plate. The heat switch has been mounted on the IC stage of the sorption fridge. The Mini Pump has been mounted on the side of the Fridge Bracket. The 1 K Kevlar intercept has been connected to the 4He stage of the sorption fridge. The 300 mK Kevlar has been connected to the IC. The mini-pump heat switch is used to either connect or isolate the ADR system from BICEP fridge.The ADR Rox and ADR cernox are used to monitor the temperature of the ADR cold end. The other side of the ADR contains the 2 NbTi current leads that are connected to the magnet. The magnet connected to feed-through with two external terminals that we used to apply the current to the magnet for magnetization test. The 300 mk and 100 mk thermometers have been thermalized away from 4K for a better cryogenic operation. The thermometers are wired to the cryostat and read-out using lake-shore devices. Figure 8.2 shows the calibration profiles for the ADR Rox and cernox. BICEP Fridge has started cooling down. The ADR system has started cooling down once we connect it to BICEP cooler by closing the heat switch. The ADR Rox and cernox cooled down to 4K and then the baseline temperature 350 mK after we cycled BICEP fridge, as shown in Figure 8.3.

8.2 ADR Magnetization and Demagnetization Test

The ADR system is cyclic. The AMI 430 programming device is used to control the applied current through the KEPCO power supply. The full system set-up is shown in Figure 8.4. We charge the ADR while connected to BICEP Fridge. We magnetize the ADR by gradually applying maximum current = 6A (1.3 tesla) to avoid quenching the inner coils. Python data acquisition has been used to control the current ramping rate for a constant temperature of 550 mK. Once the current reached our target current and became fully magnetized, we wait for the ADR system to stabilize and then isolate it from BICEP fridge by turning off the mini-pump heat switch. The ADR is ready for demagnetization. During the demagnetisation process, we lower the coil current gradually while having the cold temperature set-point of 100 mK. The current must decrease according to the set current ramp which must not be too high to reduce losses by the eddy currents. The ADR ROX and Cernox temperatures are going down during demagnetization until they settled at the temperature set point of 100 mK (current = 1.6 A), as shown in Figure 8.5. The reading values are summarized in table 8.1. The ADR could be connected to the cold load during the cold phase. We control the slat pill at 100 mK temperature by slowly reducing the current from 1.6 A to 0 A using an adjustable current ramp rate. The full ADR cycle is shown in Figure 8.6. When the current reached zero, the system must be recycled again following the same procedure. This is the adiabatic demagnetization process. At 6A, the thermal motions of the molecules on the salt pill are aligned with the external magnetic field. As the current reduced (magnetic

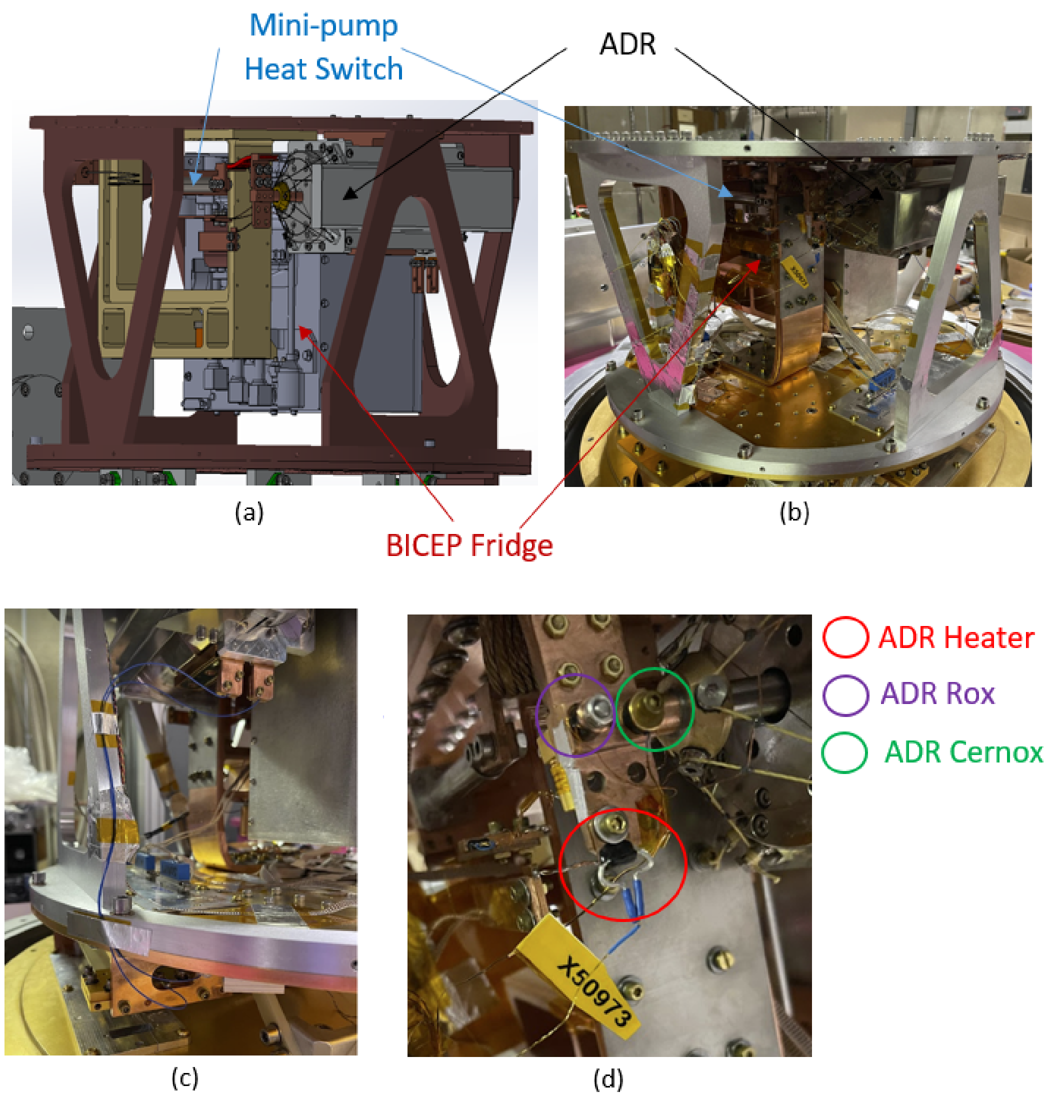

Figure 8.1: The modelled and real ADR connected to BICEP Fridge. (a) Solid work model, (b) The actual implementation, (c) The ADR connected to the magnet through 2 NbTi current leads, and (d) zoom-in of the ADR Rox, ADR cernox, and ADR heater connected at the ADR cold-end side.

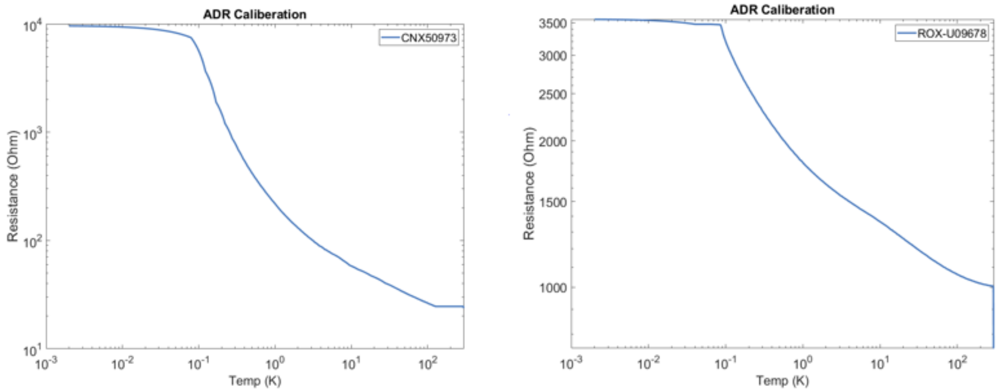

Figure 8.2: The calibration profiles of the ADR cernox and Rox, calibrated by our ADR cryostat at JPL. Left: ADR cernox. Right: ADR Rox.

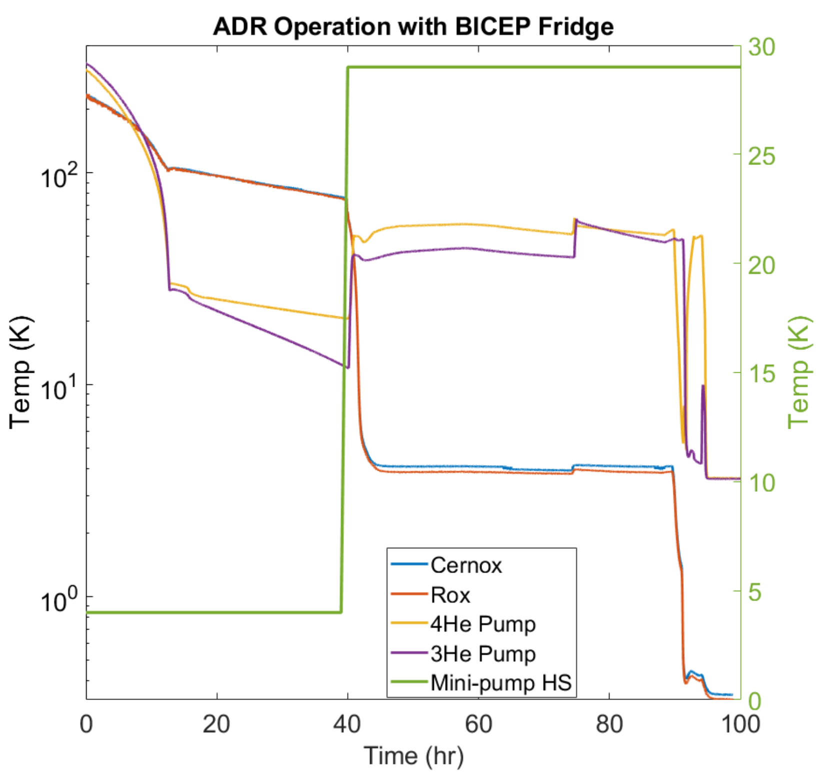

Figure 8.3: ADR operation with BICEP fridge during the cooling down process.

field is also reduced), they became de-aligned with each other. The thermal energy is thus transformed into magnetic energy, resulting in a cooling of salt pill and the attached load to the target temperature (100 mK) where the detectors can operate.

Figure 8.4: The ADR connection to the AMI430 and Kepco power supply and the cryostat through the two external terminals. The lake-shore device is reading the resistance of the ADR Rox.

Thermometer	Measured Temperature
ADR Cold End Rox	88 mk
ADR Cold End cernox	110 mk
Mini-Pump Heat Switch	29K ON 4K OFF

Table 8.1: ADR Rox and cernox readings during the cold phase after demagnetization process. We successfully implemented the ADR with BICEP fridge.

ADR energy

The energy of the ADR is obtained from the current ramping data during the magnetization. The current to the magnetic field ratio of the coil = 0.218 T/A. The resulting energy of the ADR as function of the magnetic field is shown in Figure 8.7. The measured Energy of the ADR system is 0.32 Joule.

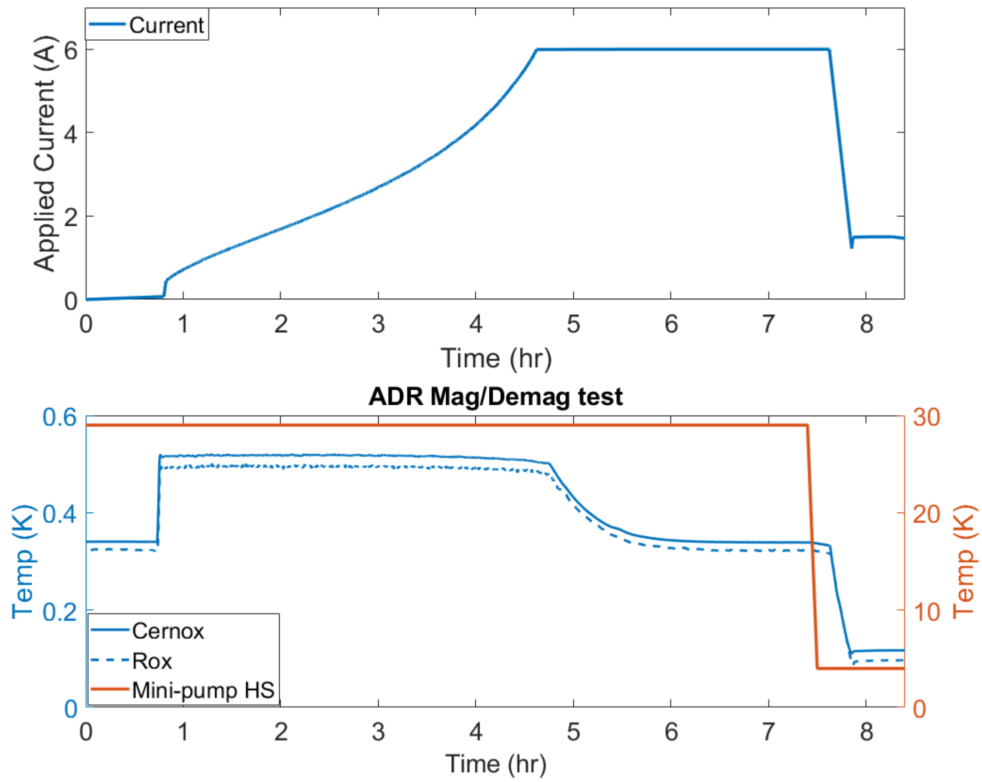

Figure 8.5: The ADR Magnetization/demagnetization: Top: the current profile, and Bottom: ADR Rox/cernox. ADR is magnetized at 550 mK while connected to the IC stage, after we cycled the sorption fridge.

8.3 ADR Enthalpy Measurement

We measured the enthalpy of the system by regulating the magnetic field through the applied current around 100 mK while applying different power to the ADR heater. We have applied 2 uW, 5 uW, 6 uW and 10 uW to the ADR heater through the attached power supply. We can then calculate the parasitic power due to thermal losses on the ADR by solving for $P_{parasitic}$ in the Enthalpy equation H:

$$H = t_1(P_{parasitic}) = t_2(P_{parasitic} + P_{applied}) \tag{8.1}$$

where t_1 and t_1 are the hold time. The measured H and $P_{parasitic}$ are listed in table 1 for different input power. As we increase the applied power, the ADR ran out sooner, as shown in Figure 8.8. Additionally, the parasitic load slightly reduces due to the change in the salt temperature as we go higher in the applied power in order

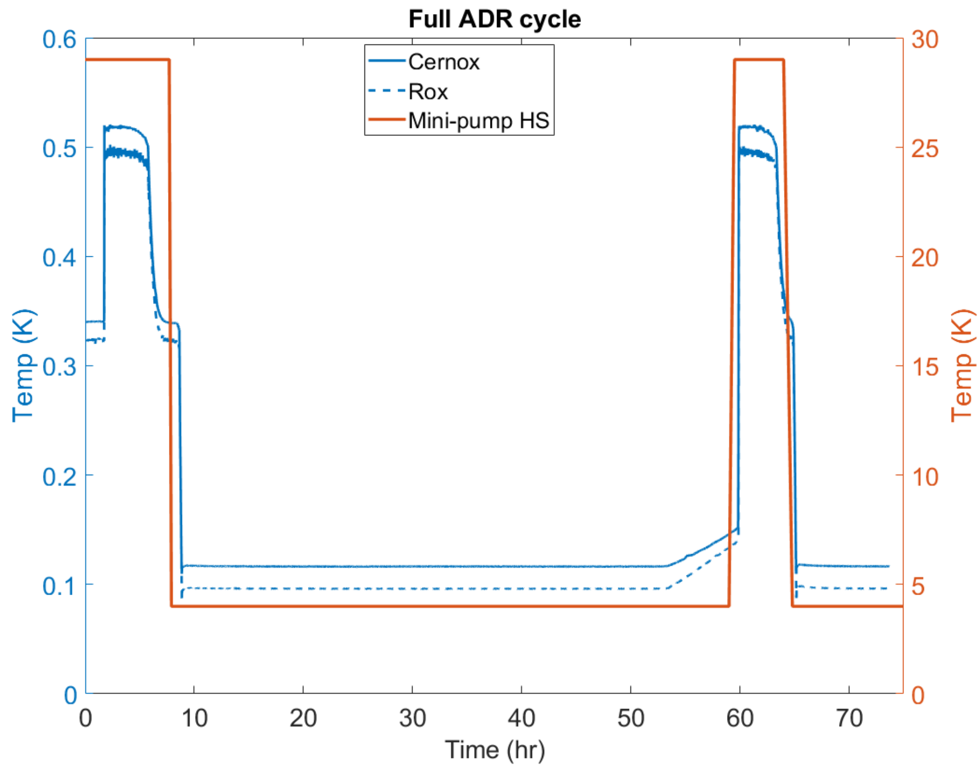

Figure 8.6: Full ADR cycle magnetization and demagnetization test.

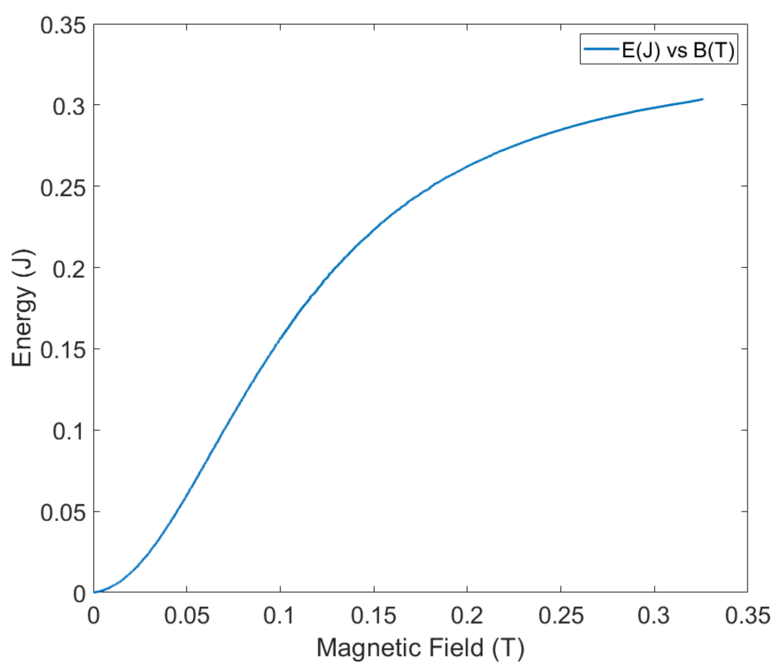

Figure 8.7: ADR energy as function of magnetic field.

to achieve the same exterior temperature. The measured heat load is about 2 uW, which is higher than expected. The ADR cycle hold time with 2 µW of applied power was 21 hours. The heat load on the ADR by itself should be a lot less than 2 uW. A possible cause of that high parasitic loss is some conducted power that is not intercepted by 300 mK, coming from Kevlar or wires or thermal conduction through the thermal switch, which tend to be about 15× smaller than 2 uW. The other most likely possible cause is some radiation bouncing around the cryostat since we did not blacken with stycast material inside 4K and we might have some light penetrations into the 4 K space. We concluded that the radiation background leakage should be the primary reason for that high parasitic load and we focused to close these radiation leaks in the following run.

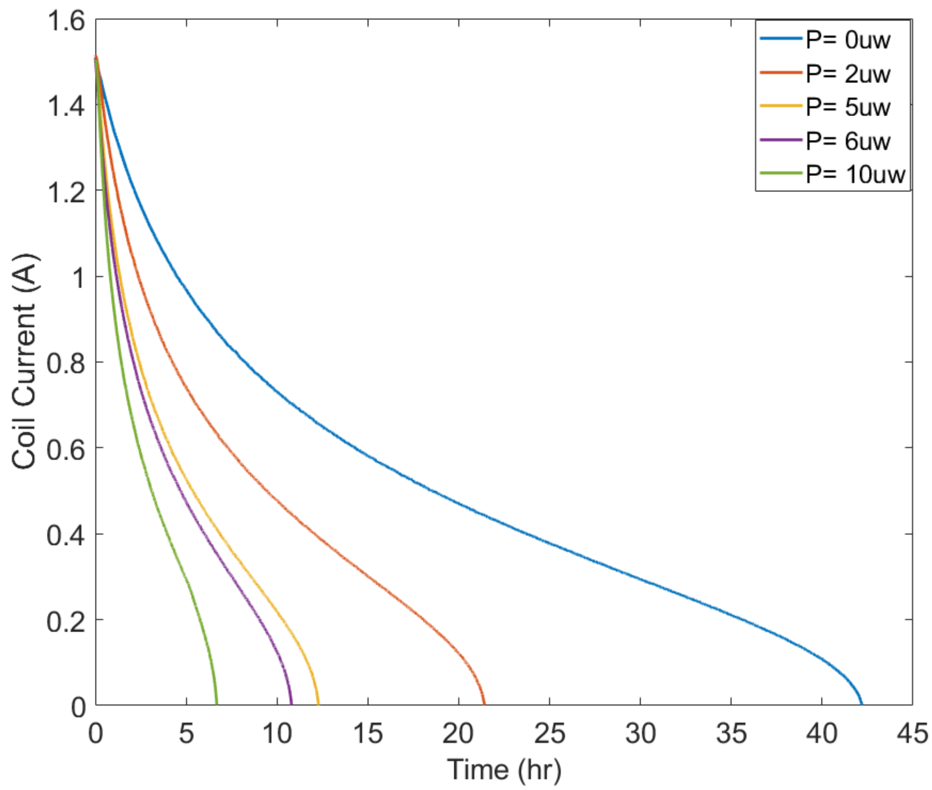

Figure 8.8: The current regulation profiles for 100 mK base temperature while different power applied during the first ADR cryogenic run.

Applied Power (uW)	Hold Time (hr)	$P_{parasitic}$ (uW)	Enthalpy (J)
0	42.12	2	0.315
2	21.42	2.068	0.3137
5	12.29	2.06	0.312
6	10.8	2.06	0.313
10	6.69	1.89	0.286

Table 8.2: The Enthalpy (H) measurement for different input power. The ADR has a bit less heat capacity than intended due to radiation leakage into the cryostat which we fixed in the second ADR run shown in section 8.4.

Thermal conductance (G) measurement

The thermal conductance (G) of salt pill has been measured around the baseline temperature. We did this measurement by taking a small step in power and record ΔT caused by that step so that we can calculate G at that reference temperature to be $\Delta P/\Delta T$. The resulting G is plotted in Figure 8.9 at three different temperatures around the operating baseline temperature, $G \approx$ 6-7 uW/mK at our base temperature of interest (90-120 mK). The measured G is proportional to the temperature, but it is consistently small around 100 mK.

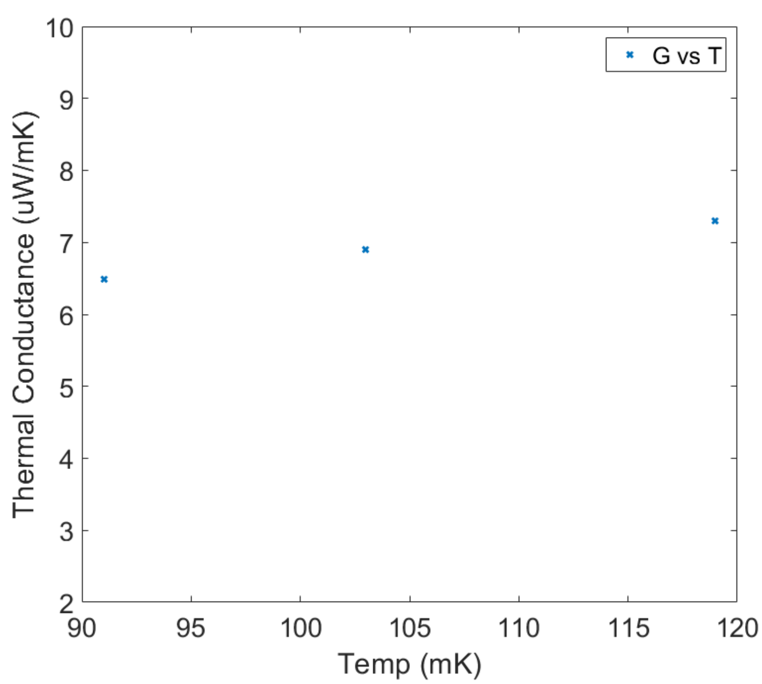

Figure 8.9: Thermal Conductance (G) as function of temperature around the baseline temperature of 100 mK.

8.4 Parasitic Losses Reduction

The second ADR cryogenic run diagnoses the possible causes for higher parasitic losses shown in Table 8.2 from the first run. Major modifications have been conducted in this run for minimizing the expected radiation leakage into 4K space. The first modification is that the 4K interior has been blackened with a stycast material to minimize the interior reflections. Few light leaking holes in the 4K have been found in the first run. We fully covered these light leaks with aluminum tape during the second run. Figure 8.10 shows that the modifications have successfully minimized the heat load by a factor of 4, from 2 uW (first run) to 0.49 uW (second run) at 100 mK. The ADR cycle lasted for about 172 hours compared to the 42 hours hold time during the first run without any applied power. The estimated ADR cycle hold time is about 36 hours with 2 uW applied power. The designed hold time is 48 hours with 2 uW applied power. The residual magnetic field is measured to be in order of few uT outside the ADR. Further cryogenic optimization is in progress. The resulting measured Enthalpy is $\sim$ 0.34 J. The ADR has been successfully implemented and tested with BICEP Fridge and it is working as it should be for 100 mK CMB-S4 detector arrays. Our next step is to integrate the ADR system with PSAT BICEP Array cryostat to be tested with the S4 full optical system and dual-color detectors with the goal of deployment to the South Pole by 2024-2025.

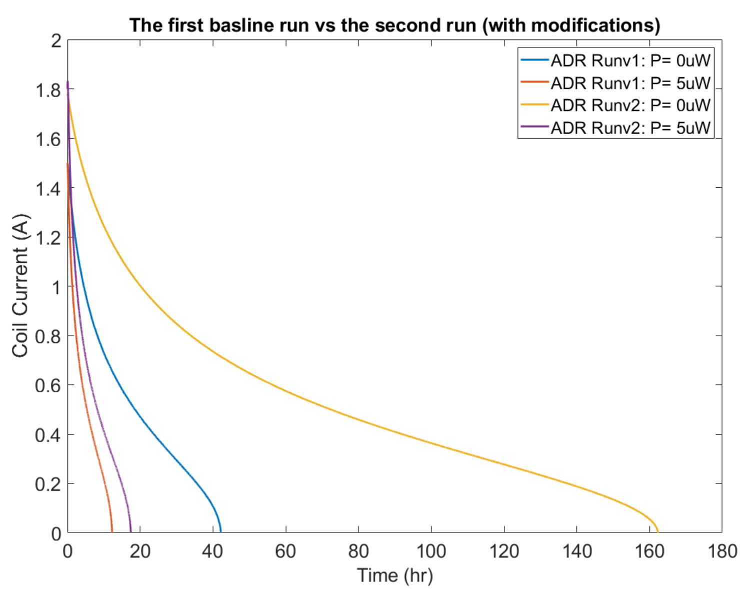

Figure 8.10: The current regulation profiles for the first run versus the second run (with modifications). The radiation leakage has been fixed during the second ADR run. The resulting hold time of the ADR is about 170 hours without load.

Chapter 9

CONCLUSION

The detection of the “B-mode polarization pattern” that arises from “the inflationary gravitational waves” would open a new window to probe the early Universe $\approx 10^{-35}$s after the Big Bang. The inflation predicts “the primordial gravitational-wave (PGW)” to be at a detectable level. We are chasing it but we do not have an absolute confidence of its existence. My thesis aims to develop highly sensitive detectors and instrumentation to reach the ultimate sensitivity to search for this very faint pattern that left over from the creation of the universe, revealing to us what it was like in the beginning. Our attempts to measure such faint signature reminded me with my chat with Kip Thorne in his office at Caltech back to 2016. Kip mentioned the challenges and the incremental development of “LIGO” on chasing “the gravitational waves” for more than three decades until it was finally detected for the first time, as it was predicted by Albert Einstein in his general theory of relativity, 1916. So, I wish to detect the PGW in the near future.

The growth of technology improvement on BICEP/Keck experiments has led our team to have the world-leading constraints on PGWs through the data collected up to the 2018 season, which helps us to better understanding how (or if) this rapid expansion occurred. Our latest BK18 data (Ade, et al. (BICEP/Keck Collaboration), 2021) has the strongest constraints on r to-date, $r_{0.05} < 0.036$ (95% C.L.) and $\sigma(r) = 0.009$, as shown in Figure 9.1. The contamination resources on r are mainly coming from the foregrounds and gravitational lensing. Our team members ran MLsearch as well as Fisher simulations for $\sigma(r)$ without dust nor gravitational lensing, yields $\sigma(r) = 0.002$ based on BK18 baseline data. $\sigma(r)$ is estimated to be 0.004 without lensing, while $\sigma(r)$ is simulated to be 0.007 without foreground parameters (dust amplitude is set to zero). The major uncertainty on r comes from the sample variance on lensing foreground. The preliminary collaboration between BICEP/Keck and SPT-3G successfully demonstrated the B-mode lensing removal (The BICEP/Keck and SPTpol Collaborations, 2020) based on old BK14 data. Further interesting analysis enabling a deeper search for inflationary gravitational waves is coming soon.

BICEP Array telescope has the significant role on constraining the foregrounds.

BICEP Array expects to achieve $\sigma(r) < 0.002$-0.004 by 2027, depending on foreground complexity and delensing with the SPT-3G, as shown in Figure 9.2. BICEP Array is mapping the polarization of the CMB with four receivers. The fourth receiver will be a collaboration between BICEP/Keck and CMB-S4 program to observe the sky of the South Pole with detector tiles operating with 100 mK base temperature, as I introduced in Chapter 8. The first BICEP Array receiver (BA1) has been developed for constraining the synchrotron foreground at 30/40 GHz. The engineering design of BICEP Array detectors has been presented in Chapter 3. The design and demonstration of the focal plane frame has been introduced on Chapter 4 for tight control of the beam systematic and consequently improving our limits on r. The laboratory measurements demonstrated and validated our modelled response at Caltech, as shown in Chapter 5. The demonstration of the dual-band detector technology has been presented in Chapter 7 as well as this promising technology has been extended to cover two CMB observing bands at 90/150 GHz. BA1 has been successfully deployed to the South Pole during the 2019 austral season. Chapter 6 details our efforts on the optical characterization to validate our optical design and other calibration tests at the South Pole. This chapter also addressed the engineering challenges during the first observing season and the diagnostic tests that we have done at Caltech to solve these problems. Our upgrades during the second and third observation seasons successfully addressed most of these challenges. The filter configuration upgrades during the second observation season eliminated the out-band loading and consequently highly improved the mapping speed. During the third observation season, we upgraded BA1 with high-performing detector tiles fabricated with the new "Inverted TES process." These new deployed detector tiles have high optical efficiency and much better 6" wafer uniformity and a reasonable normal resistance for lower magnetic susceptibility. Our challenging experience with BA1 benefits us for other BICEP Array receiver at 150 GHz (deployed this season) and 220/270 GHz to have a better performance. The 2020 30/40 GHz observation data improved the synchrotron amplitude A_{sync} by factor of $\approx$2, from 1.4 uK^2 to 0.88 uK^2 (95% Confidence) in the maximum likelihood search (Figure 9.1) despite all the problems described in Chapter 6. The 2023 observation season for BA1 is expected to have much better CMB data compared to 2020 and 2021 seasons after the receiver upgrades. The 2023 on-sky science data is currently analyzed. Since we have sufficient information about the polarized dust emission from the previous high frequency BICEP/Keck telescopes, the BA1 data about the polarized synchrotron foreground would be an essential step with the "delensing" efforts for constraining the inflationary gravitational waves in the near future.

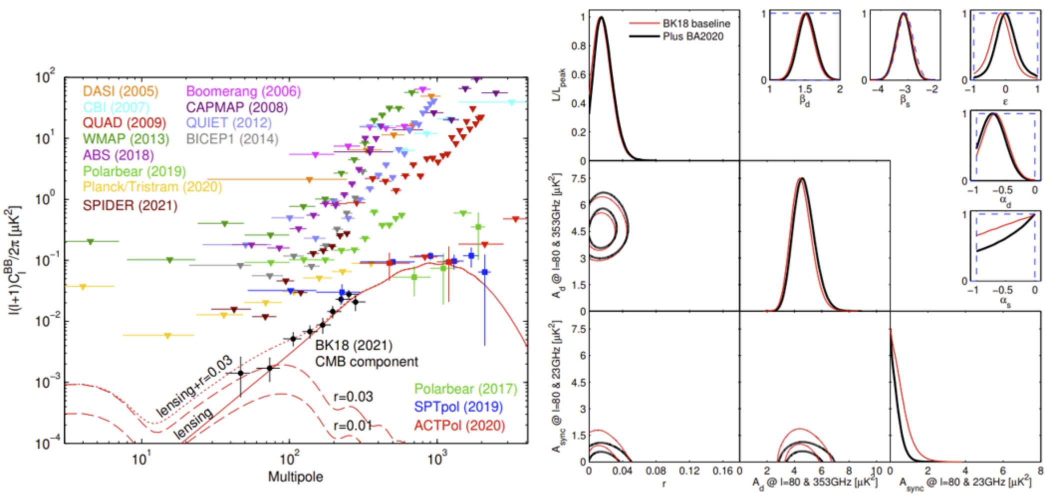

Figure 9.1: The effect of BA1 receiver data during the first deployment season. Left: summary of up-to-date B-mode polarization upper limit constraints from different experiments (Ade, et al. (BICEP/Keck Collaboration), 2021). The theoretical prediction for the lensing B-modes is plotted in solid red, while the gravitational wave B-modes is plotted in dashed red for two values. The BK18 data is shown after removing Galactic foregrounds. Right: Results of a multi-component multi-spectral likelihood analysis for synchrotron foreground parameters by using BICEP/Keck, WMAP, and Planck plus the 2020 BA1 observation season (Crumrine, 2022). This additional BA1 data tightens the constraints on A_{sync} by factor of $\sim$ 2 compared to the estimated value from BK18. We expect to have much deeper constraints on synchrotron with the additional 2022 and 2023 seasons after the instrument upgrades.

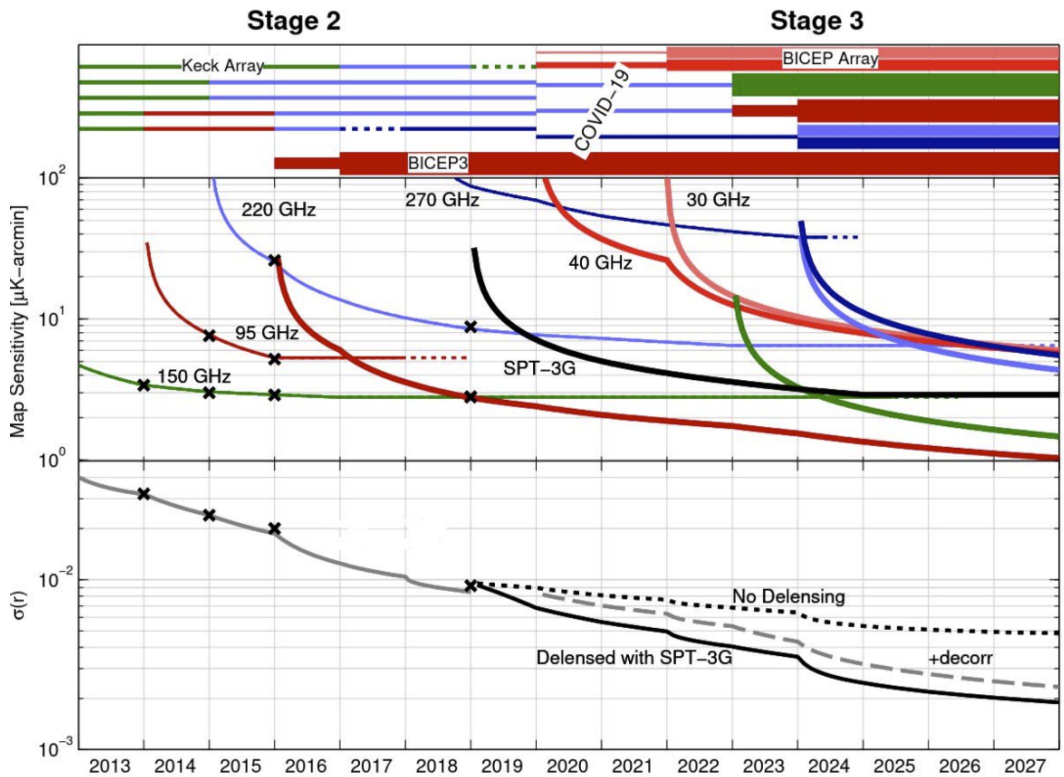

Figure 9.2: The projected sensitivity (achieved and planned) with BICEP Array telescope. The top panel represents the receiver throughput at the various frequencies by observing season. The middle panel shows map sensitivity at each frequency. Each color represents one frequency band. The light red curve represent the low frequency receiver which is the topic of this thesis. The black line indicates the depth of the SPT-3G combined 95/150 GHz map projected from the achieved sensitivity of the 2019/20 data. We deployed 30/40 receiver and has started observation in 2020. The deployment of new upgraded detectors to address the 2020 challenges has been delayed by COVID-19. 2023 season works better for BA1. BA2 has been deployed to the South Pole this season. We plan to deploy the other two receivers in the next few years. The bottom panel is the sensitivity versus time. The crosses are the achieved sensitivities reported in our publications (up to BK18). The uncertainty on r will be also highly depend on the "delensing" with the SPT-3G for BICEP Array data, which becomes increasingly important.

BIBLIOGRAPHY

Adam, R., P. A. R. Ade, N. Aghanim, Y. Akrami, et al. (Planck Collaboration) (2016). "Planck 2015 results-i. overview of products and scientific results." In: *The Astronomy and Astrophysical Journal*. DOI: 10.1051/0004-6361/201527101.

Ade, P. A. R., et al. (BICEP/Keck Collaboration) (2021). "Improved constraints on primordial gravitational waves using Planck, WMAP, and BICEP/Keck observations through the 2018 observing season." In: *Phys. Rev. Lett.* DOI: 10.1103/PhysRevLett.127.151301.

– (2022). "Bicep/keck xv: The bicep3 cosmic microwave background polarimeter and the first three-year data set." In: *The Astrophysical Journal*. DOI: 10.3847/1538-4357/ac4886.

Ade, P. A. R., et al. (BICEP2, Keck Array, and Spider Collaborations) (2015). "Antenna-coupled TES bolometers used in BICEP2, Keck array, and SPIDER." In: *The Astrophysical Journal*. DOI: 10.1088/0004-637X/812/2/176.

Ade, P. A. R., G. Pisano, et al. (2006). "A review of metal mesh filters." In: *Proc. SPIE*. DOI: 10.1117/12.673162.

Ade, P.A.R., et al. (BICEP/Keck Collaboration) (2018). "Improved constraints on primordial gravitational waves using Planck, WMAP, and new BICEP2/Keck observations through the 2015 season." In: *Phys. Rev. Lett.* DOI: 0.1103/PhysRevLett.121.221301.

– (2019). "BICEP2/Keck Array XI: Beam Characterization and Temperature-to-Polarization Leakage in the BK15 Data Set." In: *The Astrophysical Journal*. DOI: 10.3847/1538-4357/ab391d.

Ade, P.A.R., et al. (BICEP2 Collaboration) (2015). "BICEP2 III: Instrumental Systematics." In: *The Astrophysical Journal*. DOI: 10.1088/0004-637X/814/2/110.

Aghanim, N., et al. (Planck Collaboration) (2021). "Planck 2018 results. VI. Cosmological parameters." In: *The Astronomy and Astrophysical Journal*. DOI: 10.1051/0004-6361/201833910.

Aghanim, N., Y. Akrami, et al. (Planck Collaboration) (2018). "Planck 2018 results. I. Overview and the cosmological legacy of Planck." In: *Astronomy and Astrophysics*. DOI: 10.1051/0004-6361/201833880.

Alan H. Guth (1981). "Inflationary universe: A possible solution to the horizon and flatness problems." In: *Physics Rev. D*. DOI: 10.1103/PhysRevD.23.347.

Andre, Clapp, et al. (1993). "100-mK magnetic refrigerators for low background bolometric receivers." In: *Proceedings of Infrared Detectors and Instrumentation (SPIE)*. DOI: 10.1117/12.158723.

Andreas Albrecht and Paul Steinhardt (1982). "Cosmology for Grand Unified Theories with Radiatively Induced Symmetry Breaking." In: *Phys. Rev. Lett.* DOI: 10.1103/PhysRevLett.48.1220.

CMB-S4 Collaboration (2019). "CMB-S4 science case, reference design, and project plan." In: *arxiv*. DOI: 10.48550/arXiv.1907.04473.

Cornelison, J., et al. (BICEP/Keck Collaboration) (2020). "Polarization calibration of the Bicep3 cmb polarimeter at the south pole." In: *Proc. SPIE*. DOI: 10.1016/j.cryogenics.2012.01.029.

Crumrine, Michael (2022). "BICEP Array: Searching for Signals of Inflation from the South Pole." PhD thesis. University of Minnesota.

Duband, L., T. Prouve, et al. (2018). "Sub-Kelvin cooling for the BICEP array project." In: *Proceedings of the 20th International Cryocooler Conference*. DOI: 10.48550/arXiv.2009.09997.

Edward Kolb and Michael Turner (1994). "The Early Universe." In: *Front.Phys.*

Einstein, Albert (1915). "Die Feldgleichungen der Gravitation." In: *Sitzungberichte der Königlich Preußischen Akademie der Wissenschaften*.

Emory, F., et al. (2003). "E/B decomposition of finite pixelized CMB maps." In: *Physics Rev. D*. DOI: 10.1103/PhysRevD.67.023501.

Fixsen, D. J. (2009). "The temperature of the cosmic microwave background." In: *The Astrophysical Journal*. DOI: 10.1088/0004-637X/707/2/916.

Fixsen, D. J., et al. (1996). "The cosmic microwave background spectrum from the Full COBE FIRAS data set." In: *The Astrophysical Journal*. DOI: 10.1086/178173.

Friedman, A. (1922). "Über die Krümmung des Raumes." In: *Zeitschrift fur Physik 10*. DOI: 10.1007/BF01332580.

Fuskeland, U., et al. (2014). "Spatial variations in the spectral index of polarized synchrotron emission in the 9 YR WMAP sky maps." In: *Astrophysical Journal*. DOI: 10.1088/0004-637X/790/2/104.

Germaine, Tyler St. (2021). "Beam Systematics and Primordial Gravitational Wave Constraints from the BICEP/Keck Array CMB Experiments." PhD thesis. Harvard University.

Hubble, Edwin (1929). "Relation between distance and radial velocity among extragalactic nebulae." In: *Proceedings of the National Academy of Sciences*. DOI: 10.1073/pnas.15.3.168.

Hui, H. (2018). "Measuring the Polarization of the Cosmic Microwave Background with BICEP3." PhD thesis. California Institute of Technology.

Hui H., P. A. R. Ade, et al. (BICEP/Keck Collaboration) (2018). “BICEP Array: a multi-frequency degree-scale CMB polarimeter.” In: *Proceedings of Millimeter, Submillimeter, and Far-Infrared Detectors and Instrumentation for Astronomy (SPIE)*. DOI: 10.1117/12.2311725.

Irwin, K. D. and G.C. Hilton (2005). “Transition-edge sensors.” In: *Cryogenic Particle Detection Book*. DOI: 10.1007/10933596_3.

Kamionkowski, M. and E. D. Kovetz (2016). “The Quest for B Modes from inflationary gravitational waves.” In: *Annual Review of Astronomy and Astrophysics*. DOI: 10.1146/annurev-astro-081915-023433.

Kamionkowski, M., A. Kosowsky, and A. Stebbins (1997). “A Probe of Primordial Gravity Waves and Vorticity.” In: *Phys. Rev. Lett.* DOI: 10.1103/PhysRevLett.78.2058.

Kang, Jae Hwan (2020). “Measurement of the Polarization of the Cosmic Microwave Background with the BICEP3 and Keck Array Telescopes.” PhD thesis. Stanford University.

Karkare, Kirit S. (2017). “Multifrequency Beam Systematics and Measurements of B-Mode Polarization with the BICEP/Keck Array Cosmic Microwave Background Experiments.” PhD thesis. Harvard University.

Kovac, J. M., et al. (2002). “Detection of polarization in the cosmic microwave background using DASI.” In: *Nature*. DOI: 10.1038/nature01269.

Lewis, A., et al. (2002). “Efficient computation of cosmic microwave background anisotropies in closed friedmann-robertson-walker models.” In: *Astrophysical Journal*. DOI: 10.1086/309179.

Linde, A.D. (1982). “A new inflationary universe scenario: A possible solution of the horizon, flatness, homogeneity, isotropy and primordial monopole problems.” In: *Physics Rev. B*. DOI: 10.1016/0370-2693(82)91219-9.

Mather, J. C., et al. (1994). “Measurement of the cosmic microwave background spectrum by the cobe firas instrument.” In: *The Astrophysical Journal*. DOI: 10.1086/173574.

Mather, John C. (1982). “Bolometer noise: nonequilibrium theory.” In: *Applied Optics*. DOI: 10.1364/AO.21.001125.

Matias Zaldarriaga and Uros Seljak (1997). “An all-sky analysis of polarization in the microwave background.” In: *Physics Rev. D*. DOI: 10.1103/PhysRevD.55.1830.

Moncelsi, L., P. A. R. Ade, et al. (BICEP/Keck Collaboration) (2020). “Receiver development for BICEP Array, a next generation CMB polarimeter at the South Pole.” In: *Proceedings of Millimeter, Submillimeter, and Far-Infrared Detectors and Instrumentation for Astronomy (SPIE)*. DOI: 10.1117/12.2561995.

N. Luchier, J.M. Duval, L. Duband, T. Tirolien (2012). "Performances of the 50 mK ADR/sorption cooler." In: *Cryogenics*. DOI: 10.1016/j.cryogenics.2012.01.029.

National Research Council (2021). "Pathways to Discovery in Astronomy and Astrophysics for the 2020s." In: *The National Academies Press*. DOI: 10.17226/26141.

O'Brient, R., et al. (2018). "Thermal kinetic inductance detectors for CMB and sub millimeter observations." In: *Millimeter, Submillimeter, and Far-Infrared Detectors and Instrumentation for Astronomy IX*. DOI: 10.1117/12.2314372.

O'Brient, Roger (2010). "A Log-Periodic Focal-Plane Architecture for Cosmic Microwave Background Polarimetry." PhD thesis. University of California, Berkeley.

Palladino, Steven (2021). "Constraining Primordial Gravitational Waves with BICEP/Keck Array Telescopes and Developing the BICEP Array HousekeepingSystem." PhD thesis. University of Cincinnati.

Penzias, A. A. and Wilson, R. W. (1965). "A measurement of excess antenna temperature at 4080 mc/s." In: *The Astrophysical Journal*. DOI: 10.1086/148307.

Piet de Korte, et al. (2002). "Time-division superconducting quantum interference device multiplexer for transition-edge sensors." In: *Review of Scientific Instruments*. DOI: 10.1063/1.1593809.

Pozar, David M. (2004). In: *Microwave Engineering*.

Schillaci, A., P. A. R. Ade, et al. (BICEP/Keck Collaboration) (2020). "Design and Performance of the First BICEP Array Receiver." In: *Journal of Low Temperature Physics*. DOI: 10.1007/s10909-020-02394-6.

Smoot, G. F. et al. (1992). "Structure in the COBE differential microwave radiometer first-year maps." In: *The Astrophysical Journal*. DOI: 10.1086/186504.

Soliman, A., P. A. R. Ade, et al. (BICEP/Keck Collaboration) (2018). "Design and performance of wide-band corrugated walls for the BICEP Array detector modules at 30/40 GHz." In: *Proceedings of Millimeter, Submillimeter, and Far-Infrared Detectors and Instrumentation for Astronomy (SPIE)* 10708. DOI: 10.1117/12.2312942.

– (2020). "Optical design and characterization of 40-GHz detector and module for the BICEP Array." In: *Journal of Low Temperature Physics*. DOI: 10.1007/s10909-019-02299-z.

– (2022). "2022 upgrade and improved low frequency camera sensitivity for CMB observation at the South Pole." In: *Proceedings of Millimeter, Submillimeter, and Far-Infrared Detectors and Instrumentation for Astronomy (SPIE)*. DOI: 10.1117/12.2628058.

Starobinsky, A.A. (1980). "A new type of isotropic cosmological models without singularity." In: *Phys. Rev. B*. DOI: 10.1016/0370-2693(80)90670-X.

The BICEP/Keck and SPTpol Collaborations (2020). "A demonstration of improved constraints on primordial gravitational waves with delensing." In: *Phys. Rev. D*. DOI: 10.1103/PhysRevD.103.022004.

Wayne Hu and Scott Dodelson (2002). "Cosmic microwave background anisotropies." In: *Ann. Rev. Astron. Astroph.* DOI: 10.48550/arXiv.astro-ph/0110414.

Willmert, Justin (2019). "Constraining Inflationary B-Modes with the BICEP/Keck Array Telescopes." PhD thesis. University of Minnesota.

Yang, Hung-I (2021). "Constraining Primordial Gravitational Waves and Characterizing B-Modes with the Keck Array and BICEP3 CMB Experiments." PhD thesis. Stanford University.

Zhang, Cheng (2023). "The Development and Performance of the First BICEP Array Receiver at 30/40 GHz for Measuring the Polarized Synchrotron Foreground." PhD thesis. California Institute of Technology.

Zmuidzinas, J. (2003). "Thermal noise and correlations in photon detection." In: *Applied Optics*. DOI: 10.1364/AO.42.004989.